Sede Amministrativa: Università degli Studi di Padova

Dipartimento di TECNICA E GESTIONE DEI SISTEMI INDUSTIALI

CORSO DI DOTTORATO DI RICERCA IN INGEGNERIA MECCATRONICA E DELL'INNOVAZIONE DEL PRODOTTO

CURRICOLO IN MECCANICA DEI MATERIALI

CICLO XXXVI

ADVANCED STRESS ANALYSIS OF LONG FIBRE COMPOSITE COMPONENTS MADE WITH ADDITIVE MANUFACTURING

Coordinatore: Ch.ma Prof. Daria Battini

Supervisore: Ch.mo Prof. Michele Zappalorto

Co-Supervisore: Dr. Lucio Maragoni

Dottorando: Matteo Pastrello

Ringraziamenti

Tre anni di dottorato sono un percorso di grandi soddisfazioni e crescita personale accompagnati da grandi difficoltà. Sarebbe stato impossibile terminare questo percorso senza le persone che in questo periodo mi sono state vicine e mi hanno supportato.

Un profondo ringraziamento va al Professor Zappalorto, per la possibilità che mi ha dato e l'immensa fiducia dimostrata nei miei confronti durante tutti questi anni. Lo ringrazio per avermi permesso di esplorare e sfruttare al meglio le mie capacità, fornendomi sempre consigli preziosi e rivelandosi una guida inestimabile per questo lavoro e in queste fasi delicate della mia carriera. Lo ringrazio inoltre per la passione che è riuscito a trasmettermi in questi argomenti, principale motore che mi ha spinto attraverso tutte le difficoltà incontrate in questo percorso.

Un ringraziamento particolare va a mia mamma e mio papà, che in tutta la mia vita si sono sempre dimostrati essere genitori eccezionali, sopportando enormi sacrifici per il mio bene. Forte del fatto che, qualunque fosse la mia scelta, avrei avuto il loro supporto incondizionato, ho potuto intraprendere la rischiosa e difficile strada del mondo accademico. Li ringrazio infinitamente per tutto l'affetto e l'aiuto che mi hanno fornito durante questi tre anni.

In egual misura voglio ringraziare Elisa, per la forza e la pazienza di sopportare e supportare un partner che, in questi tre anni, è stato fin troppo assente. Nonostante tutte le difficoltà di questo percorso non ha mai smesso di credere in noi e di ricambiare il mio amore incondizionatamente.

Ringrazio Marco per la sua disponibilità nel sopperire ai bisogni della famiglia con un fratello troppo impegnato a lavorare per essere presente. Il nostro rapporto a molti sembra strano ma la fiducia ed enorme stima che ci lega non è messa in discussione da nessuno che ci conosce sufficientemente a fondo.

Ringrazio Paola, Renzo e Chiara che mi hanno dato accoglienza, comprensione ed aiuto ad ogni occasione, facendomi sempre sentire parte integrante della loro famiglia.

Un ringraziamento particolare va ad Alessandro, che con la sua immensa disponibilità e costante guida mi ha aiutato a diventare un miglior ricercatore, i suoi consigli saranno sempre ben accetti e la sua opinione sempre tenuta in altissima considerazione.

Ringrazio infine Giulia, senza la quale non sarei arrivato alla fine di questo percorso. Siamo sempre stati in grado di darci supporto reciproco in questo percorso comune, sopperendo uno alle mancanze dell'altro. La ringrazio inoltre per la sua immensa disponibilità, pazienza e onestà nei miei confronti, delle qualità rare da trovare nelle persone.

Contents

Abstract

Additive Manufacturing (AM), commonly known as 3D printing, has revolutionized traditional manufacturing by enabling the production of intricate and customized structures. It brings advantages such as the creation of components with complex geometries and the potential for cost savings, especially in scenarios with low production volumes. However, drawback of this technology exists, notably the propensity for unwanted porosity in parts. Among the various technologies falling under the umbrella of Additive Manufacturing, this thesis focuses on Fused Deposition Modeling (FDM), prevalent in the field of composite materials. The main contributions of the thesis include the development of several analytical models that consider the effects of defects and design features introduced by FDM manufacturing processes. These models specifically address stress states in composite bodies, focusing on factors like porosities and localized reinforcements. The analytical models are validated against Finite Element methods, demonstrating their reliability in describing stress field in the studied areas.

Despite the challenges posed by AM, the analytical models presented in this thesis serve as a robust foundation for developing effective tools to predict the elastic behavior and fatigue life of components manufactured using additive manufacturing technology, particularly in the context of FDM.

Sommario

L'Additive Manufacturing (AM), comunemente nota come stampa 3D, ha rivoluzionato i processi manifatturieri consentendo la produzione di strutture complesse e personalizzate precedentemente impossibili da creare. L'AM porta vantaggi come la creazione di componenti con geometrie complesse e il potenziale risparmio di costi, specialmente in scenari con bassi volumi di produzione. Tuttavia, esistono svantaggi nell'utilizzo di questa tecnologia, in particolare la propensione alla creazione di porosità indesiderata nelle parti. Tra le varie tecnologie che rientrano nella famiglia dell'Additive Manufacturing questa tesi si concentra sulla Fused Deposition Modelling (FDM), prevalente nell'ambito dei materiali compositi.

In questa tesi si sviluppano diversi modelli analitici che tengono conto degli effetti dei difetti e delle caratteristiche di progettazione introdotti dai processi di fabbricazione FDM. Questi modelli affrontano specificamente gli stati di tensione nei componenti in materiale composito, concentrandosi su fattori come porosità e rinforzi localizzati. I modelli analitici sono validati mediante metodi degli Elementi Finiti, dimostrando la loro affidabilità nel descrivere i campi di tensione nelle aree studiate. Nonostante le sfide poste dalla AM, i modelli analitici presentati in questa tesi fungono da solida base per lo sviluppo di strumenti efficaci per prevedere il comportamento elastico e la vita a fatica dei componenti fabbricati utilizzando la tecnologia di fabbricazione additiva, in particolare nel contesto della FDM.

Introduction

Additive Manufacturing (AM), commonly known as 3D printing, has revolutionized traditional manufacturing processes by enabling the creation of complex and customized structures that would be impossible to create with more traditional subtractive technologies[1]. Among the many advantages of AM when compared with traditional technologies there is the ability to create components with significantly more complex geometries, ranging from the ability to create deep cavities and sharp internal features to the substitution of full solid bodies with complex filler patterns. The ability to print complex components without the necessity to divide them in simple machinable or castable parts to be assemble afterward, gives a new possibility to organize production, potentially saving costs and optimize the production line for many products. In particular for components with relatively low production volume, AM can be an excellent manufacturing process to optimize the production costs, it being a technology which is highly adaptable and with low initial capital investment. AM is a broad term that can refer to many manufacturing processes, in this work particular attention is given to Fused Deposition Modelling (FDM) which use thermoplastic material extruded through a heated nozzle to manufacture components, with the ability to co-extrude continuous fibres acting as reinforcement. This process has also the advantage to be usable with a large variety of plastic material (ABS, PA, PC and many others) and fibres materials (carbon, glass, Kevlar). One big advantage of this ability to place reinforcement material on specific parts of the component, is the possibility to reinforced the component where the it is most stressed under working conditions. This practice can go from very complex fibre placements paths, following the max main stress flows in the component or a process of optimization of the rigidity of the component, to very simple reinforcements along the boundaries of the geometrical features of the component. In all cases the main objective is to focus the rigid and strong material only in those area where it is really needed and optimize the weight and cost of the component for a given rigidity or strength.

In spite of all the advantages of AM, one has also to consider some severe disadvantages of this technology when compared to traditional manufacturing processes. These disadvantages mainly come from the strong dependence of mechanical properties of the final component to a vast array of processing parameters, more so than in traditional processes. One of the biggest drawbacks of AM is the proclivity of the process to leave unwanted porosity in the part. Porosities are kinds of defects that are most commonly present in powder-based manufacturing, particularly for metallic materials, but FDM can also exhibit this tendency. Particularly for FDM, printing parameters like nozzle and bed temperature, humidity of the feeding material, printing speed and printed bid width are the driving factors that contributes to high porosity in the component. These process parameters are also linked to residual thermal stresses in the component, that for the very nature of the printing procedure are going to be present. Particularly for FDM with continuous fibre reinforcements, where two different material coexists while the printed part cools down, thermal stresses are a big factor that needs to be taken into account.

All of these manufacturing problems can be overcome with post-processing procedures, in particular for the aforementioned disadvantages, with a pressurized thermal-postprocessing. This procedure however also cuts against the main economic advantages of the technology, having to include the cost and time to post-process all the printed components.

In order to study the effects of defects on mechanical properties and taking full advantage of the benefits of FDM technologies, adequate designing tools that account for all these features need to be developed. In particular, wheatear to account for the weakening effects of defects or to optimize the deposition of reinforcement material in a component, failure or stiffness criteria need to be used to understand the behavior of the component under working conditions. All the failure criteria, wheatear using the strain energy accumulating in the component or the stress state in a particular zone of the component, rely on the knowledge of the stress and displacement fields at least in the most critically stressed part of the component. This can be achieved in a variety of ways, on one end it is possible to measure experimentally displacement fields in a loaded part using DIC technology, it can be done by numerical simulations using Finite Element Analysis or it can be done via analytical modelling. In this thesis, primary focus is given to the latter strategy, analytical modelling. When compared to the other strategies, analytical modelling usually gives a greater understanding of the driving parameters that bring about failure in a component, and is a perfect tool to lay the foundations for what might be the development of new and improved failure criteria. These advantages though, come at a cost. Sound analytical modelling is generally much more difficult to develop then the alternatives, and generally it is possible to fully analytically model only simple cases where the complexity of a real world component is simplified by some assumptions. If these assumptions are reasonable enough to be representative of a real world situation, the explanatory power of an analytical model is unparallel. If, on the other hand, the complexity of the real component and working conditions cannot be dismissed, analytical modelling can serve as a solid basis for a more complete model that uses numerical methods as complementary tools.

In this thesis several analytical models are developed to study the stress fields of components that explicitly take into account the effects of defects, geometrical and design features produced by FDM manufacturing processes.

In the first introductory chapters, the basic mathematical framework is laid out, along with the most important solutions, previously developed by different authors[2-11], that are essential to better understand effective and useful analytical descriptions that will be developed in later chapters. Going from the basic general solutions to the elastic problem derived from the most common simplifying assumptions, to particular solutions where the elastic problem is solved for very specific cases that are relevant to the rest of the work.

The main body then presents different analytical models describing stress state in composite bodies developed to account for the specific features of FDM mentioned above, starting with the effect of porosities. Different studies can be found in the literature that characterize the shape and geometries of the typical FDM porosity in a thermoplastic medium [12-14]. A local approach is used to model the stress fields in the proximity of these kind of porosities, focusing only on the zone where the defect creates the most concentrated stresses. Thanks to this approach it is possible to analytically model the porosity in the area with the most concentrated stresses as a rounded notch. The area is then studied under different loading conditions and the results of the developed analytical models is compared with the numerical results obtained with Finite Element methods. This localized approach yields a mathematical description that describes the shapes of the stress fields in the studied area, it does nothing to address the magnitude of the stresses. Commonly this information is calculated via Finite Element numerical simulations, but this requires the use and development of heavy and computationally intense models. To overcome this problem a new semi-analytical approach is developed which tries to use the information given by the localized approach about the shape of the stress fields to calculate the magnitude of the stress fields without the need of numerical modelling. This method is then tested in very simple cases of plates with sharp notches and bi-material joints aimed at the calculation of the stress fields generalized stress intensity factors. This method can then be expanded in future works to include rounded notches and in general more complicated cases.

Lastly the effects of localized reinforcements in a component are studied, considering continuous fibres as the main strategy to achieve reinforced materials. The simple case of a polarly reinforced hole in a plate is considered, it being one of the most commonly used reinforcement arrangements. For this case several analytical models are already developed in the literature, and what characterize all of these models are some basic assumptions that greatly simplify the problem: infinite plates and extremely stiff reinforcement. Two new analytical models are developed to describe the stress state of a plate with a reinforced hole in which these two main assumptions are relaxed. The first model maintains the assumption of an infinite plate but admits all orthotropic materials as reinforcement, relaxing the extreme stiffness condition found in the literature. The second and more complex model builds on the structure of the first and relaxes also the infinite plate condition, arriving at an analytical description of the stress and displacement fields in plates of all shapes that have a polarly reinforced hole under extremely general loading conditions. The developed models are then compared with results from Finite Element analyses and with experimental results using DIC technology to measure displacement fields in 3D printed plates with continuous fibre reinforcements.

All the presented models are found to be in excellent agreement with the experimental and numerical results, proving to be a solid base to further development of effective tools to predict the elastic behavior and fatigue life of composite components made with additive manufacturing technology.

1. Basic equations of elasticity

1.1. Mathematical preliminaries

An important preliminary clarification about this work is the usage of the Einstein summation notation when not indicated otherwise, so repeated indices in a single term indicate a summation over those indices if no other definition are given.

Basic but important aspect of any stress fields analysis is the definition of a coordinate system in which to express elasticity variables and field equation, as well as the relation between different coordinate systems. The two main types of coordinate systems that are considered in this work are Cartesian and Curvilinear coordinate systems.

Considering two Cartesian frames $\{x_1, x_2, x_3\}$ and $\{x'_1, x'_2, x'_3\}$ differing only in orientation in Figure I.1, for each frame the unit basis vectors are $\{\boldsymbol{e_1}, \boldsymbol{e_2}, \boldsymbol{e_3}\}$ and $\{\boldsymbol{e'_1}, \boldsymbol{e'_2}, \boldsymbol{e'_3}\}$

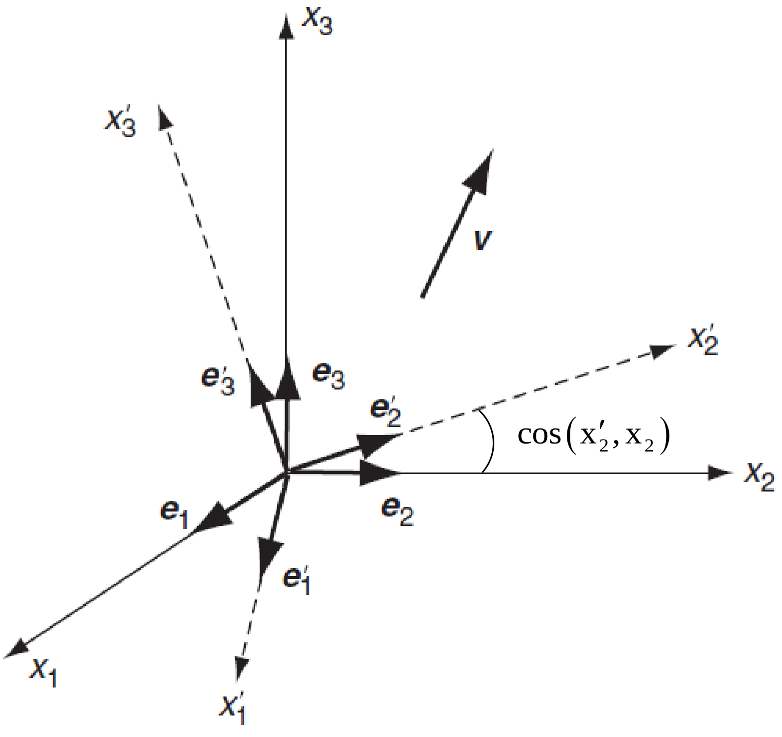

Figure I.1 Cartesian coordinates frames and their relation

Let Q_{ij} be the cosine of the angle between the x'_i axis and the x_j axis

$$Q_{ij} = \cos\left(x'_i, x_j\right) \tag{I.1}$$

The relation linking the two frames is

$$\boldsymbol{e}_i = Q_{ij}\boldsymbol{e}'_j \tag{I.2}$$

And considering a vector $\mathbf{v}$ expressed in in the non-prime frame,

$$v = \{v_1, v_2, v_3\} \tag{I.3}$$

It is possible to find its coordinates in the prima frame as follows

$$v'_i = Q_{ij} v_j \tag{I.4}$$

Another important aspect of a Cartesian coordinate system is the nabla operator, which can be expressed as follows:

$$\nabla = \frac{\partial}{\partial x_i}\boldsymbol{e}_i \tag{I.5}$$

The second important type of coordinate system is the curvilinear coordinate system, an example is shown in Figure I.2

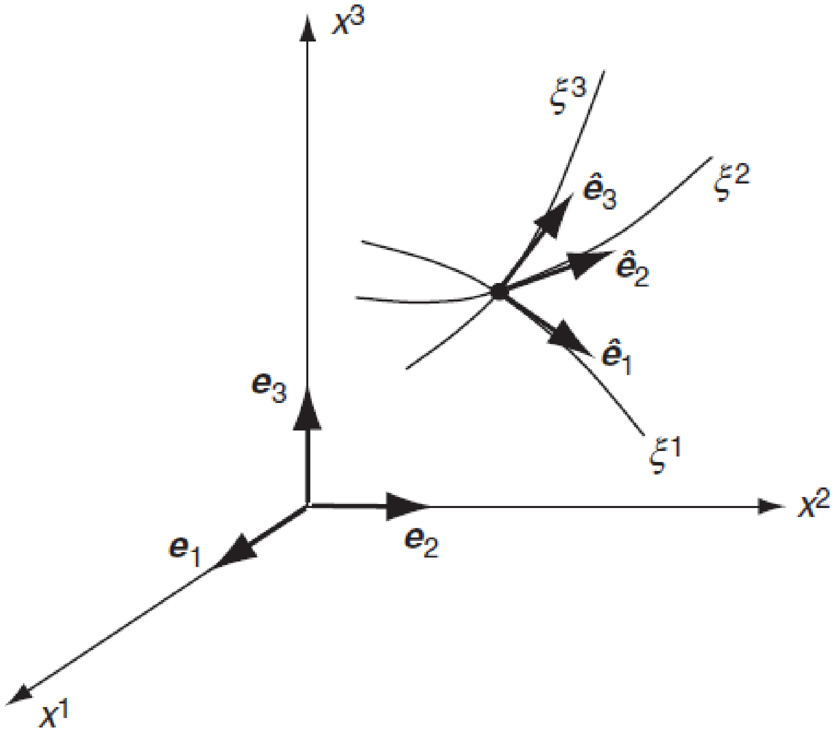

Figure I.2 Curvilinear coordinates system and its relation with a cartesian frame.

Assuming that an invertible coordinate transformation exists between the curvilinear coordinates $\{\xi^1, \xi^2, \xi^3\}$ and the cartesian coordinates $\{x^1, x^2, x^3\}$:

$$\xi^m = \xi^m\left(x^1, x^2, x^3\right), \quad x^m = x^m\left(\xi^1, \xi^2, \xi^3\right) \qquad \text{I.6}$$

The differential length in space can be expressed by:

$$(ds)^2 = \left(h_1 d\xi^1\right)^2 + \left(h_2 d\xi^2\right)^2 + \left(h_3 d\xi^3\right)^2 \qquad \text{I.7}$$

Where:

$$\left(h_j\right)^2 = \frac{\partial x^k}{\partial \xi^j}\frac{\partial x^k}{\partial \xi^j} \qquad \textit{no sum on j} \qquad \text{I.8}$$

The transformation tensor that links the two frame of reference is:

$$Q_r^k = \frac{1}{h_r}\frac{\partial x^k}{\partial \xi^r} \qquad \textit{no sum on r} \qquad \text{I.9}$$

While the general transformation of a tensor from the Cartesian coordinate system to the curvilinear one is given by:

$$a_{\langle ik...k \rangle} = Q_i^p Q_j^q \cdots Q_k^s a_{pq...s} \qquad \text{I.10}$$

Where $a_{pq...s}$ are the components of the tensor in the Cartesian frame.

The curvilinear frame of reference has also some complication for the nabla operator which becomes:

$$\nabla = \frac{1}{h_i} \frac{\partial}{\partial \xi^i} \hat{\boldsymbol{e}}_i \qquad \text{I.11}$$

1.2. Displacements and Strains

Applying an external load to an elastic body will cause it to deform. In Figure I.3 are shown the two configurations of the body before and after the application of the load, continuous and dashed line respectively. Two neighbouring points of the body are considered, P_0 and P in the unloaded state, and their relative position vector **r**, while their mapping in the loaded configuration are denoted with a prime symbol. The vectors are expressed in a coordinate system $\{x_1, x_2, x_3\}$ and their components are:

$$\boldsymbol{r} = \{r_1, r_2, r_3\}; \qquad \boldsymbol{r'} = \{r_1', r_2', r_3'\} \qquad \text{I.12}$$

It is possible to also define the displacement vector of the two points, which maps them between the two states:

$$\boldsymbol{u} = \{u_1, u_2, u_3\}; \qquad \boldsymbol{u}^0 = \{u_1^0, u_2^0, u_3^0\} \qquad \text{I.13}$$

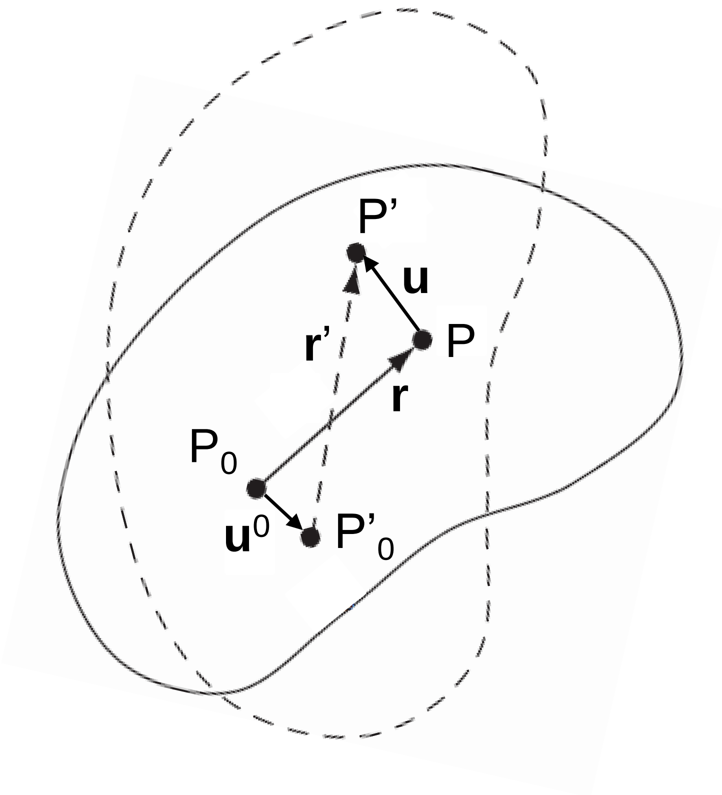

Figure I.3 Deformed and undeformed state of a body before and after the application of a load.

If the two points are close to each other and the displacements are small compared to the relative dimensions of the body, it is possible to express the displacement around point P with a Taylor series expansion around point P_0 as follows:

$$u_i = u_i^0 + \frac{\partial u_i}{\partial x_1} r_1 + \frac{\partial u_i}{\partial x_2} r_2 + \frac{\partial u_i}{\partial x_3} r_3 \tag{I.14}$$

We can then define the vector:

$$\Delta \boldsymbol{r} = \boldsymbol{r}' - \boldsymbol{r} = \boldsymbol{u} - \boldsymbol{u}^0 \tag{I.15}$$

And using relations I.14 we obtain:

$$\Delta r_i = u_{i,j} r_j \tag{I.16}$$

Where $u_{i,j}$ are the components of the displacement gradient tensor:

$$\begin{bmatrix} \frac{\partial u_1}{\partial x_1} & \frac{\partial u_1}{\partial x_2} & \frac{\partial u_1}{\partial x_3} \\ \frac{\partial u_2}{\partial x_1} & \frac{\partial u_2}{\partial x_2} & \frac{\partial u_2}{\partial x_3} \\ \frac{\partial u_3}{\partial x_1} & \frac{\partial u_3}{\partial x_2} & \frac{\partial u_3}{\partial x_3} \end{bmatrix} \qquad \text{I.17}$$

This tensor can be decomposed into its symmetric and antisymmetric part

$$u_{i,j} = \varepsilon_{ij} + \omega_{ij} \qquad \text{I.18}$$

Where

$$\begin{aligned} \varepsilon_{ij} &= \frac{1}{2}\left(u_{i,j} + u_{j,i}\right) \\ \omega_{ij} &= \frac{1}{2}\left(u_{i,j} - u_{j,i}\right) \end{aligned} \qquad \text{I.19}$$

So that:

$$\begin{aligned} \boldsymbol{\varepsilon} &= \frac{1}{2}\left(\nabla\boldsymbol{u} + \left(\nabla\boldsymbol{u}\right)^{\mathrm{T}}\right) \\ \boldsymbol{\omega} &= \frac{1}{2}\left(\nabla\boldsymbol{u} - \left(\nabla\boldsymbol{u}\right)^{\mathrm{T}}\right) \end{aligned} \qquad \text{I.20}$$

The tensor $\boldsymbol{\varepsilon}$ is called the strain tensor while $\boldsymbol{\omega}$ is the rotation tensor.

Combining relations I.14, I.16 and I.19, and remembering that in small deformation theory **r** is small so that $r_i = dx_i$, it is possible to obtain:

$$u_i = u_i^0 + \varepsilon_{ij} dx_j + \omega_{ij} dx_j \qquad \text{I.21}$$

Another often useful decomposition of the strain tensor is into two parts, the spherical strain tensor $\tilde{\boldsymbol{\varepsilon}}$ and the deviatoric strain tensor $\widehat{\boldsymbol{\varepsilon}}$, which are defined as follows:

$$\tilde{\varepsilon}_{ij} = \frac{1}{3}\varepsilon_{kk}\delta_{ij} \qquad \text{I.22}$$

$$\widehat{\varepsilon}_{ij} = \varepsilon_{ij} - \tilde{\varepsilon}_{ij} \qquad \text{I.23}$$

With:

$$\delta_{ij} = \begin{cases} 1 & i = j \\ 0 & i \neq j \end{cases} \tag{I.24}$$

Considering the relation between displacement and strain in an elastic body, it is possible to construct equations of compatibility, which ensure that the displacement field is continuous.

The strain compatibility equations are:

$$\varepsilon_{ij,kl} + \varepsilon_{kl,ij} - \varepsilon_{ik,jl} - \varepsilon_{jl,ik} = 0 \tag{I.25}$$

Or in tensorial form:

$$\nabla \times \left(\nabla \times \boldsymbol{\varepsilon}\right)^{\mathrm{T}} = 0 \tag{I.26}$$

Leading to six non-trivial equations, that can be further reduced to three independent equations:

$$\begin{aligned} \frac{\partial^4 \varepsilon_{11}}{\partial x_2^2 \partial x_3^2} &= \frac{\partial^3}{\partial x_1 \partial x_2 \partial x_3}\left(\frac{\partial \varepsilon_{12}}{\partial x_3} + \frac{\partial \varepsilon_{13}}{\partial x_2} - \frac{\partial \varepsilon_{23}}{\partial x_1}\right) \\ \frac{\partial^4 \varepsilon_{22}}{\partial x_3^2 \partial x_1^2} &= \frac{\partial^3}{\partial x_1 \partial x_2 \partial x_3}\left(\frac{\partial \varepsilon_{23}}{\partial x_1} + \frac{\partial \varepsilon_{12}}{\partial x_3} - \frac{\partial \varepsilon_{13}}{\partial x_2}\right) \\ \frac{\partial^4 \varepsilon_{33}}{\partial x_1^2 \partial x_2^2} &= \frac{\partial^3}{\partial x_1 \partial x_2 \partial x_3}\left(\frac{\partial \varepsilon_{13}}{\partial x_2} + \frac{\partial \varepsilon_{23}}{\partial x_1} - \frac{\partial \varepsilon_{12}}{\partial x_3}\right) \end{aligned} \tag{I.27}$$

Important are also the relation of the strain tensor between different coordinate frames:

$$\varepsilon'_{ij} = Q_{ip} Q_{jq} \varepsilon_{pq} \tag{I.28}$$

Which in the case of Cartesian coordinate system in the two-dimensional case can be expressed by:

$$\begin{aligned} \varepsilon'_{11} &= \frac{\varepsilon_{11} + \varepsilon_{22}}{2} + \frac{\varepsilon_{11} - \varepsilon_{22}}{2}\cos(2\theta) + \varepsilon_{12}\sin(2\theta) \\ \varepsilon'_{22} &= \frac{\varepsilon_{11} + \varepsilon_{22}}{2} - \frac{\varepsilon_{11} - \varepsilon_{22}}{2}\cos(2\theta) - \varepsilon_{12}\sin(2\theta) \\ \varepsilon'_{12} &= -\frac{\varepsilon_{11} - \varepsilon_{22}}{2}\sin(2\theta) + \varepsilon_{12}\cos(2\theta) \end{aligned} \tag{I.29}$$

1.3. Stress and Equilibrium

Important aspect of an elastic body is how forces are transmitted through the material, and the resulting stress distribution in the system. The first important object that needs to be defined is the traction vector $\mathbf{T}^{\mathrm{n}}$ over the plane whose normal vector is $\mathbf{n}$. Considering the grey plane in Figure I.4

as the analysed plane, and **n** its normal vector, in any point of the plane is possible to define the traction vector as follows:

$$\mathbf{T}^n = \left\{T_1^n, T_2^n, T_3^n\right\} \qquad \text{I.30}$$

$$T_j^n = \sigma_{ij} n_i \qquad \text{I.31}$$

Where σ_{ij} are the components of the stress tensor $\boldsymbol{\sigma}$, and:

$$\sigma_{ij} = \sigma_{ji} \qquad \text{I.32}$$

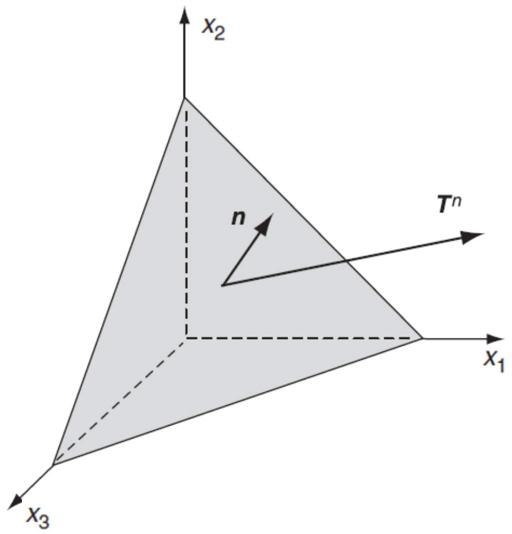

Figure I.4 Plane of analysis for the definition of the traction vector.

As for the strain tensor, it is also useful to further decompose the stress tensor $\boldsymbol{\sigma}$ into the spherical stress tensor $\tilde{\boldsymbol{\sigma}}$ and the deviatoric stress tensor $\widehat{\boldsymbol{\sigma}}$:

$$\tilde{\sigma}_{ij} = \frac{1}{3}\sigma_{kk}\delta_{ij} \qquad \text{I.33}$$

$$\widehat{\sigma}_{ij} = \sigma_{ij} - \tilde{\sigma}_{ij} \qquad \text{I.34}$$

The principal stresses are the stress value associated with a coordinate system such that the stress tensor in that coordinate system is a diagonal matrix:

$$\boldsymbol{\sigma} = \begin{bmatrix} \sigma_1 & 0 & 0 \\ 0 & \sigma_2 & 0 \\ 0 & 0 & \sigma_3 \end{bmatrix} \qquad \text{I.35}$$

The main focus of this work are bodies which are in equilibrium, as such it is important that the traction vector and the body forces in every point of the body are in equilibrium. This results in a constrain that the stress fields must satisfy, the equilibrium constrain, that is expressed as follow:

$$\sigma_{ji,j} + F_i = 0 \qquad \text{I.36}$$

Or in tensorial notation:

$$\nabla \cdot \boldsymbol{\sigma} + \boldsymbol{F} = 0 \qquad \text{I.37}$$

As for the strain tensor, the relation between stress tensor in different coordinate systems, follows the same relation:

$$\sigma'_{ij} = Q_{ip} Q_{jq} \sigma_{pq} \qquad \text{I.38}$$

Which in two dimensions translates into:

$$\begin{aligned}
\sigma'_{11} &= \frac{\sigma_{11}+\sigma_{22}}{2} + \frac{\sigma_{11}-\sigma_{22}}{2}\cos(2\theta) + \sigma_{12}\sin(2\theta) \\
\sigma'_{22} &= \frac{\sigma_{11}+\sigma_{22}}{2} - \frac{\sigma_{11}-\sigma_{22}}{2}\cos(2\theta) - \sigma_{12}\sin(2\theta) \\
\sigma'_{12} &= -\frac{\sigma_{11}-\sigma_{22}}{2}\sin(2\theta) + \sigma_{12}\cos(2\theta)
\end{aligned} \qquad \text{I.39}$$

1.4. Material behaviour, Linear Elastic Solids

The response that any specific material gives to an applied force is embodied in the relation that links the stress and strain tensor. In this work only linear elastic solids are considered and so the elastic equations are linear:

$$\sigma_{ij} = C_{ijkl}\varepsilon_{kl} \qquad \text{I.40}$$

Or in tensor notation:

$$\boldsymbol{\sigma} = \hat{\boldsymbol{C}} : \boldsymbol{\varepsilon} \qquad \text{I.41}$$

Where $\hat{\boldsymbol{C}}$ is a fourth order tensor called compliance tensor with particular symmetries:

$$\begin{aligned}
C_{ijkl} &= C_{jikl} \\
C_{ijkl} &= C_{ijlk} \\
C_{ijkl} &= C_{klij}
\end{aligned} \qquad \text{I.42}$$

This relation can also be inverted to obtain the stiffness tensor, with simar symmetries:

$$\boldsymbol{\varepsilon} = \hat{\boldsymbol{S}} : \boldsymbol{\sigma} \tag{I.41}$$

$$\begin{aligned} S_{ijkl} &= S_{jikl} \\ S_{ijkl} &= S_{ijlk} \\ S_{ijkl} &= S_{klij} \end{aligned} \tag{I.42}$$

Compliance and stiffness tensors are referred to a specific coordinate system and their relation between different coordinate systems can be expressed as follows:

$$C_{ijkl} = Q_{im} Q_{jn} Q_{kp} Q_{lq} C_{mnpq} \tag{I.43}$$

Using tensor notation and fourth order tensor can sometimes be inconvenient, and a vector notation can be more intuitive and easier to use. All the previous equations can then be transformed without losing any information into a formulation that involves only vectors and matrices.

The stress and strain tensor are transformed into the strain and stress vector:

$$\bar{\boldsymbol{\sigma}} = \{\sigma_{11}, \sigma_{22}, \sigma_{33}, \sigma_{23}, \sigma_{13}, \sigma_{12}\} \tag{I.44}$$

$$\bar{\boldsymbol{\varepsilon}} = \{\varepsilon_{11}, \varepsilon_{22}, \varepsilon_{33}, 2\varepsilon_{23}, 2\varepsilon_{13}, 2\varepsilon_{12}\} \tag{I.45}$$

With:

$$\gamma_{ij} = 2\varepsilon_{ij} \tag{I.46}$$

$$\sigma_i = C_{ij} \varepsilon_j \tag{I.47}$$

$$\bar{\boldsymbol{\sigma}} = \boldsymbol{C} \cdot \bar{\boldsymbol{\varepsilon}} \tag{I.48}$$

$$\boldsymbol{C} = \begin{bmatrix} C_{11} & C_{12} & C_{13} & C_{14} & C_{15} & C_{16} \\ & C_{22} & C_{23} & C_{24} & C_{25} & C_{26} \\ & & C_{33} & C_{24} & C_{35} & C_{36} \\ & & & C_{44} & C_{45} & C_{46} \\ & & & & C_{55} & C_{56} \\ & & & & & C_{66} \end{bmatrix} = \begin{bmatrix} C_{1111} & C_{1122} & C_{1133} & C_{1123} & C_{1113} & C_{1112} \\ & C_{2222} & C_{2233} & C_{2223} & C_{1322} & C_{1222} \\ & & C_{3333} & C_{2333} & C_{1333} & C_{1233} \\ & & & C_{2323} & C_{1323} & C_{1223} \\ & & & & C_{1313} & C_{1213} \\ & & & & & C_{1212} \end{bmatrix} \tag{I.49}$$

$$C_{ij} = C_{ji} \tag{I.50}$$

$$\varepsilon_i = S_{ij} \sigma_j \tag{I.51}$$

$$\bar{\boldsymbol{\varepsilon}} = \boldsymbol{S} \cdot \bar{\boldsymbol{\sigma}} \tag{I.52}$$

$$\boldsymbol{S} = \begin{bmatrix} S_{11} & S_{12} & S_{13} & S_{14} & S_{15} & S_{16} \\ & S_{22} & S_{23} & S_{24} & S_{25} & S_{26} \\ & & S_{33} & S_{24} & S_{35} & S_{36} \\ & & & S_{44} & S_{45} & S_{46} \\ & & & & S_{55} & S_{56} \\ & & & & & S_{66} \end{bmatrix} = \begin{bmatrix} S_{1111} & S_{1122} & S_{1133} & 2S_{1123} & 2S_{1113} & 2S_{1112} \\ & S_{2222} & S_{2233} & 2S_{2223} & 2S_{1322} & 2S_{1222} \\ & & S_{3333} & 2S_{2333} & 2S_{1333} & 2S_{1233} \\ & & & 4S_{2323} & 4S_{1323} & 4S_{1223} \\ & & & & 4S_{1313} & 4S_{1213} \\ & & & & & 4S_{1212} \end{bmatrix} \tag{I.53}$$

$$S_{ij} = S_{ji} \tag{I.54}$$

Beside the previous symmetries, for different materials the compliance and stiffness tensor can present more symmetries depending on their microstructure. If the microstructure has a plane of elastic symmetry, then the following applies:

$$S_{14} = S_{24} = S_{34} = S_{46} = S_{15} = S_{25} = S_{35} = S_{56} = 0 \tag{I.55}$$

With three mutually perpendicular planes of elastic symmetry the material is typically called orthotropic, and the following applies:

$$S_{14} = S_{24} = S_{34} = S_{46} = S_{15} = S_{25} = S_{35} = S_{56} = S_{16} = S_{26} = S_{36} = S_{45} = 0 \tag{I.56}$$

In this case it is also useful to express the components of the stiffness and compliance tensor in terms of more commonly used engineering constants:

$$S_{11} = \frac{1}{E_1}\; S_{22} = \frac{1}{E_2}\; S_{33} = \frac{1}{E_3}\; S_{44} = \frac{1}{G_{23}}\; S_{55} = \frac{1}{G_{13}}\; S_{66} = \frac{1}{G_{12}}\; S_{12} = -\frac{\nu_{21}}{E_2}\; S_{13} = -\frac{\nu_{31}}{E_3}\; S_{23} = -\frac{\nu_{32}}{E_3} \tag{I.57}$$

And, from symmetries relations:

$$\frac{\nu_{ij}}{E_i} = \frac{\nu_{ji}}{E_j} \tag{I.58}$$

If the material present infinite parallel planes on which every direction is elastically equivalent, then it is said to possess an axis of rotational symmetry which is perpendicular to all the planes. These materials are commonly known as transversely isotropic and their stiffness tensor present the orthotropic properties as well as the following:

$$S_{11}=S_{22}=\frac{1}{E_T},\ S_{33}=\frac{1}{E_N},\ S_{44}=S_{55}=\frac{1}{G_{TN}},\ S_{66}=\frac{2(1+\nu_{TT})}{E_T},\ S_{12}=-\frac{\nu_{TT}}{E_T},\ S_{13}=S_{23}=-\frac{\nu_{NT}}{E_N} \qquad \text{I.59}$$

Where T is a direction laying on a symmetry plane and N is the direction parallel to the axis of rotational symmetry, in this case it is assumed that $\boldsymbol{e}_3$ is parallel to the axis of symmetry.

The easiest materials to study are the isotropic materials in which all directions in the entire body are elastically equivalent. In this case the stiffness and compliance tensor are significantly simplified:

$$S_{11}=S_{22}=S_{33}=\frac{1}{E},\ S_{44}=S_{55}=S_{66}=\frac{2(1+\nu)}{E},\ S_{12}=S_{13}=S_{23}=-\frac{\nu}{E} \qquad \text{I.60}$$

And some of the shear stress modulus, Lame constant, and bulk modulus are defined respectively as follows:

$$G=\frac{E}{2(1+\nu)},\ \lambda=\frac{E\nu}{(1-2\nu)(1+\nu)},\ k=\frac{E}{3(1-2\nu)} \qquad \text{I.61}$$

All the cases discussed so far assumed a compliance and stiffness tensor that are constant and do not vary for different points in space. This kind of behavior define what is normally called homogeneous-material, but of course this are not the only type of material that can be found in applications. If the elastic material properties are a function of the position in a particular frame of reference, then the material is non-homogeneous and in general all the parts of the stiffness and compliance tensor are a function of space.

1.5. The elastic problem of an anisotropic body

The basic field relations discussed until now are the strain-displacement relations Eq. I.20, the compatibility relations Eq. I.26, the equilibrium equations Eq. I.37 and lastly the constitutive law Eq. I.52. These equations are valid for all linearly elastic bodies, but although extremely comprehensive and general, are also quite challenging to solve. For this reason, analytical investigations need to restrict the framework to more manageable cases, aiming to study problems where appropriate external forces, applied to the body, imply a simplified elastic problem. These restrictions however need not to make the problem less interesting or irrelevant for practical applications, in fact the vast majority of applications can be studied with the frameworks that are discussed in this chapter.

1.5.1. Cylindrically shaped, rectilinearly anisotropic, homogeneous bodies in which stresses do not vary along the generators

Consider a cylindrically shaped homogeneous body made of anisotropic material, the coordinate frame system $\{x, y, z\}$ is defined such that the direction z is parallel to the generator of the body. Assume that there are body forces **F** acting on it such that they do not vary along the direction z and have a potential function Γ such that:

$$\boldsymbol{F} = \left\{ -\frac{\partial \Gamma(x,y)}{\partial x}, -\frac{\partial \Gamma(x,y)}{\partial y}, 0 \right\} \tag{I.62}$$

Assume also that surface forces applied to the lateral boundary of the body act in plane orthogonal to the z direction, while forces acting on the ending surfaces of the cylinder are reducible to bending moments, twisting moments and axial forces. In this scenario it is safe to assume that stresses are only a function of two coordinates, x and y, and so the equilibrium equations I.37 become:

$$\begin{cases} \dfrac{\partial}{\partial x}\left(\sigma_{xx} - \Gamma\right) + \dfrac{\partial \sigma_{xy}}{\partial x} = 0 \\ \dfrac{\partial \sigma_{xy}}{\partial x} + \dfrac{\partial}{\partial y}\left(\sigma_{yy} - \Gamma\right) = 0 \\ \dfrac{\partial \sigma_{xz}}{\partial x} + \dfrac{\partial \sigma_{yz}}{\partial y} = 0 \end{cases} \tag{I.63}$$

Combining the elastic relations I.52 with the strain-displacement relations I.20, after integration and some algebraic manipulation, is possible to define the displacements as follows:

$$\begin{aligned} u_x &= -\frac{A}{2} z^2 - \vartheta yz + U_x(x,y) + \omega_2 z - \omega_3 y + u_x^0 \\ u_y &= -\frac{B}{2} z^2 - \vartheta xz + U_y(x,y) + \omega_3 x - \omega_1 z + u_y^0 \\ u_z &= \left(Ax + By + C\right) z + U_z(x,y) + \omega_1 y - \omega_2 x + u_z^0 \end{aligned} \tag{I.64}$$

Where $\omega_1, \omega_2, \omega_3, u_x^0, u_y^0, u_z^0$ are real constants related to rigid body displacements, while A, B, C, ϑ are real constants and $U_x(x,y), U_y(x,y), U_z(x,y)$ are integration functions that needs to be determined imposing boundary conditions on the body.

The stress functions can be expressed in terms of two potential functions Φ, Ψ :

$$\begin{aligned}
&\sigma_{xx} = \frac{\partial^2 \Phi}{\partial x^2} + \Gamma; \qquad \sigma_{xz} = \frac{\partial \Psi}{\partial y} \\
&\sigma_{yy} = \frac{\partial^2 \Phi}{\partial y^2} + \Gamma \qquad \sigma_{yz} = -\frac{\partial \Psi}{\partial x} \\
&\sigma_{xy} = -\frac{\partial^2 \Phi}{\partial x \partial y} \\
&\sigma_{zz} = \frac{Ax + By + C - S_{13}\sigma_{xx} - S_{23}\sigma_{yy} - S_{34}\sigma_{yz} - S_{35}\sigma_{xz} - S_{36}\sigma_{xy}}{S_{33}}
\end{aligned} \tag{I.65}$$

and substituting I.64, I.65 and 1.20 into I.52, with little algebraic manipulations one obtains:

$$\begin{cases}
L_4\Phi + L_3\Psi = \left(b_{16} + b_{26}\right)\dfrac{\partial^2 \Gamma}{\partial x \partial y} - \left(b_{12} + b_{22}\right)\dfrac{\partial^2 \Gamma}{\partial x^2} - \left(b_{11} + b_{12}\right)\dfrac{\partial^2 \Gamma}{\partial y^2} \\
L_3\Phi + L_2\Psi = \dfrac{AS_{34} - BS_{35}}{S_{33}} - 2\vartheta + \left(b_{14} + b_{24}\right)\dfrac{\partial \Gamma}{\partial x} - \left(b_{15} + b_{25}\right)\dfrac{\partial \Gamma}{\partial y}
\end{cases} \tag{I.66}$$

Where L_4, L_3, L_2 are differential operators:

$$\begin{aligned}
&L_4 = b_{22}\frac{\partial^4}{\partial x^4} - 2b_{26}\frac{\partial^4}{\partial x^3 \partial y} + \left(2b_{12} + b_{66}\right)\frac{\partial^4}{\partial x^2 \partial y^2} - 2b_{16}\frac{\partial^4}{\partial x \partial y^3} + b_{11}\frac{\partial^4}{\partial y^4} \\
&L_3 = b_{15}\frac{\partial^3}{\partial y^3} - \left(b_{14} + b_{56}\right)\frac{\partial^3}{\partial x \partial y^2} + \left(b_{25} + b_{46}\right)\frac{\partial^3}{\partial x^2 \partial y} - b_{24}\frac{\partial^3}{\partial x^3} \\
&L_2 = b_{44}\frac{\partial^2}{\partial x^2} - 2b_{45}\frac{\partial^2}{\partial x \partial y} + b_{55}\frac{\partial^2}{\partial y^2}
\end{aligned} \tag{I.67}$$

And:

$$b_{ij} = S_{ij} - \frac{S_{i3}S_{j3}}{S_{33}} \tag{I.68}$$

System I.66 is the general differential system that solves the problem and, finding the two potential functions will give all the stress and displacement fields of the body.

The solution to system I.66 can be dividend in the homogenous solutions parts Φ_H, Ψ_H and the particular solutions Φ_P, Ψ_P

$$\begin{aligned}\Phi &= \Phi_H + \Phi_P \\ \Psi &= \Psi_H + \Psi_P\end{aligned} \qquad \text{I.69}$$

Considering the homogeneous system first, substituting the second equation of system I.66 into the first one obtains:

$$\left(L_4 L_2 - L_3^2\right)\Phi_H = 0 \qquad \text{I.70}$$

Which can be decomposed into six linear operators:

$$\begin{aligned}&D_6 D_5 D_4 D_3 D_2 D_1 \Phi_H = 0 \\ &D_j = \frac{\partial}{\partial y} - \mu_j \frac{\partial}{\partial x}\end{aligned} \qquad \text{I.71}$$

Where μ_j are the six roots of the characteristic equation:

$$l_4(\mu) l_2(\mu) - l_3^2(\mu) = 0 \qquad \text{I.72}$$

With:

$$\begin{aligned}l_4(\mu) &= b_{22} - 2b_{26}\mu + \left(2b_{12} + b_{66}\right)\mu^2 - 2b_{16}\mu^3 + b_{11}\mu^4 \\ l_3(\mu) &= b_{15}\mu^3 - \left(b_{14} + b_{56}\right)\mu^2 + \left(b_{25} + b_{46}\right)\mu - b_{24} \\ l_2(\mu) &= b_{44} - 2b_{45}\mu + b_{55}\mu^2\end{aligned} \qquad \text{I.73}$$

Generally, μ_j are complex constants that are defined as follows:

$$\begin{aligned}&\mu_j = \alpha_j + \boldsymbol{i}\beta_j \quad j \in \{1,2,3\} \\ &\mu_4 = \bar{\mu}_1 \qquad \mu_5 = \bar{\mu}_2 \qquad \mu_6 = \bar{\mu}_3\end{aligned} \qquad \text{I.74}$$

The solution to Eq. (I.70) can be rewritten as a combination of three potential functions $\Phi_{H1}, \Phi_{H2}, \Phi_{H3}$ of the variables:

$$z_j = x + \mu_j y \qquad \bar{z}_j = x + \bar{\mu}_j y \qquad \text{I.75}$$

$$\begin{aligned}\Phi &= 2\,\mathrm{Re}\left[\Phi_{H1}(z_1) + \Phi_{H2}(z_2) + \Phi_{H3}(z_3)\right] + \Phi_P \\ \Psi &= 2\,\mathrm{Re}\left[\lambda_1 \frac{\partial \Phi_{H1}(z_1)}{\partial z_1} + \lambda_2 \frac{\partial \Phi_{H2}(z_2)}{\partial z_2} + \frac{1}{\lambda_3}\frac{\partial \Phi_{H3}(z_3)}{\partial z_3}\right] + \Psi_P\end{aligned} \qquad \text{I.76}$$

With:

$$\lambda_1 = -\frac{l_3(\mu_1)}{l_2(\mu_1)} \qquad \lambda_2 = -\frac{l_3(\mu_2)}{l_2(\mu_2)} \qquad \lambda_3 = -\frac{l_3(\mu_3)}{l_4(\mu_3)} \tag{I.77}$$

It is possible to define three new potential functions as follows:

$$\begin{aligned} &\phi_j(z_j) = \frac{\partial \Phi_{Hj}(z_j)}{\partial z_j} \qquad j \in \{1,2\} \\ &\phi_3(z_3) = \frac{1}{\lambda_3}\frac{\partial \Phi_{H3}(z_3)}{\partial z_3} \end{aligned} \tag{I.78}$$

Which can be substituted in Eq I.65 to explicitly obtain expressions for the stress fields

$$\begin{aligned} \sigma_{xx} &= 2\,\mathrm{Re}\left[\mu_1^2\phi'_{H1}(z_1) + \mu_2^2\phi'_{H2}(z_2) + \mu_3^2\lambda_3\phi'_{H3}(z_3)\right] + \frac{\partial^2\Phi_P}{\partial y^2} + \Gamma \\ \sigma_{yy} &= 2\,\mathrm{Re}\left[\phi'_{H1}(z_1) + \phi'_{H2}(z_2) + \lambda_3\phi'_{H3}(z_3)\right] + \frac{\partial^2\Phi_P}{\partial x^2} + \Gamma \\ \sigma_{xy} &= -2\,\mathrm{Re}\left[\mu_1\phi'_{H1}(z_1) + \mu_2\phi'_{H2}(z_2) + \mu_3\lambda_3\phi'_{H3}(z_3)\right] - \frac{\partial^2\Phi_P}{\partial x\partial y} \\ \sigma_{yz} &= -2\,\mathrm{Re}\left[\lambda_1\phi'_{H1}(z_1) + \lambda_2\phi'_{H2}(z_2) + \phi'_{H3}(z_3)\right] - \frac{\partial\Psi_P}{\partial x} \\ \sigma_{xz} &= 2\,\mathrm{Re}\left[\mu_1\lambda_1\phi'_{H1}(z_1) + \mu_2\lambda_2\phi'_{H2}(z_2) + \mu_3\phi'_{H3}(z_3)\right] + \frac{\partial\Psi_P}{\partial y} \end{aligned} \tag{I.79}$$

And the displacement functions:

$$\begin{aligned} U_x &= 2\,\mathrm{Re}\left[\sum_{k=1}^{3} p_k\phi_{Hk}(z_k)\right] + U_x^0 \\ U_y &= 2\,\mathrm{Re}\left[\sum_{k=1}^{3} q_k\phi_{Hk}(z_k)\right] + U_y^0 \\ U_z &= 2\,\mathrm{Re}\left[\sum_{k=1}^{3} t_k\phi_{Hk}(z_k)\right] + U_z^0 \end{aligned} \tag{I.80}$$

Where U_x^0, U_y^0, U_z^0 are the solution to the system:

$$\begin{cases} \dfrac{\partial U_x}{\partial x} = b_{11}\sigma_{xx} + b_{12}\sigma_{yy} + b_{14}\sigma_{yz} + b_{15}\sigma_{xz} + b_{16}\sigma_{xy} + \dfrac{S_{13}}{S_{33}}\left(Ax + By + C\right) \\ \dfrac{\partial U_y}{\partial y} = b_{12}\sigma_{xx} + b_{22}\sigma_{yy} + b_{24}\sigma_{yz} + b_{25}\sigma_{xz} + b_{26}\sigma_{xy} + \dfrac{S_{23}}{S_{33}}\left(Ax + By + C\right) \\ \dfrac{\partial U_x}{\partial y} + \dfrac{\partial U_y}{\partial x} = b_{16}\sigma_{xx} + b_{26}\sigma_{yy} + b_{46}\sigma_{yz} + b_{56}\sigma_{xz} + b_{66}\sigma_{xy} + \dfrac{S_{36}}{S_{33}}\left(Ax + By + C\right) \\ \dfrac{\partial U_z}{\partial x} = b_{15}\sigma_{xx} + b_{25}\sigma_{yy} + b_{45}\sigma_{yz} + b_{55}\sigma_{xz} + b_{56}\sigma_{xy} + \dfrac{S_{35}}{S_{33}}\left(Ax + By + C\right) + \vartheta y - \omega_2 \\ \dfrac{\partial U_z}{\partial y} = b_{14}\sigma_{xx} + b_{24}\sigma_{yy} + b_{44}\sigma_{yz} + b_{45}\sigma_{xz} + b_{46}\sigma_{xy} + \dfrac{S_{34}}{S_{33}}\left(Ax + By + C\right) - \vartheta x + \omega_1 \end{cases} \tag{I.81}$$

Corresponding to the particular solutions Φ_P, Ψ_P, the body forces Γ and the linear terms $Ax + By + C, \vartheta x$ and ϑy. While:

$$\begin{aligned} p_k &= b_{11}\mu_k^2 + b_{12} - b_{16}\mu_k + \lambda_k\left(b_{15}\mu_k - b_{14}\right) \\ q_k &= b_{12}\mu_k + \frac{b_{22}}{\mu_k} - b_{26} + \lambda_k\left(b_{25} - \frac{b_{24}}{\mu_k}\right) \qquad k \in \{1, 2\} \\ t_k &= b_{12}\mu_k + \frac{b_{22}}{\mu_k} - b_{26} + \lambda_k\left(b_{45} - \frac{b_{44}}{\mu_k}\right) \end{aligned} \tag{I.82}$$

$$\begin{aligned} p_3 &= \lambda_3\left(b_{11}\mu_3^2 + b_{12} - b_{16}\mu_3\right) + b_{15}\mu_k - b_{14} \\ q_3 &= \lambda_3\left(b_{12}\mu_3 + \frac{b_{22}}{\mu_3} - b_{26}\right) + b_{25} - \frac{b_{24}}{\mu_3} \\ t_3 &= \lambda_3\left(b_{12}\mu_3 + \frac{b_{22}}{\mu_3} - b_{26}\right) + b_{45} - \frac{b_{44}}{\mu_3} \end{aligned} \tag{I.83}$$

In the end to fully describe the stress and displacement fields of the body, the following must be found through the imposition of boundary conditions specific for every application:

1) 6 constants related to rigid body displacements:

   $\omega_1, \omega_2, \omega_3, u_x^0, u_y^0, u_z^0$

2) 4 constants related to the boundary conditions applied at the ending faces of the cylinder: A, B, C, ϑ

3) 3 potential functions related to the boundary conditions in each cross section:

   $\Phi_{H1}, \Phi_{H2}, \Phi_{H3}$

4) 2 particular solutions:

Φ_P, Ψ_P

1.5.2. Cylindrically shaped, rectilinearly anisotropic, non-homogeneous bodies in which stresses do not vary along the generators

In the case of a non-homogeneous material, solutions to the elastic problem are much more difficult to find and study. That said some important similarities and differences can be drawn between the underlying mathematical foundation of the homogeneous and non-homogeneous problems. Firstly, the general definition of the displacement fields I.64 remains the same, and these displacement fields must also solve the same differential system I.81. The relations between the stress fields and the potential functions Φ, Ψ are also the same of the homogeneous case I.76, but the differential system that must be solved to obtain the solution changes dramatically, and becomes significantly more complicated:

$$\begin{cases} \frac{\partial^2}{\partial x^2}\left(b_{22}\frac{\partial\Phi^2}{\partial x^2}+b_{12}\frac{\partial\Phi^2}{\partial y^2}-b_{26}\frac{\partial\Phi^2}{\partial x\partial y}\right)+\frac{\partial^2}{\partial y^2}\left(b_{12}\frac{\partial\Phi^2}{\partial x^2}+b_{11}\frac{\partial\Phi^2}{\partial y^2}-b_{16}\frac{\partial\Phi^2}{\partial x\partial y}\right)- \\ \qquad -\frac{\partial^2}{\partial x\partial y}\left(b_{26}\frac{\partial\Phi^2}{\partial x^2}+b_{16}\frac{\partial\Phi^2}{\partial y^2}-b_{66}\frac{\partial\Phi^2}{\partial x\partial y}\right)=-\frac{\partial^2}{\partial x^2}\left(\frac{S_{22}}{S_{33}}\left(Ax+By+C\right)\right)- \\ \qquad -\frac{\partial^2}{\partial y^2}\left(\frac{S_{13}}{S_{33}}\left(Ax+By+C\right)\right)+\frac{\partial^2}{\partial x\partial y}\left(\frac{S_{36}}{S_{33}}\left(Ax+By+C\right)\right)- \\ \qquad -\frac{\partial^2}{\partial x^2}\left(\left(b_{12}+b_{22}\right)\Gamma\right)-\frac{\partial^2}{\partial y^2}\left(\left(b_{11}+b_{12}\right)\Gamma\right)+\frac{\partial^2}{\partial x\partial y}\left(\left(b_{16}+b_{26}\right)\Gamma\right) \\ \frac{\partial}{\partial x}\left(S_{44}\frac{\partial\Psi}{\partial x}-S_{45}\frac{\partial\Psi}{\partial y}\right)+\frac{\partial}{\partial y}\left(S_{55}\frac{\partial\Psi}{\partial y}-S_{45}\frac{\partial\Psi}{\partial x}\right)=-2\vartheta \end{cases} \qquad \text{I.84}$$

1.5.3. Cylindrically shaped, polarly anisotropic, homogeneous bodies in which stresses do not vary along the generators

Considering the same geometry and loading conditions seen in the previous chapter, the case of a material presenting polar anisotropy is more and more common in applications, thanks to the development of new manufacturing technology, namely additive manufacturing. When the material is polarly anisotropic the general differential system gets more complicated, and the solution is much more difficult to define. It is nonetheless worth giving the general form of the differential system, the displacement and stress fields.

Assuming that the body forces applied can be expressed with a potential function as follows:

$$\boldsymbol{F} = \left\{ -\frac{\partial\Gamma(r,\theta)}{\partial r}, -\frac{1}{r}\frac{\partial\Gamma(r,\theta)}{\partial\theta}, 0 \right\} \qquad \text{I.85}$$

Following the same procedure discussed for a linear anisotropic material, the displacement fields can be expressed by

$$\begin{aligned}
u_r &= U_r(r,\theta) - \frac{z^2}{2}\left(A\cos(\theta) + B\sin(\theta)\right) + z\left(\omega_2\cos(\theta) - \omega_1\sin(\theta)\right) + u_x^0\cos(\theta) + u_y^0\sin(\theta) \\
u_\theta &= U_\theta(r,\theta) - \frac{z^2}{2}\left(B\cos(\theta) - A\sin(\theta)\right) + \vartheta rz - z\left(\omega_2\sin(\theta) + \omega_1\cos(\theta)\right) + \omega_3 r - u_x^0\sin(\theta) + u_y^0\cos(\theta) \\
u_z &= U_z(r,\theta) + z\left(Ar\cos(\theta) + Br\sin(\theta) + C\right) - r\left(\omega_2\cos(\theta) - \omega_1\sin(\theta)\right) + u_z^0
\end{aligned} \qquad \text{I.86}$$

$$\begin{aligned}
&\sigma_{rr} = \frac{1}{r}\frac{\partial\Phi}{\partial r} + \frac{1}{r^2}\frac{\partial^2\Phi}{\partial\theta^2} + \Gamma; && \sigma_{rz} = \frac{1}{r}\frac{\partial\Psi}{\partial\theta} \\
&\sigma_{\theta\theta} = \frac{\partial^2\Phi}{\partial r^2} + \Gamma && \sigma_{\theta z} = -\frac{\partial\Psi}{\partial r} \\
&\sigma_{r\theta} = -\frac{\partial^2}{\partial r\partial\theta}\left(\frac{\Phi}{r}\right) \\
&\sigma_{zz} = \frac{Ax + By + C - S_{13}\sigma_{rr} - S_{23}\sigma_{\theta\theta} - S_{34}\sigma_{\theta z} - S_{35}\sigma_{rz} - S_{36}\sigma_{r\theta}}{S_{33}}
\end{aligned} \qquad \text{I.87}$$

Defining all constants and new functions similarly to the rectilinearly anisotropic case.

Combining I.86, I.87 and 1.20 into I.52, one obtains the general differential system for the polarly anisotropic case:

$$\begin{cases}
L_4'\Phi + L_3'\Psi = \frac{2\sin(\theta)}{rS_{33}}\left((S_{13} - S_{33})B - S_{36}A\right) + \frac{2\cos(\theta)}{rS_{33}}\left((S_{13} - S_{23})A + S_{36}B\right) - (b_{12} + b_{22})\frac{\partial^2\Gamma}{\partial r^2} - \\
\qquad -(b_{11} + b_{12})\frac{1}{r^2}\frac{\partial^2\Gamma}{\partial\theta^2} + (b_{16} + b_{26})\frac{1}{r}\frac{\partial^2\Gamma}{\partial r\partial\theta} + (b_{11} - 2b_{22} - b_{12})\frac{1}{r}\frac{\partial\Gamma}{\partial r} + (b_{16} + b_{26})\frac{1}{r^2}\frac{\partial\Gamma}{\partial\theta} \\
L_3''\Phi + L_2'\Psi = \frac{\cos(\theta)}{S_{33}}\left(2S_{34}A - S_{25}B\right) + \frac{\sin(\theta)}{S_{33}}\left(S_{35}A + 2S_{34}B\right) + C\frac{S_{34}}{r} - 2\vartheta + (b_{14} + b_{24})\left(\frac{\partial\Gamma}{\partial r} - \frac{\Gamma}{r}\right) - \\
\qquad -(b_{15} + b_{25})\frac{1}{r}\frac{\partial\Gamma}{\partial\theta}
\end{cases} \qquad \text{I.88}$$

Where L_4', L_3', L_3'', L_2' are differential operators:

$$\begin{aligned}
L_4' &= b_{22}\frac{\partial^4}{\partial r^4} - 2b_{26}\frac{1}{r}\frac{\partial^4}{\partial r^3\partial\theta} + \left(2b_{12}+b_{66}\right)\frac{1}{r^2}\frac{\partial^4}{\partial r^2\partial\theta^2} - 2b_{16}\frac{1}{r^3}\frac{\partial^4}{\partial r\partial\theta^3} + b_{11}\frac{1}{r^4}\frac{\partial^4}{\partial\theta^4} + \\
&\quad + 2b_{22}\frac{1}{r}\frac{\partial^3}{\partial r^3} - \left(2b_{12}+b_{66}\right)\frac{1}{r^3}\frac{\partial^3}{\partial r\partial\theta^2} + 2b_{16}\frac{1}{r^4}\frac{\partial^3}{\partial\theta^3} - b_{11}\frac{1}{r^2}\frac{\partial^2}{\partial r^2} - \\
&\quad - 2\left(b_{16}+b_{26}\right)\frac{1}{r^3}\frac{\partial^2}{\partial r\partial\theta} + \left(2b_{11}+2b_{12}+b_{66}\right)\frac{1}{r^4}\frac{\partial^2}{\partial\theta^2} + b_{11}\frac{1}{r^3}\frac{\partial}{\partial r} + 2\left(b_{12}+b_{26}\right)\frac{1}{r^4}\frac{\partial}{\partial\theta} \\
L_3' &= b_{15}\frac{1}{r^3}\frac{\partial^3}{\partial\theta^3} - \left(b_{14}+b_{56}\right)\frac{1}{r^2}\frac{\partial^3}{\partial r\partial\theta^2} + \left(b_{25}+b_{46}\right)\frac{1}{r}\frac{\partial^3}{\partial r^2\partial\theta} - b_{24}\frac{\partial^3}{\partial r^3} + \left(b_{14}-2b_{24}\right)\frac{1}{r}\frac{\partial^2}{\partial r^2} + \\
&\quad + \left(b_{46}-b_{15}\right)\frac{1}{r^2}\frac{\partial^2}{\partial r\partial\theta} + b_{15}\frac{1}{r^3}\frac{\partial}{\partial\theta} \\
L_3'' &= b_{15}\frac{1}{r^3}\frac{\partial^3}{\partial\theta^3} - \left(b_{14}+b_{56}\right)\frac{1}{r^2}\frac{\partial^3}{\partial r\partial\theta^2} + \left(b_{25}+b_{46}\right)\frac{1}{r}\frac{\partial^3}{\partial r^2\partial\theta} - b_{24}\frac{\partial^3}{\partial r^3} - \left(b_{14}-b_{24}\right)\frac{1}{r}\frac{\partial^2}{\partial r^2} + \\
&\quad + \left(b_{15}-b_{46}\right)\frac{1}{r^2}\frac{\partial^2}{\partial r\partial\theta} + \left(b_{14}-b_{56}\right)\frac{1}{r^3}\frac{\partial^2}{\partial\theta^2} + b_{46}\frac{1}{r^3}\frac{\partial}{\partial\theta} \\
L_2' &= b_{44}\frac{\partial^2}{\partial r^2} - 2b_{45}\frac{1}{r}\frac{\partial^2}{\partial r\partial\theta} + b_{55}\frac{1}{r^2}\frac{\partial^2}{\partial\theta^2} + b_{44}\frac{1}{r}\frac{\partial}{\partial r}
\end{aligned} \qquad \text{I.89}$$

Solving system I.88 will lead to the general solution for this case.

1.5.4. Cylindrically shaped, polarly orthotropic, non-homogeneous bodies in which stresses do not vary along the generators

In this section the general elastic problem for the particular case of a non-homogeneous polarly orthotropic material is presented, as for the case of a complete anisotropy would be out of the scope for the present work. As for the rectilinear anisotropic case, also for polarly anisotropic material the elastic problem presents several similarities between the homogeneous and non-homogeneous case. Displacement I.86 and stress I.87 expressions remain the same. As for the differential equation system to be solved, it becomes:

$$
\begin{cases}
\left(\frac{\partial^2}{\partial\theta^2}-r\frac{\partial}{\partial r}\right)\left(\frac{b_{11}}{r}\frac{\partial\Phi}{\partial r}+\frac{b_{11}}{r^2}\frac{\partial^2\Phi}{\partial\theta^2}+b_{12}\frac{\partial^2\Phi}{\partial r^2}\right)+r\frac{\partial^2}{\partial r^2}\left(r\left(\frac{b_{12}}{r}\frac{\partial\Phi}{\partial r}+\frac{b_{12}}{r^2}\frac{\partial^2\Phi}{\partial\theta^2}+b_{22}\frac{\partial^2\Phi}{\partial r^2}\right)\right)+ \\
\qquad +\frac{\partial^2}{\partial r\partial\theta}\left(b_{66}r\frac{\partial^2}{\partial r\partial\theta}\left(\frac{\Phi}{r}\right)\right)=\left(\frac{\partial^2}{\partial\theta^2}-r\frac{\partial}{\partial r}\right)\left(\nu_{zr}\left(Ar\cos(\theta)+Br\sin(\theta)+C\right)\right)+ \\
\qquad +r\frac{\partial^2}{\partial r^2}\left(\nu_{zr}\left(Ar\cos(\theta)+Br\sin(\theta)+C\right)\right)-\left(\frac{\partial^2}{\partial\theta^2}-r\frac{\partial}{\partial r}\right)\left(\left(b_{11}+b_{12}\right)\Gamma\right)- \\
\qquad -r\frac{\partial^2}{\partial r^2}\left(\left(b_{12}+b_{22}\right)r\Gamma\right) \\
\frac{\partial}{\partial\theta}\left(\frac{1}{rG_{rz}}\frac{\partial\Psi}{\partial\theta}\right)+\frac{\partial}{\partial r}\left(\frac{r}{G_{rz}}\frac{\partial\Psi}{\partial r}\right)=-2\vartheta r
\end{cases}
\qquad \text{I.90}
$$

1.5.5. Generalized plain strain in cylindrically shaped, rectilinearly anisotropic, homogeneous bodies

Consider the same elastic problem discussed above but in addition it is known that after the deformation, the cross section of the cylinder along the z direction remain plane. This situation is known as generalized plain strain, the differential system I.66 and its solutions simplifies significantly because these constrain must be valid:

$$A=B=C=\vartheta=\omega_1=\omega_2=0 \qquad \text{I.91}$$

If, in addition, no body forces are acting:

$$\Gamma=\Phi_P=\Psi_P=U_x^0=U_y^0=0 \qquad \text{I.92}$$

One can express the displacement and stress fields as follows:

$$
\begin{aligned}
\sigma_{xx}&=2\,\mathrm{Re}\left[\mu_1^2\phi'_{H1}(z_1)+\mu_2^2\phi'_{H2}(z_2)+\mu_3^2\lambda_3\phi'_{H3}(z_3)\right]\\
\sigma_{yy}&=2\,\mathrm{Re}\left[\phi'_{H1}(z_1)+\phi'_{H2}(z_2)+\lambda_3\phi'_{H3}(z_3)\right]\\
\sigma_{xy}&=-2\,\mathrm{Re}\left[\mu_1\phi'_{H1}(z_1)+\mu_2\phi'_{H2}(z_2)+\mu_3\lambda_3\phi'_{H3}(z_3)\right]\\
\sigma_{yz}&=-2\,\mathrm{Re}\left[\lambda_1\phi'_{H1}(z_1)+\lambda_2\phi'_{H2}(z_2)+\phi'_{H3}(z_3)\right]\\
\sigma_{xz}&=2\,\mathrm{Re}\left[\mu_1\lambda_1\phi'_{H1}(z_1)+\mu_2\lambda_2\phi'_{H2}(z_2)+\mu_3\phi'_{H3}(z_3)\right]
\end{aligned}
\qquad \text{I.93}
$$

$$\sigma_{zz}=\frac{-S_{13}\sigma_{xx}-S_{23}\sigma_{yy}-S_{34}\sigma_{yz}-S_{35}\sigma_{xz}-S_{36}\sigma_{xy}}{S_{33}} \qquad \text{I.94}$$

$$U_x = 2\,\mathrm{Re}\left[\sum_{k=1}^{3} p_k \phi_{Hk}\left(z_k\right)\right]$$
$$U_y = 2\,\mathrm{Re}\left[\sum_{k=1}^{3} q_k \phi_{Hk}\left(z_k\right)\right] \qquad \text{I.95}$$
$$U_z = 2\,\mathrm{Re}\left[\sum_{k=1}^{3} t_k \phi_{Hk}\left(z_k\right)\right] + U_z^0$$

1.5.6. Plain strain in cylindrically shaped, rectilinearly anisotropic, homogeneous bodies

The plain strain state is very similar to the generalized plain strain one, but if the material presents a plane of elastic symmetry that is normal to the generator of the cylinder (parallel to all the cross sections), it is possible to impose further restrictions to the solution. Assuming that the displacement along the z direction is constant:

$$u_z = U_z^0 = const \qquad \text{I.96}$$

Leading to:

$$\varepsilon_{zz} = \varepsilon_{yz} = \varepsilon_{xz} = \sigma_{xz} = \sigma_{yz} = 0 \qquad \text{I.97}$$

Substituting all these conditions into the general differential system I.66, one obtain a very simple fourth order differential equation:

$$L_4\Phi = \left(b_{16} + b_{26}\right)\frac{\partial^2\Gamma}{\partial x \partial y} - \left(b_{12} + b_{22}\right)\frac{\partial^2\Gamma}{\partial x^2} - \left(b_{11} + b_{12}\right)\frac{\partial^2\Gamma}{\partial y^2} \qquad \text{I.98}$$

with corresponding characteristic equation:

$$l_4\left(\mu\right) = 0 \qquad \text{I.99}$$

The solution to this equation can be divided into 3 cases, each leading to a different form of the potential function Φ .

1) Four different complex eigenvalues $\mu_1 = \bar{\mu}_3 \neq \mu_2 = \bar{\mu}_4$

Which leads to the potential function:

$$\Phi = 2\,\mathrm{Re}\left[\Phi_{H1}(z_1) + \Phi_{H2}(z_2)\right] + \Phi_P \qquad \text{I.100}$$

2) Two pair of equal complex eigenvalues $\mu_1 = \bar{\mu}_3 = \mu_2 = \bar{\mu}_4$

Which leads to the potential function:

$$\Phi = 2\,\mathrm{Re}\left[\bar{z}_1 \Phi_{H1}(z_1) + \Phi_{H2}(z_1)\right] + \Phi_P \qquad \text{I.101}$$

Two pair of equal pure imaginary eigenvalues $\mu_1 = \bar{\mu}_3 = \mu_2 = \bar{\mu}_4 = \boldsymbol{i}$

In this case: $z_1 = z$ potential function takes the form found by Kolosov-Muskhelishvili:

$$\Phi = 2\,\mathrm{Re}\left[\bar{z} \Phi_{H1}(z) + \Phi_{H2}(z)\right] + \Phi_P \qquad \text{I.102}$$

If no body forces are acting on the body, further constraints can be imposed:

$$\Gamma = \Phi_P = \Psi_P = U_x^0 = U_y^0 = 0 \qquad \text{I.103}$$

And, in the case of four different eigenvalues, the final expressions for the stress and displacement fields are:

$$\begin{aligned} \sigma_{xx} &= 2\,\mathrm{Re}\left[\mu_1^2 \phi'_{H1}(z_1) + \mu_2^2 \phi'_{H2}(z_2)\right] \\ \sigma_{yy} &= 2\,\mathrm{Re}\left[\phi'_{H1}(z_1) + \phi'_{H2}(z_2)\right] \\ \sigma_{xy} &= -2\,\mathrm{Re}\left[\mu_1 \phi'_{H1}(z_1) + \mu_2 \phi'_{H2}(z_2)\right] \end{aligned} \qquad \text{I.104}$$

$$\begin{aligned} U_x &= 2\,\mathrm{Re}\left[\sum_{k=1}^{2} p_k \phi_{Hk}(z_k)\right] - \omega_3 y + u_x^0 \\ U_y &= 2\,\mathrm{Re}\left[\sum_{k=1}^{2} q_k \phi_{Hk}(z_k)\right] + \omega_3 x + u_y^0 \end{aligned} \qquad \text{I.105}$$

With:

$$\begin{aligned} p_k &= b_{11}\mu_k^2 + b_{12} - b_{16}\mu_k \\ q_k &= b_{12}\mu_k + \frac{b_{22}}{\mu_k} - b_{26} \qquad k \in \{1, 2\} \end{aligned} \qquad \text{I.106}$$

1.5.7. Plain stress in cylindrically shaped, rectilinearly anisotropic, homogeneous bodies

Considering the case of a cylindrical body of uniform thickness, made with a homogeneous anisotropic material having a plane of elastic symmetry parallel to the cross sections of the body along the generator. Further assume that the thickness is very small compared to the other two dimensions of the cross sections, and that external forces acting on the body don't vary very much along the thickness. In this case it is reasonable to assume that the variance of the stress and displacement fields along the thickness is very limited, and so it is convenient to assuming them constant and equal to the average value along the thickness. In this case the average value of σ_{zz} is neglectable if compared with the in-plane stresses $\sigma_{xx}, \sigma_{yy}, \sigma_{xy}$, and this elastic state is known as plane stress state. Reasonably, the problem can be simplified by only analyzing the middle plane of the body where it is assumed that the average stresses and displacement act, leaving:

$$\sigma_{zz} = \sigma_{xz} = \sigma_{yz} = 0 \qquad \text{I.107}$$

All these restrictions lead to the same exact general differential system and solution to the plain strain case, with the only difference being that:

$$b_{ij} = S_{ij} \,. \qquad \text{I.108}$$

1.5.8. Generalized torsion in cylindrically shaped, rectilinearly anisotropic, homogeneous bodies with no body forces and no lateral forces

Consider the case of a cylindrical homogeneous body with rectilinear anisotropic behaviour, to which no body forces are applied and with lateral surface free from external forces. Further assume that external forces applied to the end faces of the body can be reduce to a twisting moment M_t. This case in known as generalized torsion. The condition of no body forces imply:

$$\Gamma = \Phi_P = 0 \qquad \text{I.109}$$

Which reduce the general differential system to:

$$\begin{cases} L_4\Phi + L_3\Psi = 0 \\ L_3\Phi + L_2\Psi = \dfrac{AS_{34} - BS_{35}}{S_{33}} - 2\vartheta \end{cases} \qquad \text{I.110}$$

Imposing the boundary conditions on the end faces of the cylinder one finds:

$$A = \frac{S_{34}M_t}{2I_2} \qquad B = -\frac{S_{35}M_t}{2I_1} \qquad C = 0 \qquad \text{I.111}$$

And that the remaining particular solution is:

$$\Psi_p = \left(\frac{M_t}{8S_{33}} \left(\frac{S_{34}^2}{I_2} + \frac{S_{35}^2}{I_1} \right) - \frac{\vartheta}{2} \right) \frac{b_{55}x^2 + 2b_{45}xy + b_{44}y^2}{b_{44}b_{55} - b_{45}^2} \qquad \text{I.112}$$

1.5.9. Twisting and bending in cylindrically shaped, rectilinearly anisotropic, homogeneous bodies with no body forces and no lateral forces

Taking the previous example, it is also possible to imagine the situation where in addition to the twisting moment M_t the body is also loaded with two bending moments M_x, M_y around the axis x and y respectively. In the case of a generic anisotropic material, it is possible to impose the boundary conditions at the end faces of the cylinder and find:

$$A = \frac{S_{34}M_t}{2I_2} + \frac{M_2}{I_2} \qquad B = -\frac{S_{35}M_t}{2I_1} + \frac{M_1}{I_1} \qquad C = 0 \qquad \text{I.113}$$

1.5.10. Pure torsion in cylindrically shaped, rectilinearly anisotropic, homogeneous bodies with no body forces and no lateral forces

This scenario is a specific case of the generalized torsion problem in which the anisotropic material presents a plane of elastic symmetry parallel to the cross sections of the bar:

$$S_{34} = S_{35} = 0 \qquad \text{I.114}$$

In this case the differential system simplifies greatly since:

$$\Gamma = \Phi = A = B = C = U_x = U_y = 0 \qquad \text{I.115}$$

$$\sigma_{xx} = \sigma_{yy} = \sigma_{xy} = \sigma_{zz} = 0 \qquad \text{I.116}$$

and becomes a very simple second order differential equation:

$$L_2 \Psi = -2\vartheta \qquad \text{I.117}$$

With characteristic equation:

$$l_2(\mu) = 0 \qquad \text{I.118}$$

In this case only two components of the stress tensor are different from zero and their expression become:

$$\begin{aligned} \sigma_{yz} &= -2\,\mathrm{Re}\left[\phi'_{H3}(z_3)\right] - \frac{\partial \Psi_P}{\partial x} \\ \sigma_{xz} &= 2\,\mathrm{Re}\left[\mu_3 \phi'_{H3}(z_3)\right] + \frac{\partial \Psi_P}{\partial y} \end{aligned} \qquad \text{I.119}$$

While the displacement field is:

$$\begin{aligned} U_x &= -\vartheta yz + \omega_2 z - \omega_3 y + u_x^0 \\ U_y &= \vartheta xz + \omega_3 x - \omega_1 z + u_y^0 \\ U_z &= 2\,\mathrm{Re}\left[\left(S_{45} - \frac{S_{44}}{\mu_3}\right)\phi_{H3}(z_3)\right] + \omega_1 y - \omega_2 x + u_z^0 \end{aligned} \qquad \text{I.120}$$

1.6. Some important solutions to for various geometries and loading conditions

1.6.1. Introduction

In this chapter are presented some of the most classical and important solutions for a variety of elastic problems. Ranging from plates with holes, cracks and notches to torsion of bars, these important elastic problems will be discussed and their solution presented. The analytical methods used by the authors and developers cited in this chapter are an invaluable insight into some of the most advanced and powerful techniques for studying stress states of an elastic body.

1.6.2. Plane problems around holes

1.6.2.1. Infinite non-simply connected anisotropic plates

Consider an infinite anisotropic plate weakened by a hole of shape Ω (Fig.I.5-a). It is assumed that an invertible mapping function $\varpi(\zeta)$ exists such that the region S outside the hole is mapped into the interior of a unit circle.

$$z = x + \boldsymbol{i}y \qquad z = \varpi(\zeta) \tag{I.121}$$

It is also assumed that there exists an external force F applied to the boundary of the hole:

$$F(s) = X_n(s) + \boldsymbol{i}Y_n(s) \tag{I.122}$$

Where $X_n(s)$ and $Y_n(s)$ are the components of the force in x and y direction respectively;

as well as external remote stresses applied to the plate $\sigma_{xx}^{\infty}, \sigma_{yy}^{\infty}, \sigma_{xy}^{\infty}$.

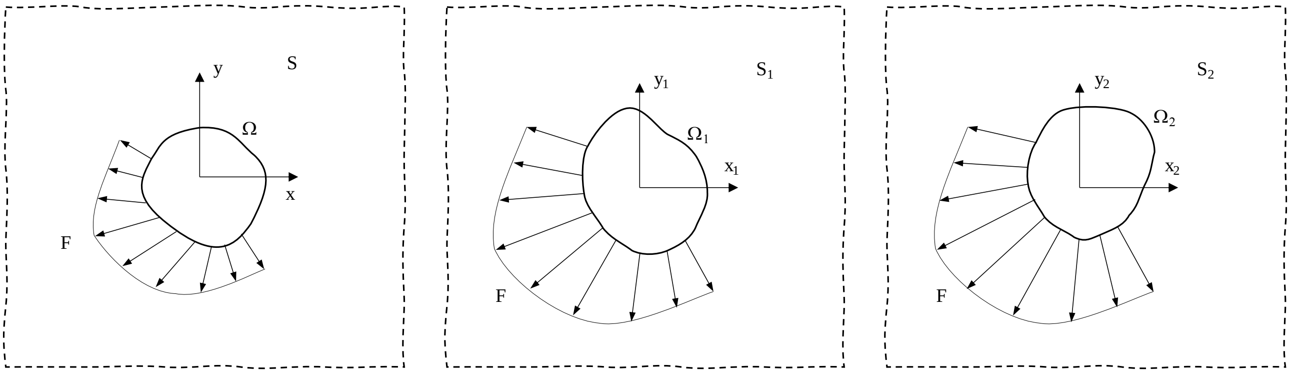

(a) (b) (c)

Figure I.5 Domain transformation of a non-simply connected plate for variables z_1 and z_2

Applying the affine transformation due to the anisotropic behavior of the material to the coordinate system:

$$z_1 = x + \mu_1 y = x_1 + \boldsymbol{i} y_1 \qquad z_2 = x + \mu_2 y = x_2 + \boldsymbol{i} y_2 \tag{I.123}$$

The region S can be mapped into regions S_1 and S_2 respectively (Fig.I.5-b/c), which can themselves be mapped into the interior of a unit circle:

$$z_1 = \varpi_1(\zeta) \qquad z_2 = \varpi_2(\zeta) \tag{I.124}$$

In plane stress or strain conditions, the stress and displacement fields are, according to I.104-I.105:

$$\begin{aligned} \sigma_{xx} &= 2\,\mathrm{Re}\left[\mu_1^2 \phi'_{H1}(z_1) + \mu_2^2 \phi'_{H2}(z_2)\right] \\ \sigma_{yy} &= 2\,\mathrm{Re}\left[\phi'_{H1}(z_1) + \phi'_{H2}(z_2)\right] \\ \sigma_{xy} &= -2\,\mathrm{Re}\left[\mu_1 \phi'_{H1}(z_1) + \mu_2 \phi'_{H2}(z_2)\right] \end{aligned} \tag{I.125}$$

$$\begin{aligned} U_x &= 2\,\mathrm{Re}\left[\sum_{k=1}^{2} p_k \phi_{Hk}(z_k)\right] - \omega_3 y + u_x^0 \\ U_y &= 2\,\mathrm{Re}\left[\sum_{k=1}^{2} q_k \phi_{Hk}(z_k)\right] + \omega_3 x + u_y^0 \end{aligned} \tag{I.126}$$

The two potential functions $\phi_{H1}(z_1)$ and $\phi_{H2}(z_2)$ can be divided as follows:

$$\begin{aligned} \phi_{H1}(z_1) &= A^* \ln(z_1) + B^{**} z_1 + \phi_{H1}^0(z_1) \\ \phi_{H2}(z_2) &= B^* \ln(z_2) + \left(B'^{**} + \boldsymbol{i} C'^{**}\right) z_2 + \phi_{H2}^0(z_2) \end{aligned} \tag{I.127}$$

Where B^{**}, B'^{**} and C'^{**} are real constants so defined:

$$B^{**}=\frac{\sigma_{xx}^{\infty}+\left(\alpha_2^2+\beta_2^2\right)\sigma_{yy}^{\infty}+2\alpha_2\sigma_{xy}^{\infty}}{2\left(\left(\alpha_2-\alpha_1\right)^2+\left(\beta_2^2-\beta_1^2\right)\right)}$$

$$B'^{**}=\frac{\left(\alpha_1^2+\beta_1^2\right)\sigma_{yy}^{\infty}-2\alpha_1\alpha_2\sigma_{yy}^{\infty}-\sigma_{xx}^{\infty}-2\alpha_2\sigma_{xy}^{\infty}}{2\left(\left(\alpha_2-\alpha_1\right)^2+\left(\beta_2^2-\beta_1^2\right)\right)} \tag{I.128}$$

$$C'^{**}=\frac{\left(\alpha_2-\alpha_1\right)\sigma_{xx}^{\infty}+\left(\alpha_2\left(\alpha_1^2-\beta_1^2\right)-\alpha_1\left(\alpha_2^2-\beta_2^2\right)\right)\sigma_{yy}^{\infty}+\left(\left(\alpha_1^2-\beta_1^2\right)-\left(\alpha_2^2-\beta_2^2\right)\right)\sigma_{xy}^{\infty}}{2\beta_2\left(\left(\alpha_2-\alpha_1\right)^2-\left(\beta_2^2-\beta_1^2\right)\right)}$$

While A^* and B^* are complex constants found by solving the system:

$$\begin{cases}\left(1+\boldsymbol{i}\mu_1\right)A^*-\left(1+\boldsymbol{i}\bar{\mu}_1\right)\bar{A}^*+\left(1+\boldsymbol{i}\mu_2\right)B^*-\left(1+\boldsymbol{i}\bar{\mu}_2\right)\bar{B}^*=-\dfrac{X_n^{tot}+\boldsymbol{i}Y_n^{tot}}{2\pi}\\ \left(p_1+\boldsymbol{i}q_1\right)A^*-\left(\bar{p}_1+\boldsymbol{i}\bar{q}_1\right)\bar{A}^*+\left(p_2+\boldsymbol{i}q_2\right)B^*-\left(\bar{p}_2+\boldsymbol{i}\bar{q}_2\right)\bar{B}^*=0\\ \left(1-\boldsymbol{i}\bar{\mu}_1\right)\bar{A}^*-\left(1-\boldsymbol{i}\mu_1\right)A^*+\left(1-\boldsymbol{i}\bar{\mu}_2\right)\bar{B}^*-\left(1-\boldsymbol{i}\mu_2\right)B^*=-\dfrac{X_n^{tot}-\boldsymbol{i}Y_n^{tot}}{2\pi}\\ \left(\bar{p}_1-\boldsymbol{i}\bar{q}_1\right)\bar{A}^*-\left(p_1-\boldsymbol{i}q_1\right)A^*+\left(\bar{p}_2-\boldsymbol{i}\bar{q}_2\right)\bar{B}^*-\left(p_2-\boldsymbol{i}q_2\right)B^*=0\end{cases} \tag{I.129}$$

Where X_n^{tot} and Y_n^{tot} are the total resultants of force F in the x and y direction respectively.

Applying the boundary conditions along the boundary of the hole one finds that the following conditions must be met:

$$\begin{cases}2\,\mathrm{Re}\left[\phi_{H1}^0\left(z_1\right)+\phi_{H2}^0\left(z_2\right)\right]=-\int_0^s Y_n\left(s\right)ds+C_1-\\ \qquad -2\,\mathrm{Re}\left[A^*\ln\left(z_1\right)+B^{**}z_1+B^*\ln\left(z_2\right)+\left(B'^{**}+\boldsymbol{i}C'^{**}\right)z_2\right]=f_1^0\\ 2\,\mathrm{Re}\left[\mu_1\phi_{H1}^0\left(z_1\right)+\mu_2\phi_{H2}^0\left(z_2\right)\right]=\int_0^s X_n\left(s\right)ds+C_2-\\ \qquad -2\,\mathrm{Re}\left[A^*\mu_1\ln\left(z_1\right)+B^{**}\mu_1 z_1+B^*\mu_2\ln\left(z_2\right)+\mu_2\left(B'^{**}+\boldsymbol{i}C'^{**}\right)z_2\right]=f_2^0\end{cases} \tag{I.130}$$

To find the potential functions that solve system I.130 it is necessary to first use the mapping functions I.124 and define two new potential functions in the ζ coordinate system:

$$\begin{aligned}\phi_{H1}^{\zeta}\left(\zeta\right)&=\phi_{H1}\left(\varpi_1\left(\zeta\right)\right)\\ \phi_{H2}^{\zeta}\left(\zeta\right)&=\phi_{H2}\left(\varpi_2\left(\zeta\right)\right)\end{aligned} \tag{I.131}$$

Remembering that in the new coordinate system the boundary of the hole is represented by the contour of a unit disk:

$$\Omega_1(z_1) = \Omega_1(\varpi_1(\zeta)) = e^{\boldsymbol{i}Arg(\zeta)}$$
$$\Omega_2(z_2) = \Omega_2(\varpi_2(\zeta)) = e^{\boldsymbol{i}Arg(\zeta)} \qquad \text{I.132}$$

It is possible to use the Schwarz integral formula to find the new potential functions:

$$\phi_{H1}^{\zeta}(\zeta) = \frac{\boldsymbol{i}}{4\pi(\mu_1 - \mu_2)} \int_{\Omega_1} (\mu_2 f_1^0 - f_2^0) \frac{s+\zeta}{s(s-\zeta)} ds$$
$$\phi_{H2}^{\zeta}(\zeta) = -\frac{\boldsymbol{i}}{4\pi(\mu_1 - \mu_2)} \int_{\Omega_2} (\mu_1 f_1^0 - f_2^0) \frac{s+\zeta}{s(s-\zeta)} ds \qquad \text{I.133}$$

And inverting the mapping functions I.131:

$$\phi_{H1}(z_1) = \phi_{H1}^{\zeta}(\varpi_1^{-1}(z_1))$$
$$\phi_{H2}(z_2) = \phi_{H2}^{\zeta}(\varpi_2^{-1}(z_2)) \qquad \text{I.134}$$

1.6.2.2. Infinite anisotropic plates with nearly elliptical hole

This chapter will consider the specific case of an infinite anisotropic plate with a nearly elliptical hole. This case is particularly interesting and important since it allows to solve a large variety of problems despite its relatively simple formulation. Using the same solving procedure described in the previous chapter, this case requires more attention to the analytical formulation, given the nature of the mapping function. A nearly elliptical hole can be described as a slight deformation of a pure elliptical hole of major axis R and minor axis b. In Figure I.6 is shown as an example a nearly elliptical hole with four sides.

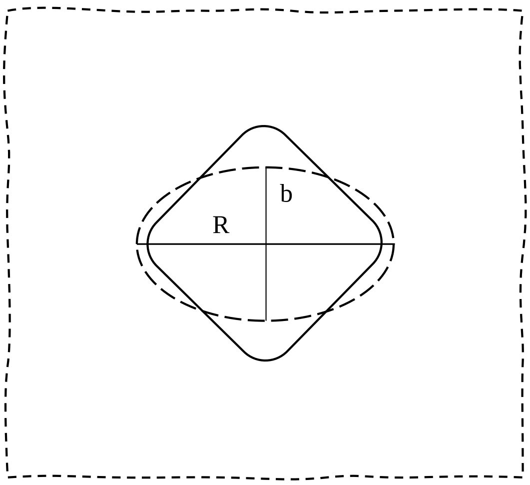

Figure I.6 Nearly elliptical hole with four sides.

A nearly elliptical contour can be described using this parametric expression:

$$\begin{aligned} x &= R\left(\cos(\theta)+\varepsilon\sum_{k=2}^{N}\left(\alpha_k^g\cos(k\theta)-\beta_k^g\sin(k\theta)\right)\right) \\ y &= R\left(-c\sin(\theta)+\varepsilon\sum_{k=2}^{N}\left(\alpha_k^g\sin(k\theta)+\beta_k^g\cos(k\theta)\right)\right) \end{aligned} \qquad \text{I.135}$$

Where R and b are the major and minor axis of the ellipse respectively, α_k^g and β_k^g are constants, ε is a small parameter, N is a positive natural number greater than 2 and

$$c=\frac{b}{R} \qquad \text{I.136}$$

The mapping function for this contour is:

$$\varpi(\zeta)=R\left(\frac{1-c}{2}\zeta+\frac{1+c}{2}\frac{1}{\zeta}+\varepsilon\Upsilon(\zeta)\right) \qquad \text{I.137}$$

Where:

$$\Upsilon(\zeta)=\sum_{k=2}^{N}\left(\alpha_k^g+\boldsymbol{i}\beta_k^g\right)\zeta^k \qquad \text{I.138}$$

The potential functions can be divided as discussed in the previous chapter, following the same definitions for parameters A^*, B^*, B^{**}, B'^{**} and C'^{**}:

$$\begin{aligned} \phi_{H1}(z_1) &= A^*\ln(z_1)+B^{**}z_1+\phi_{H1}^0(z_1) \\ \phi_{H2}(z_2) &= B^*\ln(z_2)+\left(B'^{**}+\boldsymbol{i}C'^{**}\right)z_2+\phi_{H2}^0(z_2) \end{aligned} \qquad \text{I.139}$$

And to obtain the potential functions in the ζ coordinate system one has to substitute the relevant mapping functions into the potentials:

$$\begin{aligned} \phi_{H1}^{\zeta}(\zeta) &= \phi_{H1}\left(\varpi_1(\zeta)\right) \\ \phi_{H2}^{\zeta}(\zeta) &= \phi_{H2}\left(\varpi_2(\zeta)\right) \end{aligned} \qquad \text{I.140}$$

Following S. G. Lekhnitskiy’s method[4], the two potentials can be represented as follows:

$$\phi_{H1}^{\zeta}(\zeta)= f_{10}(\zeta_1)+\varepsilon\left(f_{11}(\zeta_1)+\left(\Upsilon(\zeta)+\lambda_1\bar{\Upsilon}(\zeta)\right)\frac{df_{10}(\zeta_1)}{d\zeta_1}\right)+\cdots+$$
$$+\varepsilon^k\left(f_{1k}(\zeta_1)+\left(\Upsilon(\zeta)+\lambda_1\bar{\Upsilon}(\zeta)\right)\frac{df_{1,k-1}(\zeta_1)}{d\zeta_1}+\cdots+\frac{1}{k!}\left(\Upsilon(\zeta)+\lambda_1\bar{\Upsilon}(\zeta)\right)^k\frac{d^k f_{1,k-1}(\zeta_1)}{d\zeta_1^k}\right)+\cdots;$$
$$\phi_{H2}^{\zeta}(\zeta)= f_{20}(\zeta_2)+\varepsilon\left(f_{21}(\zeta_2)+\left(\Upsilon(\zeta)+\lambda_2\bar{\Upsilon}(\zeta)\right)\frac{df_{20}(\zeta_2)}{d\zeta_2}\right)+\cdots+$$
$$+\varepsilon^k\left(f_{2k}(\zeta_2)+\left(\Upsilon(\zeta)+\lambda_2\bar{\Upsilon}(\zeta)\right)\frac{df_{2,k-1}(\zeta_2)}{d\zeta_2}+\cdots+\frac{1}{k!}\left(\Upsilon(\zeta)+\lambda_2\bar{\Upsilon}(\zeta)\right)^k\frac{d^k f_{2,k-1}(\zeta_2)}{d\zeta_2^k}\right)+\cdots; \qquad \text{I.141}$$

Where:

$$\lambda_i=\frac{1+\boldsymbol{i}\mu_i}{1-\boldsymbol{i}\mu_i} \qquad \text{I.142}$$

$$\boldsymbol{\zeta}_i(\zeta)=\frac{1-c}{2}\zeta+\frac{1+c}{2}\frac{1}{\zeta}+\lambda_i\left(\frac{1-c}{2}\zeta+\frac{1+c}{2}\frac{1}{\zeta}\right) \qquad \text{I.143}$$

And $f_{ij}(\zeta_i)$ are functions defined in regions S_i which represent infinite planes with elliptical holes, and to be defined applying the boundary conditions.

Assuming that the external forces applied to the hole boundaries can be expressed using a power series in the parameter ε:

$$-\int_0^s Y_n(s)\,ds+C_1=\sum_{k=0}^{N} p_{1k}\varepsilon^k$$
$$\int_0^s X_n(s)\,ds+C_2=\sum_{k=0}^{N} p_{2k}\varepsilon^k \qquad \text{I.144}$$

It is possible to obtain the following expression by applying the boundary conditions along the hole contour:

$$2\,\mathrm{Re}\left[f_{10}(\zeta_1) + f_{20}(\zeta_2) \right] = p_{10} -$$
$$-2\,\mathrm{Re}\left[A^* \ln(\zeta_1) + B^{**}\zeta_1 + B^* \ln(\zeta_2) + \left(B'^{**} + \boldsymbol{i}C'^{**}\right)\zeta_2 \right] = \Theta_{10}$$
$$2\,\mathrm{Re}\left[\mu_1 f_{10}(\zeta_1) + \mu_2 f_{20}(\zeta_2) \right] = p_{20} -$$
$$-2\,\mathrm{Re}\left[A^*\mu_1 \ln(\zeta_1) + B^{**}\mu_1\zeta_1 + B^*\mu_2 \ln(\zeta_2) + \mu_2\left(B'^{**} + \boldsymbol{i}C'^{**}\right)\zeta_2 \right] = \Theta_{20}$$
$$\vdots$$
$$2\,\mathrm{Re}\left[f_{1k}(\zeta_1) + f_{2k}(\zeta_2) \right] = p_{1k} - 2\,\mathrm{Re}\left[\left(\Upsilon(\zeta) + \lambda_1\bar{\Upsilon}(\zeta)\right)\frac{df_{1,k-1}(\zeta_1)}{d\zeta_1} + \cdots + \right.$$
$$+\frac{1}{k!}\left(\Upsilon(\zeta) + \lambda_1\bar{\Upsilon}(\zeta)\right)^k \frac{d^k f_{1,0}(\zeta_1)}{d\zeta_1^k} + \left(\Upsilon(\zeta) + \lambda_2\bar{\Upsilon}(\zeta)\right)\frac{df_{2,k-1}(\zeta_2)}{d\zeta_2} + \cdots +$$
$$\left. +\frac{1}{k!}\left(\Upsilon(\zeta) + \lambda_2\bar{\Upsilon}(\zeta)\right)^k \frac{d^k f_{2,0}(\zeta_2)}{d\zeta_2^k} \right] = \Theta_{1k}$$
$$2\,\mathrm{Re}\left[\mu_1 f_{1k}(\zeta_1) + \mu_2 f_{2k}(\zeta_2) \right] = p_{2k} - 2\,\mathrm{Re}\left[\mu_1\left(\Upsilon(\zeta) + \lambda_1\bar{\Upsilon}(\zeta)\right)\frac{df_{1,k-1}(\zeta_1)}{d\zeta_1} + \cdots + \right. \qquad \text{I.145}$$
$$+\frac{\mu_1}{k!}\left(\Upsilon(\zeta) + \lambda_1\bar{\Upsilon}(\zeta)\right)^k \frac{d^k f_{1,0}(\zeta_1)}{d\zeta_1^k} + \mu_2\left(\Upsilon(\zeta) + \lambda_2\bar{\Upsilon}(\zeta)\right)\frac{df_{2,k-1}(\zeta_2)}{d\zeta_2} + \cdots +$$
$$\left. +\frac{\mu_2}{k!}\left(\Upsilon(\zeta) + \lambda_2\bar{\Upsilon}(\zeta)\right)^k \frac{d^k f_{2,0}(\zeta_2)}{d\zeta_2^k} \right] = \Theta_{2k}$$

Remembering that the hole contour is defined by a unit disk boundary in the ζ coordinate system:

$$\begin{aligned} \Omega_1(z_1) &= \Omega_1(z_1(\zeta)) = e^{\boldsymbol{i}Arg(\zeta)} = \delta \\ \Omega_2(z_2) &= \Omega_2(z_2(\zeta)) = e^{\boldsymbol{i}Arg(\zeta)} = \delta \end{aligned} \qquad \text{I.146}$$

$$\delta_i = \frac{1-c}{2}\delta + \frac{1+c}{2}\frac{1}{\delta} + \lambda_i\left(\frac{1-c}{2}\delta + \frac{1+c}{2}\frac{1}{\delta}\right) \qquad \text{I.147}$$

And using the chain rule to find:

$$\frac{df_{p,k}(\delta_p)}{d\delta_p} = -\frac{\omega_p\delta^2}{1-\eta_p\delta^2}\frac{df_{p,k}(\delta_p)}{d\delta} \qquad \text{I.148}$$

Where:

$$\begin{aligned} \omega_p &= -\frac{2}{1+c+\lambda_p(1-c)} \\ \eta_p &= \frac{1-c+\lambda_p(1+c)}{1+c+\lambda_p(1-c)} \end{aligned} \qquad \text{I.149}$$

It is finally possible to apply the Schwarz integral formula to find all the potential functions:

$$f_{1k}(\zeta)=\frac{\boldsymbol{i}}{4\pi(\mu_1-\mu_2)}\int_{\Omega}(\mu_2\Theta_{1k}-\Theta_{2k})\frac{s+\zeta}{s(s-\zeta)}ds$$
$$f_{2k}(\zeta)=-\frac{\boldsymbol{i}}{4\pi(\mu_1-\mu_2)}\int_{\Omega}(\mu_1\Theta_{1k}-\Theta_{2k})\frac{s+\zeta}{s(s-\zeta)}ds \qquad \text{I.150}$$

And inverting Eq. I.143:

$$\zeta=\boldsymbol{\zeta}_i^{-1}(\zeta_i)=\frac{\zeta_i-\sqrt{\zeta_i^2-\left(\left(1+\lambda_i^2\right)\left(1-c^2\right)+2\lambda_i\left(1+c^2\right)\right)}}{1-c+\lambda_i(1+c)} \qquad \text{I.151}$$

One finds all the expressions for $f_{ik}(\zeta_i)$ and $\phi_{H1}^{\zeta}(\zeta)$. Finally:

$$\phi_{H1}(z_1)=\phi_{H1}^{\zeta}\left(\varpi_1^{-1}(z_1)\right)$$
$$\phi_{H2}(z_2)=\phi_{H2}^{\zeta}\left(\varpi_2^{-1}(z_2)\right) \qquad \text{I.152}$$

1.6.2.3. Stress distribution in polarly transversely isotropic annulus

In this chapter a simple case of polar anisotropic behaviour is analysed, a polarly transversely isotropic annulus. Despite the simplicity of the geometry, this model is quite useful in multiple applications, especially in components made with additive manufacturing technologies, where, taking advantage of the ability to place reinforced material along customizable paths, has led many to use this configuration to reinforce holes in many components.

Considering an annular region of polarly transversely isotropic material with internal radius of r_0 and external radius of r_1, the elastic stress-strain relations are, according to I.53-I.59:

$$\begin{Bmatrix}\varepsilon_{rr}\\\varepsilon_{\theta\theta}\\\varepsilon_{zz}\\\varepsilon_{rz}\\\varepsilon_{\theta z}\\\varepsilon_{r\theta}\end{Bmatrix}=\begin{bmatrix}\frac{1}{E_T} & -\frac{\nu_{NT}}{E_N} & -\frac{\nu_{TT}}{E_T} & 0 & 0 & 0\\ & \frac{1}{E_N} & -\frac{\nu_{NT}}{E_N} & 0 & 0 & 0\\ & & \frac{1}{E_T} & 0 & 0 & 0\\ & & & \frac{2(1+\nu_{TT})}{E_T} & 0 & 0\\ & & & & \frac{1}{G_{TN}} & 0\\ & & & & & \frac{1}{G_{TN}}\end{bmatrix}\cdot\begin{Bmatrix}\sigma_{rr}\\\sigma_{\theta\theta}\\\sigma_{zz}\\\sigma_{rz}\\\sigma_{\theta z}\\\sigma_{r\theta}\end{Bmatrix} \qquad \text{I.153}$$

Applying plane stress or strain condition these relations can be rewritten as follows:

$$\begin{aligned} \sigma_{\theta\theta} &= M\varepsilon_{\theta\theta} + N\varepsilon_{rr} \\ \sigma_{\theta\theta} &= L\varepsilon_{\theta\theta} + M\varepsilon_{rr} \\ \sigma_{r\theta} &= 2G_{TN} \end{aligned} \qquad \text{I.154}$$

Where:

$$L = \begin{cases} \dfrac{E_T E_N \left(\nu_{TT} - 1\right)}{E_T \left(\nu_{TT} - 1\right) + 2E_N \nu_{NT}^2} & \textit{Plain Strain} \\ \dfrac{E_T E_N}{E_T - E_N \nu_{NT}^2} & \textit{Plain Stress} \end{cases}$$

$$M = \begin{cases} \dfrac{-E_T E_N \nu_{NT}}{E_T \left(\nu_{TT} - 1\right) + 2E_N \nu_{NT}^2} & \textit{Plain Strain} \\ \dfrac{E_T E_N \nu_{NT}}{E_T - E_N \nu_{NT}^2} & \textit{Plain Stress} \end{cases} \qquad \text{I.155}$$

$$N = \begin{cases} \dfrac{E_T \left(E_N \nu_{NT}^2 - E_T\right)}{E_T \left(\nu_{TT}^2 - 1\right) + 2E_N \left(\nu_{TT} + 1\right)\nu_{NT}^2} & \textit{Plain Strain} \\ \dfrac{E_T^2}{E_T - E_N \nu_{NT}^2} & \textit{Plain Stress} \end{cases}$$

Which can be used to define new elastic parameters:

$$\epsilon^2 = \frac{G_{TN}}{L}; \qquad d^2 = \frac{G_{TN}}{M}; \qquad c^2 = \frac{G_{TN}}{N} \qquad \text{I.156}$$

Substituting the strain displacement relation I.20 into I.153 and then into the equilibrium equations I.37 one obtains the following differential system:

$$\begin{cases} \dfrac{1}{c^2}\dfrac{\partial^2 u_r}{\partial r^2} + \dfrac{1}{r^2}\dfrac{\partial^2 u_r}{\partial \theta^2} + \dfrac{1}{r}\left(1 + \dfrac{1}{d^2}\right)\dfrac{\partial^2 u_\theta}{\partial \theta \partial r} + \dfrac{1}{rc^2}\dfrac{\partial u_r}{\partial r} - \dfrac{1}{r^2}\left(1 + \dfrac{1}{\epsilon^2}\right)\dfrac{\partial u_\theta}{\partial \theta} - \dfrac{u_r}{r^2 \epsilon^2} = 0 \\ \dfrac{1}{r}\left(1 + \dfrac{1}{d^2}\right)\dfrac{\partial^2 u_r}{\partial \theta \partial r} + \dfrac{\partial^2 u_\theta}{\partial r^2} + \dfrac{1}{r^2 \epsilon^2}\dfrac{\partial^2 u_\theta}{\partial \theta^2} + \dfrac{1}{r^2}\left(1 + \dfrac{1}{\epsilon^2}\right)\dfrac{\partial u_r}{\partial \theta} + \dfrac{1}{r}\dfrac{\partial u_\theta}{\partial r} - \dfrac{u_\theta}{r^2} = 0 \end{cases} \qquad \text{I.157}$$

The solution of this system is:

$$u_r = A_0\left(\frac{r_0}{r}\right)^{\alpha_0} + a_0\left(\frac{r}{r_1}\right)^{\alpha_0} - E_1\left(\frac{1+d^{-2}}{1+\epsilon^{-2}}\right)\cos\theta + \left(E_1\cos\theta + F_1\sin\theta\right)\log\left(\frac{r}{r_0}\right) +$$
$$+\sum_{n=1}^{N}\left(\left(A_n\cos n\theta + B_n\sin n\theta\right)\left(\frac{r_0}{r}\right)^{\alpha_n} + \left(a_n\cos n\theta + b_n\sin n\theta\right)\left(\frac{r}{r_1}\right)^{\alpha_n}\right) + \quad \text{I.158}$$
$$+\sum_{n=2}^{N}\left(\left(E_n\cos n\theta + F_n\sin n\theta\right)\left(\frac{r_0}{r}\right)^{\beta_n} + \left(e_n\cos n\theta + f_n\sin n\theta\right)\left(\frac{r}{r_1}\right)^{\beta_n}\right)$$

$$u_\theta = F_1\left(\frac{1+d^{-2}}{1+\epsilon^{-2}}\right)\cos\theta - H_0\left(\frac{r_0}{r}\right) + \left(F_1\cos\theta - E_1\sin\theta\right)\log\left(\frac{r}{r_0}\right) +$$
$$+\sum_{n=1}^{N}\left(\left(C_n\sin n\theta - D_n\cos n\theta\right)\left(\frac{r_0}{r}\right)^{\alpha_n} + \left(c_n\sin n\theta - d_n\cos n\theta\right)\left(\frac{r}{r_1}\right)^{\alpha_n}\right) + \quad \text{I.159}$$
$$+\sum_{n=2}^{N}\left(\left(G_n\sin n\theta - H_n\cos n\theta\right)\left(\frac{r_0}{r}\right)^{\beta_n} + \left(g_n\sin n\theta - h_n\cos n\theta\right)\left(\frac{r}{r_1}\right)^{\beta_n}\right)$$

Where $A_n, a_n, B_n, b_n, C_n, c_n, D_n, d_n, E_n, e_n, F_n, f_n, G_n, g_n, H_n, h_n \ \forall n \le N \in \mathbb{N}$ are linearly dependent constants to determine by applying proper boundary conditions and linked through the following relations:

$$\begin{array}{lll} A_n = C_n\phi_{\alpha,n} & a_n = c_n\phi_{-\alpha,n} & n \ge 1 \\ B_n = D_n\phi_{\alpha,n} & b_n = d_n\phi_{-\alpha,n} & n \ge 1 \\ E_n = G_n\phi_{\beta,n} & e_n = g_n\phi_{-\beta,n} & n \ge 2 \\ F_n = H_n\phi_{\beta,n} & f_n = h_n\phi_{-\beta,n} & n \ge 2 \end{array} \quad \text{I.160}$$

In Eq. I.160:

$$\phi_{\gamma,n} = \frac{\gamma_n{}^2 - \epsilon^{-2}n^2 - 1}{n\left(\left(1+\epsilon^{-2}\right) - \gamma_n\left(1+d^{-2}\right)\right)} \quad \text{I.161}$$

whilst $\pm\alpha_n$ and $\pm\beta_n$ $\forall n \in \mathbb{N}$ are the roots of the following characteristic equations:

$$f(\gamma_n) = \gamma_n{}^4 - \gamma_n{}^2\left(\epsilon^{-2}\left(n^2+c^2\right) - n^2c^2d^{-2}\left(2+d^{-2}\right) + 1\right) + c^2\epsilon^{-2}\left(n^2-1\right)^2 = 0 \quad \text{I.162}$$

1.6.3. Multi-material corners

Stress singularities in an elastic material arise due to some discontinuities in the domain and they can be caused by geometrical features, like cracks or V-notches, by material properties discontinuities, with many different materials bonded together, or both. This singularities in the stress fields are in many cases the cause of failure initiations in a component and for this reason it is vital to have a very good understanding of their elastic behaviour. A generic case where geometrical and material discontinuities are both present in a domain is a multi-material corner Fig. 6. This configuration has M material connected with straight interfaces all meeting at one point, called notch tip, where the centre of the coordinate system is placed. The connecting interfaces can either be perfectly or imperfectly bonded with the assumption of no friction between the imperfect bonds. Wedges are defined as the sub-domain of the multi-material corner between two imperfectly bonded interfaces, and having M materials and W total wedges, it is necessary that $W \leq M$. In this chapter a general formulation is presented in which boundary conditions on the free edges of the corner and on the different interfaces are homogeneous and orthogonal, meaning that the stress and displacement vectors defining the boundary conditions are orthogonal to each other. This formulation is taken from M. A. Herrera-Garrido et al.[9], and reported in a concise form, referencing several papers that contributed over the years at the development of this mathematical tool like Ting[11] for the development of the transfer matrix concept, Mantič et al.[10] for the development of a matrix formalism for the boundary conditions and many others.

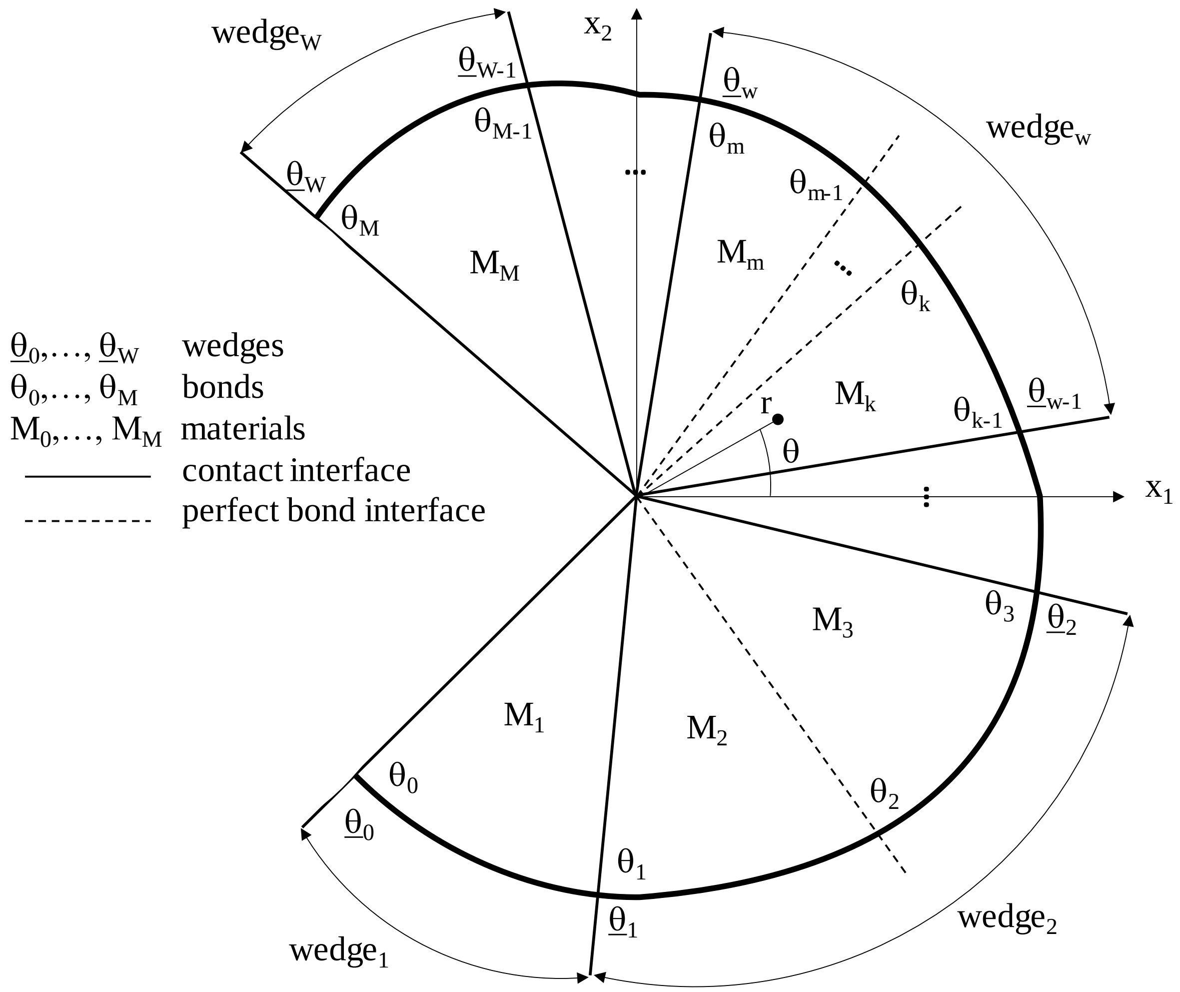

Figure I.7 Multi-material corner 2D view

Assuming generalized plain strain conditions the stresses and displacements in each material of a multi-material corner can be described according to I.79:

$$
\begin{aligned}
\sigma_{11} &= 2\,\mathrm{Re}\left[\mu_1^2\phi'_{H1}(z_1)+\mu_2^2\phi'_{H2}(z_2)+\mu_3^2\lambda_3\phi'_{H3}(z_3)\right]\\
\sigma_{22} &= 2\,\mathrm{Re}\left[\phi'_{H1}(z_1)+\phi'_{H2}(z_2)+\lambda_3\phi'_{H3}(z_3)\right]\\
\sigma_{12} &= -2\,\mathrm{Re}\left[\mu_1\phi'_{H1}(z_1)+\mu_2\phi'_{H2}(z_2)+\mu_3\lambda_3\phi'_{H3}(z_3)\right]\\
\sigma_{23} &= -2\,\mathrm{Re}\left[\lambda_1\phi'_{H1}(z_1)+\lambda_2\phi'_{H2}(z_2)+\phi'_{H3}(z_3)\right]\\
\sigma_{13} &= 2\,\mathrm{Re}\left[\mu_1\lambda_1\phi'_{H1}(z_1)+\mu_2\lambda_2\phi'_{H2}(z_2)+\mu_3\phi'_{H3}(z_3)\right]
\end{aligned}
\qquad \text{I.163}
$$

$$
\begin{aligned}
U_1 &= 2\,\mathrm{Re}\left[\sum_{k=1}^{3} p_k \phi_{Hk}\left(z_k\right)\right] \\
U_2 &= 2\,\mathrm{Re}\left[\sum_{k=1}^{3} q_k \phi_{Hk}\left(z_k\right)\right] \\
U_3 &= 2\,\mathrm{Re}\left[\sum_{k=1}^{3} t_k \phi_{Hk}\left(z_k\right)\right]
\end{aligned}
\qquad \text{I.164}
$$

Which can be rewritten in the following form:

$$
\begin{aligned}
\sigma_{11} &= -\mu_i b_{i,1} \phi'_{Hi}(z_i) - \bar{\mu}_i \bar{b}_{i,1} \bar{\phi}'_{Hi}(z_i) \\
\sigma_{22} &= b_{i,2} \phi'_{Hi}(z_i) + \bar{b}_{i,2} \bar{\phi}'_{Hi}(z_i) \\
\sigma_{12} &= b_{i,1} \phi'_{Hi}(z_i) + \bar{b}_{i,1} \bar{\phi}'_{Hi}(z_i) \\
\sigma_{13} &= -\mu_i b_{i,3} \phi'_{Hi}(z_i) - \bar{\mu}_i \bar{b}_{i,3} \bar{\phi}'_{Hi}(z_i) \\
\sigma_{23} &= b_{i,3} \phi'_{Hi}(z_i) + \bar{b}_{i,3} \bar{\phi}'_{Hi}(z_i) \\
U_1 &= a_{i,1} \phi_{Hi}(z_i) + \bar{a}_{i,1} \bar{\phi}_{Hi}(z_i) \\
U_2 &= a_{i,2} \phi_{Hi}(z_i) + \bar{a}_{i,2} \bar{\phi}_{Hi}(z_i) \\
U_3 &= a_{i,3} \phi_{Hi}(z_i) + \bar{a}_{i,3} \bar{\phi}_{Hi}(z_i)
\end{aligned}
\qquad \text{I.165}
$$

Where:

$$
\boldsymbol{B} = \left[\boldsymbol{b}_1 \quad | \quad \boldsymbol{b}_2 \quad | \quad \boldsymbol{b}_3\right] = \begin{bmatrix} -\mu_1 & -\mu_2 & -\lambda_3\mu_3 \\ 1 & 1 & \lambda_3 \\ -\lambda_1\mu_1 & -\lambda_2\mu_2 & \mu_3 \end{bmatrix} \qquad \text{I.166}
$$

$$
\boldsymbol{A} = \left[\boldsymbol{a}_1 \quad | \quad \boldsymbol{a}_2 \quad | \quad \boldsymbol{a}_3\right] = \begin{bmatrix} p_1 & p_2 & p_3 \\ q_1 & q_2 & q_3 \\ t_1 & t_2 & t_3 \end{bmatrix} \qquad \text{I.167}
$$

From these matrixes one can fairly easily obtain the standard matrixes used in the standard Stroh notation by the following transformation:

$$
\begin{aligned}
\bar{\boldsymbol{A}} &= \boldsymbol{A} \cdot \boldsymbol{K}^{-(1/2)} \\
\bar{\boldsymbol{B}} &= \boldsymbol{B} \cdot \boldsymbol{K}^{-(1/2)}
\end{aligned}
\qquad \text{I.168}
$$

Where:

$$
\boldsymbol{K} = \boldsymbol{A}^T \cdot \boldsymbol{B} + \boldsymbol{B}^T \cdot \boldsymbol{A} = diag(\kappa_1^2, \kappa_2^2, \kappa_3^2) \qquad \text{I.169}
$$

Setting:

$$\boldsymbol{\Phi} = \left[\boldsymbol{B} \quad | \quad \bar{\boldsymbol{B}} \right] \cdot \begin{Bmatrix} \boldsymbol{\phi}_H \\ \bar{\boldsymbol{\phi}}_H \end{Bmatrix} \qquad \text{I.170}$$

With:

$$\boldsymbol{\phi}_H = \left\{ \phi_{H1}(z_1), \phi_{H2}(z_2), \phi_{H3}(z_3) \right\}^T \qquad \text{I.171}$$

One obtaines from I.65:

$$\begin{aligned} &\sigma_{11} = -\frac{\partial \Phi_1}{\partial x_2} \qquad \sigma_{13} = -\frac{\partial \Phi_3}{\partial x_2} \\ &\sigma_{22} = \frac{\partial \Phi_2}{\partial x_1} \qquad \sigma_{23} = \frac{\partial \Phi_3}{\partial x_1} \\ &\sigma_{12} = \frac{\partial \Phi_1}{\partial x_1} \end{aligned} \qquad \text{I.172}$$

And:

$$\begin{aligned} &\boldsymbol{U} = \begin{Bmatrix} U_1 \\ U_2 \\ U_3 \end{Bmatrix} = \boldsymbol{a}_i \phi_{Hi}(z_i) + \bar{\boldsymbol{a}}_i \bar{\phi}_{Hi}(z_i) \\ &\boldsymbol{\Phi} = \begin{Bmatrix} \Phi_1 \\ \Phi_2 \\ \Phi_3 \end{Bmatrix} = \boldsymbol{b}_i \phi_{Hi}(z_i) + \bar{\boldsymbol{b}}_i \bar{\phi}_{Hi}(z_i) \end{aligned} \qquad \text{I.173}$$

For a corner singularity the potential functions will be in the following form:

$$\phi_{Hi}(z_i) = z_i^{\lambda} \delta_{1i} + z_i^{\bar{\lambda}} \delta_{2i} \qquad \text{I.174}$$

With no summation over i. Considering that:

$$\begin{aligned} &z_i = r\left(\cos(\theta) + \mu_i \sin(\theta)\right) = r\zeta_i\left(\theta\right) \\ &z_i^{\lambda} = r^{\lambda} \zeta_i^{\lambda}\left(\theta\right) \end{aligned} \qquad \text{I.175}$$

Substituting I.174 in I.173 leads to:

$$\begin{aligned} &\boldsymbol{U} = r^{\lambda}\left(\boldsymbol{a}_i \zeta_i^{\lambda}\left(\theta\right)\delta_{1i} + \bar{\boldsymbol{a}}_i \overline{\zeta_i^{\bar{\lambda}}}\left(\theta\right)\bar{\delta}_{2i}\right) + r^{\bar{\lambda}}\left(\bar{\boldsymbol{a}}_i \zeta_i^{\bar{\lambda}}\left(\theta\right)\bar{\delta}_{1i} + \boldsymbol{a}_i \overline{\zeta_i^{\lambda}}\left(\theta\right)\delta_{2i}\right) \\ &\boldsymbol{\Phi} = r^{\lambda}\left(\boldsymbol{b}_i \zeta_i^{\lambda}\left(\theta\right)\delta_{1i} + \bar{\boldsymbol{b}}_i \overline{\zeta_i^{\bar{\lambda}}}\left(\theta\right)\bar{\delta}_{2i}\right) + r^{\bar{\lambda}}\left(\bar{\boldsymbol{b}}_i \zeta_i^{\bar{\lambda}}\left(\theta\right)\bar{\delta}_{1i} + \boldsymbol{b}_i \overline{\zeta_i^{\lambda}}\left(\theta\right)\delta_{2i}\right) \end{aligned} \qquad \text{I.176}$$

And noticing how:

$$\overline{\zeta_i^{\bar{\lambda}}}(\theta) = \bar{\zeta}_i^{\lambda}(\theta)$$
$$\overline{\zeta_i^{\lambda}}(\theta) = \bar{\zeta}_i^{\bar{\lambda}}(\theta) \qquad \text{I.177}$$

It is possible to rewrite I.176 as:

$$\begin{aligned} \boldsymbol{U} &= \boldsymbol{a}_i z_i^{\lambda}\delta_{1i} + \bar{\boldsymbol{a}}_i \bar{z}_i^{\lambda}\bar{\delta}_{2i} + \bar{\boldsymbol{a}}_i z_i^{\bar{\lambda}}\bar{\delta}_{1i} + \boldsymbol{a}_i \bar{z}_i^{\bar{\lambda}}\delta_{2i} = \\ &= r^{\lambda}\left(\boldsymbol{A}\cdot\left\langle\zeta_*^{\lambda}\right\rangle\cdot\boldsymbol{\delta}_1 + \bar{\boldsymbol{A}}\cdot\left\langle\bar{\zeta}_*^{\lambda}\right\rangle\cdot\bar{\boldsymbol{\delta}}_2\right) + r^{\bar{\lambda}}\left(\bar{\boldsymbol{A}}\cdot\left\langle\zeta_*^{\bar{\lambda}}\right\rangle\cdot\bar{\boldsymbol{\delta}}_1 + \boldsymbol{A}\cdot\left\langle\bar{\zeta}_*^{\bar{\lambda}}\right\rangle\cdot\boldsymbol{\delta}_2\right) \\ \boldsymbol{\Phi} &= \boldsymbol{b}_i z_i^{\lambda}\delta_{1i} + \bar{\boldsymbol{b}}_i \bar{z}_i^{\lambda}\bar{\delta}_{2i} + \bar{\boldsymbol{b}}_i z_i^{\bar{\lambda}}\bar{\delta}_{1i} + \boldsymbol{b}_i \bar{z}_i^{\bar{\lambda}}\delta_{2i} = \\ &= r^{\lambda}\left(\boldsymbol{B}\cdot\left\langle\zeta_*^{\lambda}\right\rangle\cdot\boldsymbol{\delta}_1 + \bar{\boldsymbol{B}}\cdot\left\langle\bar{\zeta}_*^{\lambda}\right\rangle\cdot\bar{\boldsymbol{\delta}}_2\right) + r^{\bar{\lambda}}\left(\bar{\boldsymbol{B}}\cdot\left\langle\zeta_*^{\bar{\lambda}}\right\rangle\cdot\bar{\boldsymbol{\delta}}_1 + \boldsymbol{B}\cdot\left\langle\bar{\zeta}_*^{\bar{\lambda}}\right\rangle\cdot\boldsymbol{\delta}_2\right) \end{aligned} \qquad \text{I.178}$$

Or in a compact way:

$$\mathbf{w}(\mathrm{r},\theta) = r^{\lambda}\mathbf{X}\mathbf{Z}^{\lambda}\boldsymbol{\delta} + r^{\bar{\lambda}}\bar{\mathbf{X}}\mathbf{Z}^{\bar{\lambda}}\bar{\boldsymbol{\delta}} = \mathbf{w}^{(\lambda)}(\mathrm{r},\theta) + \mathbf{w}^{(\bar{\lambda})}(\mathrm{r},\theta) \qquad \text{I.179}$$

Where:

$$\left\langle\zeta_*^{\lambda}\right\rangle = diag(\zeta_1^{\lambda},\zeta_2^{\lambda},\zeta_3^{\lambda}) \qquad \text{I.180}$$

$$\boldsymbol{\delta} = \left\{\boldsymbol{\delta}_1 \mid \bar{\boldsymbol{\delta}}_2\right\}^T = \left\{\delta_{11},\delta_{12},\delta_{13},\bar{\delta}_{21},\bar{\delta}_{22},\bar{\delta}_{23}\right\}^T \qquad \text{I.181}$$

$$\mathbf{X} = \begin{bmatrix} \boldsymbol{A} & \bar{\boldsymbol{A}} \\ \boldsymbol{B} & \bar{\boldsymbol{B}} \end{bmatrix} \qquad \text{I.182}$$

$$\mathbf{Z}^{\lambda} = \begin{bmatrix} \left\langle\zeta_*^{\lambda}\right\rangle & \mathbf{0} \\ \mathbf{0} & \left\langle\bar{\zeta}_*^{\lambda}\right\rangle \end{bmatrix} \qquad \text{I.183}$$

At this point it is useful to introduce the concept of transfer matrix developed by Ting[11]. The transfer matrix $\mathbf{E}_m$ for a particular material sub-domain M_m of the multi-material corner is a matrix that relates the vector $\mathbf{w}_m(\mathrm{r},\theta_m)$ at one interface to $\mathbf{w}_m(\mathrm{r},\theta_{m-1})$ at the other interface of the sub-domain:

$$\mathbf{w}_m^{(\lambda)}(\mathrm{r},\theta_m) = \mathbf{E}_m^{(\lambda)}\left(\lambda,\theta_m,\theta_{m-1}\right)\mathbf{w}_m^{(\lambda)}(\mathrm{r},\theta_{m-1})$$
$$\mathbf{w}_m^{(\bar{\lambda})}(\mathrm{r},\theta_m) = \mathbf{E}_m^{(\bar{\lambda})}\left(\bar{\lambda},\theta_m,\theta_{m-1}\right)\mathbf{w}_m^{(\bar{\lambda})}(\mathrm{r},\theta_{m-1}) \qquad \text{I.184}$$

Where:

$$\mathbf{E}_m^{(\lambda)}\left(\lambda,\theta_m,\theta_{m-1}\right) = \mathbf{X}\cdot\mathbf{Z}^{\lambda}\left(\theta_m,\theta_{m-1}\right)\cdot\mathbf{X}^{-1}$$
$$\mathbf{E}_m^{(\bar{\lambda})}\left(\bar{\lambda},\theta_m,\theta_{m-1}\right) = \bar{\mathbf{X}}\cdot\mathbf{Z}^{\bar{\lambda}}\left(\theta_m,\theta_{m-1}\right)\cdot\bar{\mathbf{X}}^{-1} \qquad \text{I.185}$$

$$\mathbf{Z}^{\lambda}\left(\theta_m,\theta_{m-1}\right)=\begin{bmatrix}\left\langle \zeta_*^{\lambda}\left(\theta_m,\theta_{m-1}\right)\right\rangle & \mathbf{0}\\ \mathbf{0} & \left\langle \bar{\zeta}_*^{\lambda}\left(\theta_m,\theta_{m-1}\right)\right\rangle\end{bmatrix} \qquad \text{I.186}$$

$$\zeta_i^{\lambda}\left(\theta_m,\theta_{m-1}\right)=\cos(\theta_m-\theta_{m-1})+\mu_i\left(\theta_{m-1}\right)\sin(\theta_m-\theta_{m-1}) \qquad \text{I.187}$$

$$\mu_i\left(\theta_{m-1}\right)=\frac{\mu_i\cos(\theta_{m-1})-\sin(\theta_{m-1})}{\mu_i\sin(\theta_{m-1})+\cos(\theta_{m-1})} \qquad \text{I.188}$$

Having a way to relate the stress and displacement state at the interface of every material in the multi-material corner, it is possible to chain relation I.184 to obtain a transfer matrix that can relate the vector $\mathbf{w}_w(\mathrm{r},\underline{\theta}_w)$ describing the stress state at one interface of the wedge$_w$ to $\mathbf{w}_w(\mathrm{r},\underline{\theta}_{w-1})$ at the other interface. In similar fashion to I.184 it is possible to write:

$$\begin{aligned}\mathbf{w}_w^{(\lambda)}(\mathrm{r},\theta_w)&=\mathbf{K}_w^{(\lambda)}\left(\lambda\right)\mathbf{w}_w^{(\lambda)}(\mathrm{r},\theta_{w-1})\\ \mathbf{w}_w^{(\bar{\lambda})}(\mathrm{r},\theta_w)&=\mathbf{K}_w^{(\bar{\lambda})}\left(\bar{\lambda}\right)\mathbf{w}_w^{(\bar{\lambda})}(\mathrm{r},\theta_{w-1})\end{aligned} \qquad \text{I.189}$$

And considering that in wedge$_w$ there are $\underline{M}$ different material sub-domains, $M_{\underline{m}}$ to $M_{\underline{m+M}}$ the wedge transfer matrix is defined as:

$$\mathbf{K}_w^{(\lambda)}\left(\lambda\right)=\mathbf{E}_{\underline{m+M}}^{(\lambda)}\left(\lambda,\theta_{\underline{m+M}},\theta_{\underline{m+M}-1}\right)\cdot\mathbf{E}_{\underline{m+M}-1}^{(\lambda)}\left(\lambda,\theta_{\underline{m+M}-1},\theta_{\underline{m+M}-2}\right)\cdots\mathbf{E}_{\underline{m}}^{(\lambda)}\left(\lambda,\theta_{\underline{m}},\theta_{\underline{m}-1}\right) \qquad \text{I.190}$$

And rewriting I.189 to obtain the characteristic system of the wedge:

$$\left[\mathbf{K}_w^{(\lambda)}\left(\lambda\right)\quad|\quad-\mathbf{I}_{6\times6}\right]\cdot\left\{\mathbf{w}_w^{(\lambda)}(\mathrm{r},\theta_{w-1})\quad|\quad\mathbf{w}_w^{(\lambda)}(\mathrm{r},\theta_w)\right\}^T=\mathbf{0}_{6\times1} \qquad \text{I.191}$$

With analogous expression for the second equation of I.184.

Coming back to the entirety of the multi-material corner it is possible now to list all of the characteristic equations for all the wedges in a compact way using the multi-material corner transfer matrix:

$$\begin{aligned}\mathbf{K}_C^{(\lambda)}\left(\lambda\right)\mathbf{w}_C^{(\lambda)}&=\mathbf{0}_{6W\times1}\\ \mathbf{K}_C^{(\bar{\lambda})}\left(\bar{\lambda}\right)\mathbf{w}_C^{(\bar{\lambda})}&=\mathbf{0}_{6W\times1}\end{aligned} \qquad \text{I.192}$$

Where:

$$\mathbf{K}_C^{(\lambda)}(\lambda)=\begin{bmatrix} \mathbf{K}_1^{(\lambda)}(\lambda) & -\mathbf{I}_{6\times6} & \mathbf{0}_{6\times6} & \mathbf{0}_{6\times6} & \cdots & \cdots & \mathbf{0}_{6\times6} \\ \mathbf{0}_{6\times6} & \mathbf{0}_{6\times6} & \mathbf{K}_2^{(\lambda)}(\lambda) & -\mathbf{I}_{6\times6} & \cdots & \cdots & \mathbf{0}_{6\times6} \\ \vdots & \vdots & \vdots & \vdots & \ddots & \vdots & \vdots \\ \mathbf{0}_{6\times6} & \mathbf{0}_{6\times6} & \mathbf{0}_{6\times6} & \mathbf{0}_{6\times6} & \cdots & \mathbf{K}_W^{(\lambda)}(\lambda) & -\mathbf{I}_{6\times6} \end{bmatrix} \qquad \text{I.193}$$

$$\mathbf{w}_C^{(\lambda)}=\left\{\mathbf{w}_1^{(\lambda)}(\mathrm{r},\theta_0) \ | \ \mathbf{w}_1^{(\lambda)}(\mathrm{r},\theta_1) \ | \ \mathbf{w}_2^{(\lambda)}(\mathrm{r},\theta_1) \ | \ \mathbf{w}_2^{(\lambda)}(\mathrm{r},\theta_2) \ \cdots \ \mathbf{w}_W^{(\lambda)}(\mathrm{r},\theta_{W-1}) \ | \ \mathbf{w}_W^{(\lambda)}(\mathrm{r},\theta_W)\right\}^T \qquad \text{I.194}$$

Lastly the boundary conditions at the external boundaries and between wedges are taken into consideration, starting with the former. A single wedge corner is analyzed at first, for the sake of simplicity, and then the formulation will be expanded to the full case in a second moment.

It is necessary to define a coordinate system that is suitable to the description of displacement and traction boundary conditions on an inclined plane that passes through the x_3 axis, that will represent the interfaces of every subdomain, Figure I.8.

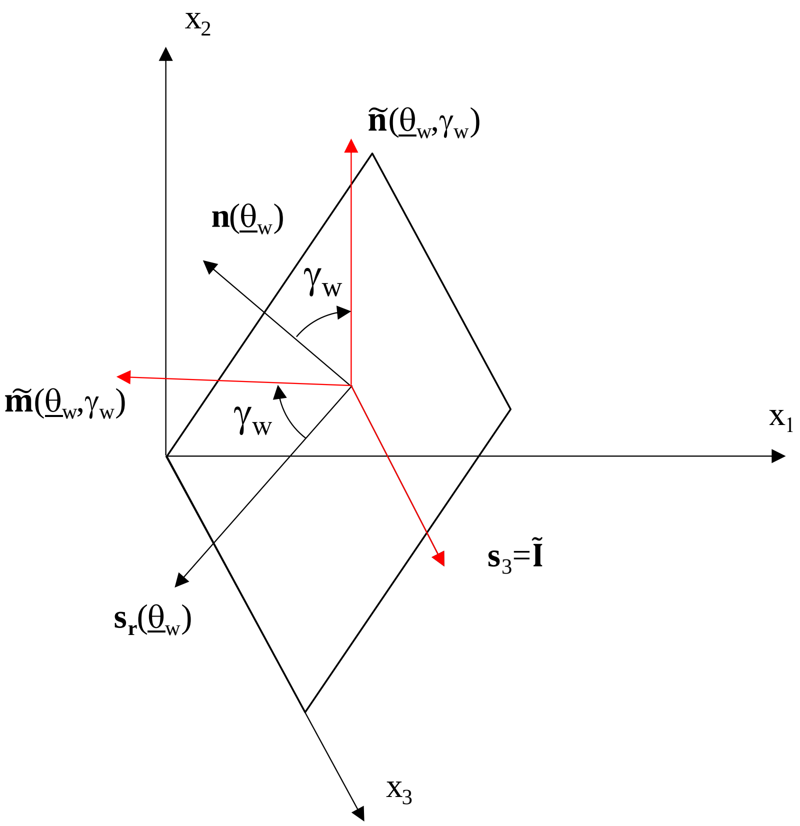

Figure I.8 Reference systems for boundary conditions on a wedge interface

The following vectors are defined forming an orthonormal basis:

$$\mathbf{s}_r(\theta) = \begin{Bmatrix} -\cos(\theta) \\ -\sin(\theta) \\ 0 \end{Bmatrix}; \quad \mathbf{s}_3(\theta) = \begin{Bmatrix} 0 \\ 0 \\ 1 \end{Bmatrix}; \quad \mathbf{n}(\theta) = \begin{Bmatrix} -\sin(\theta) \\ \cos(\theta) \\ 0 \end{Bmatrix}$$
$$\tilde{\mathbf{m}}(\theta,\gamma) = \begin{Bmatrix} -\cos(\theta+\gamma) \\ -\sin(\theta+\gamma) \\ 0 \end{Bmatrix}; \qquad \tilde{\mathbf{n}}(\theta,\gamma) = \begin{Bmatrix} -\sin(\theta+\gamma) \\ \cos(\theta+\gamma) \\ 0 \end{Bmatrix} \qquad \text{I.195}$$

The boundary conditions on the external interface of the single-wedge corner can be written in a compact way as follows:

$$\mathbf{D}_u(\underline{\theta}_w)\cdot\mathbf{U}(r,\underline{\theta}_w)+\mathbf{D}_t(\underline{\theta}_w)\cdot\mathbf{t}(r,\underline{\theta}_w)=\mathbf{0} \qquad \text{I.196}$$

Where:

$$\mathbf{t}(x_1,x_2) = -\frac{\partial\mathbf{\Phi}(x_1,x_2)}{\partial \boldsymbol{s}} \qquad \text{I.197}$$

Is the traction vector and **s** in the tangential vector to the interface plane, equal to $\mathbf{s}_r(\theta)$ or -$\mathbf{s}_r(\theta)$ depending on the orientation, which must be clockwise in I.195.

Considering a homogeneous boundary condition that impose a zero value for one component of the traction vector, t_i=0, and considering that the tangential vector correspond to the radial direction or its opposite, one can see that

$$t_i = \pm\frac{\partial\Phi_i}{\partial r} = 0 \qquad \text{I.198}$$

And so, considering the structure of $\mathbf{\Phi}$ proportional to r^{λ}, it is clear that:

$$\frac{\partial\Phi_i}{\partial r} = 0 \rightarrow \Phi_i = 0 \qquad \text{I.199}$$

So that the boundary conditions I.196 can be reformulated as:

$$\mathbf{D}_u(\underline{\theta}_w)\cdot\mathbf{U}(r,\underline{\theta}_w)+\mathbf{D}_\Phi(\underline{\theta}_w)\cdot\mathbf{\Phi}(r,\underline{\theta}_w)=\mathbf{0} \qquad \text{I.200}$$

Where the matrixes $\mathbf{D}_u(\theta)$ and $\mathbf{D}_\Phi(\theta)$ depend on the imposed boundary condition and are defined in Table 1.

Boundary condition	$\mathbf{D}_u(\theta)$	$\mathbf{D}_\Phi(\theta)$
Free	$\mathbf{0}_{3x3}$	$\mathbf{I}_{3x3}$
Clamped	$\mathbf{I}_{3x3}$	$\mathbf{0}_{3x3}$
Only u_θ restricted (Sym.)	$[\mathbf{n}(\theta) \mid \mathbf{0} \mid \mathbf{0}]^T$	$[\mathbf{0} \mid \mathbf{s}_r(\theta) \mid \mathbf{s}_3]^T$
Only u_θ allowed (A-Sym.)	$[\mathbf{0} \mid \mathbf{s}_r(\theta) \mid \mathbf{s}_3]^T$	$[\mathbf{n}(\theta) \mid \mathbf{0} \mid \mathbf{0}]^T$
Only u_r restricted	$[\mathbf{s}_r(\theta) \mid \mathbf{0} \mid \mathbf{0}]^T$	$[\mathbf{0} \mid \mathbf{n}(\theta) \mid \mathbf{s}_3]^T$
Only u_r allowed	$[\mathbf{n}(\theta) \mid \mathbf{s}_3 \mid \mathbf{0}]^T$	$[\mathbf{0} \mid \mathbf{0} \mid \mathbf{s}_r(\theta)]^T$
Only u_3 restricted	$[\mathbf{s}_3 \mid \mathbf{0} \mid \mathbf{0}]^T$	$[\mathbf{0} \mid \mathbf{s}_r(\theta) \mid \mathbf{n}(\theta)]^T$
Only u_3 allowed	$[\mathbf{s}_r(\theta) \mid \mathbf{n}(\theta) \mid \mathbf{0}]^T$	$[\mathbf{0} \mid \mathbf{0} \mid \mathbf{s}_3]^T$
Only $\mathbf{u}_{\tilde{\mathbf{n}}}$ restricted	$[\tilde{\mathbf{n}}(\theta) \mid \mathbf{0} \mid \mathbf{0}]^T$	$[\mathbf{0} \mid \tilde{\mathbf{m}}(\theta) \mid \mathbf{s}_3]^T$
Only $\mathbf{u}_{\tilde{\mathbf{n}}}$ allowed	$[\tilde{\mathbf{m}}(\theta) \mid \mathbf{s}_3 \mid \mathbf{0}]^T$	$[\mathbf{0} \mid \mathbf{0} \mid \tilde{\mathbf{n}}(\theta)]^T$

Table 1 Definitions of the boundary condition matrixes for different imposed conditions

With these matrixes it is possible to construct the orthogonal boundary conditions matrix:

$$\mathbf{D}_{BC}(\underline{\theta}_w) = \begin{bmatrix} \mathbf{D}_u(\underline{\theta}_w) & \mathbf{D}_\Phi(\underline{\theta}_w) \\ \mathbf{D}_\Phi(\underline{\theta}_w) & \mathbf{D}_u(\underline{\theta}_w) \end{bmatrix} \tag{I.201}$$

And obtain all the components of vector $\mathbf{w}_w(\mathrm{r},\underline{\theta}_w)$ that are not prescribed by the boundary conditions:

$$\begin{gathered} \mathbf{w}_w(\mathrm{r},\underline{\theta}_w)\mathbf{D}_{BC}(\underline{\theta}_w) = \left\{\mathbf{w}_P(\mathrm{r},\underline{\theta}_w) \quad | \quad \mathbf{w}_U(\mathrm{r},\underline{\theta}_w)\right\}^T \\ \downarrow \\ \mathbf{w}_w(\mathrm{r},\underline{\theta}_w) = \mathbf{D}_{BC}^T(\underline{\theta}_w)\cdot\left\{\mathbf{w}_P(\mathrm{r},\underline{\theta}_w) \quad | \quad \mathbf{w}_U(\mathrm{r},\underline{\theta}_w)\right\}^T \end{gathered} \tag{I.202}$$

Where the prescribed components, $\mathbf{w}_P(\mathrm{r},\underline{\theta}_w)$ are null given boundary conditions I.200:

$$\mathbf{w}_P(\mathrm{r},\underline{\theta}_w) = \mathbf{0} \tag{I.203}$$

And $\mathbf{w}_U(\mathrm{r},\underline{\theta}_w)$ is the 3x1 vector of the only remaining components of $\mathbf{w}_w(\mathrm{r},\underline{\theta}_w)$, so that:

$$\mathbf{w}_w(\mathrm{r},\underline{\theta}_w)=\begin{bmatrix}\mathbf{D}_\Phi^T\left(\underline{\theta}_w\right)\\ \mathbf{D}_u^T\left(\underline{\theta}_w\right)\end{bmatrix}\cdot\mathbf{w}_U(\mathrm{r},\underline{\theta}_w)=\tilde{\mathbf{D}}_{BC}^T\left(\underline{\theta}_w\right)\cdot\mathbf{w}_U(\mathrm{r},\underline{\theta}_w) \qquad \text{I.204}$$

The same procedure is now followed to analyze boundary conditions between different wedges.

In similar fashion to I.200 one can write the boundary conditions between different interfaces as:

$$\mathbf{D}_1\left(\underline{\theta}_w\right)\cdot\mathbf{w}_w(\mathrm{r},\underline{\theta}_w)+\mathbf{D}_2\left(\underline{\theta}_w\right)\cdot\mathbf{w}_{w+1}(\mathrm{r},\underline{\theta}_w)=\mathbf{0} \qquad \text{I.205}$$

Where matrixes $\mathbf{D}_1\left(\theta\right)$, $\mathbf{D}_2\left(\theta\right)$ and their associated matrixes $\tilde{\mathbf{D}}_1\left(\theta\right)$ and $\tilde{\mathbf{D}}_2\left(\theta\right)$ satisfy the following orthogonality relations:

$$\begin{aligned}&\mathbf{D}_1\cdot\mathbf{D}_1^T+\mathbf{D}_2\cdot\mathbf{D}_2^T=\mathbf{I}_{6\times6}\\&\tilde{\mathbf{D}}_1\cdot\tilde{\mathbf{D}}_1^T+\tilde{\mathbf{D}}_2\cdot\tilde{\mathbf{D}}_2^T=\mathbf{I}_{6\times6}\\&\mathbf{D}_1\cdot\tilde{\mathbf{D}}_1^T+\mathbf{D}_2\cdot\tilde{\mathbf{D}}_2^T=\mathbf{0}_{6\times6}\end{aligned} \qquad \text{I.206}$$

And are defined in Table 2.

Boundary condition	Perfect bond	Frictionless slide
$\mathbf{D}_1\left(\theta\right)$	$-\frac{1}{\sqrt{2}}\mathbf{I}_{6\times6}$	$\frac{1}{\sqrt{2}}\begin{bmatrix}-\mathbf{n}\left(\theta\right) & \mathbf{0}_{3\times1} & \mathbf{0}_{3\times3} & \mathbf{0}_{3\times1}\\ \mathbf{0}_{3\times1} & \mathbf{s}_r\left(\theta\right) & -\mathbf{I}_{3\times3} & \mathbf{s}_3\end{bmatrix}^T$
$\mathbf{D}_2\left(\theta\right)$	$\frac{1}{\sqrt{2}}\mathbf{I}_{6\times6}$	$\frac{1}{\sqrt{2}}\begin{bmatrix}\mathbf{n}\left(\theta\right) & \mathbf{0}_{3\times1} & \mathbf{0}_{3\times3} & \mathbf{0}_{3\times1}\\ \mathbf{0}_{3\times1} & \mathbf{s}_r\left(\theta\right) & \mathbf{I}_{3\times3} & \mathbf{s}_3\end{bmatrix}^T$
$\tilde{\mathbf{D}}_1\left(\theta\right)$	$\frac{1}{\sqrt{2}}\mathbf{I}_{6\times6}$	$\frac{1}{\sqrt{2}}\begin{bmatrix}\mathbf{n}\left(\theta\right) & \mathbf{0}_{3\times1} & \sqrt{2}\mathbf{s}_r\left(\theta\right) & \mathbf{0}_{3\times1} & \sqrt{2}\mathbf{s}_3 & \mathbf{0}_{3\times1}\\ \mathbf{0}_{3\times1} & \mathbf{n}\left(\theta\right) & \mathbf{0}_{3\times1} & \mathbf{0}_{3\times1} & \mathbf{0}_{3\times1} & \mathbf{0}_{3\times1}\end{bmatrix}^T$
$\tilde{\mathbf{D}}_2\left(\theta\right)$	$\frac{1}{\sqrt{2}}\mathbf{I}_{6\times6}$	$\frac{1}{\sqrt{2}}\begin{bmatrix}\mathbf{n}\left(\theta\right) & \mathbf{0}_{3\times1} & \mathbf{0}_{3\times1} & \sqrt{2}\mathbf{s}_r\left(\theta\right) & \mathbf{0}_{3\times1} & \sqrt{2}\mathbf{s}_3\\ \mathbf{0}_{3\times1} & \mathbf{n}\left(\theta\right) & \mathbf{0}_{3\times1} & \mathbf{0}_{3\times1} & \mathbf{0}_{3\times1} & \mathbf{0}_{3\times1}\end{bmatrix}^T$

Table 2 Definitions of the interface condition matrixes for different imposed conditions

Worth noting how the perfect bond condition is truly a redundant condition since if it holds true than the two wedges related by this condition can be redefined as a single united wedge.

Repeating the same procedure followed in I.201:2

$$\mathbf{D}_{In}\left(\underline{\theta}_w\right)=\begin{bmatrix}\mathbf{D}_1\left(\underline{\theta}_w\right) & \mathbf{D}_2\left(\underline{\theta}_w\right)\\ \tilde{\mathbf{D}}_1\left(\underline{\theta}_w\right) & \tilde{\mathbf{D}}_2\left(\underline{\theta}_w\right)\end{bmatrix} \tag{I.207}$$

$$\begin{gathered}\mathbf{D}_{In}\left(\underline{\theta}_w\right)\cdot\left\{\mathbf{w}_w(\mathrm{r},\underline{\theta}_w) \quad | \quad \mathbf{w}_{w+1}(\mathrm{r},\underline{\theta}_w)\right\}^T=\left\{\mathbf{w}_P(\mathrm{r},\underline{\theta}_w) \quad | \quad \mathbf{w}_U(\mathrm{r},\underline{\theta}_w)\right\}^T\\ \downarrow\\ \left\{\mathbf{w}_w(\mathrm{r},\underline{\theta}_w) \quad | \quad \mathbf{w}_{w+1}(\mathrm{r},\underline{\theta}_w)\right\}^T=\mathbf{D}_{In}^T\left(\underline{\theta}_w\right)\cdot\left\{\mathbf{w}_P(\mathrm{r},\underline{\theta}_w) \quad | \quad \mathbf{w}_U(\mathrm{r},\underline{\theta}_w)\right\}^T\\ \downarrow\\ \left\{\mathbf{w}_w(\mathrm{r},\underline{\theta}_w) \quad | \quad \mathbf{w}_{w+1}(\mathrm{r},\underline{\theta}_w)\right\}^T=\begin{bmatrix}\tilde{\mathbf{D}}_1^T\left(\underline{\theta}_w\right)\\ \tilde{\mathbf{D}}_2^T\left(\underline{\theta}_w\right)\end{bmatrix}\cdot\mathbf{w}_U(\mathrm{r},\underline{\theta}_w)\end{gathered} \tag{I.208}$$

It is now possible to combine these relations for interfaces and external boundary conditions which will take into account the entire domain of the multi-material corner:

$$\mathbf{D}_C\mathbf{w}_C=\mathbf{w}_{PU} \tag{I.209}$$

Where:

$$\mathbf{D}_C=\begin{bmatrix}\mathbf{D}_{BC}\left(\underline{\theta}_0\right) & \mathbf{0}_{6\times12} & \mathbf{0}_{6\times12} & \cdots & \mathbf{0}_{6\times6}\\ \mathbf{0}_{12\times6} & \mathbf{D}_{In}\left(\underline{\theta}_1\right) & \mathbf{0}_{12\times12} & \cdots & \mathbf{0}_{12\times6}\\ \vdots & \vdots & \vdots & \ddots & \vdots\\ \mathbf{0}_{6\times6} & \mathbf{0}_{6\times12} & \mathbf{0}_{6\times12} & \cdots & \mathbf{D}_{BC}\left(\underline{\theta}_W\right)\end{bmatrix} \tag{I.210}$$

$$\mathbf{w}_{PU}=\left\{\mathbf{w}_P(\mathrm{r},\theta_0) \quad | \quad \mathbf{w}_U(\mathrm{r},\theta_0) \quad | \quad \mathbf{w}_P(\mathrm{r},\theta_1) \quad | \quad \mathbf{w}_U(\mathrm{r},\theta_1) \quad \cdots \quad \mathbf{w}_P(\mathrm{r},\theta_W) \quad | \quad \mathbf{w}_U(\mathrm{r},\theta_W)\right\} \tag{I.211}$$

And at last, it is possible to substitute boundary condition relations I.192 into I.209 and obtain the final system that needs to be solved to obtain the solution to the multi-material corner:

$$\begin{gathered}\mathbf{K}_C^{(\lambda)}\left(\lambda\right)\cdot\mathbf{D}_C^T\cdot\mathbf{w}_{PU}^{(\lambda)}=\mathbf{0}_{6W\times1}\\ \mathbf{K}_C^{(\bar{\lambda})}\left(\bar{\lambda}\right)\cdot\mathbf{D}_C^T\cdot\mathbf{w}_{PU}^{(\bar{\lambda})}=\mathbf{0}_{6W\times1}\end{gathered} \tag{I.212}$$

And recalling I.203 these equations can be simplified by eliminating all the columns of $\mathbf{K}_C^{(\lambda)}\left(\lambda\right)\cdot\mathbf{D}_C^T$ and $\mathbf{K}_C^{(\bar{\lambda})}\left(\bar{\lambda}\right)\cdot\mathbf{D}_C^T$ that would be multiplied by zero:

$$\begin{gathered}\mathbf{K}_{Tot}^{(\lambda)}\left(\lambda\right)\cdot\mathbf{w}_U^{(\lambda)}=\mathbf{0}_{6W\times1}\\ \mathbf{K}_{Tot}^{(\bar{\lambda})}\left(\bar{\lambda}\right)\cdot\mathbf{w}_U^{(\bar{\lambda})}=\mathbf{0}_{6W\times1}\end{gathered} \tag{I.213}$$

Where:

$$\mathbf{w}_U^{(\lambda)} = \left\{ \mathbf{w}_U^{(\lambda)}(\mathrm{r},\theta_0) \quad | \quad \mathbf{w}_U^{(\lambda)}(\mathrm{r},\theta_1) \quad \cdots \quad \mathbf{w}_U^{(\lambda)}(\mathrm{r},\theta_W) \right\}^T \qquad \text{I.214}$$

$$\mathbf{K}_{Tot}^{(\lambda)}(\lambda) = \begin{bmatrix} \mathbf{K}_1^{(\lambda)}(\lambda)\cdot\tilde{\mathbf{D}}_{BC}^T(\underline{\theta}_0) & -\tilde{\mathbf{D}}_1^T(\underline{\theta}_1) & \mathbf{0}_{6\times6} & \cdots & \mathbf{0}_{6\times6} & \mathbf{0}_{6\times3} \\ \mathbf{0}_{6\times3} & \mathbf{K}_2^{(\lambda)}(\lambda)\cdot\tilde{\mathbf{D}}_2^T(\underline{\theta}_1) & -\tilde{\mathbf{D}}_1^T(\underline{\theta}_2) & \cdots & \mathbf{0}_{6\times6} & \mathbf{0}_{6\times3} \\ \vdots & \vdots & \vdots & \ddots & \vdots & \vdots \\ \mathbf{0}_{6\times3} & \mathbf{0}_{6\times6} & \mathbf{0}_{6\times6} & \cdots & \mathbf{K}_W^{(\lambda)}(\lambda)\cdot\tilde{\mathbf{D}}_2^T(\underline{\theta}_{W-1}) & -\tilde{\mathbf{D}}_{BC}^T(\underline{\theta}_W) \end{bmatrix} \qquad \text{I.215}$$

These are the characteristic equations for an open multi-material corner.

Systems I.213 have non-trivial solution only if

$$\begin{aligned} &\mathrm{Det}\left[\mathbf{K}_{Tot}^{(\lambda)}(\lambda)\right] = 0 \\ &\mathrm{Det}\left[\mathbf{K}_{Tot}^{(\bar{\lambda})}(\bar{\lambda})\right] = 0 \end{aligned} \qquad \text{I.216}$$

These equations are equivalent to each other so that solving the first gives also the solution for the second one, making them redundant.

Solving either one will give the eigenvalue λ and the singularity degree of the corner.

Furthermore, from I.213 one can obtain the relation between all the complex constants $\boldsymbol{\delta}$

$$\boldsymbol{\delta} = \delta^* \left\{1, \chi_{12}, \chi_{13}, \chi_{21}, \chi_{22}, \chi_{23}\right\}^T \qquad \text{I.217}$$

Where δ^* is a constant, known as Generalized Stress Intensity Factor (GSIF), that links the local stress fields of the corner to the remote geometrical and loading conditions, and found only applying those conditions.

1.6.3.1. Particular cases

It is also useful to briefly list some particular cases where some definitions shown until now have different expressions without impacting the final result and derivation.

Closed corners:

Assume that the multi-material corner does not have any external boundaries but only internal interfaces. In this case the following definitions apply:

$$\mathbf{D}_C = \begin{bmatrix} \mathbf{D}_2(\underline{\theta}_0) & \mathbf{0}_{6\times12} & \mathbf{0}_{6\times12} & \cdots & \mathbf{0}_{6\times12} & \mathbf{D}_1(\underline{\theta}_W) \\ \tilde{\mathbf{D}}_2(\underline{\theta}_0) & \mathbf{0}_{6\times12} & \mathbf{0}_{6\times12} & \cdots & \mathbf{0}_{6\times12} & \tilde{\mathbf{D}}_1(\underline{\theta}_W) \\ \mathbf{0}_{12\times6} & \mathbf{D}_{In}(\underline{\theta}_1) & \mathbf{0}_{12\times12} & \cdots & \mathbf{0}_{12\times12} & \mathbf{0}_{12\times6} \\ \vdots & \vdots & \vdots & \ddots & \vdots & \vdots \\ \mathbf{0}_{12\times6} & \mathbf{0}_{12\times12} & \mathbf{0}_{12\times12} & \cdots & \mathbf{D}_{In}(\underline{\theta}_{W-1}) & \mathbf{0}_{12\times6} \end{bmatrix} \qquad \text{I.218}$$

$$\mathbf{K}_{Tot}^{(\lambda)}(\lambda) = \begin{bmatrix} \mathbf{K}_1^{(\lambda)}(\lambda)\tilde{\mathbf{D}}_2^T(\underline{\theta}_0) & -\tilde{\mathbf{D}}_1^T(\underline{\theta}_1) & \mathbf{0}_{6\times6} & \cdots & \mathbf{0}_{6\times6} & \mathbf{0}_{6\times6} \\ \mathbf{0}_{6\times6} & \mathbf{K}_2^{(\lambda)}(\lambda)\tilde{\mathbf{D}}_2^T(\underline{\theta}_1) & -\tilde{\mathbf{D}}_1^T(\underline{\theta}_2) & \cdots & \mathbf{0}_{6\times6} & \mathbf{0}_{6\times6} \\ \vdots & \vdots & \vdots & \ddots & \vdots & \vdots \\ \mathbf{0}_{6\times6} & \mathbf{0}_{6\times6} & \mathbf{0}_{6\times6} & \cdots & \mathbf{K}_{W-1}^{(\lambda)}(\lambda)\tilde{\mathbf{D}}_2^T(\underline{\theta}_{W-1}) & -\tilde{\mathbf{D}}_1^T(\underline{\theta}_W) \\ -\tilde{\mathbf{D}}_1^T(\underline{\theta}_0) & \mathbf{0}_{6\times6} & \mathbf{0}_{6\times6} & \cdots & \mathbf{0}_{6\times6} & \mathbf{K}_W^{(\lambda)}(\lambda)\tilde{\mathbf{D}}_2^T(\underline{\theta}_W) \end{bmatrix} \qquad \text{I.219}$$

Degenerate materials:

In the previous derivation it was always assumed that matrix $\mathbf{X}$ in I.179 was a full ranked matrix, but that might not always be the case. Two other different scenarios are possible:

1) The matrix $[\mathbf{A}\,|\,\mathbf{B}]$ has rank 2, meaning that one of the three vectors $\{\boldsymbol{a}_i\,|\,\boldsymbol{b}_i\}^T$ is linearly dependent. This is the case of a degenerate material.

2) The matrix $[\mathbf{A}\,|\,\mathbf{B}]$ has rank 1, meaning that two of the three vectors $\{\boldsymbol{a}_i\,|\,\boldsymbol{b}_i\}^T$ are linearly dependent. This is the case of an extraordinary degenerate material.

Considering first the first case, the following modification needs to be made:

$$\langle \zeta_*^\lambda \rangle = \begin{bmatrix} \zeta_1^\lambda & \lambda\sin(\theta)\zeta_1^{\lambda-1} & 0 \\ 0 & \zeta_1^\lambda & 0 \\ 0 & 0 & \zeta_3^\lambda \end{bmatrix} \qquad \text{I.220}$$

While for the second case:

$$\langle \zeta_*^\lambda \rangle = \begin{bmatrix} \zeta_1^\lambda & \lambda\sin(\theta)\zeta_1^{\lambda-1} & \lambda(\lambda-1)\sin(\theta)\zeta_1^{\lambda-2} \\ 0 & \zeta_1^\lambda & \lambda\sin(\theta)\zeta_1^{\lambda-1} \\ 0 & 0 & \zeta_1^\lambda \end{bmatrix} \qquad \text{I.221}$$

1.6.4. Stress distribution in presence of rounded notches

Despite the corner-singularity case being one of the most studied geometrical configurations, in real life application it is seldom the case to have a perfectly sharp notch. In most cases notches and corners have a rounding at the notch tip which eliminates any stress singularity in the material. The presence of a rounding on the other hand, significantly increases the modelling difficulty of the stress fields. In this chapter, three models are presented for this problem, the first one by Filippi, Lazzarin and Tovo[8] for isotropic materials under plane stress or strain conditions, the second by Zappalorto and Carraro[3] for a particular type of orthotropic materials under plane stress or strain tension and the third one of out of plane torsion in orthotropic materials by Zappalorto and Salviato[7]. The latter model will then be improved and expanded in later chapters.

1.6.4.1. Plain strain and stress for rounded notches in isotropic medium

The edge of a blunt notch with a generic opening angle and curvature radius can be described with the following mapping function:

$$z = \xi^{q} \tag{I.222}$$

where $z = x + iy$ and $\xi = u + iv$ the notch edge is described by the equation $u = u_0$

The following particular cases can be treated using Eq. I.222:

1. A pointed V-notch with rectilinear flanks and a generic opening angle 2α by setting $u_0 = 0$ and $q = \frac{2\pi - 2\alpha}{\pi} = \frac{2\gamma}{\pi}$;
2. A parabolic (blunt crack) notch profile with a generic notch root radius ρ setting q=2 and $u_0 = \sqrt{\frac{\rho}{2}}$;

3. A rounded notch (hyperbola-like profile) with a certain notch root radius ρ and a certain notch opening angle 2 α by setting $q = \frac{2\pi - 2\alpha}{\pi}$ and $u_0 = \left(\frac{q-1}{q}\rho\right)^{\frac{1}{q}}$. In this more general case, the notch tip occurs at $x = r_0 = \frac{q-1}{q}\rho$.

The geometry is illustrated in Figure I.9

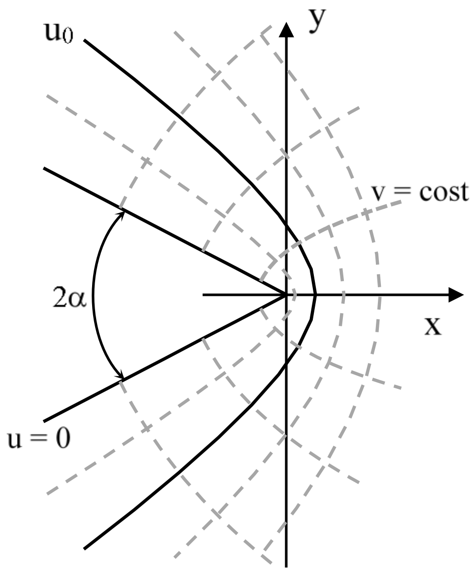

Figure I.9 Schematic of the conformal mapping defined in Eq. I.222

Considering Eq. I.104 the following potential function are chosen to describe the stress fields:

$$\begin{aligned} \Phi_{H1}(z) &= Az^{\lambda} + Dz^{\mu} \\ \Phi_{H2}(z) &= Bz^{\lambda} + Cz^{\mu} \end{aligned} \qquad \text{I.223}$$

Where A, B, C and D are complex constants, while λ and μ are real constants with $1 < \lambda < \mu$. These can be used to obtain the stress fields according to I.102:

$$\begin{aligned} \sigma_{xx} &= 2\,\mathrm{Re}\left[\Phi'_{H1}(z) - \frac{\bar{z}\Phi''_{H1}(z) + \Phi'_{H2}(z)}{2}\right] \\ \sigma_{yy} &= 2\,\mathrm{Re}\left[\Phi'_{H1}(z) + \frac{\bar{z}\Phi''_{H1}(z) + \Phi'_{H2}(z)}{2}\right] \\ \sigma_{xy} &= 2\,\mathrm{Im}\left[\bar{z}\Phi''_{H1}(z) + \Phi'_{H2}(z)\right] \end{aligned} \qquad \text{I.224}$$

Considering that the rotation angle between the curvilinear coordinate system $\xi = u + iv$ and the polar coordinate system defined by $z = x + iy$ is $-\frac{\theta}{q}$, one can obtain the stresses in the curvilinear coordinate system by a simple rotation according to I.39:

$$\begin{aligned}
\sigma_{uu} &= \frac{\sigma_{rr}+\sigma_{\theta\theta}}{2} + \frac{\sigma_{rr}-\sigma_{\theta\theta}}{2}\cos\left(\frac{2\theta}{q}\right) - \sigma_{r\theta}\sin\left(\frac{2\theta}{q}\right) \\
\sigma_{vv} &= \frac{\sigma_{rr}+\sigma_{\theta\theta}}{2} - \frac{\sigma_{rr}-\sigma_{\theta\theta}}{2}\cos\left(\frac{2\theta}{q}\right) + \sigma_{r\theta}\sin\left(\frac{2\theta}{q}\right) \\
\sigma_{uv} &= \frac{\sigma_{rr}-\sigma_{\theta\theta}}{2}\sin\left(\frac{2\theta}{q}\right) + \sigma_{r\theta}\cos\left(\frac{2\theta}{q}\right)
\end{aligned} \qquad \text{I.225}$$

It can be noted that for r→∞

$$\sigma_{\mathrm{uu}}\Big|_{\substack{\mathrm{u=u_0}\\ \mathrm{r}\to\infty}} \cong \sigma_{\theta\theta}\Big|_{\substack{\mathrm{r}\to\infty\\ \theta\cong\gamma}} = 0 \qquad \tau_{\mathrm{uv}}\Big|_{\substack{\mathrm{u=u_0}\\ \mathrm{r}\to\infty}} \cong \tau_{\mathrm{r}\theta}\Big|_{\substack{\mathrm{r}\to\infty\\ \theta\cong\gamma}} = 0 \qquad \text{I.226}$$

And that for r→∞

$$\begin{aligned}
\Phi_{H1}(z) &\cong Az^{\lambda} \\
\Phi_{H2}(z) &\cong Bz^{\lambda}
\end{aligned} \qquad \text{I.227}$$

Which are the conditions characterizing a material corner described in chapter 1.6.3. Following the procedure above described one obtains the characteristic equation of the problem, I.216:

$$\left(\sin(\lambda q\pi) + \lambda\sin(q\pi)\right)\left(\sin(\lambda q\pi) - \lambda\sin(q\pi)\right) = 0 \qquad \text{I.228}$$

Which can be divided into a symmetric and a skew symmetric part with a symmetric and a skew symmetric related problem:

$$\begin{aligned}
\sin(\lambda_1 q\pi) + \lambda_1\sin(q\pi) &= 0 \\
\sin(\lambda_2 q\pi) - \lambda_2\sin(q\pi) &= 0
\end{aligned} \qquad \text{I.229}$$

Defining then constants A, B, C and D as follows:

$$\begin{aligned}
A &= A_1 + \mathbf{i}A_2 \qquad B = B_1 + \mathbf{i}\mathrm{B}_2 \\
C &= C_1 + \mathbf{i}C_2 \qquad D = D_1 + \mathbf{i}\mathrm{D}_2
\end{aligned} \qquad \text{I.230}$$

One can effectively divide the symmetric problem (subscript 1) and the skew symmetric one (subscript 2).

From I.213 one obtains the relations between the constants B_i and A_i:

$$B_1 = \chi_{B_1}\left(1-\lambda_1\right)A_1$$

$$\chi_{B_1} = -\frac{\sin\left(\left(1-\lambda_1\right)\frac{q\pi}{2}\right)}{\sin\left(\left(1+\lambda_1\right)\frac{q\pi}{2}\right)} \qquad \text{I.231}$$

$$B_2 = -\chi_{B_2}\left(1+\lambda_2\right)A_2$$

$$\chi_{B_2} = -\frac{\sin\left(\left(1-\lambda_2\right)\frac{q\pi}{2}\right)}{\sin\left(\left(1+\lambda_2\right)\frac{q\pi}{2}\right)} \qquad \text{I.232}$$

To obtain the remaining coefficients one must impose additional boundary conditions, which are chosen to be:

$$\begin{aligned} &\sigma_{\mathrm{uu}}\Big|_{\substack{\mathrm{u=u_0}\\ \mathrm{v<<-v_0}}} + \sigma_{\mathrm{uu}}\Big|_{\substack{\mathrm{u=u_0}\\ \mathrm{v>>v_0}}} = 0 \Rightarrow \lim_{\substack{\mathrm{r}\to\infty\\ \theta\to\frac{\mathrm{q}\pi}{2}}}\left(\mathrm{r}^{1-\mu}\sigma_{\theta\theta}\right) + \lim_{\substack{\mathrm{r}\to\infty\\ \theta\to\frac{\mathrm{q}\pi}{2}}}\left(\mathrm{r}^{1-\mu}\sigma_{\theta\theta}\right) = 0 \\ &\sigma_{\mathrm{uv}}\Big|_{\substack{\mathrm{u=u_0}\\ \mathrm{v<<-v_0}}} - \sigma_{\mathrm{uv}}\Big|_{\substack{\mathrm{u=u_0}\\ \mathrm{v>>v_0}}} = 0 \Rightarrow \lim_{\substack{\mathrm{r}\to\infty\\ \theta\to\frac{\mathrm{q}\pi}{2}}}\left(\mathrm{r}^{1-\mu}\sigma_{\mathrm{r}\theta}\right) - \lim_{\substack{\mathrm{r}\to\infty\\ \theta\to-\frac{\mathrm{q}\pi}{2}}}\left(\mathrm{r}^{1-\mu}\sigma_{\mathrm{r}\theta}\right) = 0 \end{aligned} \qquad \text{I.233}$$

Applying these boundary conditions, it is possible to find the remaining constants, obtaining μ_i by solving the following equations:

$$\begin{aligned} &\left(\left(\frac{1-q\left(1+\mu_1\right)}{q}\right)\left(3-\lambda_1-\chi_{B_1}\left(1-\lambda_1\right)\right)-\varepsilon_1\right)\left(1+\mu_1\right)\cos\left(\left(1-\mu_1\right)\frac{q\pi}{2}\right)+ \\ &\quad +\left(\left(\left(1+\mu_1\right)^2-\frac{1+\mu_1}{q}\right)\left(3-\lambda_1-\chi_{B_1}\left(1-\lambda_1\right)\right)-\left(3-\mu_1\right)\varepsilon_1\right)\left(1+\mu_1\right)\cos\left(\left(1+\mu_1\right)\frac{q\pi}{2}\right)=0 \end{aligned} \qquad \text{I.234}$$

$$\begin{aligned} &\left(\left(\frac{q\left(1+\mu_2\right)-2}{q}\right)\left(\lambda_2-1-\chi_{B_2}\left(1+\lambda_2\right)\right)-\varepsilon_2\right)\left(1-\mu_2\right)\cos\left(\left(1-\mu_2\right)\frac{q\pi}{2}\right)+ \\ &\quad +\left(\left(\mu_2-1\right)\left(\frac{q\left(\mu_2-3\right)-2}{q}\right)\left(\lambda_2-1-\chi_{B_2}\left(\lambda_2+1\right)\right)+\left(1-\mu_2\right)\varepsilon_2\right)\cos\left(\left(1+\mu_2\right)\frac{q\pi}{2}\right)=0 \end{aligned} \qquad \text{I.235}$$

Where:

$$\varepsilon_1 = (1-\lambda_1)^2 + \chi_{B_1}(1-\lambda_1^2) - \frac{1}{q}(1+\lambda_1) - \frac{1}{q}\chi_{B_1}(1-\lambda_1)$$
$$\varepsilon_2 = (3-\lambda_2)(1-\lambda_2) - \chi_{B_2}(1+\lambda_2)^2 + \frac{2}{q}(1-\lambda_2) + \frac{2}{q}\chi_{B_2}(1+\lambda_2) \qquad \text{I.236}$$

While C_1, C_2, D_1 and D_2 are:

$$C_1 = \chi_{C_1}\frac{q\lambda_1 r_0^{\lambda_1-\mu_1}}{4\mu_1(q-1)}A_1$$
$$\chi_{C_1} = \left((1-\mu_1)^2 - \frac{1}{q}(1+\mu_1)\right)\left((3-\lambda_1)^2 - \chi_{B_1}(1-\lambda_1)\right) - (3-\mu_1)\varepsilon_1 \qquad \text{I.237}$$

$$D_1 = \chi_{D_1}\frac{q\lambda_1 r_0^{\lambda_1-\mu_1}}{4\mu_1(q-1)}A_1$$
$$\chi_{D_1} = \left(\frac{1-q(1+\mu_1)}{q}\right)\left(3-\lambda_1 - \chi_{B_1}(1-\lambda_1)\right) - \varepsilon_1 \qquad \text{I.238}$$

$$C_2 = \chi_{C_2}\frac{\lambda_2 r_0^{\lambda_2-\mu_2}}{4\mu_2(\mu_2-1)}A_2$$
$$\chi_{C_2} = (\mu_2-1)\left(\frac{q(\mu_2-3)-2}{q}\right)\left((\lambda_2-1) - \chi_{B_2}(1+\lambda_2)\right) + (1-\mu_2)\varepsilon_2 \qquad \text{I.239}$$

$$D_2 = \chi_{D_2}\frac{\lambda_2 r_0^{\lambda_2-\mu_2}}{4\mu_2(\mu_2-1)}A_2$$
$$\chi_{D_2} = -\left(\frac{q(1+\mu_2)-1}{q}\right)\left(\lambda_2 - 1 - \chi_{B_2}(1+\lambda_2)\right) + (1-\mu_2)\varepsilon_2 \qquad \text{I.240}$$

1.6.4.2. Plain strain and stress for rounded notches in orthotropic medium

Moving to an orthotropic material, the rounded notch geometry pose a great challenge to the analytical framework due to the conformal mapping that needs to be used. For this reason, in this derivation only orthotropic materials that presents pure imaginary elastic values are considered:

$$\mu_j = \pm i\beta_j \qquad \text{I.241}$$

Analysing the same geometry and conformal map used in the isotropic case, eq. I.222 and figure I.9, it is necessary to transform it accounting for the material properties.

Defining the two complex variables z_1 and z_2:

$$z_j = x_j + iy_j = r_j e^{i\theta_j} \tag{I.242}$$

Where:

$$x_j = x' + r_0\beta_j^t \qquad y_j = \beta_j y' \qquad r_j = \sqrt{x_j^2 + y_j^2} \qquad \theta_j = Arg(x_j + iy_j) \tag{I.243}$$

And $x' = x - r_0$, $y' = y$, while t is a positive real parameter to be determined with appropriate boundary conditions.

The stress fields are found from these complex variables, following Eq I.104, using two potential functions:

$$\begin{aligned} \phi'_{H1}(z_1) &= A\left(\frac{z_1}{r_0}\right)^{\lambda-1} \\ \phi'_{H2}(z_2) &= B\left(\frac{z_2}{r_0}\right)^{\lambda-1} \end{aligned} \tag{I.244}$$

Where A and B are real constants.

One can follow similar procedure shown for the isotropic case, and apply boundary conditions very far away from the notch tip, where the formulation reduces to the case of an orthotropic material corner under symmetric loading conditions, and obtain the eigenvalue of the problem solving the following equation:

$$\begin{aligned} &\cos(1-\lambda)\underline{\theta}_2(\gamma)\left\{\cos(1-\lambda)\underline{\theta}_1(\gamma)\left[m_{11}(\gamma)n_{21}(\gamma) - m_{21}(\gamma)n_{11}(\gamma)\right] - \right. \\ &\left. \sin(1-\lambda)\underline{\theta}_1(\gamma)\left[m_{21}(\gamma)n_{12}(\gamma) - m_{12}(\gamma)n_{21}(\gamma)\right]\right\} - \\ &\sin(1-\lambda)\underline{\theta}_2(\gamma)\left\{\cos(1-\lambda)\underline{\theta}_1(\gamma)\left[m_{22}(\gamma)n_{11}(\gamma) - m_{11}(\gamma)n_{22}(\gamma)\right] - \right. \\ &\left. \sin(1-\lambda)\underline{\theta}_1(\gamma)\left[m_{12}(\gamma)n_{22}(\gamma) - m_{22}(\gamma)n_{12}(\gamma)\right]\right\} = 0 \end{aligned} \tag{I.245}$$

Where:

$$\underline{\theta}_j(\gamma) = Arg\left(\cos\gamma + i\beta_j \sin\gamma\right) \tag{I.246}$$

As well as the relation between A and B from eq I.213:

$$B = \chi_B A$$
$$\chi_B = -\frac{\rho_1^{\lambda-1}(\gamma)\left(m_{11}(\gamma)\cos(1-\lambda)\underline{\theta}_1(\gamma) + m_{12}(\gamma)\sin(1-\lambda)\underline{\theta}_1(\gamma)\right)}{\rho_2^{\lambda-1}(\gamma)\left(m_{21}(\gamma)\cos(1-\lambda)\underline{\theta}_2(\gamma) + m_{22}(\gamma)\sin(1-\lambda)\underline{\theta}_2(\gamma)\right)} \quad \text{I.247}$$

The last step is to impose an additional boundary condition to find the value for t:

$$\sigma_{uu}\Big|_{\substack{\theta=0\\ r=r_0}} = 0 \quad \text{I.248}$$

From which one obtains:

$$t = \frac{2 - \dfrac{Ln(-\chi_B)}{Ln\left(\dfrac{\beta_1}{\beta_2}\right)}}{1-\lambda} \quad \text{I.249}$$

1.6.4.3. Anti-plane shear stresses for rounded notches in orthotropic medium

The case of out of plane shear stress in the vicinity of a rounded notch can also be solved using similar methods to the in-plane case. Using the same geometry and conformal mapping as the previous cases, it is possible to calculate the stress fields from I.119 using the following potential function:

$$\phi_{H3}(z_3) = -A\left(\frac{z_3}{r_0}\right)^{\lambda} \quad \text{I.250}$$

With A being a real constant and similar definitions as before for z_3:

$$z_3 = x_3 + iy_3 = r_3 e^{i\theta_3} \quad \text{I.251}$$

Where:

$$x_3 = x' + r_0\beta_3^t \qquad y_3 = \beta_3 y' \qquad r_3 = \sqrt{x_3^2 + y_3^2} \qquad \theta_3 = Arg(x_3 + iy_3) \quad \text{I.252}$$

And $x' = x - r_0$, $y' = y$, while t is a positive real parameter to be determined with appropriate boundary conditions.

Very far from the notch tip the free edge boundary condition is:

$$\sigma_{uz}\Big|_{\substack{u=u_0\\ r\to\infty}} \cong \sigma_{\theta z}\Big|_{\substack{r\to\infty\\ \theta\cong\gamma}} = 0 \quad \text{I.253}$$

Which reduce to the same case of a material corner, with eigenvalue calculated from I.216:

$$\lambda = \frac{\pi}{2\left(\arctan\left(\beta_3 \tan\left(\gamma\right)\right) + \pi\right)} \qquad \text{I.254}$$

Leaving only t as a parameter to be determined.

Similarly to the in plane case, the additional imposed boundary condition is:

$$\sigma_{uz}\Big|_{\substack{\theta \cong 0 \\ r = r_0}} = 0 \qquad \text{I.255}$$

And noting that near the notch tip:

$$\theta_3 \approx \beta_3^{1-t}\theta \qquad \text{I.256}$$

One obtains that

$$\sigma_{uz}\Big|_{\substack{\theta \cong 0 \\ r = r_0}} \cong A\left(\frac{r_3}{r_0}\right)^{\lambda-1}\theta\left(\frac{q-1}{q} - \beta_3^{2-t}\left(1-\lambda\right)\right) = 0 \qquad \text{I.257}$$

And finally:

$$t = 2 - \frac{Ln\left(\dfrac{q-1}{q\left(1-\lambda\right)}\right)}{Ln\left(\beta_3\right)} \qquad \text{I.258}$$

1.7. References

1. Bahnini, I., Rivette, M., Rechia, A., et al. (2018). "Additive manufacturing technology: the status, applications, and prospects." Int J Adv Manuf Technol, 97, 147–161. https://doi.org/10.1007/s00170-018-1932-y

2. Zappalorto, M., Carraro, P. A. (2015). "Stress distributions for blunt cracks and radiused slits in anisotropic plates under in-plane loadings." Int. J. Solids Struct., 56–57, 136-141. https://doi.org/10.1016/j.ijsolstr.2014.11.024

3. Zappalorto, M., Carraro, P. A. (2017). "Two-dimensional stress distributions in tensioned orthotropic plates weakened by blunt V-shaped notches." Fatigue Fract. Eng. M., 40, 804-819. https://doi.org/10.1111/ffe.12554

4. Lekhnitskii, S. G. (1984). "Theory of Elasticity of an Anisotropic Body." Mir Publishers, Moscow.

5. Savin, G. N. (1961). "Stress Concentration Around Holes." Pergamon, London.

6. Muskhelishvili, N. I. (1977). "Some Basic Problems of the Mathematical Theory of Elasticity." Noordhoff International Publishing, Leyden.

7. Salviato, M., Zappalorto, M. (2016). "A unified solution approach for a large variety of antiplane shear and torsion notch problems: Theory and examples." Int J Solids Struct, 102–103, 10–20.

8. Lazzarin, L., Tovo, R., 1996. "A unified approach to the evaluation of linear elastic stress fields in the neighborhood of cracks and notches," Int. J. Fract. 78, 3-19. https://doi.org/10.1007/BF00018497

9. Herrera, G. M., Mantič, V., Barroso, A. (2022). "A powerful matrix formalism for stress singularities in anisotropic multi-material corners. Homogeneous (orthogonal) boundary and interface conditions." Theoretical and Applied Fracture Mechanics, 119, 103271. https://doi.org/10.1016/j.tafmec.2022.103271

10. Mantič V., París F., Cañas J., (1997) “Stress singularities in 2D orthotropic corners”, Int. J. Fract. 83, 67–90.

11. Ting T.T.C., Wang M.Z., (1992) “Generalized Stroh formalism for anisotropic elasticity for general boundary conditions”, Acta Mech. Sinica 8193–207.

12. Zhang, X., Fan, W., Liu, T. (2020). "Fused deposition modeling 3D printing of polyamide-based composites and its applications." Composites Communications, 21, 100413. https://doi.org/10.1016/j.coco.2020.100413

13. Polyzos, E., Katalagarianakis, A., Polyzos, D., Van Hemelrijck, D., Pyl, L. (2020). "A multi-scale analytical methodology for the prediction of mechanical properties of 3D-printed materials with continuous fibres." Additive Manufacturing, 36, 101394.

14. He, Qinghao, Wang, Hongjian, Fu, Kunkun, Ye, Lin. (2020). "3D printed continuous CF/PA6 composites: Effect of microscopic voids on mechanical performance." Composites Science and Technology, 191, 108077.

2. In-plane solutions for a rounded notch in an orthotropic body

2.1 Introduction

Geometric features or defects like holes, notches and porosities impact the mechanical properties of solids, resulting in well-documented stress concentration regions under various loading conditions and materials. In practical mechanical component designs, these inevitable geometric variations often contribute to crack formation under both static and fatigue loads. These variations act as stress raisers, inducing stress concentration regions that may lead to crack nucleation and failure under static or fatigue loads (Neuber[28]). The formulation of reliable failure criteria for notches necessitates a thorough understanding of local stress distributions, driving ongoing efforts to provide precise solutions for stress fields around notches under diverse loading conditions.

Efforts to establish accurate failure criteria for notched solids have been a focal point in the scientific community, with numerous exact or approximate solutions proposed for stress caused by holes and notches (Berto et al[3]; Chen[9]; Salviato and Zappalorto[44]; Mirzaei[24]). Finding accurate expressions for stress fields at rounded notches is challenging, especially when the notch root radius is nonzero, causing the elastic stress field to lose singularity. Lazzarin and Tovo[22] proposed modifying Kolosov-Muskhelishvili complex potentials for isotropic plates with rounded notches, resulting in universal equations for stress fields in the vicinity of rounded notches with a generic opening angle under both mode I and mode II. This approach was later used for an improved version (Filippi et al.[13]) and by Zappalorto and Lazzarin for the V-notch with-end-hole problem (Zappalorto and Lazzarin[41]) or the torsion problem (Zappalorto et al.[43]). Authors proposed minor changes, considering non-singular terms (Mirzaei et al.[26]) or slightly modifying boundary conditions (Lazzarin et al.[21], Mirzaei et al.[25]). Notably, these contributions focused on isotropic materials.

Shifting to orthotropic or anisotropic plates, the past literature explored the analysis of holes in infinite solids (Bonora et al.[5-6], Chern and Tuttle[9]). Zappalorto and Carraro[39] addressed a blunt crack in an anisotropic solid under in-plane loadings, obtaining an exact solution for local stress distributions. The solution for the quasi-orthotropic wedge problem was provided by Kazberuk and Savruk[17], and Zappalorto[38] presented an analytical study on 2D stress distributions close to blunt V-notches in orthotropic plates under tension. Analytical solutions for stress fields induced by various geometric variations in orthotropic solids under mode III were provided by Zappalorto and Salviato[44]. Salviato and Phenisee[32] formulated a general framework for solving governing equations of electrostatic and heat transfer problems in media featuring curvilinear transverse isotropy, underlying the stress distribution in materials featuring curvilinear fibers under anti-plane shear stresses.

However, despite the extensive literature, a comprehensive analytical study of mode II stress fields in orthotropic solids with rounded notches is notably absent.

In this chapter two highly accurate new solutions will be presented for stress distributions induced by radiused V-notches with a hyperbolic profile in orthotropic solids.

The first solution aims to improve upon the previous solution by Zappalorto and Carraro[40] presented in a previous chapter for radiused V-notches. The second one is proposed to fill the literature gap existing for in-plane shear in notched orthotropic solids.

To achieve this, the research introduces novel complex potential functions in Lekhnitskii's approach and utilizes Neuber conformal mapping. Stress-free conditions are carefully imposed away from the notch tip, and precise boundary conditions are applied in the remaining domain using a Maclaurin series expansion of relevant stress components. This advanced methodology considers both material elasticity and notch geometry, resulting in a solution that exhibits superior accuracy compared to numerical analyses. Leveraging Lekhnitskii's potential function approach and the conformal mapping technique, these proposed solutions inherently account for notch geometrical features and material parameters. This provides a promising avenue for addressing mixed-mode fracture problems prevalent in engineering applications. The efficacy of these new solutions is demonstrated through meticulous comparisons with numerical results obtained from two-dimensional finite element analyses on plates with rounded notches.

2.2 A new explicit solution for the mode I stress fields in notched orthotropic solids

2.2.1. Analytical description of the notch profile and solution for the stress fields

Consider an orthotropic plate weaken by a radiused notch, the stress-strain relationships can be written according to I.49 and I.59. The edge of a blunt notch with a generic opening angle and curvature radius at its tip can be described using the mapping function described in chapter 1.64:

$$z = \xi^{q} \tag{II.1}$$

where $z = x + iy$ and $\xi = u + iv$ and the notch edge is described by the equation $u = u_0$ (figure I.9)

A solution can be sought by employing a series formulation for the complex potentials: $\phi'_{Hj}\left(z_j\right) = \sum_{j=1}^{\infty} \tilde{A}_j z_j^{\lambda_j - 1}$. However, for the sake of obtaining manageable expressions for the stress fields, it becomes necessary to truncate the series expansion to a finite number of terms. This introduces a tradeoff between the simplicity and accuracy of the resulting solution.

In a previous chapter on the same problem, the solution developed by Zappalorto and Carraro was described in which the authors opted for a one-term-based solution. This approach offered the advantage of simplicity and demonstrated satisfactory agreement with numerical results, especially in the vicinity of the notch tip and along the bisector line. In an effort to enhance this existing solution and achieve highly accurate stress fields both along and outside the notch bisector line, the present work adopts enriched forms for complex potentials as outlined below:

$$\phi'_{H1}\left(z_1\right) = A\left(\frac{z_1}{r_0}\right)^{\lambda-1} + C\left(\frac{z_1}{r_0}\right)^{\mu-1} \qquad \phi'_{H2}\left(z_2\right) = B\left(\frac{z_2}{r_0}\right)^{\lambda-1} + D\left(\frac{z_2}{r_0}\right)^{\mu-1} + E\left(\frac{z_2}{r_0}\right)^{\zeta-1} \tag{II.2}$$

where $z_j = x_j + iy_j = r_j e^{i\theta_j}$ and:

$$x_j = x' + r_0\beta_j^t \qquad y_j = \beta_j y' \qquad r_j = \sqrt{\xi_j^2 + \eta_j^2} \qquad \theta_j = \mathrm{Arg}(\xi_j + i\eta_j) \tag{II.3}$$

wherein Eq. II.3 x'=x-r_0 and y'=y represent the distances from the apex of the notch; instead, A, B, C, D, E, λ, μ, ζ and t are real constants to be determined with proper boundary conditions, under the hypothesis that $1 > \lambda > \mu > \zeta$.

Stress components explicitly read as:

$$\begin{aligned}
\sigma_{rr} = \frac{\sigma_{tip}}{\tilde{A}}\Bigg\{ & \left(\frac{r_1}{r_0}\right)^{\lambda-1}\left[k_{11}\cos(1-\lambda)\theta_1 + k_{12}\sin(1-\lambda)\theta_1\right] + \\
& \chi_{12}\left(\frac{r_1}{r_0}\right)^{\mu-1}\left[k_{11}\cos(1-\mu)\theta_1 + k_{12}\sin(1-\mu)\theta_1\right] + \\
& \chi_{21}\left(\frac{r_2}{r_0}\right)^{\lambda-1}\left[k_{21}\cos(1-\lambda)\theta_2 + k_{22}\sin(1-\lambda)\theta_2\right] + \\
& \chi_{22}\left(\frac{r_2}{r_0}\right)^{\mu-1}\left[k_{21}\cos(1-\mu)\theta_2 + k_{22}\sin(1-\mu)\theta_2\right] + \\
& \chi_{23}\left(\frac{r_2}{r_0}\right)^{\zeta-1}\left[k_{21}\cos(1-\zeta)\theta_2 + k_{22}\sin(1-\zeta)\theta_2\right]\Bigg\}
\end{aligned} \tag{II.4}$$

$$\begin{aligned}
\sigma_{\theta\theta} = \frac{\sigma_{tip}}{\tilde{A}}\Bigg\{ & \left(\frac{r_1}{r_0}\right)^{\lambda-1}\left[m_{11}\cos(1-\lambda)\theta_1 + m_{12}\sin(1-\lambda)\theta_1\right] + \\
& \chi_{12}\left(\frac{r_1}{r_0}\right)^{\mu-1}\left[m_{11}\cos(1-\mu)\theta_1 + m_{12}\sin(1-\mu)\theta_1\right] + \\
& \chi_{21}\left(\frac{r_2}{r_0}\right)^{\lambda-1}\left[m_{21}\cos(1-\lambda)\theta_2 + m_{22}\sin(1-\lambda)\theta_2\right] + \\
& \chi_{22}\left(\frac{r_2}{r_0}\right)^{\mu-1}\left[m_{21}\cos(1-\mu)\theta_2 + m_{22}\sin(1-\mu)\theta_2\right] + \\
& \chi_{23}\left(\frac{r_2}{r_0}\right)^{\zeta-1}\left[m_{21}\cos(1-\zeta)\theta_2 + m_{22}\sin(1-\zeta)\theta_2\right]\Bigg\}
\end{aligned} \tag{II.5}$$

$$\tau_{r\theta} = \frac{\sigma_{tip}}{\tilde{A}}\left\{\left(\frac{r_1}{r_0}\right)^{\lambda-1}\left[n_{11}\cos(1-\lambda)\theta_1 + n_{12}\sin(1-\lambda)\theta_1\right]+\right.$$

$$\chi_{12}\left(\frac{r_1}{r_0}\right)^{\mu-1}\left[n_{11}\cos(1-\mu)\theta_1 + n_{12}\sin(1-\mu)\theta_1\right]+$$

$$\chi_{21}\left(\frac{r_2}{r_0}\right)^{\lambda-1}\left[n_{21}\cos(1-\lambda)\theta_2 + n_{22}\sin(1-\lambda)\theta_2\right]+ \qquad \text{II.6}$$

$$\chi_{22}\left(\frac{r_2}{r_0}\right)^{\mu-1}\left[n_{21}\cos(1-\mu)\theta_2 + n_{22}\sin(1-\mu)\theta_2\right]+$$

$$\left.\chi_{23}\left(\frac{r_2}{r_0}\right)^{\zeta-1}\left[n_{21}\cos(1-\zeta)\theta_2 + n_{22}\sin(1-\zeta)\theta_2\right]\right\}$$

where:

$$\chi_{12} = \frac{C}{A} \qquad \chi_{21} = \frac{B}{A} \qquad \text{II.7}$$

$$\chi_{22} = \frac{D}{A} \qquad \chi_{23} = \frac{E}{A} \qquad \text{II.8}$$

$$1 > \lambda > \mu > \zeta \qquad Abs\left(\chi_{12}\right) \neq 0 \qquad \text{II.9}$$

$$Abs(\chi_{12}) \neq Abs\left(\chi_{21}\right) \neq Abs\left(\chi_{22}\right) \neq Abs\left(\chi_{23}\right) \qquad \text{II.10}$$

$$\tilde{A}=2\left\{\beta_1^{t(\lambda-1)} + \chi_{12}\beta_1^{t(\mu-1)} + \chi_{21}\beta_2^{t(\lambda-1)} + \chi_{22}\beta_2^{t(\mu-1)} + \chi_{23}\beta_2^{t(\zeta-1)}\right\} \qquad \text{II.11}$$

Free-of-stress boundary conditions have to be applied to curvilinear stress components σ_{uu} and τ_{uv}, which must be zero along the notch edge ($u=u_0$):

$$\sigma_{uu}\big|_{u=u_0} = \tau_{uv}\big|_{u=u_0} = 0 \qquad \text{II.12}$$

where:

$$\sigma_{uu} = \frac{\sigma_{rr} + \sigma_{\theta\theta}}{2} + \frac{\sigma_{rr} - \sigma_{\theta\theta}}{2}\cos\frac{2\theta}{q} - \tau_{r\theta}\sin\frac{2\theta}{q}$$

$$\tau_{uv} = \frac{\sigma_{rr} - \sigma_{\theta\theta}}{2}\sin\frac{2\theta}{q} + \tau_{r\theta}\cos\frac{2\theta}{q} \qquad \text{II.13}$$

Along the notch edge ($u = u_0$) and very far from the notch tip ($v \gg 0$) $\theta \approx \pm\gamma = \pm\frac{q\pi}{2}$ so that (see Eq. II.13), boundary conditions can be rewritten as:

$$\sigma_{uu}\Big|_{\substack{u=u_0\\v>>0}} \cong \sigma_{\theta\theta}\Big|_{\substack{r>>0\\\theta\cong\gamma}} = 0 \qquad \sigma_{uv}\Big|_{\substack{u=u_0\\v>>0}} \cong \sigma_{r\theta}\Big|_{\substack{r>>0\\\theta\cong\gamma}} = 0 \tag{II.14}$$

Moreover, from Eq. II.3 one obtains:

$$r_j \approx \sqrt{\left(x'\right)^2 + \left(\beta_j y'\right)^2} \cong r \cdot \rho_j(\gamma) \tag{II.15}$$

and:

$$\theta_j \approx \mathrm{Arg}\left(\cos\gamma + i\beta_j \sin\gamma\right) = \theta_j(\gamma) \tag{II.16}$$

where:

$$\rho_j(\gamma) = \sqrt{\cos^2\gamma + \left(\beta_j \sin\gamma\right)^2} \tag{II.17}$$

In addition to this, since $1 < \lambda < \mu < \zeta$, far from the notch tip ($y' \gg 0$) Eq. II.5 and II.6 can be simplified to give:

$$\begin{aligned}\sigma_{\theta\theta} = \frac{\sigma_{tip}}{\tilde{A}}\left(\frac{r}{r_0}\right)^{\lambda-1} &\left\{\rho_1^{\lambda-1}(\gamma)\left[m_{11}\cos(1-\lambda)\theta_1(\gamma) + m_{12}\sin(1-\lambda)\theta_1(\gamma)\right] + \right.\\ &\left.\chi_{21}\rho_2^{\lambda-1}(\gamma)\left[m_{21}\cos(1-\lambda)\theta_2(\gamma) + m_{22}\sin(1-\lambda)\theta_2(\gamma)\right]\right\}\end{aligned} \tag{II.18}$$

and

$$\begin{aligned}\tau_{r\theta} = \frac{\sigma_{tip}}{\tilde{A}}\left(\frac{r}{r_0}\right)^{\lambda-1} &\left\{\rho_1^{\lambda-1}(\gamma)\left[n_{11}\cos(1-\lambda)\theta_1(\gamma) + n_{12}\sin(1-\lambda)\theta_1(\gamma)\right] + \right.\\ &\left.\chi_{21}\rho_2^{\lambda-1}(\gamma)\left[n_{21}\cos(1-\lambda)\theta_2(\gamma) + n_{22}\sin(1-\lambda)\theta_2(\gamma)\right]\right\}\end{aligned} \tag{II.19}$$

Substituting Eq. II.18 and II.19 into Eq. II.14 results in the same system describing the boundary conditions of a corner singularity, I.216, which implies the same eigenvalue equation for λ:

$$\begin{aligned}&\cos(1-\lambda)\theta_2(\gamma)\left\{\cos(1-\lambda)\theta_1(\gamma)\left[m_{11}(\gamma)n_{21}(\gamma)-m_{21}(\gamma)n_{11}(\gamma)\right]-\right.\\&\left.\sin(1-\lambda)\theta_1(\gamma)\left[m_{21}(\gamma)n_{12}(\gamma)-m_{12}(\gamma)n_{21}(\gamma)\right]\right\}-\\&\sin(1-\lambda)\theta_2(\gamma)\left\{\cos(1-\lambda)\theta_1(\gamma)\left[m_{22}(\gamma)n_{11}(\gamma)-m_{11}(\gamma)n_{22}(\gamma)\right]-\right.\\&\left.\sin(1-\lambda)\theta_1(\gamma)\left[m_{12}(\gamma)n_{22}(\gamma)-m_{22}(\gamma)n_{12}(\gamma)\right]\right\}=0\end{aligned} \tag{II.20}$$

With the aim to determine the remaining 7 constants, the Maclaurin series expansion for σ_{uu} and σ_{uv} along the notch edge, $r = r(\theta) = u_0^q / \cos^q \dfrac{\theta}{q}$, will be used:

$$\begin{aligned}&\sigma_{uu}\Big|_{u=u_0} \cong \sum_{k=0}^{\infty}\frac{1}{k!}\frac{\partial^k \sigma_{uu}(\theta)}{\partial\theta^k}\bigg|_{\theta=0}\times\theta^k\\&\tau_{uv}\Big|_{u=u_0} \cong \sum_{k=0}^{\infty}\frac{1}{k!}\frac{\partial^k \tau_{uv}(\theta)}{\partial\theta^k}\bigg|_{\theta=0}\times\theta^k\end{aligned} \tag{II.21}$$

Accordingly, boundary conditions $\sigma_{uu}\big|_{u=u_0} = \sigma_{uv}\big|_{u=u_0} = 0$ can be approximated setting to zero the first six terms of the Maclaurin series expansion, namely:

$$\begin{aligned}&\sigma_{uu}(\theta)\big|_{\theta=0}=0 &&\frac{\partial\tau_{uv}(\theta)}{\partial\theta}\bigg|_{\theta=0}=0\\&\frac{\partial^2\sigma_{uu}(\theta)}{\partial\theta^2}\bigg|_{\theta=0}=0 &&\frac{\partial^3\tau_{uv}(\theta)}{\partial\theta^3}\bigg|_{\theta=0}=0\\&\frac{\partial^4\sigma_{uu}(\theta)}{\partial\theta^4}\bigg|_{\theta=0}=0 &&\frac{\partial^5\tau_{uv}(\theta)}{\partial\theta^5}\bigg|_{\theta=0}=0\\&\frac{\partial^6\sigma_{uu}(\theta)}{\partial\theta^6}\bigg|_{\theta=0}=0\end{aligned} \tag{II.22}$$

also considering that $\dfrac{\partial^{2k-1}\sigma_{uu}(\theta)}{\partial\theta^{2k-1}}\bigg|_{\theta=0} = \dfrac{\partial^{2k-2}\tau_{uv}(\theta)}{\partial\theta^{2k-2}}\bigg|_{\theta=0} = 0$ for symmetry reasons.

By explicitly substituting stress components into Equation II.22, a non-linear system of seven equations is obtained. This system can be numerically solved using the Newton-Raphson method, considering different starting points in the 7-dimensional space $\{t, \mu, \zeta, \chi_{12}, \chi_{21}, \chi_{22}, \chi_{23}\}$. Due to the non-linearity of the problem, the solution is not unique. Among all possible numerical values that satisfy Equation (35), the combination minimizing the residual stress components $\sigma_{uu}\big|_{u=u_0}$ and $\sigma_{uv}\big|_{u=u_0}$ is selected.

To this end, the following function to be minimized is defined:

$$F = \sum_{n=0}^{N} \sqrt{\left[\sigma_{uv}\Big|_{\substack{u=u_0\\v=v_n}}\right]^2 + \left[\sigma_{u}\Big|_{\substack{u=u_0\\v=v_n}}\right]^2} \quad \text{with } 0 < v_n < v_{n+1} \text{ and } n \in \{1;2;...;N\} \qquad \text{II.23}$$

where v_n is the point of the curve $u = u_0$ associated to a certain angle θ_n, $N = 10$ and θ_n are equally distanced angles between 0 and γ.

The steps taken to determine the 8 constants: t, λ, μ, ζ, χ_{12}, χ_{21}, χ_{22}, χ_{23}, are summarised here below:

1) λ value is calculated by solving Eq. II.20;
2) a starting point for the Newton method is chosen in a 7-D sphere centred at the origin of the space {t, μ, ζ, χ_{12}, χ_{21}, χ_{22}, χ_{23}};
3) the system given by Eq. II.22 is solved using Newton method and the starting point previously chosen;
4) Does the found solution respect the following basic conditions?
   a. $1 > \lambda > \mu > \zeta$
   b. $Abs(\chi_{12}) \neq Abs(\chi_{21}) \neq Abs(\chi_{22}) \neq Abs(\chi_{23})$
   c. $Abs(\chi_{12}) \neq 0$

   If not, the solution is not compatible, and a different starting point has to be selected (back to point 2);
5) Whenever the basic conditions at point 4 are respected, the optimizing function F is calculated and:
   a. if $F \approx 0$ the algorithm succeeded, and the obtained solution is regarded as the optimal one;

b. otherwise, a different starting point has to be selected (back to point 2).

2.2.2. Discussion and comparison with numerical results

The stress fields obtained from the new solution were subjected to comparison with results from numerous numerical analyses to evaluate the accuracy of the findings. Three distinct materials were considered:

- **Material 1** characterized by E_x=10 GPa, E_y=160 GPa, G_{xy}=5 GPa, and ν_{xy}=0.01875;
- **Material 2** with properties E_x=160 GPa, E_y=10 GPa, G_{xy}=5 GPa, and ν_{xy}=0.30;
- **Material 3**, an isotropic material with E_x=10 GPa, E_y=10 GPa, G_{xy}=3.846 GPa, and ν_{xy}=0.3.

It is notable that Material 1 is highly stiff in the loading direction (E_y/E_x=16), causing intense stress concentration at the notch, while Material 2 is stiff in the direction normal to the load (E_y/E_x=0.0625), resulting in lower stress concentration.

The analyses focused on plates subjected to tension and featuring symmetric lateral hyperbolic notches, characterized by a profile described by Eq. II.1, Figure II.1. Three different notched geometries were analyzed for each material, with dimensions summarized in Table II.1. Stress parameters for the analyzed geometries and materials were summarized in Table II.2.

All finite element (FE) analyses were conducted using Ansys®, version 19, with parabolic isoparametric elements (PLANE183) creating regular mesh patterns. A fine discretization close to the notch tip was ensured, with elements sized around $\rho/40$, figure II.2. Stresses in the FE models were evaluated along the bisector line, on the notch edge, and on circular paths centered on the origin, figure II.3.

The numerical results, depicted in figures II.4-II.15, were compared with the new analytical solution and the previous solution by Zappalorto and Carraro[40]. In general, the accuracy of Eqs. II.4-II.6 was exceptionally high. Specifically, for a notch opening angle 2α=30°, stress along the bisector line exhibited excellent agreement with numerical data (Figure II.4). Even for larger opening angles

(2α=90° and 2α=135°, Figures II.5 and II.6), the new solution maintained a high level of accuracy, surpassing the precision of the previous formulation.

Further examinations of stress distributions along circular paths (Figures II.7-II.8) and along the notch edge (Figures II.10-II.12) for different materials and notch opening angles revealed consistently satisfactory accuracy for the new equations proposed in this work. Notably, the accuracy remained high irrespective of the material and the notch opening angle, from very stiff loading direction materials (Material 1) to those stiff in the direction normal to the loading (Material 2).

The influence of the notch root radius was investigated (Figures II.13-II.15), showing that the accuracy of the new solution was independent of the notch root radius and consistently high across various radii.

In summary, the comprehensive numerical study affirmed the satisfactory accuracy of the new solution (Eqs. II.4-II.6) across diverse materials and notched geometries. Overall, the new solution outperformed the previous formulation by Zappalorto and Carraro[40], especially in scenarios involving materials highly stiff in the loading direction and large notch opening angles.

Geometry	Opening angle 2α (°)	Semi-width W (mm)	Semi-height L (mm)	Notch depth a (mm)	Root radius ρ (mm)
G1	30	100	150	10	0.1, 1, 2.5
G2	90	100	150	10	0.1, 1, 2.5
G3	135	100	150	10	0.1, 1, 2.5

Table II.1. Summary of the notched plates studied.

Opening angle 2α (°)	$\tilde{A}$	λ	μ	ζ	t	χ_{12}	χ_{21}	χ_{22}	χ_{23}
30	0.0537	0.5014	0.1014	-0.8172	1.9074	-0.0515	-0.9896	0.0518	-0.0002
45	0.0494	0.5050	0.2211	-0.2818	1.7006	-0.0957	-0.9897	0.0961	0.0004
60	0.0467	0.5122	0.2569	0.1048	1.6191	-0.1260	-0.9892	0.1249	0.0015
90	0.0436	0.5445	0.2706	0.2028	1.4311	-0.1425	-0.9881	0.1396	0.0033
120	0.0426	0.6157	0.3024	0.2380	1.2511	-0.1143	-0.9862	0.1124	0.0022
135	0.0428	0.6736	0.2736	0.2236	1.1464	-0.0757	-0.9848	0.0739	0.0021
150	0.0431	0.7520	0.2293	-0.6233	1.1199	-0.0394	-0.9832	0.0395	0

Table II.2. Stress fields parameters to be used in Eqs. II.4-II.6. Hyperbolic notched in plate under mode I. Material 3 (isotropic) and different opening angles

Geometry	Material	$\tilde{A}$	λ	μ	ζ	t	χ_{12}	χ_{21}	χ_{22}	χ_{23}
G1	M1	10.1530	0.5003	0.4703	-1.6466	1.9476	-0.0249	-0.1642	0.0464	-0.0024
G1	M2	2.5057	0.5101	0.3801	-0.9021	1.8123	-0.0448	-0.1315	0.0651	-0.8084
G1	M3	0.0537	0.5014	0.1014	-0.8172	1.9074	-0.0515	-0.9896	0.0518	-0.0002
G2	M1	8.8311	0.5087	-0.440	-0.5103	1.7378	0.0023	-0.1059	0.1153	-0.1089
G2	M2	2.4312	0.5936	0.2188	0.1687	1.4130	0.0199	-0.0896	0.7857	-0.7916
G2	M3	0.0436	0.5445	0.2706	0.2028	1.4311	-0.1425	-0.9881	0.1396	0.0033
G3	M1	6.6374	0.5456	-0.0707	-0.3078	1.4986	0.0102	-0.0807	0.0329	-0.0219
G3	M2	2.2894	0.7261	0.2783	0.1057	1.1859	0.0075	0.0357	0.0164	-0.0133
G3	M3	0.0428	0.6736	0.2736	0.2236	1.1464	-0.0757	-0.9848	0.0739	0.0021

Table II.3. Stress fields parameters to be used in Eqs. II.4-II.6. Hyperbolic notched in plate under mode I. Different materials and opening angles.

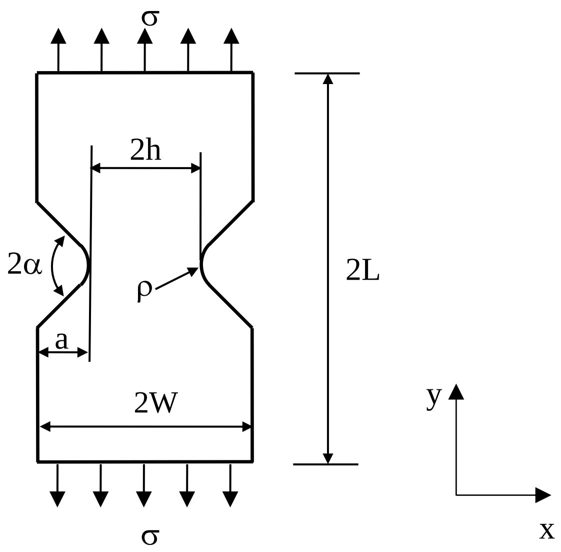

Figure II.1. Schematic of the plate with two symmetric hyperbolic notches under tension.

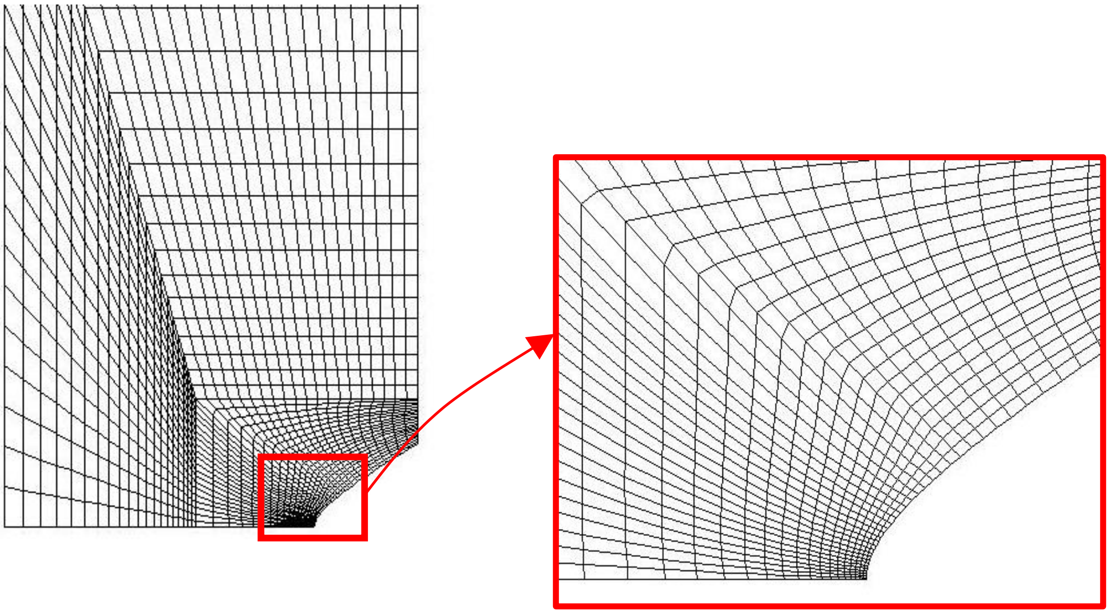

Figure II.2. Example of one FE model used to analyse hyperbolic notches (one quarter of the entire plate and details of the notch tip). Notch opening angle $2\alpha=90°$, notch root radius $\rho=1$ mm, notch depth $a=10$ mm.

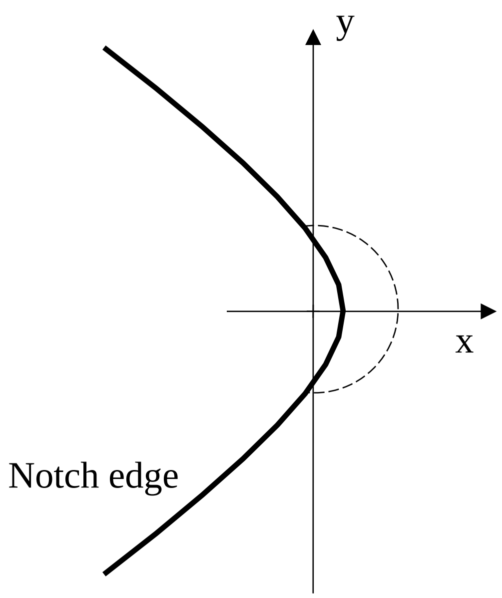

Figure II.3. Schematic of the circular paths where stresses were evaluated. The paths are centered on the origin of the coordinate system used for Eqs. II.4-II.6.

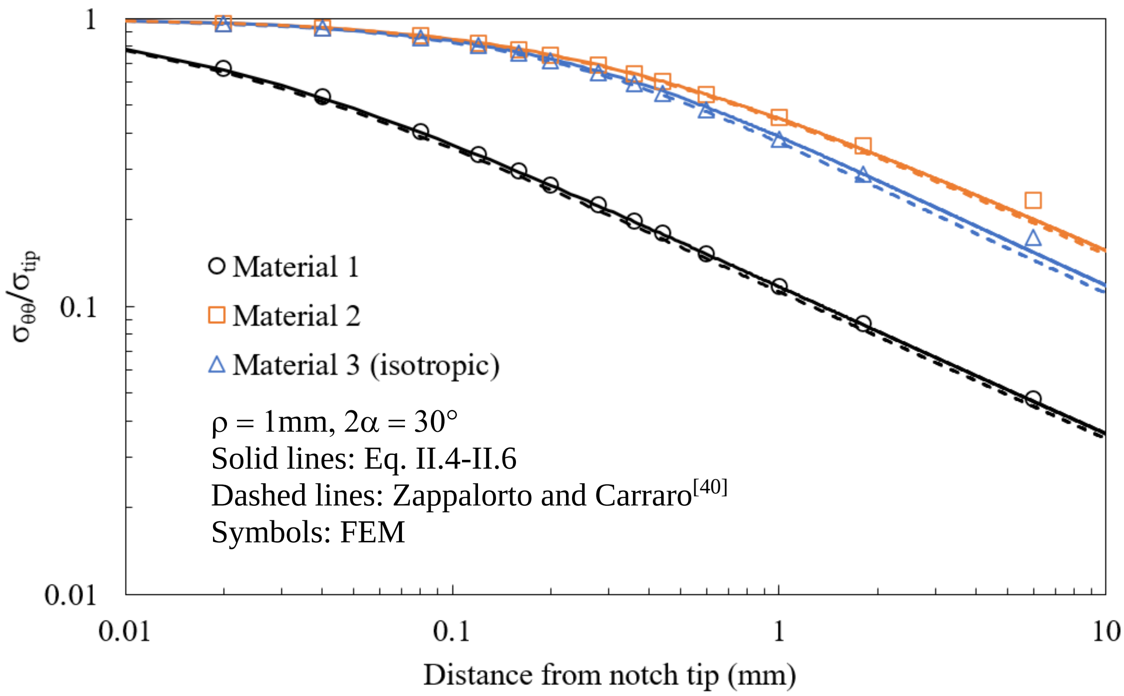

Figure II.4. Mode I normalised stress component $\sigma_{\theta\theta}$ evaluated along the bisector; hyperbolic notch with 2α=30°, a=10 mm, ρ=1 mm and W=100 mm. Results from Eq. II.5 compared with FE results and with the solution by Zappalorto and Carraro[40]. Different materials.

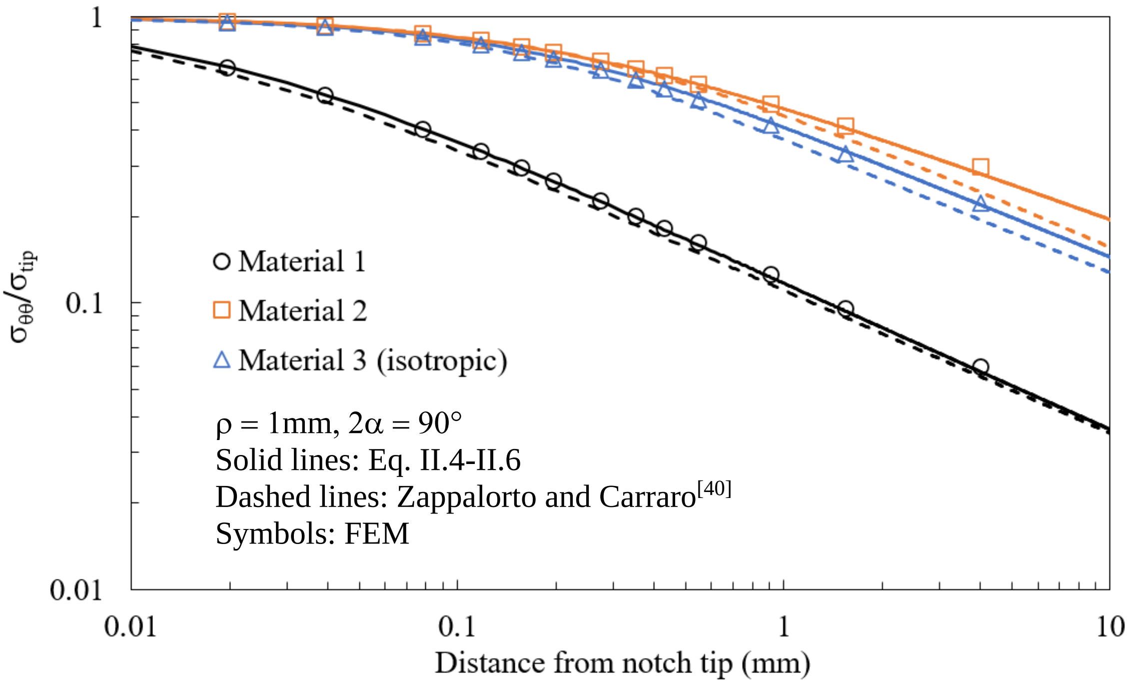

Figure II.5. Mode I normalised stress component $\sigma_{\theta\theta}$ evaluated along the bisector; hyperbolic notch with 2α=90°, a=10 mm, ρ=1 mm and W=100 mm. Results from Eq. II.5 compared with FE results and with the solution by Zappalorto and Carraro[40]. Different materials.

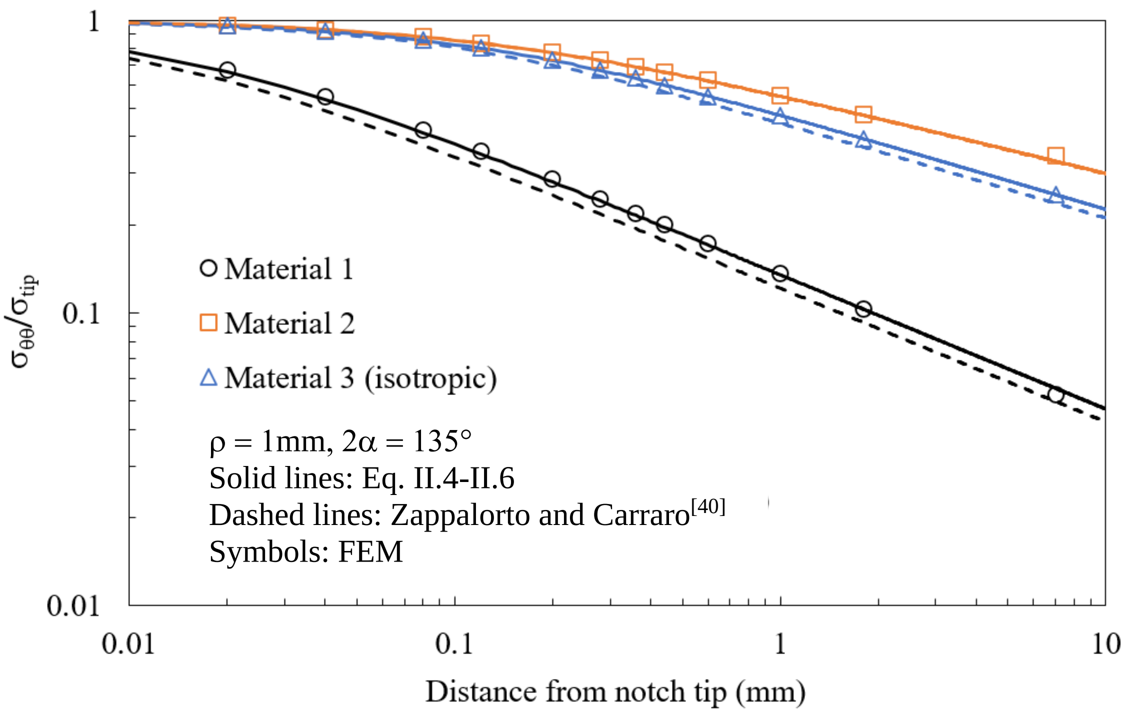

Figure II.6. Mode I normalised stress component $\sigma_{\theta\theta}$ evaluated along the bisector; hyperbolic notch with 2α=135°, a=10 mm, ρ=1 mm and W=100 mm. Results from Eq. II.5 compared with FE results and with the solution by Zappalorto and Carraro[40]. Different materials.

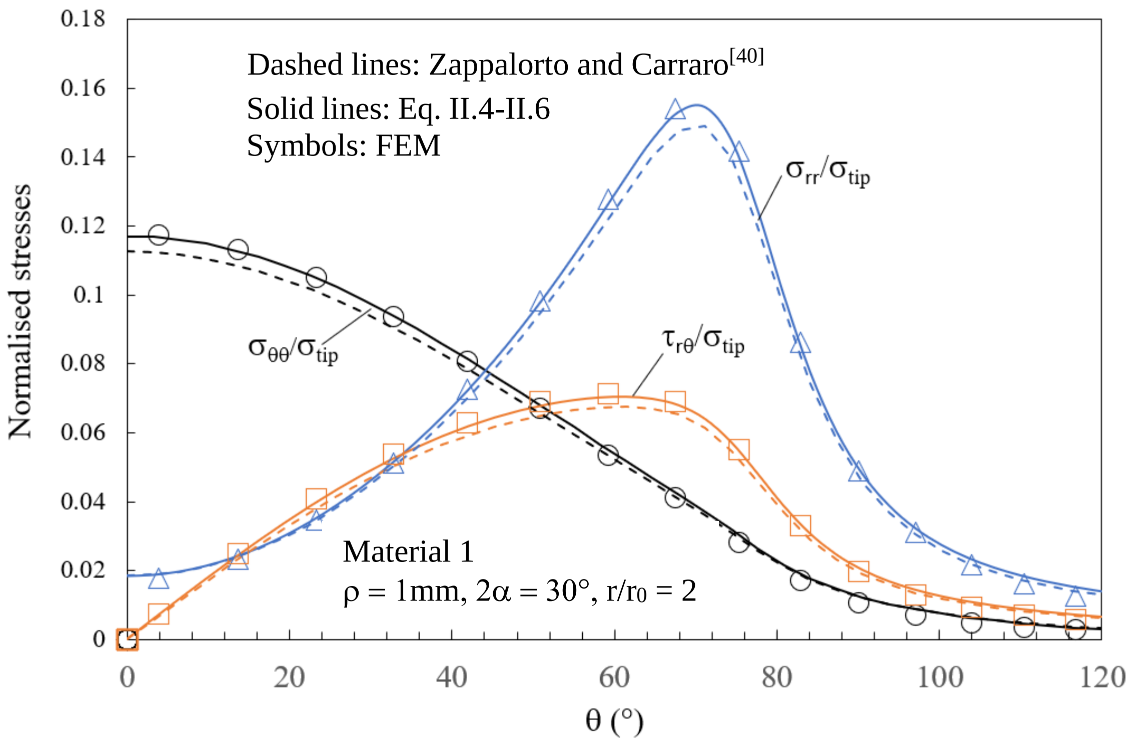

Figure II.7. Mode I normalised stress components evaluated along a circular path or radius $r = 2r_0$ embracing the notch tip. Hyperbolic notch with $2\alpha=30°$, a=10 mm, ρ=1 mm and W=100 mm. Material 1. Results from Eq. II.4-II.6 compared with FE results and with the solution by Zappalorto and Carraro[40].

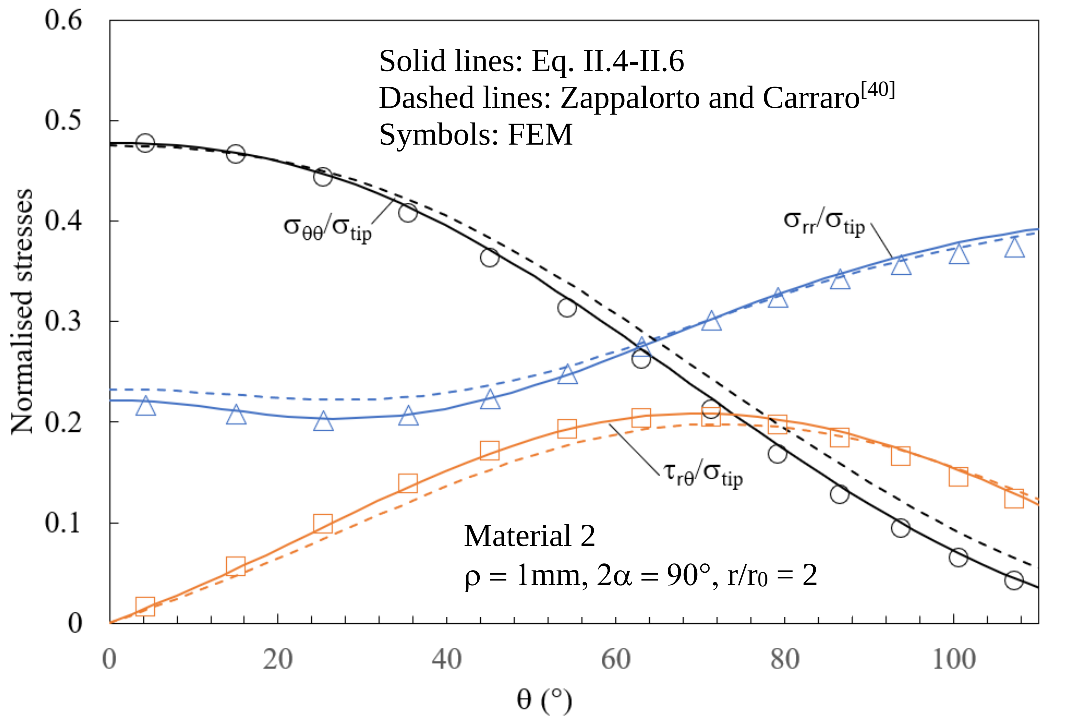

Figure II.8. Mode I normalised stress components evaluated along a circular path or radius $r = 2r_0$ embracing the notch tip. Hyperbolic notch with $2\alpha=90°$, a=10 mm, ρ=1 mm and W=100 mm. Material 2. Results from Eq. II.4-II.6 compared with FE results and with the solution by Zappalorto and Carraro[40].

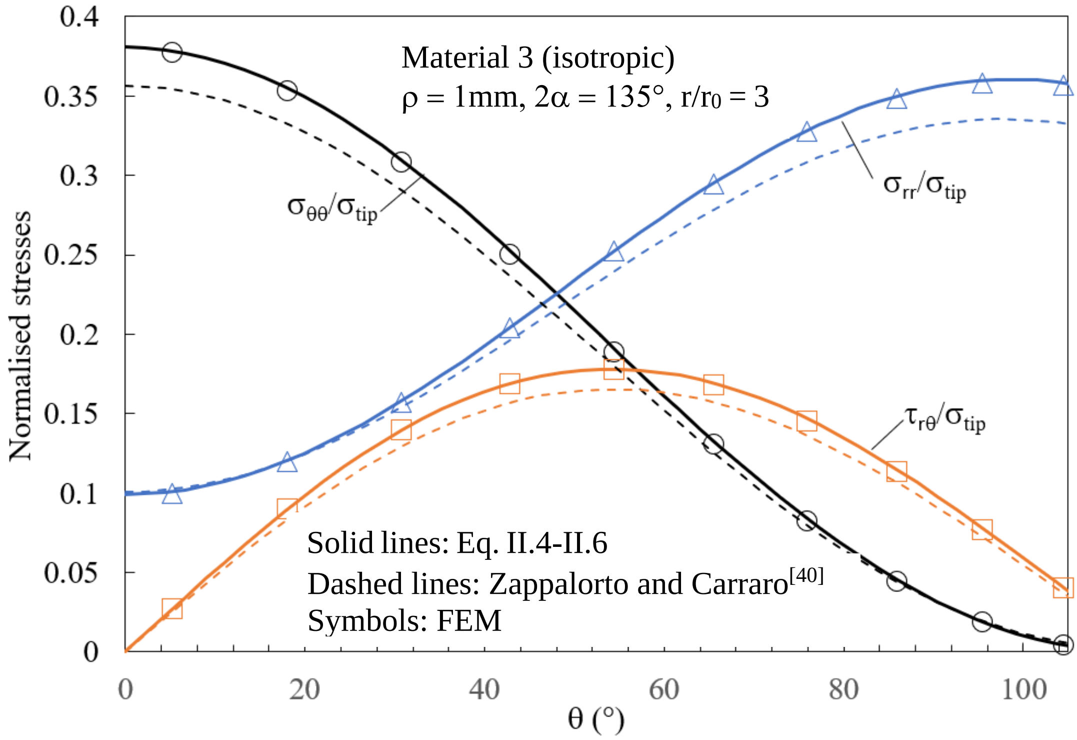

Figure II.9. Mode I normalised stress components evaluated along a circular path or radius $r = 3r_0$ embracing the notch tip. Hyperbolic notch with $2\alpha=135°$, a=10 mm, ρ=1 mm and W=100 mm. Material 3. Results from Eq. II.4-II.6 compared with FE results and with the solution by Zappalorto and Carraro[40].

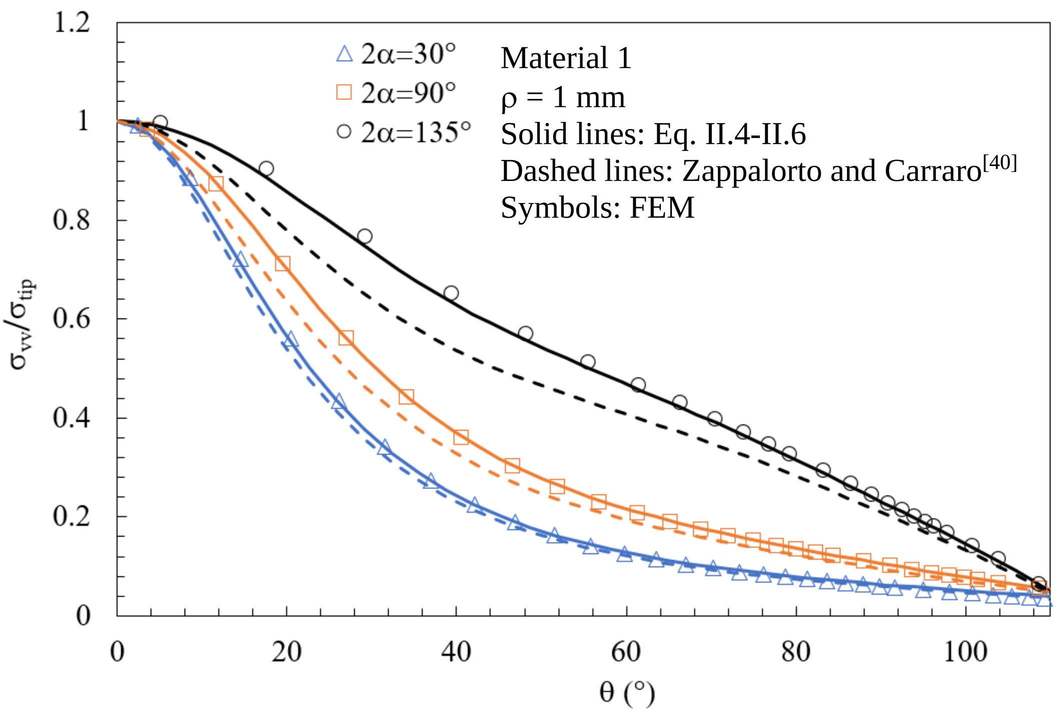

Figure II.10. Mode I normalised stress component σ_{vv} (maximum principal stress) evaluated along the notch edge. Hyperbolic notches with $2\alpha=30°$, 90° and 135°, a=10 mm, ρ=1 mm and W=100 mm. Material 1. Results from Eq. II.4-II.6 compared with FE results and with the solution by Zappalorto and Carraro[40].

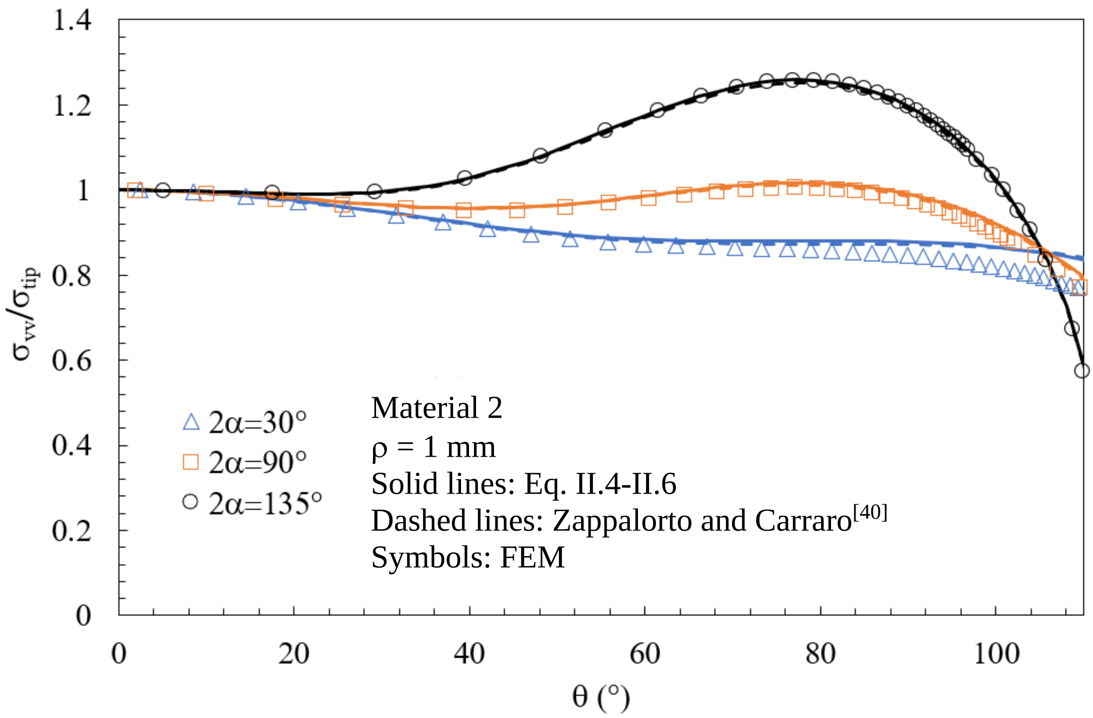

Figure II.11. Mode I normalised stress component σ_{vv} (maximum principal stress) evaluated along the notch edge. Hyperbolic notches with 2α=30°, 90° and 135°, a=10 mm, ρ=1 mm and W=100 mm. Material 2. Results from Eq. II.4-II.6 compared with FE results and with the solution by Zappalorto and Carraro[40].

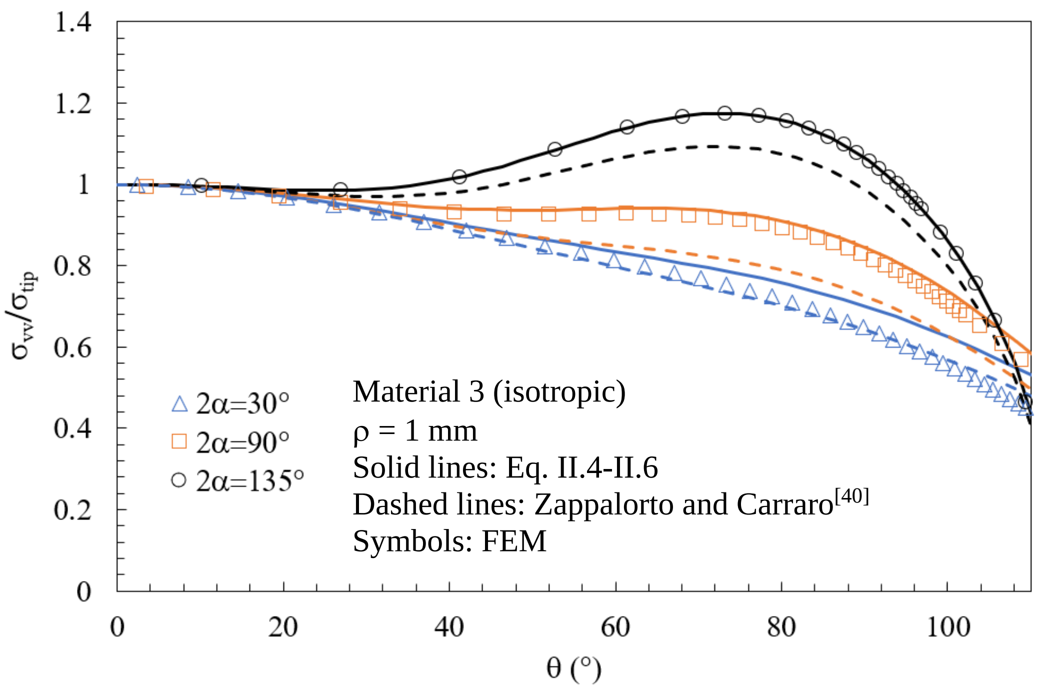

Figure II.12. Mode I normalised stress component σ_{vv} (maximum principal stress) evaluated along the notch edge. Hyperbolic notches with 2α=30°, 90° and 135°, a=10 mm, ρ=1 mm and W=100 mm. Material 3. Results from Eq. II.4-II.6 compared with FE results and with the solution by Zappalorto and Carraro[40].

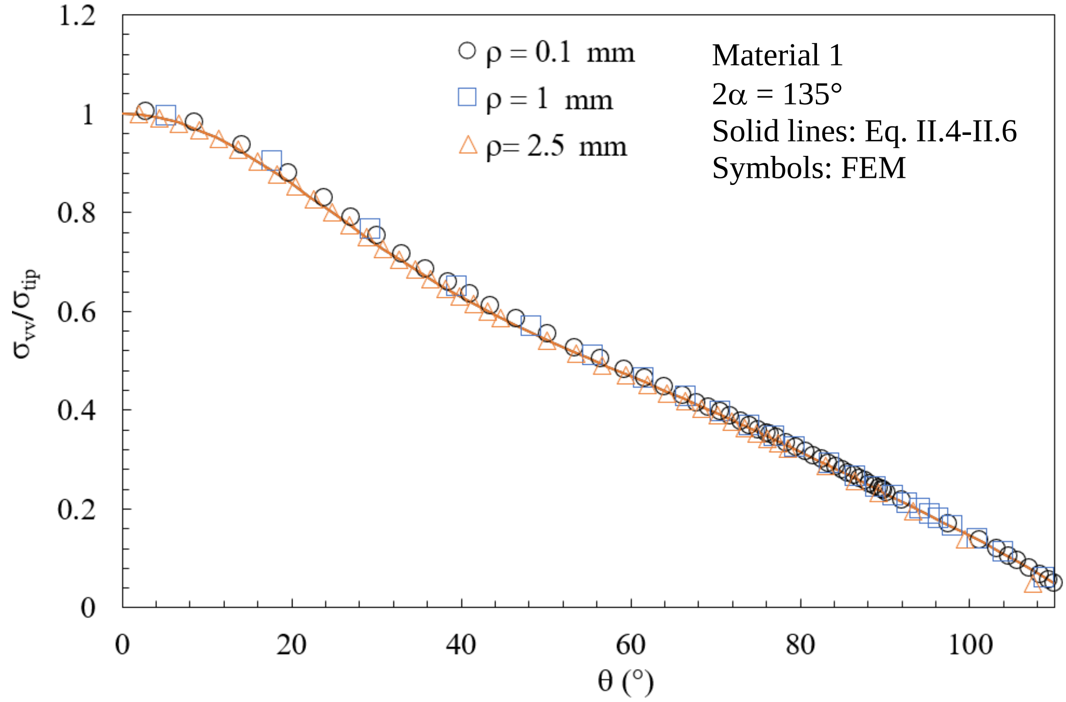

Figure II.13. Mode I normalised stress component σ_{vv} (maximum principal stress) evaluated along the notch edge. Hyperbolic notches with 2α=135°, a=10 mm, and W=100 mm. Material 1 and different root radiuses. Results from Eq. II.4-II.6 compared with FE results.

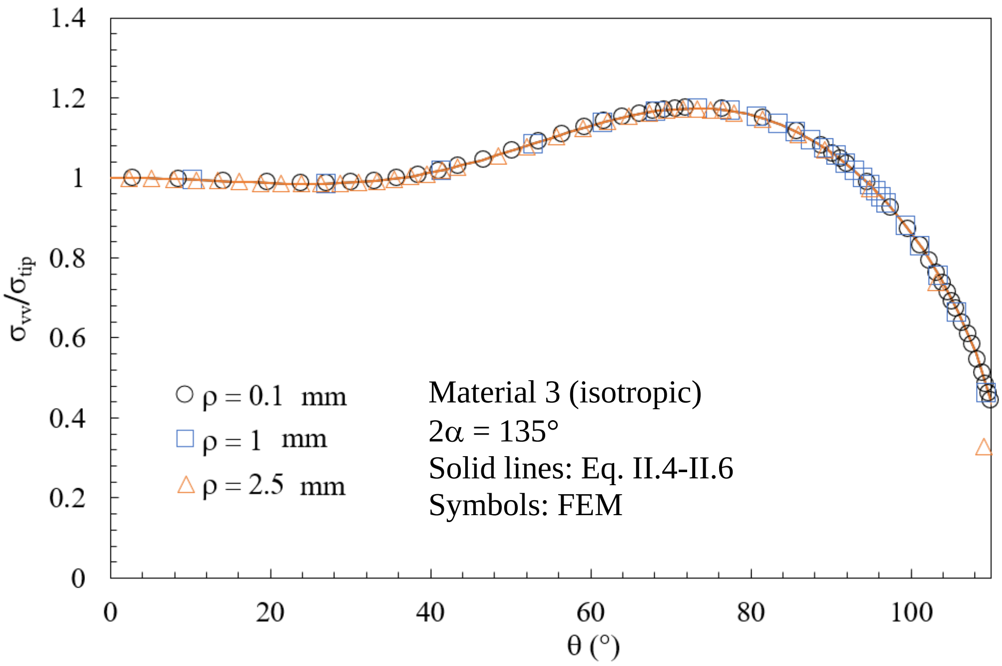

Figure II.14 Mode I normalised stress component σ_{vv} (maximum principal stress) evaluated along the notch edge. Hyperbolic notches with 2α=135°, a=10 mm, and W=100 mm. Material 3 and different root radiuses. Results from Eq. II.4-II.6 compared with FE results.

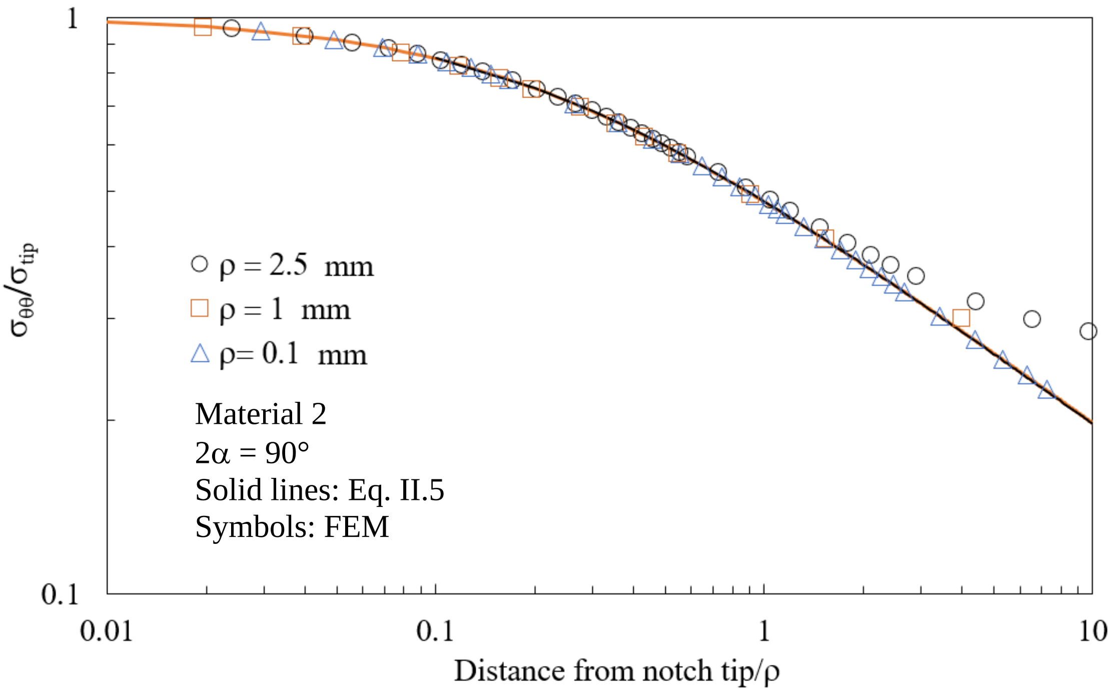

Figure II.15. Mode I normalised stress component $\sigma_{\theta\theta}$ evaluated along the bisector; hyperbolic notch with 2α=90°, a=10 mm and W=100 mm. Material 2, different root radii. Results from Eq. II.5 compared with FE results.

2.2.3. Advantages and limitations of the developed solution

The authors have invested significant efforts in formulating an analytical yet straightforward solution for stress fields induced by lateral rounded notches in orthotropic plates under tension. The proposed solution incorporates terms accounting for crucial geometrical parameters (notch angle, notch root radius) and material characteristics (orthotropy ratio). The calculation of stress field parameters in this solution involves a numerical optimization procedure for a given notch opening angle and material. Despite the necessity of numerical optimization, the algorithm proves highly efficient, allowing for the rapid determination of optimal parameters. Notably, after calibration, the obtained parameters remain applicable to any notched plate or component with the specified opening angle and material, independent of specific geometric details, notch root radius, or notch depth.

In contrast to a fully numerical approach like the Finite Element (FE) method, where approximations are introduced at the outset, the developed solution offers an advantage. Its ability to provide general insights into the effects of key geometrical and material parameters sets it apart from purely numerical investigations. An additional noteworthy aspect is the role of stress field solutions in the development of failure criteria for notched bodies, a crucial consideration in fracture mechanics. Many established failure criteria implicitly or explicitly rely on stress field solutions. Consequently, refining and introducing accurate solutions for stress fields near geometrical variations, represents a vital step in formulating effective fracture criteria for notched bodies. From a mathematical standpoint, the new solution is applicable to infinite bodies, as indicated by the conformal mapping in Eq. II.1 used to describe the notch boundary. However, as demonstrated in the preceding section, the solution effectively characterizes the local stress field near the notch tip in finite-sized plates. This aligns with similar local stress field solutions in existing literature. Furthermore, the solution is specifically valid for orthotropic materials meeting the condition $\left(2S_{12}+S_{66}\right)^2 \geq 4S_{11}S_{22}$, satisfied by a majority of natural orthotropic materials and numerous composite configurations. It is worth noting that if this condition is not met, as exemplified by angle-ply laminates, the solution is deemed invalid.

2.3. Stress distributions in orthotropic solids with blunt notches under in-plane shear loadings

2.3.1. Finite plate with two symmetric hyperbolic notches

Consider the following mapping function, shown in figure 1 (Timoshenko and Goodier[35]):

$$z = c \cdot \sinh \xi \qquad \text{II.24}$$

In Eq. II.24 z = x +iy and $\xi=u+iv_0$ are complex variables whereas c is a proper constant. Substituting $v_0=0$ a deep crack can be obtained whereas, when $v_0>0$ a notch with a hyperbolic boundary can be described, with foci located at $x=\pm c$.

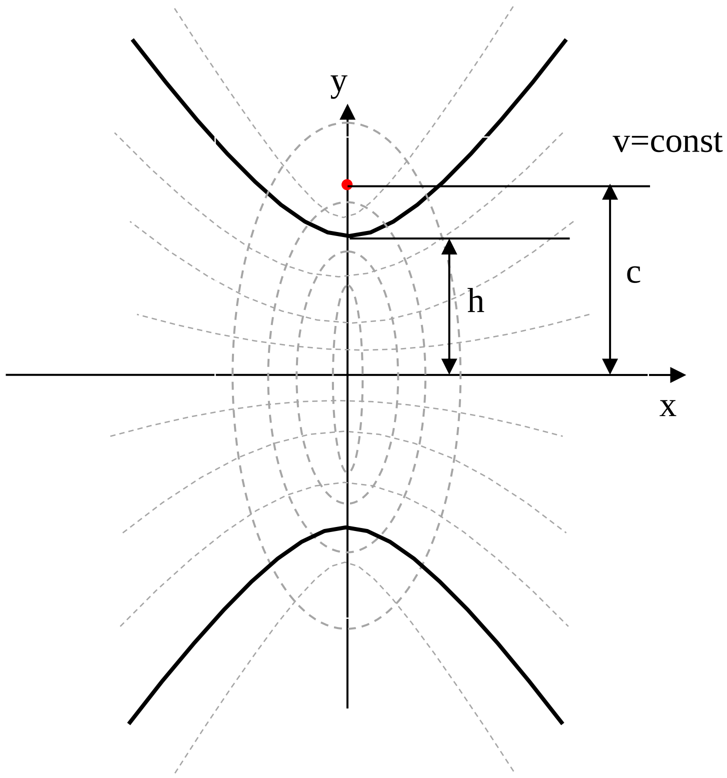

Figure II.16. Schematic of the contour lines and the corresponding notch boundary generated by Eq. II.24.

The plate net section and the radius at the tip of the notch can be assessed using the following equations:

$$\mathrm{H} = \mathrm{c} \cdot \sin \mathrm{v}_0 \qquad \rho = \mathrm{c} \cdot \cot \mathrm{v}_0 \cdot \cos \mathrm{v}_0 \tag{II.25}$$

Consider the reference system depicted in figure II.16; the stress components can be computed using the following complex potentials:

$$\begin{aligned} \phi_{H1}(z_1) &= iA \cdot \beta_2 Ln\left\{ z_1 + \sqrt{z_1^2 + b^2 - \mu_1^2 h^2} \right\} \\ \phi_{H2}(z_2) &= -iA \cdot \beta_1 Ln\left\{ z_2 + \sqrt{z_2^2 + b^2 - \mu_2^2 h^2} \right\} \end{aligned} \tag{II.26}$$

where:

$$\mathrm{b} = \sqrt{\rho \cdot \mathrm{h}} \tag{II.27}$$

and ρ is the curvature radius at the apex of the notch. Eq. II.26 guarantees the free-of-stress conditions along the notch edge ($v=v_0$). Since:

$$\frac{\partial \mathrm{Ln}\left\{ z_j + \sqrt{z_j^2 + b^2 - \mu_j^2 h^2} \right\}}{\partial z_j} = \frac{1}{\sqrt{z_j^2 + b^2 + \beta_j^2 h^2}} \tag{II.28}$$

Leads to:

$$\begin{aligned}
\sigma_{xx} &= A \cdot \mathrm{Re}\left\{ \frac{i\beta_2\beta_1^2}{\sqrt{z_1^2 + \rho h + \beta_1^2 h^2}} - \frac{i\beta_1\beta_2^2}{\sqrt{z_2^2 + \rho h + \beta_2^2 h^2}} \right\} \\
\sigma_{yy} &= A \cdot \mathrm{Re}\left\{ \frac{i\beta_2}{\sqrt{z_1^2 + \rho h + \beta_1^2 h^2}} - \frac{i\beta_1}{\sqrt{z_2^2 + \rho h + \beta_2^2 h^2}} \right\} \\
\tau_{xy} &= A \cdot \mathrm{Re}\left\{ \frac{\beta_2\beta_1}{\sqrt{z_1^2 + \rho h + \beta_1^2 h^2}} - \frac{\beta_1\beta_2}{\sqrt{z_2^2 + \rho h + \beta_2^2 h^2}} \right\}
\end{aligned} \tag{II.29}$$

Parameter A can be linked to the nominal shear stress on the net section, using to the following expression:

$$\int_0^h \tau_{xy} dy = \tau_{nn} h \tag{II.30}$$

Substituting Eq. II.29 into Eq. II.30 allows one to obtain $A = \tau_{nn} \frac{h}{\tilde{g}}$, where:

$$\tilde{g} = \left\{ \frac{\beta_2}{2} \mathrm{Arg}\left[i2\beta_1\sqrt{\rho / h} + \left(\rho / h - \beta_1^2\right) \right] - \frac{\beta_1}{2} \mathrm{Arg}\left[i2\beta_2\sqrt{\rho / h} + \left(\rho / h - \beta_2^2\right) \right] \right\} \tag{II.31}$$

Eventually, stresses can be re-written taking advantage of the following variables:

$$\hat{\rho}_j = \sqrt{\hat{x}_j^2 + \hat{y}_j^2} \qquad \hat{\theta}_j = \mathrm{Arg}\left\{ \hat{x}_j + i\hat{y}_j \right\} \tag{II.32}$$

$$\hat{x}_j = x^2 - \beta_j^2 y^2 + \rho h + h^2\beta_j^2 \qquad \hat{y}_j = 2\beta_j x\ y \tag{II.33}$$

providing:

$$\sigma_{xx} = \tau_{nn}\,\frac{h}{\tilde{g}}\left\{\beta_2\beta_1^2\hat{\rho}_1^{-1/2}\sin\frac{\hat{\theta}_1}{2} - \beta_1\beta_2^2\hat{\rho}_2^{-1/2}\sin\frac{\hat{\theta}_2}{2}\right\}$$

$$\sigma_{yy} = \tau_{nn}\,\frac{h}{\tilde{g}}\left\{\beta_2\hat{\rho}_1^{-1/2}\sin\frac{\hat{\theta}_1}{2} - \beta_1\hat{\rho}_2^{-1/2}\sin\frac{\hat{\theta}_2}{2}\right\} \qquad \text{II.34}$$

$$\tau_{xy} = \tau_{nn}\,\frac{h}{\tilde{g}}\beta_1\beta_2\left\{\hat{\rho}_1^{-1/2}\cos\frac{\hat{\theta}_1}{2} - \hat{\rho}_2^{-1/2}\cos\frac{\hat{\theta}_2}{2}\right\}$$

It is important to note that a limitation of the suggested solution is that, for a specific net section (2h), the notch opening angle (2α) is influenced by the notch root radius, as illustrated in the following expression:

$$2\alpha = 2\mathrm{Arctan}\,(\sqrt{\rho/h}) \qquad \text{II.35}$$

As indicated by equation II.35, substantial opening angles are correlated with either sizable notch root radii or constrained net sections exclusively.

2.3.2. Orthotropic plate weakened by a parabolic notch (blunt crack)

The problem of an orthotropic plate weakened by a parabolic notch (figure II.17) can be addressed taking advantage of the mapping function (Neuber[28]):

$$z = \xi^2 \qquad \text{II.36}$$

where z = x + iy and $\xi = u_0 + iv$.

The notch apex is at a distance equal to $\rho/2$ from the origin of the coordinate system, where ρ is the curvature radius at the tip (v=0).

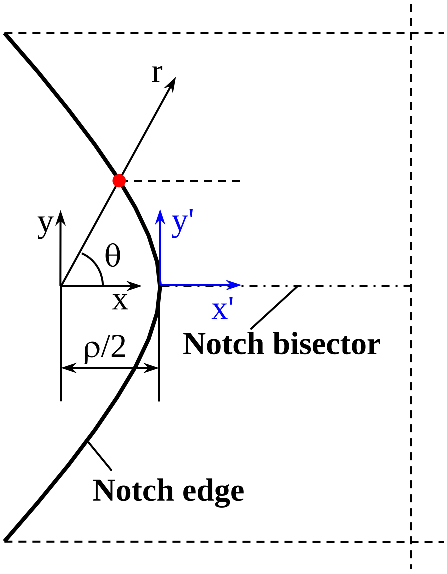

Figure II.17. Schematic of notch with a parabolic boundary as described by Eq. II.36, with the associated coordinate system.

Stress-free conditions on the notch boundary are guaranteed by the following complex functions:

$$\phi'_{H1}(z_1) = iA \cdot z_1^{-\frac{1}{2}} \qquad \phi'_{H2}(z_2) = -iA \cdot z_2^{-\frac{1}{2}} \tag{II.37}$$

where A is a real constant. Differently, z_j are complex variables defined as:

$$z_j = x_j + iy_j = r_j e^{i\theta_j} \tag{II.38}$$

where:

$$x_j = x' + \frac{\rho}{2}\beta_j^2 \qquad y_j = \beta_j y' \tag{II.39}$$

$$r_j = \sqrt{x_j^2 + y_j^2} \qquad \theta_j = \mathrm{Arg}(x_j + iy_j) \tag{II.40}$$

and x' and y' are the distances from the apex of the notch, as evaluated along the x and y directions.

Substituting Eq. II.37 into Eq. I.104 gives:

$$\begin{Bmatrix} \sigma_{xx} \\ \sigma_{yy} \\ \tau_{xy} \end{Bmatrix} = A \left\{ r_1^{-1/2} \begin{pmatrix} \beta_1^2 \sin\frac{\theta_1}{2} \\ -\sin\frac{\theta_1}{2} \\ \beta_1 \cos\frac{\theta_1}{2} \end{pmatrix} - r_2^{-1/2} \begin{pmatrix} \beta_2^2 \sin\frac{\theta_2}{2} \\ -\sin\frac{\theta_2}{2} \\ \beta_2 \cos\frac{\theta_2}{2} \end{pmatrix} \right\} \tag{II.41}$$

where A is a constant to determine, depending on the nominal applied stress, the geometry of the notched body and its elastic properties.

Accordingly, along the notch edge, the only non-vanishing stress turns out to be:

$$\sigma_{vv} = \frac{\sigma_{xx}+\sigma_{yy}}{2} - \frac{\sigma_{xx}-\sigma_{yy}}{2}\cos\theta - \tau_{xy}\sin\theta =$$
$$A r_1^{-1/2}\left\{\frac{1}{2}\left[\left(\beta_1^2-1\right)-\cos\theta\left(\beta_1^2+1\right)\right]\sin\frac{\theta_1}{2} - \beta_1\cos\frac{\theta_1}{2}\sin\theta\right\}$$
$$-A r_2^{-1/2}\left\{\frac{1}{2}\left[\left(\beta_2^2-1\right)-\cos\theta\left(\beta_2^2+1\right)\right]\sin\frac{\theta_2}{2} - \beta_2\cos\frac{\theta_2}{2}\sin\theta\right\} \qquad \text{II.42}$$

There are several ways to define parameter A:

1. As a function of the maximum shear stress along the bisector of the notch. When y'=0, equation (30) can be simplified as:

$$\tau_{xy} = A\left\{\frac{\beta_1}{\sqrt{2\frac{x'}{\rho}+\beta_1^2}} - \frac{\beta_2}{\sqrt{2\frac{x'}{\rho}+\beta_2^2}}\right\} \qquad \text{II.43}$$

From Eq. (32) it is possible to derive that:

$$A = \frac{\tau_{xy,max}}{\left\{\frac{\beta_1}{\sqrt{2\frac{\tilde{x}'}{\rho}+\beta_1^2}} - \frac{\beta_2}{\sqrt{2\frac{\tilde{x}'}{\rho}+\beta_2^2}}\right\}} = \frac{\tau_{xy,max}}{\tilde{\tau}_{xy,max}} \qquad \text{II.44}$$

where $\tilde{x}'$ represents the distance from the notch tip corresponding to the maximum value for the shear stress τ_{xy}, to be determined thanks to the following equation:

$$\partial_{x'}\left\{\frac{\beta_1}{\sqrt{2\frac{x'}{\rho}+\beta_1^2}} - \frac{\beta_2}{\sqrt{2\frac{x'}{\rho}+\beta_2^2}}\right\} = 0 \qquad \text{II.45}$$

2. It can be linked to the maximum value of the normal stress σ_{vv} along the notch boundary, where:

$$x' = \rho/2\left(\cos^{-2}\frac{\theta}{2} - 1\right) \qquad y' = \rho/2\sin^{-2}\frac{\theta}{2} \tag{II.46}$$

Accordingly:

$$A = \frac{\sigma_{vv,max}}{\tilde{\sigma}_{vv,max}} \tag{II.47}$$

where:

$$\begin{aligned}\tilde{\sigma}_{vv,max} = {} & \tilde{r}_1^{-1/2}\left\{\frac{1}{2}\left[\left(\beta_1^2 - 1\right) - \cos\tilde{\theta}\left(\beta_1^2 + 1\right)\right]\sin\frac{\tilde{\theta}_1}{2} - \beta_1\cos\frac{\tilde{\theta}_1}{2}\sin\tilde{\theta}\right\} \\ & - \tilde{r}_2^{-1/2}\left\{\frac{1}{2}\left[\left(\beta_2^2 - 1\right) - \cos\tilde{\theta}\left(\beta_2^2 + 1\right)\right]\sin\frac{\tilde{\theta}_2}{2} - \beta_2\cos\frac{\tilde{\theta}_2}{2}\sin\tilde{\theta}\right\}\end{aligned} \tag{II.48}$$

and $\tilde{\theta}$ is the solution of the following equation:

$$\left.\frac{\partial\sigma_{vv}}{\partial\theta}\right|_{\substack{x' = \rho/2\left(\cos^{-2}\frac{\theta}{2} - 1\right) \\ y' = \rho/2\sin^{-2}\frac{\theta}{2}}} = 0 \tag{II.49}$$

3. It can be linked to a generalized stress intensity factor, $K_{2\rho}$. Indeed, at a proper distance from the notch tip, Eq. II.43 simplifies to give:

$$\tau_{xy} = \frac{A\left(\beta_1 - \beta_2\right)}{\sqrt{2\frac{x'}{\rho}}} \tag{II.50}$$

At such a distance, the stress field of the blunt crack matches that the crack:

$$\tau_{xy} = \frac{K_{2\rho}}{\sqrt{2\pi x'}} \tag{II.51}$$

Equating Eq. II.51 and Eq. II.50 gives:

$$A = \frac{1}{\beta_1 - \beta_2}\frac{K_{2\rho}}{\sqrt{\pi\rho}} \tag{II.52}$$

Where $K_{2\rho}$ is the mode II generalised stress intensity factor for the orthotropic blunt crack.

Equating Eq. II.52 and Eq. II.44 or Eq. II.47 allows $K_{2\rho}$ to be expressed as a function of $\tau_{xy,max}$ or $\sigma_{vv,max}$:

$$K_{2\rho} = \frac{\beta_1 - \beta_2}{\tilde{\tau}_{xy,max}} \sqrt{\pi\rho} \cdot \tau_{xy,max} \tag{II.53}$$

$$K_{2\rho} = \frac{\beta_1 - \beta_2}{\tilde{\sigma}_{vv,max}} \sqrt{\pi\rho} \cdot \sigma_{vv,max} \tag{II.54}$$

2.3.3. Blunt notches with a generic opening angle

2.3.3.1. One term-based solution

Consider an orthotropic plate weaken by a radiused notch, the stress-strain relationships can be written according to I.49 and I.59. The edge of a blunt notch with a generic opening angle and curvature radius at its tip can be described using the mapping function described in chapter I.64:

$$z = \xi^q \tag{II.55}$$

where $z = x + iy$ and $\xi = u + iv$ and the notch edge is described by the equation $u = u_0$ (figure II.18)

Initially, for the sake of simplicity, the following one term based complex functions are proposed to address this problem:

$$\phi'_{H1}(z_1) = -iAz_1^{\lambda-1} \qquad \phi'_{H2}(z_2) = -iBz_2^{\lambda-1} \tag{II.56}$$

where A and B are real parameters, whereas $z_j = x_j + iy_j = r_j e^{i\theta_j}$ and:

$$x_j = x' + r_0\beta_j^t \qquad y_j = \beta_j y' \qquad r_j = \sqrt{\xi_j^2 + \eta_j^2} \qquad \theta_j = \mathrm{Arg}(\xi_j + i\eta_j) \tag{II.57}$$

In particular, $x'=x-r_0$ and $y'=y$ represent the distances from the apex of the notch, whilst t is a positive real number which is expected to depend on the notch angle and the material properties. Substituting Eqs. II.56 into Eqs. I.64 gives:

$$\sigma_{rr} = Ar_1^{\lambda-1}\left[k_{12}\cos(1-\lambda)\theta_1 - k_{11}\sin(1-\lambda)\theta_1\right] + Br_2^{\lambda-1}\left[k_{22}\cos(1-\lambda)\theta_2 - k_{21}\sin(1-\lambda)\theta_2\right]$$
$$\sigma_{\theta\theta} = Ar_1^{\lambda-1}\left[m_{12}\cos(1-\lambda)\theta_1 - m_{11}\sin(1-\lambda)\theta_1\right] + Br_2^{\lambda-1}\left[m_{22}\cos(1-\lambda)\theta_2 - m_{21}\sin(1-\lambda)\theta_2\right] \qquad \text{II.58}$$
$$\tau_{r\theta} = Ar_1^{\lambda-1}\left[n_{12}\cos(1-\lambda)\theta_1 - n_{11}\sin(1-\lambda)\theta_1\right] + Br_2^{\lambda-1}\left[n_{22}\cos(1-\lambda)\theta_2 - n_{21}\sin(1-\lambda)\theta_2\right]$$

Stresses in the (*u*,*v*) system can be determined assessed as (Lazzarin and Tovo[22]):

$$\sigma_{uu} = \frac{\sigma_{rr}+\sigma_{\theta\theta}}{2} + \frac{\sigma_{rr}-\sigma_{\theta\theta}}{2}\cos\frac{2\theta}{q} - \sigma_{r\theta}\sin\frac{2\theta}{q}$$
$$\sigma_{vv} = \frac{\sigma_{rr}+\sigma_{\theta\theta}}{2} - \frac{\sigma_{rr}-\sigma_{\theta\theta}}{2}\cos\frac{2\theta}{q} + \sigma_{r\theta}\sin\frac{2\theta}{q} \qquad \text{II.59}$$
$$\tau_{uv} = \frac{\sigma_{rr}-\sigma_{\theta\theta}}{2}\sin\frac{2\theta}{q} + \sigma_{r\theta}\cos\frac{2\theta}{q}$$

where, as mentioned before, $-\frac{\theta}{q}$ is the angle between the u and the r directions.

The free of stress conditions on the notch boundary read as:

$$\sigma_{uu}\big|_{u=u_0} = \tau_{uv}\big|_{u=u_0} = 0 \qquad \text{II.60}$$

Far from the notch tip, along the boundary, $\theta \approx \pm\gamma$ so that:

$$r_j \approx \sqrt{\left(x'\right)^2 + \left(\beta_j y'\right)^2} \cong r\sqrt{\cos^2\gamma + \left(\beta_j \sin\gamma\right)^2} = r \times \rho_j \qquad \text{II.61}$$

$$\theta_j \approx \mathrm{Arg}\left(\cos\gamma + i\beta_j\sin\gamma\right) = \theta_j(\gamma) \qquad \text{II.62}$$

Accordingly, Eq. II.60 can be re-written taking advantage of the following equations system:

$$\begin{pmatrix} b_{11} & b_{12} \\ b_{21} & b_{22} \end{pmatrix}\begin{Bmatrix} A \\ B \end{Bmatrix} = 0 \qquad \text{II.63}$$

where:

$$b_{11} = \rho_1^{\lambda-1}\left[m_{12}(\gamma)\cos(1-\lambda)\theta_1(\gamma) - m_{11}(\gamma)\sin(1-\lambda)\theta_1(\gamma)\right]$$
$$b_{12} = \rho_2^{\lambda-1}\left[m_{22}(\gamma)\cos(1-\lambda)\theta_2(\gamma) - m_{21}(\gamma)\sin(1-\lambda)\theta_2(\gamma)\right] \qquad \text{II.64}$$
$$b_{21} = \rho_1^{\lambda-1}\left[n_{12}(\gamma)\cos(1-\lambda)\theta_1(\gamma) - n_{11}(\gamma)\sin(1-\lambda)\theta_1(\gamma)\right]$$
$$b_{22} = \rho_2^{\lambda-1}\left[n_{22}(\gamma)\cos(1-\lambda)\theta_2(\gamma) - n_{21}(\gamma)\sin(1-\lambda)\theta_2(\gamma)\right]$$

Imposing Rouchè-Capelli conditions to the system in Eq. II.63, results in the following eigen-equation, which solved gives λ:

$$\begin{aligned}
&\cos(1-\lambda)\theta_2(\gamma)\left\{\cos(1-\lambda)\theta_1(\gamma)\left[m_{12}(\gamma)n_{22}(\gamma)-m_{22}(\gamma)n_{12}(\gamma)\right]-\right.\\
&\left.\sin(1-\lambda)\theta_1(\gamma)\left[m_{11}(\gamma)n_{22}(\gamma)-m_{22}(\gamma)n_{11}(\gamma)\right]\right\}-\\
&\sin(1-\lambda)\theta_2(\gamma)\left\{\cos(1-\lambda)\theta_1(\gamma)\left[m_{21}(\gamma)n_{12}(\gamma)-m_{12}(\gamma)n_{21}(\gamma)\right]-\right.\\
&\left.\sin(1-\lambda)\theta_1(\gamma)\left[m_{11}(\gamma)n_{21}(\gamma)-m_{21}(\gamma)n_{11}(\gamma)\right]\right\}=0
\end{aligned} \qquad \text{II.65}$$

Moreover, the following relationship between A and B holds valid:

$$B=-A\times\frac{\rho_1^{\lambda-1}(\gamma)\left[m_{12}(\gamma)\cos(1-\lambda)\theta_1(\gamma)-m_{11}(\gamma)\sin(1-\lambda)\theta_1(\gamma)\right]}{\rho_2^{\lambda-1}(\gamma)\left[m_{22}(\gamma)\cos(1-\lambda)\theta_2(\gamma)-m_{21}(\gamma)\sin(1-\lambda)\theta_2(\gamma)\right]}=A\times\chi_{12} \qquad \text{II.66}$$

Eq. II.65 exactly equates the eigen-equation associated to pointed V-notch case with the same notch angle (Zappalorto and Carraro[39]).

At the apex of the notch (x'=y'=0), the condition $\sigma_{uu}\big|_{u=u_0}=0$ is guaranteed by symmetry, whereas the condition $\tau_{uv}\big|_{u=u_0}=0$ requires that:

$$t=\frac{1-\dfrac{Ln(-\chi)}{Ln(\beta_1/\beta_2)}}{1-\lambda} \qquad \text{II.67}$$

Thanks to Eq. II.66, Eqs. II.58 can be re-arranged in the following form:

$$\begin{aligned}
\sigma_{rr}&=Ar_1^{\lambda-1}\left[k_{12}\cos(1-\lambda)\theta_1-k_{11}\sin(1-\lambda)\theta_1\right]+\chi_{12}r_2^{\lambda-1}\left[k_{22}\cos(1-\lambda)\theta_2-k_{21}\sin(1-\lambda)\theta_2\right]\\
\sigma_{\theta\theta}&=Ar_1^{\lambda-1}\left[m_{12}\cos(1-\lambda)\theta_1-m_{11}\sin(1-\lambda)\theta_1\right]+\chi_{12}r_2^{\lambda-1}\left[m_{22}\cos(1-\lambda)\theta_2-m_{21}\sin(1-\lambda)\theta_2\right]\\
\tau_{r\theta}&=Ar_1^{\lambda-1}\left[n_{12}\cos(1-\lambda)\theta_1-n_{11}\sin(1-\lambda)\theta_1\right]+\chi_{12}r_2^{\lambda-1}\left[n_{22}\cos(1-\lambda)\theta_2-n_{21}\sin(1-\lambda)\theta_2\right]
\end{aligned} \qquad \text{II.68}$$

As previously explained in the context of the parabolic notch, parameter A can be formulated based on the maximum shear stress along the notch bisector, the maximum principal stress along the notch edge, or as a function of the mode II Generalized Stress Intensity Factor.

2.3.3.2. Improved solution with additional terms

The single-term solution presented in the preceding section is advantageous for its simplicity and ease of use. However, its accuracy was found to be insufficient when $\lambda < 1$, particularly when the material exhibits high stiffness in the x-direction. To enhance the precision of the analytical solution, a novel approach is introduced here. This approach involves employing complex potentials with multiple terms and utilizing an optimization algorithm for refining the boundary conditions. This combination aims to achieve an optimal balance between solution accuracy and simplicity. In this regard, the complex potentials are selected in the following form:

$$\phi'_{H1}(z_1) = -iAz_1^{\lambda-1} - iCz_1^{\mu-1} \qquad \phi'_{H2}(z_2) = -iBz_2^{\lambda-1} - iDz_2^{\mu-1} - iEz_2^{\zeta-1} \tag{II.69}$$

where all the complex variables defined in the previous section hold valid, and A, B, C, D, E, λ, μ, ζ are real constants and, by hypothesis, $\zeta < \mu < \lambda$. Substituting Eq. II.69 into Eq. I.64 and extracting the real parts of the obtained expressions, allows the following equations for the stress components to be derived:

$$\begin{aligned}\sigma_{rr} = A\Big\{ & r_1^{\lambda-1}\left[k_{12}\cos(1-\lambda)\theta_1 - k_{11}\sin(1-\lambda)\theta_1\right] + \chi_{12} r_1^{\mu-1}\left[k_{12}\cos(1-\mu)\theta_1 - k_{11}\sin(1-\mu)\theta_1\right] + \\ & + \chi_{21} r_2^{\lambda-1}\left[k_{22}\cos(1-\lambda)\theta_2 - k_{21}\sin(1-\lambda)\theta_2\right] + \chi_{22} r_2^{\mu-1}\left[k_{22}\cos(1-\mu)\theta_2 - k_{21}\sin(1-\mu)\theta_2\right] + \\ & + \chi_{23} r_2^{\zeta-1}\left[k_{22}\cos(1-\zeta)\theta_2 - k_{21}\sin(1-\zeta)\theta_2\right]\Big\}\end{aligned} \tag{II.70}$$

$$\begin{aligned}\sigma_{\theta\theta} = A\Big\{ & r_1^{\lambda-1}\left[m_{12}\cos(1-\lambda)\theta_1 - m_{11}\sin(1-\lambda)\theta_1\right] + \chi_{12} r_1^{\mu-1}\left[m_{12}\cos(1-\mu)\theta_1 - m_{11}\sin(1-\mu)\theta_1\right] + \\ & + \chi_{21} r_2^{\lambda-1}\left[m_{22}\cos(1-\lambda)\theta_2 - m_{21}\sin(1-\lambda)\theta_2\right] + \chi_{22} r_2^{\mu-1}\left[m_{22}\cos(1-\mu)\theta_2 - m_{21}\sin(1-\mu)\theta_2\right] + \\ & + \chi_{23} r_2^{\zeta-1}\left[m_{22}\cos(1-\zeta)\theta_2 - m_{21}\sin(1-\zeta)\theta_2\right]\Big\}\end{aligned} \tag{II.71}$$

$$\begin{aligned}\tau_{r\theta} = A\Big\{ & r_1^{\lambda-1}\left[n_{12}\cos(1-\lambda)\theta_1 - n_{11}\sin(1-\lambda)\theta_1\right] + + \chi_{12} r_1^{\mu-1}\left[n_{12}\cos(1-\mu)\theta_1 - n_{11}\sin(1-\mu)\theta_1\right] \\ & + \chi_{21} r_2^{\lambda-1}\left[n_{22}\cos(1-\lambda)\theta_2 - n_{21}\sin(1-\lambda)\theta_2\right] + + \chi_{22} r_2^{\mu-1}\left[n_{22}\cos(1-\mu)\theta_2 - n_{21}\sin(1-\mu)\theta_2\right] + \\ & + \chi_{23} r_2^{\zeta-1}\left[n_{22}\cos(1-\zeta)\theta_2 - n_{21}\sin(1-\zeta)\theta_2\right]\Big\}\end{aligned} \tag{II.72}$$

where:

$$\chi_{12} = \frac{C}{A}; \qquad \chi_{21} = \frac{B}{A}; \qquad \chi_{22} = \frac{D}{A}; \qquad \chi_{23} = \frac{E}{A} \tag{II.73}$$

$$\zeta < \mu < \lambda \qquad 0.5 < \lambda \qquad Abs(\chi_{12}) \neq 0 \tag{II.74}$$

$$Abs(\chi_{12}) \neq Abs(\chi_{21}) \neq Abs(\chi_{22}) \neq Abs(\chi_{23}) \tag{II.75}$$

As previously mentioned, parameter A can be defined based on the maximum shear stress along the notch bisector, the maximum principal stress along the notch edge, or as a function of a mode II Generalized Stress Intensity Factor. The stress components in the curvilinear coordinate system (u,v) can be established using Equation II.59.

The eigenvalue λ has been calculated solving Eq. II.65 as for the one term potentials solution above presented. The remaining 7 constants have been determined approximating the free-of-stress conditions, $\sigma_{uu}\big|_{u=u_0} = \tau_{uv}\big|_{u=u_0} = 0$, using the Maclaurin expansions of σ_{uu} and τ_{uv} and setting to zero the terms of the series expansions:

$$\begin{array}{ll}
\tau_{uv}(\theta)\Big|_{\theta=0} = 0 & \left.\dfrac{\partial\ \sigma_{uu}(\theta)}{\partial\theta}\right|_{\theta=0} = 0 \\
\left.\dfrac{\partial^2\tau_{uv}(\theta)}{\partial\theta^2}\right|_{\theta=0} = 0 & \left.\dfrac{\partial^3\sigma_{uu}(\theta)}{\partial\theta^3}\right|_{\theta=0} = 0 \\
\left.\dfrac{\partial^4\tau_{uv}(\theta)}{\partial\theta^4}\right|_{\theta=0} = 0 & \left.\dfrac{\partial^5\sigma_{uu}(\theta)}{\partial\theta^5}\right|_{\theta=0} = 0 \\
\left.\dfrac{\partial^6\tau_{uv}(\theta)}{\partial\theta^6}\right|_{\theta=0} = 0 &
\end{array} \tag{II.76}$$

Such an approach was introduced, for the first time by Lazzarin and Tovo[22].

Conditions given by Eq. II.76 form a non-linear system of equations, and has been solved numerically using the Newton-Rhapson method for different starting points in the 7-D space {t, μ, ζ, $\chi_{12}, \chi_{21}, \chi_{22}, \chi_{23}$}.

It is worth noting that, given the approximate nature of such an approach, the solution is not unique, and among all the possible numerical solutions satisfying Eq. II.76, that minimizing the residual stress components $\sigma_{uu}\big|_{u=u_0}$ and $\tau_{uv}\big|_{u=u_0}$ is chosen. To this end the following objective function has been minimized:

$$F=\sum_{n=0}^{N}\sqrt{\left[\tau_{uv}\Big|_{\substack{u=u_0\\ v=v_n}}\right]^2+\left[\sigma_u\Big|_{\substack{u=u_0\\ v=v_n}}\right]^2} \quad \text{with } 0<v_n<v_{n+1} \text{ and } n\in\{1;2;...;N\} \qquad \text{II.77}$$

where v_n is the point of the curve $u=u_0$ associated to a certain angle θ_n, $N=10$, $\theta_0=0°$ and $\theta_n=\frac{\gamma}{(N+1)}*n$. To expedite the process further, it is feasible to confine the 7-dimensional region from which starting points for the Newton method are selected. This confinement involves limiting the region to a 7-dimensional sphere cantered at the origin with a radius of 1, where the final solution is anticipated. Additionally, the Euclidean distance between the current starting point and the previous ones is mandated to be greater than 0.1. If no viable solution is identified under these search parameters, it is plausible to increase the radius of the 7-dimensional sphere or decrease the minimum distance between starting points. However, in all cases examined in this study, a radius of 1 and a distance of 0.1 proved sufficient for obtaining an appropriate solution.

In summary the steps taken to determine the 8 constants: t, λ, μ, ζ, χ_{12}, χ_{21}, χ_{22}, χ_{23}, are summarised here below:

1) Calculate λ solving equation II.65.
2) Choose a starting point for the Newton method in a 7-D sphere centred at the origin of the space {t, μ, ζ, χ_{12}, χ_{21}, χ_{22}, χ_{23}};
3) Solve system (59) using Newton method and the starting point previously chosen;
4) Check if the solution found respect the basic imposition: $\zeta<\mu<\lambda$ and $0.5<\lambda$; and for notch opening angles greater than 0, $Abs(\chi_{12})\neq Abs(\chi_{21})\neq Abs(\chi_{22})\neq Abs(\chi_{23})$, $Abs(\chi_{12})\neq 0$. If the solution is not compatible restart from point 2) choosing a different starting point;

5) Calculate the optimizing function F. If $F \approx 0$ the algorithm ends and this is the solution found, otherwise return to step 2) choosing a different starting point.

2.3.4. Discussion and comparison with numerical results

To assess the precision of the newly developed solutions, several numerical analyses were conducted and directly juxtaposed with the stress field results obtained from the new equations. To achieve this, three distinct materials were taken into consideration:

1) **Material 1** with the following properties: E_x=160 GPa, E_y=10 GPa, G_{xy}=5 GPa, $\nu_{\xi\psi}$=0.30 so that β_1=0.7198, β_2=5.5572;
2) **Material 2** with the following properties: E_x=10 GPa, E_y=160 GPa, G_{xy}=5 GPa, ν_{xy}=0.01875 so that β_1=0.1799, β_2=1.3893;
3) **Material 3** with the following properties: E_x=10 GPa, E_y=10 GPa, G_{xy}=3.846 GPa, ν_{xy}=0.3 so that β_1=0.9904, β_2=1.0095;

The analyses were carried out on plates under in-plane shear weakened by central holes (see the schematic in figure 4) with a profile described according to Eq. II.25, II.36 and II.55.

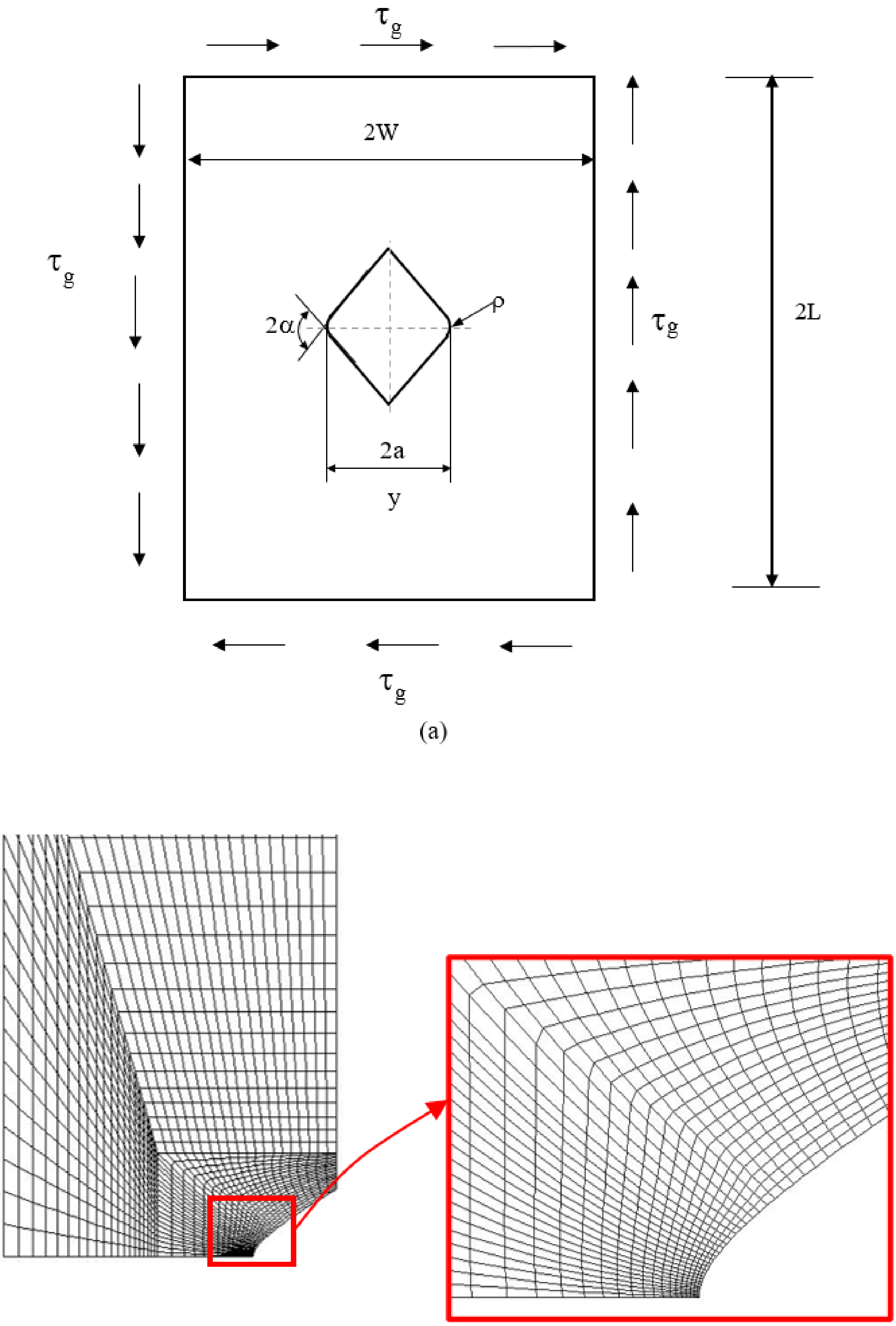

(a)

(b)

Figure II.18. Numerical investigations: schematic of a plate with a hyperbolic or parabolic hole under in-plane shear analysed in this work(a); examples of the FE models used to analyse hyperbolic notches (one quarter of the entire plate and details of the notch tip) (b).

A summary of the geometry analysed is reported in table II.4, whereas a summary of the main stress field parameters for the analysed geometries and materials is reported in table II.5.

Geometry	Contraction	Net ligament (mm)	Notch depth (mm)	Notch root radius (mm)	Notch angle (°)
Central hole with a hyperbolic profile defined according to Eq. II.25	G1	30	90	10	90
Central hole with a parabolic profile defined according to Eq. II.36	G2	90	10	1.25	0
Central hole with a hyperbolic profile defined according to Eq. II.55	G3	90	10	1.25	45
Central hole with a hyperbolic profile defined according to Eq. II.55	G4	90	10	1.25	90
Central hole with a hyperbolic profile defined according to Eq. II.55	G5	90	10	1.25	135

Table II.4. Summary of the geometries studied

Geometry	Material	A ($MPa\ mm^{(1-\lambda)}$)	λ	μ	ζ	t	χ_{12} ($mm^{(\lambda-\mu)}$)	χ_{21}	χ_{22} ($mm^{(\lambda-\mu)}$)	χ_{23} ($mm^{(\lambda-\zeta)}$)
G3	M1	-2.5501	0.883125	0.436509	-3.77389	1.76709	0.232286	-0.2636	-0.03374	-70.2644
G3	M2	-10.065	0.615966	0.437396	-1.51039	1.91219	0.591025	-1.2279	-0.05245	-0.00631
G3	M3	-0.0658	0.659691	0.416372	0.14443	1.67624	0.13761	-0.998	-0.1354	0.002903
G4	M1	0.0178901	1.1329	/	/	3.12311	/	-0.0554	/	/
G4	M2	-6.63265	0.764813	0.465017	-1.84467	1.7738	0.69392	-0.8623	-0.11115	-0.00118
G4	M3	-0.02197	0.908494	0.514887	0.354236	1.40725	0.055617	-0.9862	-0.05498	0.001425
G5	M1	0.005674	1.44127	/	/	2.68283	/	-0.0115	/	/
G5	M2	-0.1282	0.982278	0.447172	0.340341	1.51223	0.010947	-0.1474	-0.0025	0.001192
G5	M3	0.0004264	1.30203	/	/	2.6699	/	-0.9660	/	/

Table II.5. summary of the stress fields parameters to be used in Eq. II.70-72 for the geometries and the materials under investigation.

Finite Element (FE) analyses were conducted using the Ansys® version 19 software package. Parabolic isoparametric elements (PLANE183 in ANSYS) were employed, and the analyses utilized very fine meshes, particularly near the apex of the notch, with element sizes approximately equal to $\rho/50$ for enhanced accuracy in the results.

In Ansys, parabolic and hyperbolic notch profiles were generated by importing numerous keypoints (ranging from 100 to 200, depending on the specific geometry) aligned along the mathematical curve describing the notch. Each pair of keypoints was connected with a spline, accurately reproducing the notch boundary in the FE code. An illustration of the FE models and mesh patterns is presented in Figure II.18.

Theoretical results (lines) were compared with numerical results (symbols) in Figures II.19-26 and Figures II.28-31. Specifically, Figure 5 displays stress fields along the bisector of a hyperbolic notch, as described by Eq. II.25, for different materials, while Figure II.20 presents the shear stress distribution along the bisector of a parabolic notch. In both cases, there is noteworthy agreement between the analytical solutions and the numerical results. Although the solutions are exact for infinitely deep notches from a purely mathematical perspective, the developed analytical frameworks prove effective even for notches with finite depths.

Figures 5 and 6 also reveal that increasing material stiffness in the direction normal to the notch bisector line leads to a maximum shear stress value located closer to the notch tip. Conversely, solutions proposed for blunt notches with a non-zero opening angle, as described by Eq. II.55, are not exact. For this scenario, a comprehensive study was conducted, considering various notch opening angles for all materials. Stresses were evaluated not only along the notch bisector line but also along the notch edge and on circular paths of different radii cantered on the origin of the coordinate system used for stress distributions (see Figure II.27).

It is essential to note that when the linear elastic eigenvalue λ exceeds 1, the solution based on a single-term complex potential (Eq. II.58) is sufficiently accurate. However, when λ is less than 1, the solution given by Eq. 70-72, based on three-term complex potentials, was employed to enhance accuracy. Figures II.21-26 and II.28-31 present an explicit comparison between the analytical solutions and a substantial set of numerical results, demonstrating the high accuracy of the proposed analytical solutions.

Specifically, the results for the mode II stress components τ_{xy} assessed along the bisector of hyperbolic notches with opening angles of $2\alpha = 45°$, $90°$, and $135°$ are depicted in Figures II.21, II.22, and II.23, respectively. These figures reveal a strong agreement between the proposed analytical solutions and numerical results. Similar to the observations for the parabolic notch, hyperbolic notches with a non-zero opening angle exhibit an increased maximum shear stress closer to the notch apex with higher material stiffness in the direction normal to the notch bisector line.

Furthermore, for the material configurations explored, it is noteworthy that only when $2\alpha = 45°$ is the linear elastic eigenvalue λ consistently less than 1 (refer to Figure II.21 and Table II.5), irrespective of the material. In contrast, for larger angles, λ remains below 1 only when the material demonstrates sufficient stiffness in the direction normal to the notch bisector line.

Figures II.24-26 illustrate the distribution of the maximum principal stress along the notch edge for various opening angles and materials. Several observations can be made:

- For a given material configuration, a smaller notch angle corresponds to a higher stress concentration along the edge.
- Increasing the notch opening angle, for a given material, results in the maximum principal stress location along the notch edge moving away from the notch tip.
- For a given notch opening angle, the stiffer the material in the direction normal to the notch bisector line, the higher the stress concentration.

Lastly, stress components evaluated along circular paths cantered at (x=0, y=0) are presented in Figures II.28-31 for different materials and geometries. In all cases, the analytical solution demonstrates noteworthy accuracy.

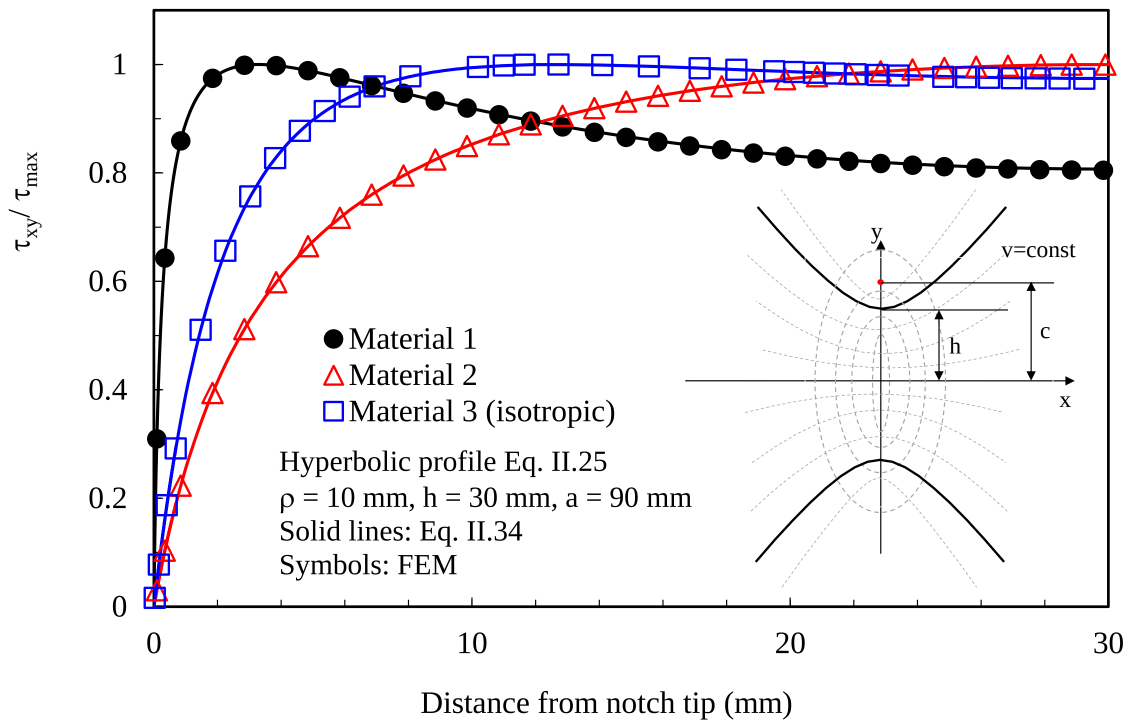

Figure II.19. Normalised stress component τ_{xy} as assessed on the bisector of a notch with a hyperbolic boundary under shear (mode II). Results from Eq. II.34 compared to Finite Element results. Different materials. Notch depth a=90 mm, notch root radius ρ=10 mm, net ligament 2h=60 mm.

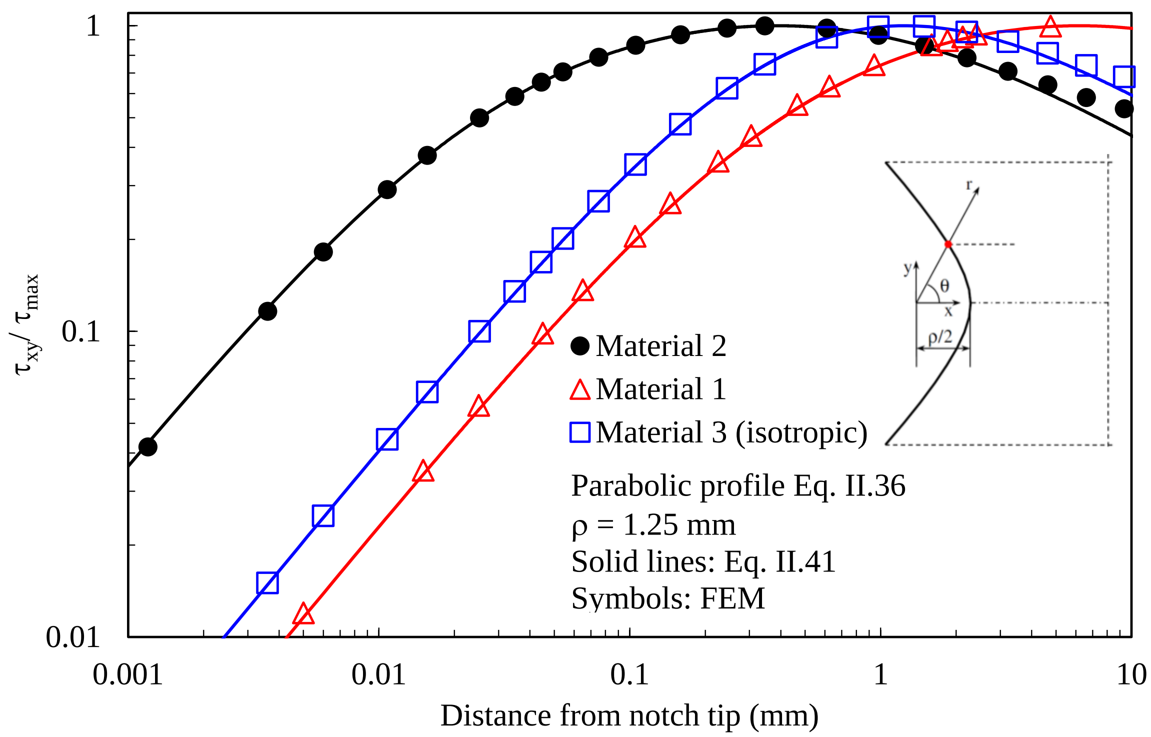

Figure II.20. Normalised stress component τ_{xy} as assessed on the bisector of a notch with a parabolic boundary under shear (mode II). Results from Eq. II.41 compared to Finite Element results. Different materials. Notch depth a=10 mm, notch root radius ρ=1.25 mm, gross ligament 2W=200 mm.

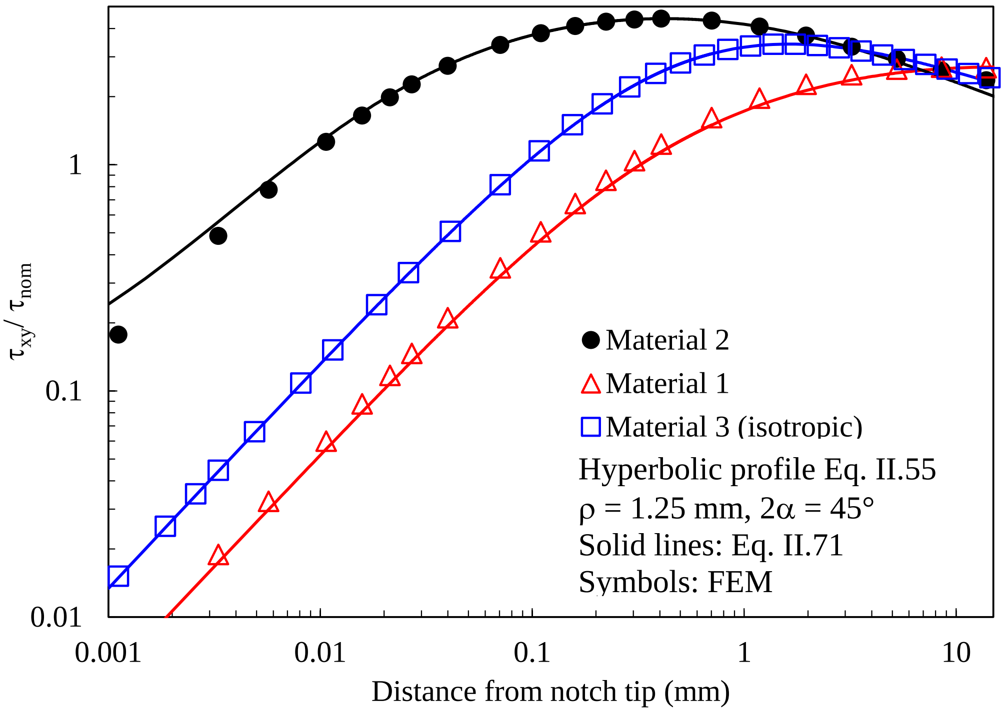

Figure II.21. Normalised stress component τ_{xy} as assessed on the bisector of a notch with a hyperbolic boundary with 2α=45°, Eq. II.55, under shear (mode II). Results from Eq. II.71 compared to Finite Element results. Different materials. Notch depth a=10 mm, notch root radius ρ=1.25 mm, gross ligament 2W=200 mm.

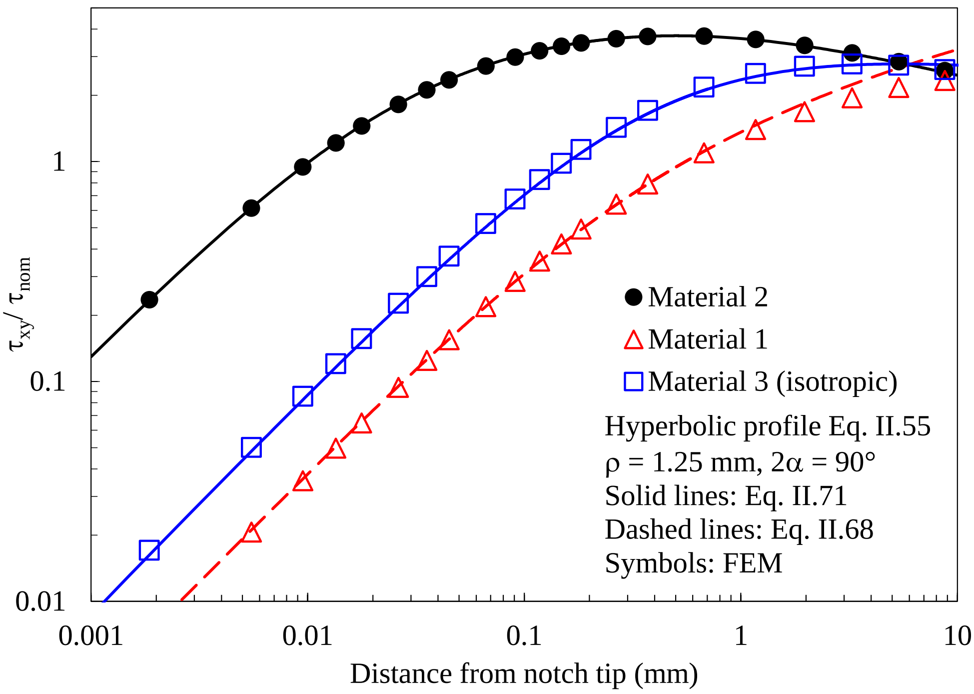

Figure II.22. Normalised stress component τ_{xy} as assessed on the bisector of a notch with a hyperbolic boundary with 2α=90°, Eq. II.55, under shear (mode II). Results from Eq. II.68 and II.71 compared to Finite Element results. Different materials. Notch depth a=10 mm, notch root radius ρ=1.25 mm, gross ligament 2W=200 mm.

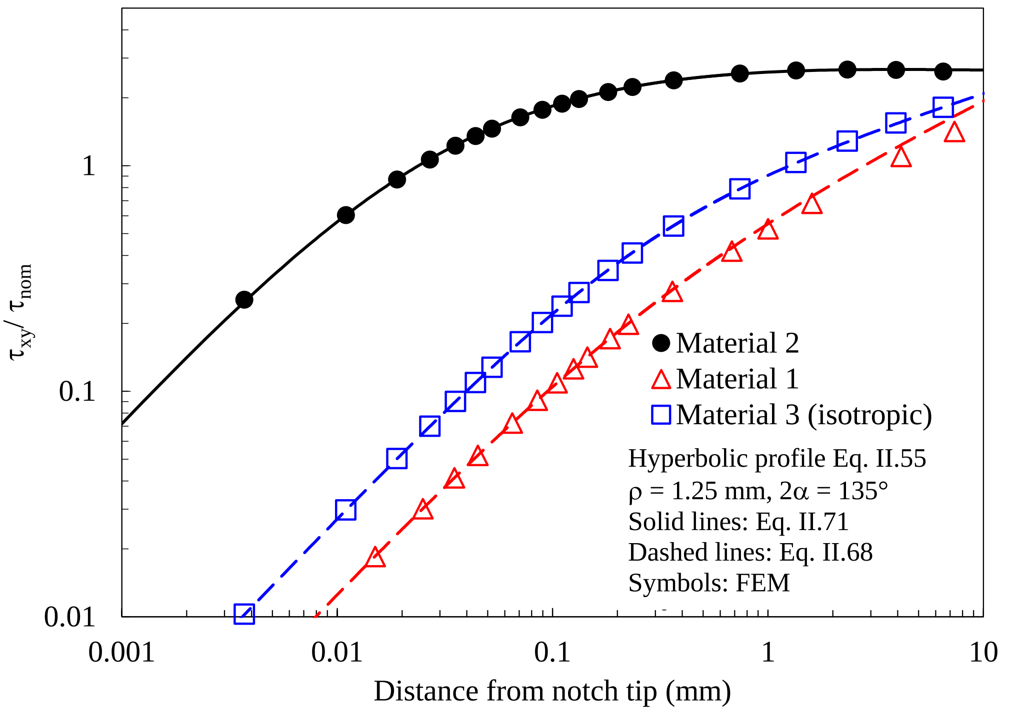

Figure II.23. Normalised stress component τ_{xy} as assessed on the bisector of a notch with a hyperbolic boundary with 2α=135°, Eq. II.55, under shear (mode II). Results from Eq. II.68 and II.71 compared to Finite Element results. Different materials. Notch depth a=10 mm, notch root radius ρ=1.25 mm, gross ligament 2W=200 mm.

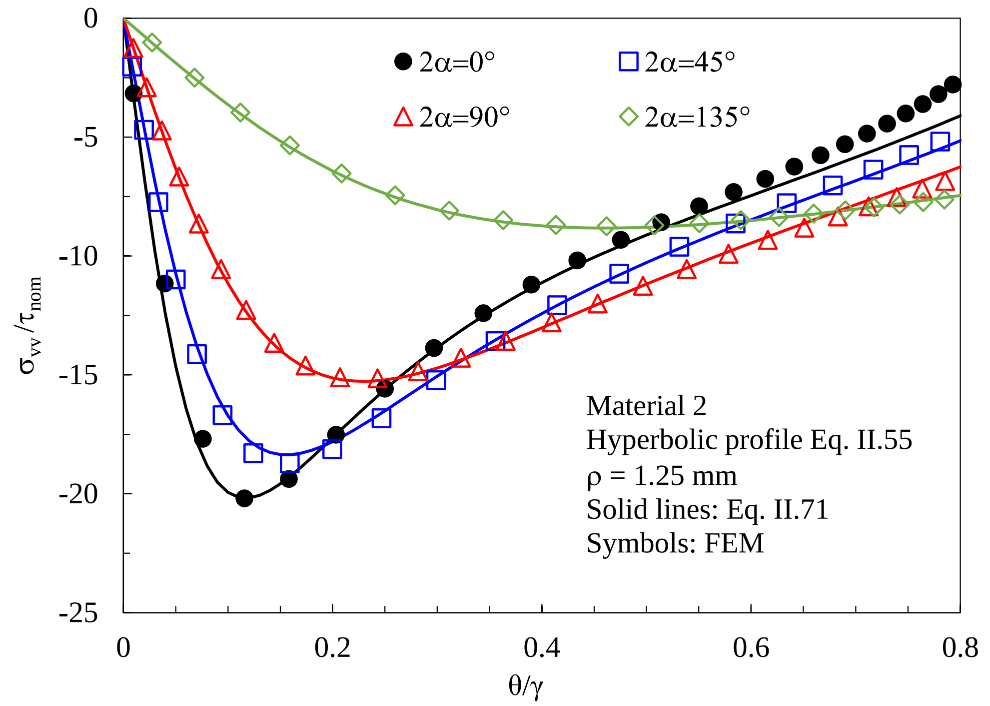

Figure II.24. Normalised stress component σ_{vv} (maximum principal stress) as assessed on the edge of a notch with a hyperbolic boundary, Eq. II.55, under shear (mode II). Results from Eq. II.71 compared to Finite Element results. Material 2, different notch opening angles. Notch depth a=10 mm, notch root radius ρ=1.25 mm, gross ligament 2W=200 mm.

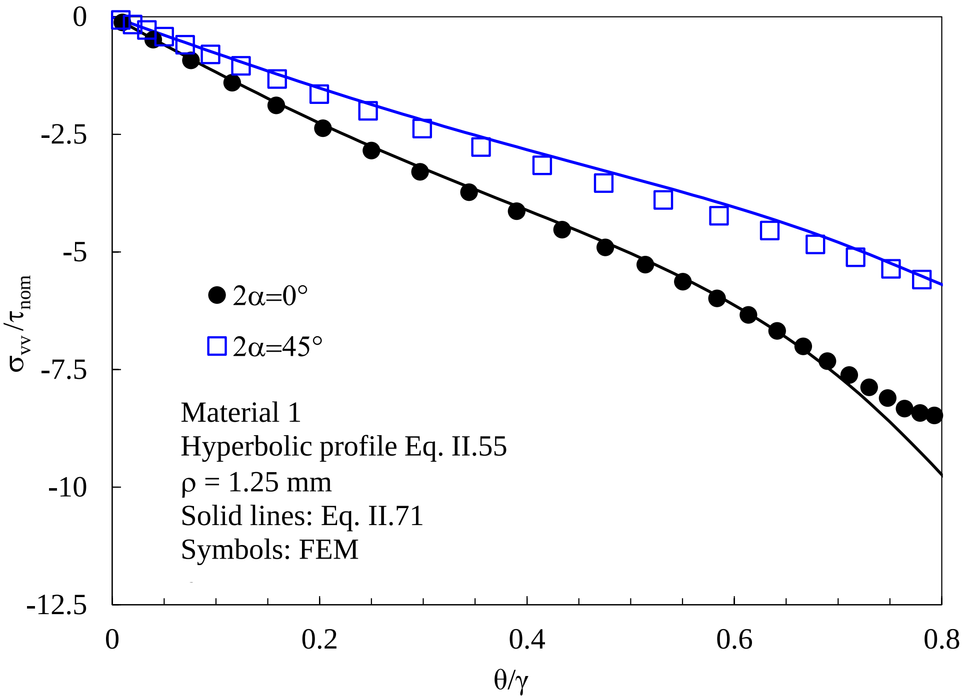

Figure II.25. Normalised stress component σ_{vv} (maximum principal stress) as assessed on the edge of a notch with a hyperbolic boundary, Eq. II.55, under shear (mode II). Results from Eq. II.71 compared to Finite Element results. Material 1, different notch opening angles. Notch depth a=10 mm, notch root radius ρ=1.25 mm, gross ligament 2W=200 mm.

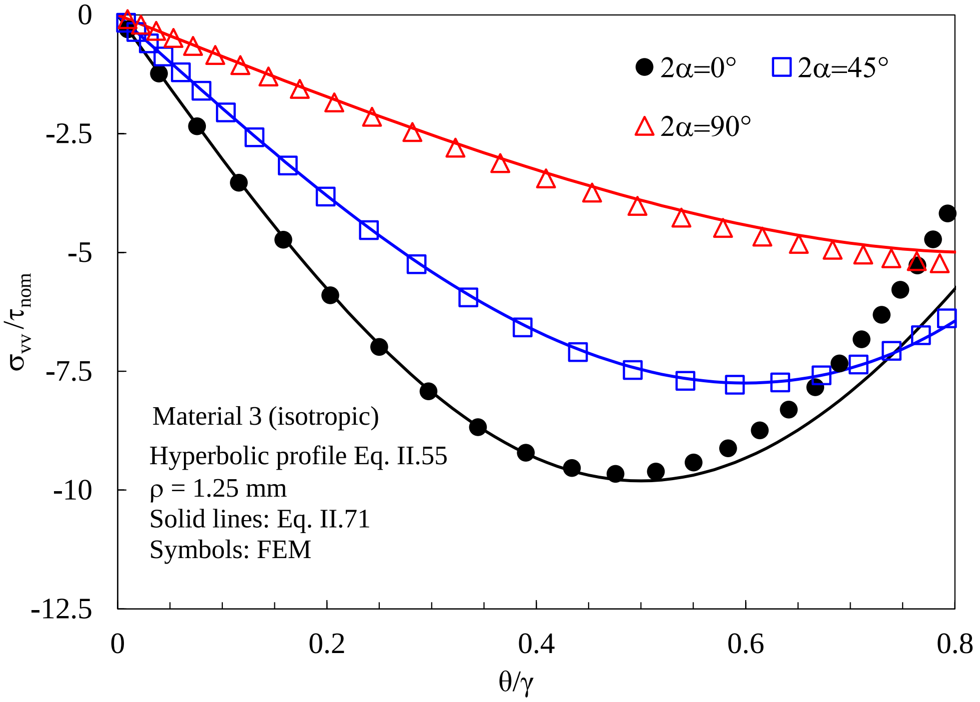

Figure II.26. Normalised stress component σ_{vv} (maximum principal stress) as assessed on the edge of a notch with a hyperbolic boundary, Eq. II.55, under shear (mode II). Results from Eq. II.71 compared to Finite Element results. Material 3, different notch opening angles. Notch depth a=10 mm, notch root radius ρ=1.25 mm, gross ligament 2W=200 mm.

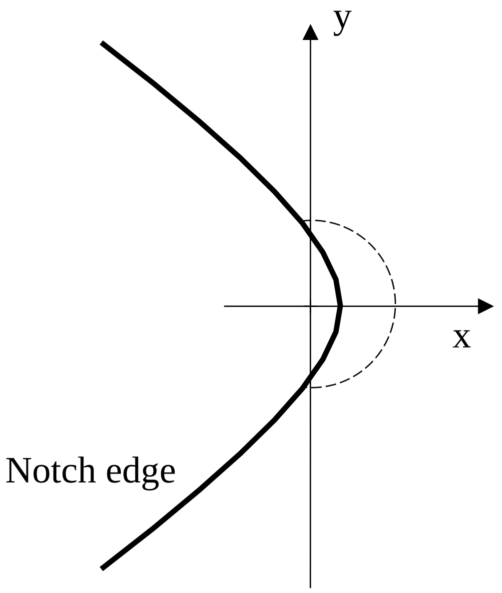

Figure II.27. Circular path along which stress components have been evaluated. The path is centred at the origin of the coordinate system used for Eq. II.68 and II.71.

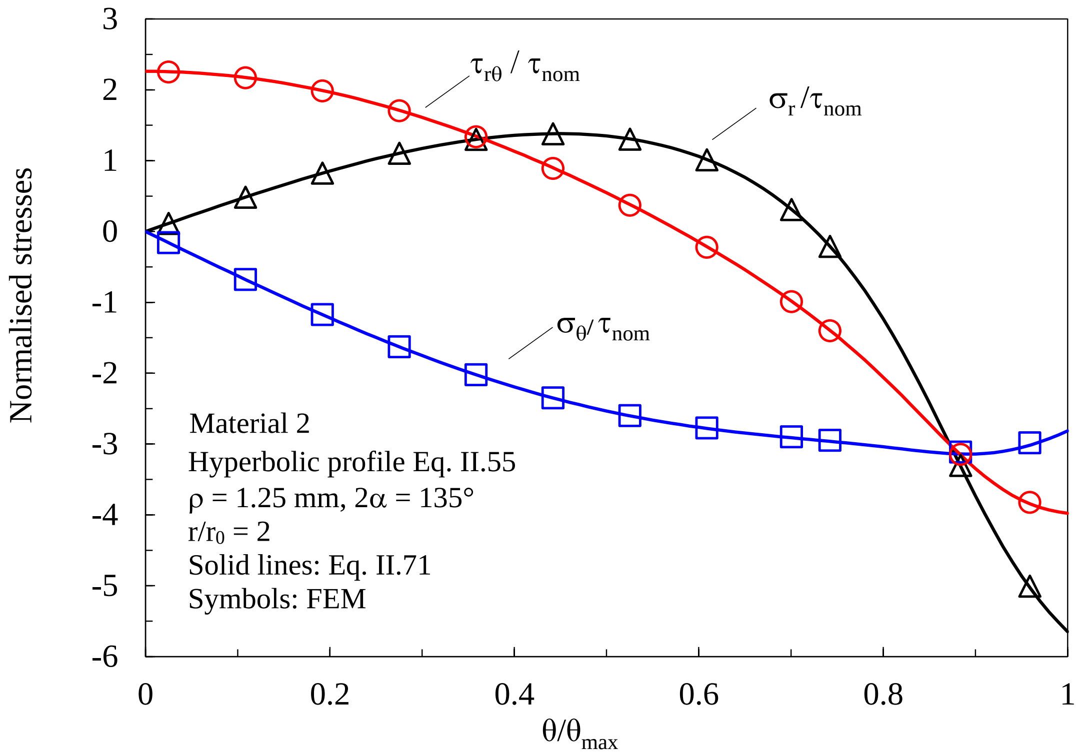

Figure II.28. Normalised stress components as evaluated along a circular path (see figure II.27). Comparison between Eq. II.71 and numerical results. Material 2, 2α=135°, path of radius r/r_0=2. Notch depth a=10 mm, notch root radius ρ=1.25 mm, gross ligament 2W=200 mm.

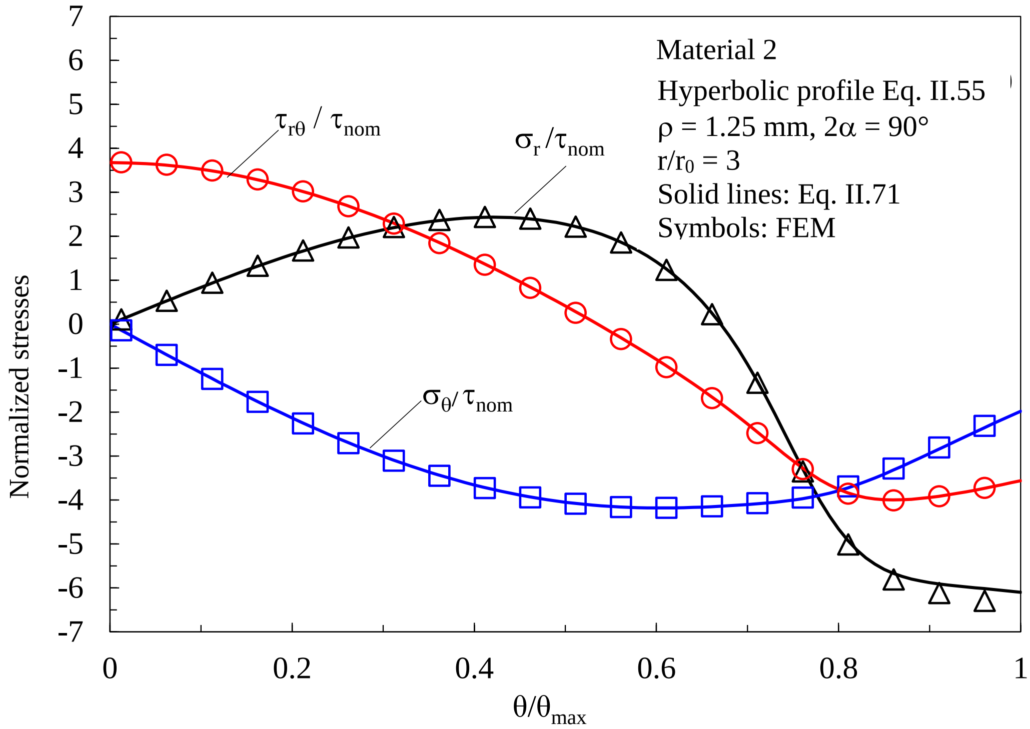

Figure II.29. Normalised stress components as evaluated along a circular path (see figure II.27). Comparison between Eq. II.71 and numerical results. Material 2, 2α=90°, path of radius r/r_0=3. Notch depth a=10 mm, notch root radius ρ=1.25 mm, gross ligament 2W=200 mm.

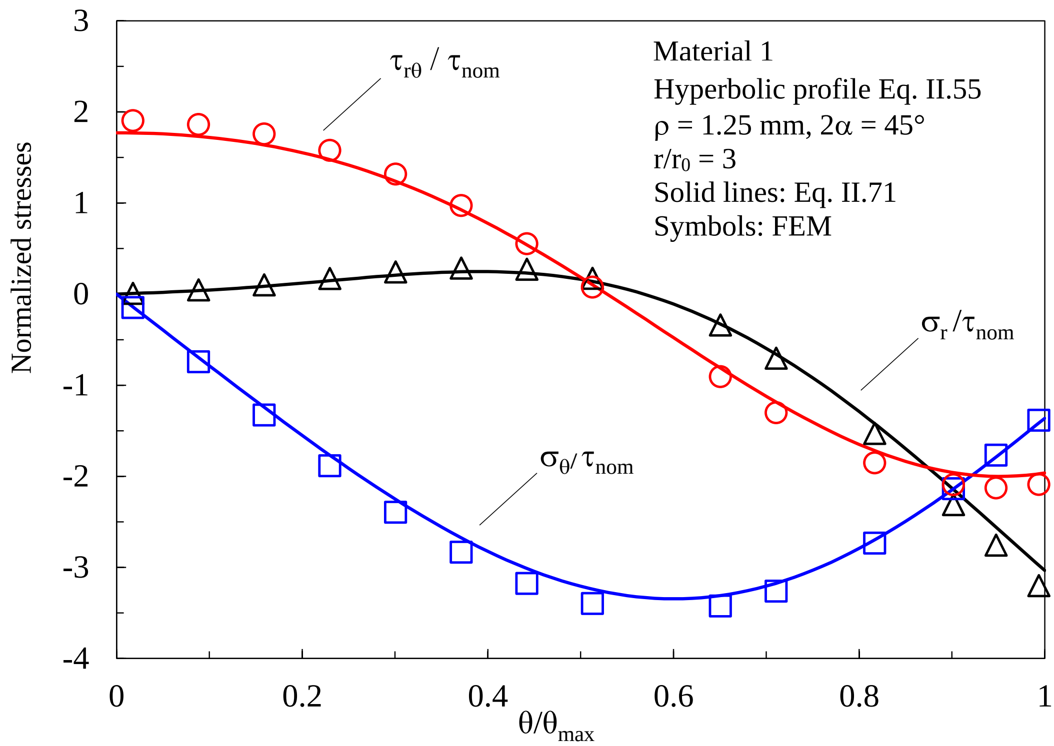

Figure II.30. Normalised stress components as evaluated along a circular path (see figure II.27). Comparison between Eq. II.71 and numerical results. Material 1, 2α=45°, path of radius r/r_0=3. Notch depth a=10 mm, notch root radius ρ=1.25 mm, gross ligament 2W=200 mm.

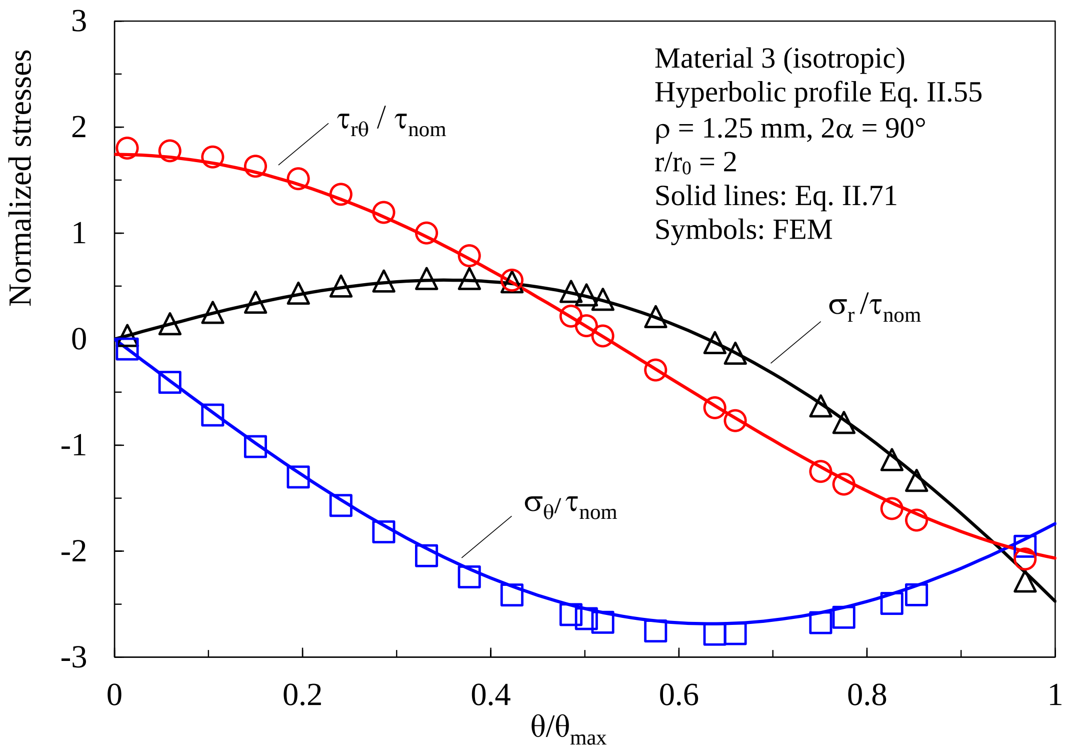

Figure II.31. Normalised stress components as evaluated along a circular path (see figure II.27). Comparison between Eq. II.71 and numerical results. Material 3, 2α=45°, path of radius r/r_0=2. Notch depth a=10 mm, notch root radius ρ=1.25 mm, gross ligament 2W=200 mm.

2.3.5. Conclusions

This chapter undertakes a comprehensive examination of stress distributions in orthotropic solids with blunted notches subjected to in-plane shear loading. Employing Lekhnitskii's approach, a new closed-form equations for stress components was developed. These equations consider the influence of notch radius, opening angle, and elastic material properties. The analysis encompasses three different notch boundary shapes:

- Symmetric deep hyperbolic notches in plates loaded under in-plane shear, for which an exact solution is presented in this work.
- Deep parabolic notches in plates loaded under in-plane shear, for which an exact solution is derived in this work.

- Deep hyperbolic-like notches in plates loaded under in-plane shear. In this case, the solution, obtained in this work by invoking free-of-stress boundary conditions along the notch edge, is approximate but highly accurate.

For each case, analytical expressions for the entire stress fields have been formulated and validated against a comprehensive set of finite element analyses. The key conclusions drawn from the numerical results can be summarized as follows:

- Generally, there is a notable agreement between the analytical solutions and numerical results.
- Higher material stiffness in the direction normal to the notch bisector line leads to increased stress concentration and a maximum stress value closer to the notch apex, both along the notch bisector line and along the notch edge.
- For a given material, the location of the maximum principal stress along the notch edge shifts away from the notch tip with an increase in the notch opening angle.

The derived equations can be effectively employed to characterize mode II stress distributions near notches in orthotropic solids or orthotropic laminated composites, provided homogenized elastic properties are used and the condition $\left(2S_{12}+S_{66}\right)^2 \geq 4S_{11}S_{22}$ is met.

2.4. References

1. Ayatollahi MR, Berto F., Campagnolo A, Gallo P, Tange K., 2017. "Review of local strain energy density theory for the fracture assessment of V-notches under mixed mode loading." Eng Solid Mech 5, 113-132.

2. Berto F., Gomez J., 2017. "Notched plates in mixed mode loading (I+II): a review based on the local strain energy density and the cohesive zone mode." Eng Solid Mech, 5(1), 1-8

3. Berto, F., Lazarin, P., Radaj, D., 2008. "Fictitious notch rounding concept applied to sharp V-notches: Evaluation of the microstructural support factor for different failure hypotheses. Part I: Basic stress equations." Eng. Fract. Mech. 75, 3060-3072. https://doi.org/10.1016/j.engfracmech.2008.01.015

4. Bonora N, Costanzi M, Marchetti M., 1994. "A computational procedure to calculate stress-strain field around simple shape holes in composite laminates." Compos. Struct. 53, 1167–1179.

5. Bonora, N., Costanzi, M., Marchetti, M. (1993). "On closed form solution for the elastic stress field around holes in orthotropic composite plates under in-plane stress conditions." Composite Structures, 25, 139-156.

6. Campagnolo, A., Berto, F. (2017). "Some recent criteria for brittle fracture assessment under mode II loading." Engineering Solid Mechanics, 5(1), 31-38.

7. Chen D.H., 2017. "Investigation on Filippi's stress equation for V-shaped notch with rounded vertex Part II: Mode II stresses." Eng. Fract. Mech. 178, 318-332. https://doi.org/10.1016/j.engfracmech.2017.03.022

8. Chen, D.H., 2017. "Investigation on Filippi's stress equation for V-shaped notch with rounded vertex Part I: Mode I stresses." Eng. Fract. Mech. 169, 163-177. https://doi.org/10.1016/j.engfracmech.2016.11.025

9. Chern, S. M., Tuttle, M. E. (2000). "On Displacement Fields in Orthotropic Laminates Containing an Elliptical Hole." Journal of Applied Mechanics, 67, 527-539.

10. Creager, M., Paris, P.C., 1967. "Elastic field equations for blunt cracks with reference to stress corrosion cracking." Int. J. Fract. Mech. 3, 247-252. https://doi.org/10.1007/BF00182890

11. England, A. H., 1971. "On stress singularities in linear elasticity." Int. J. Eng. Sci. 9, 571-585. https://doi.org/10.1016/0020-7225(71)90039-5

12. England, A. H. (June 1971). "On stress singularities in linear elasticity." International Journal of Engineering Science, 9(6), 571-585.

13. Filippi S., Lazzarin P., Tovo R. 2002. "Developments of some explicit formulas useful to describe elastic stress fields ahead of notches in plates." Int. J. Solids Struct. 39, 4543-4565. https://doi.org/10.1016/S0020-7683(02)00342-6

14. Filippi S., P. Lazzarin, 2004. "Distributions of the elastic principal stress due to notches in finite size plates and rounded bars uniaxially loaded." Int. J. Fatigue. 26, 377–391. https://doi.org/10.1016/j.ijfatigue.2003.06.001

15. Glinka G., Newport A., 1987. "Universal features of elastic notch-tip stress fields." Int. J. Fatigue. 9, 143–150. https://doi.org/10.1016/0142-1123(87)90069-7

16. Inglis, C.E., 1913. "Stresses in a plate due to the presence of cracks and sharp corners." Trans. Inst. Nav Arch. 55, 219-30.

17. Kazberuk, A., Savruk, M.P. (2016). "Distribution of Stresses Near V-Notches in an Orthotropic Plane Under Symmetric Loads." Materials Science, 52, 62-71.
18. Kirsch G., 1898. "Die Theorie der Elastizität und die Bedürfnisse der Festigkeitslehre." Zeitschriftdes VDI. 42, 797–807.

19. Kujawski D., C.S. Shin, 1997. "On the elastic longitudinal stress estimation in the neighbourhood of notches." Eng. Fract. Mech. 56, 137–138. https://doi.org/10.1016/S0013-7944(96)00113-0

20. Kullmer G., 1992. "Elastic stress fields in the vicinity of a narrow notch with circular root." Reliability and Structural Integrity of Advanced Materials. Proceedings of the 9th Biennial European Conference on Fracture (ECF 9) Vol. II; Varna; Bulgaria; 905-910.

21. Lazzarin P., Zappalorto M., Berto F., 2011. "Generalised stress intensity factors for rounded notches in plates under in-plane shear loading." Int. J. Fract. 170, 123-144. https://doi.org/10.1007/s10704-011-9613-y

22. Lazzarin, L., Tovo, R., 1996. "A unified approach to the evaluation of linear elastic stress fields in the neighborhood of cracks and notches," Int. J. Fract. 78, 3-19. https://doi.org/10.1007/BF00018497

23. Lazzarin, P., Berto, F., 2005. "Some expressions for the strain energy in a finite volume surrounding the root of blunt V-notches." Int J Fract 135, 161-85. https://doi.org/10.1007/s10704-005-3943-6

24. Mirzaei A. M., M. R. Ayatollahi, B. Bahrami, F. Berto, 2020. "Elastic stress analysis of blunt V-notches under mixed mode loading by considering higher order terms." Appl. Math. Model. 78, 665-684. https://doi.org/10.1016/j.apm.2019.09.049

25. Mirzaei, A.M., M.R. Ayatollahi, B. Bahrami, F. Berto. (2021). "A new unified asymptotic stress field solution for blunt and sharp notches subjected to mixed mode loading." International Journal of Mechanical Sciences, 193, 106176.

26. Mirzaei, A.M, M.R. Ayatollahi, B. Bahrami. (2019). "Asymptotic stress field and the coefficients of singular and higher order terms for V-notches with end holes under mixed-mode loading." International Journal of Solids and Structures, pp. 172-173.

27. Moussaoui, M., Amroune, S., Tahiri, A., Khalil Hachi, B. (2020). "Brittle fracture investigation from disc specimen weakened by U-notch in mixed mode I + II." Engineering Solid Mechanics, 8, 337-352.

28. Neuber, H., 1958. Theory of notch stresses. Springer-Verlag, Berlin.

29. Pastrello M, Zappalorto M., Salviato M., 2022. "Stress distributions in orthotropic solids with blunt notches under in-plane shear loadings." Eur. J. Mech. A-Solid. 92, 104436. https://doi.org/10.1016/j.euromechsol.2021.104436

30. Pastrello M, Pontefisso A, Zappalorto M., 2022. "A new explicit solution for the mode I stress fields in notched orthotropic solids." Eur. J. Mech. A-Solid. 97. 104819. https://doi.org/10.1016/j.euromechsol.2022.104819.

31. Salviato M, Zappalorto M., 2016. "A unified solution approach for a large variety of antiplane shear and torsion notch problems: Theory and examples." Int. J. Solids Struct. 102-103, 10-20. https://doi.org/10.1016/j.ijsolstr.2016.10.022

32. Salviato, M., Phenisee, S.E. (2019). "Enhancing the electrical and thermal conductivities of polymer composites via curvilinear fibers: An analytical study." Mathematics and Mechanics of Solids, 24, 3231-3253.

33. Sih, G.C., Paris, P.C., Irwin, G.R. (1965). "On cracks in rectilinearly anisotropic bodies." International Journal of Fracture Mechanics, 1, 189-203.

34. Stevenson, A.C., 1945. "Complex potentials in two-dimensional elasticity," Proc. Roy. Soc. Lond. A 184, 532-54. https://doi.org/10.1098/rspa.1945.0015

35. Timoshenko, S.P., Goodier, J.N. (1970). Theory of Elasticity, 3rd Edition, McGraw-Hill, New York.

36. Whitney, J.M., Nuismer, R.J., 1974. "Stress Fracture Criteria for Laminated Composites Containing Stress Concentrations." J Compos Mater 8, 253-265.

37. Xu RX, Thompson JC and Topper TH, 1995. "Practical stress expressions for stress concentration regions." Fatigue Fract. Eng. M. 18, 885-895. https://doi.org/10.1111/j.1460-2695.1995.tb00912.x

38. Zappalorto M., 2017. "On the stress state in rectilinear anisotropic thick plates with blunt cracks." Fatigue Fract. Eng. Mater. Struct. 40, 103-119. https://doi.org/10.1111/ffe.12479

39. Zappalorto M., Carraro PA, 2015. "Stress distributions for blunt cracks and radiused slits in anisotropic plates under in-plane loadings." Int. J. Solids Struct. 56–57, 136-141. https://doi.org/10.1016/j.ijsolstr.2014.11.024

40. Zappalorto M., Carraro PA, 2017. "Two-dimensional stress distributions in tensioned orthotropic plates weakened by blunt V-shaped notches." Fatigue Fract. Eng. M. 40, 804-819. https://doi.org/10.1111/ffe.12554

41. Zappalorto M., Lazzarin P., 2011b. "In-plane and out-of-plane stress field solutions for V-notches with end holes." Int. J. Fract. 168, 167-180. https://doi.org/10.1007/s10704-010-9567-5

42. Zappalorto M., Lazzarin P., 2011c. "Stress fields due to inclined notches and shoulder fillets in shafts under torsion." J. Strain Anal. Eng. 46, 187-199. https://doi.org/10.1177/0309324710396019

43. Zappalorto M., Lazzarin P., Filippi S., 2010. "Stress field equations for U and blunt V-shaped notches in axisymmetric shafts under torsion." Int. J. Fract. 164, 253-269. https://doi.org/10.1007/s10704-010-9493-6

44. Zappalorto M., Salviato M., 2019. "Antiplane shear stresses in orthotropic plates with lateral blunt notches." Eur. J. Mech. A-Solid. 77, 103815 https://doi.org/10.1016/j.euromechsol.2019.103815

45. Zappalorto M., Salviato M., Maragoni L., 2019. "Analytical study on the mode III stress fields due to blunt notches with cracks." Fatigue Fract. Eng. M. 42, 612-626. https://doi.org/10.1111/ffe.12936

3. Three-dimensional stress fields in the proximity of a sharp notch

3.1. Introduction

Regions in close proximity to geometric variations, such as notches, holes, and cutouts, exhibit a notable concentration of stress fields that play a pivotal role in crack formation under both static and cyclic loading conditions. The accurate prediction of fatigue crack initiation or static failure in notched solids is a critical concern for mechanical designers. The formulation of effective strength criteria hinges on a precise understanding of local stress fields, prompting considerable attention from researchers in this area over the years (refer to Ref. [1-12] and the cited references).

While the majority of referenced papers focus on two-dimensional analyses, it's essential to note that mechanical components are inherently three-dimensional. The literature's analytical works on 3D stress fields are limited, particularly for orthotropic materials. Noteworthy contributions in this field include Prabhu and Lambros' numerical investigation in 2000[13] into the 3D stress distribution in a cracked orthotropic plate, and Cheng et al.'s study in 2015[14] on the V-notch problem in an orthotropic solid under a generalized plane deformation state. In contrast, Pageau and Biggers[15] developed a 3D finite element formulation in 1996 for the singular stress state near material and geometric discontinuities in orthotropic and anisotropic media. Choi and Folias[16] analyzed the three-dimensional stress fields in a composite plate weakened by a hole.

In a parallel track, Kotousov and Wang[17-18] explored transversely isotropic composite plates with holes or inclusions, presenting a generalized plane-strain theory. Zappalorto and Carraro delved into thick anisotropic plates with pointed V-notches[19-20], developing a new three-dimensional theory for anisotropic blunt cracks in 2017[21].

Recent advancements include Shi et al.'s work[22] on designing thin cylindrical shells for aerospace applications, where stress concentration factors tend to zero in the presence of deep single-side notches. Zappalorto and co-workers[19-21] suggested simplifying the full 3D stress field problem into two uncoupled equations, each defined in a bi-dimensional domain, addressing plane and out-of-plane shear notch problems.

In this chapter the 3D solution previously developed by Zappalorto and Carraro for pointed notches will be expanded for orthotropic plates with holes or lateral radiused notches, assuming a sufficiently small notch tip radius. It will be shown that stress components (σ_{xx}, σ_{yy}, and σ_{xy}) in a thick 3D anisotropic notched plate (i.e., in-plane stress fields) can be accurately determined with the plane solution and that the out-of-plane shear stresses (σ_{xz} and σ_{yz}) can be assessed using the pure antiplane shear solution. The presence of coupled modes, as observed in other research articles on isotropic components, will be documented and shown in orthotropic thick plates weakened by holes or lateral notches with any notch opening angle.

3.2. Simplified Three-Dimensional Elasticity Theory for Orthotropic Thick Plates

Consider a thick orthotropic plate weaken by a radiused notch; with reference to a Cartesian orthogonal system centered on the symmetry plane of the plate (see Figure 1 or Figure 2), the stress-strain relationships can be written according to I.49 and I.59. Further suppose that the elastic material properties of the plate are such that the elastic eigenvalues $\mu_i = i\beta_i$ are pure immaginary numbers.

Supposing that 3D displacement fields near the notch tip could be written by means of separated variables[19, 28]:

$$u_x = f(z)\times u(x,y) \qquad u_y = f(z)\times v(x,y) \qquad u_z = g\left(z\right)\times w(x,y) \tag{III.1}$$

Invoking strain definitions, one obtains:

$$\varepsilon_{xx} = \frac{\partial u_x}{\partial x} = f(z) \times \frac{\partial u(x,y)}{\partial x} \qquad \gamma_{xy} = \frac{\partial u_x}{\partial y} + \frac{\partial u_y}{\partial x} = f(z) \times \left(\frac{\partial u(x,y)}{\partial y} + \frac{\partial v(x,y)}{\partial x} \right)$$
$$\varepsilon_{yy} = \frac{\partial u_y}{\partial y} = f(z) \times \frac{\partial v(x,y)}{\partial y} \qquad \gamma_{xz} = \frac{\partial u_x}{\partial z} + \frac{\partial u_z}{\partial x} = f'(z) \times u(x,y) + g(z) \times \frac{\partial w(x,y)}{\partial x} \qquad \text{III.2}$$
$$\varepsilon_{zz} = \frac{\partial u_z}{\partial z} = g'(z) \times w(x,y) \qquad \gamma_{yz} = \frac{\partial u_y}{\partial z} + \frac{\partial u_z}{\partial y} = f'(z) \times v(x,y) + g(z) \times \frac{\partial w(x,y)}{\partial y}$$

Under the hypothesis that the tip radius of the radiused notch is small enough to as-sure that $f'(z) \times u(x,y)$, $f'(z) \times v(x,y)$ and $g'(z) \times w(x,y)$ can be disregarded when compared to $g(z) \cdot \partial w(x,y)/\partial x$ and $g(z) \cdot \partial w(x,y)/\partial y$, the strain field can be written as[19-21]:

$$\varepsilon_{xx} = f(z) \times \frac{\partial u(x,y)}{\partial x} \qquad \gamma_{xy} = f(z) \times \left(\frac{\partial u(x,y)}{\partial y} + \frac{\partial v(x,y)}{\partial x} \right)$$
$$\varepsilon_{yy} = f(z) \times \frac{\partial v(x,y)}{\partial y} \qquad \gamma_{xz} \cong g(z) \times \frac{\partial w(x,y)}{\partial x} \qquad \text{III.3}$$
$$\varepsilon_{zz} \cong 0 \qquad \gamma_{yz} \cong g(z) \times \frac{\partial w(x,y)}{\partial y}$$

As shown by equation III.3, stress concentration areas near the notch tip exhibit a state of "quasi" plane strain. In this context, through-the-thickness normal strain becomes negligible, whereas out-of-plane shear strains remain significant. Equation III.3 additionally provides:

$$\sigma_{zz} \cong -\frac{S_{13}\sigma_{xx} + S_{23}\sigma_{yy}}{S_{33}} \cong f(z) \left\{ C_{13} \frac{\partial u(x,y)}{\partial x} + C_{23} \frac{\partial v(x,y)}{\partial y} \right\}$$
$$\tau_{yz} \cong C_{44} g(z) \times \frac{\partial w(x,y)}{\partial y} \qquad \text{III.4}$$
$$\tau_{xz} \cong C_{55} g(z) \times \frac{\partial w(x,y)}{\partial x}$$

Moreover, Eq. III.3 combined with the elastic stress-strain relations I.49 gives the possibility to formulate the stress components according to the following expressions:

$$\sigma_{xx} = f(z) \times \tilde{\sigma}_{xx}(x,y) \qquad \sigma_{yy} = f(z) \times \tilde{\sigma}_{yy}(x,y) \qquad \sigma_{zz} = f(z) \times \tilde{\sigma}_{zz}(x,y)$$
$$\tau_{xy} = f(z) \times \tilde{\tau}_{xy}(x,y) \qquad \tau_{xz} = g(z) \times \tilde{\sigma}_{xz}(x,y) \qquad \tau_{yz} = g(z) \times \tilde{\sigma}_{yz}(x,y) \qquad \text{III.5}$$

Consider now the equilibrium equation in the z direction:

$$\frac{\partial \tau_{xz}}{\partial x}+\frac{\partial \tau_{yz}}{\partial y}+\frac{\partial \sigma_{zz}}{\partial z}=0 \qquad \text{III.6}$$

Substituting Eq. III.4 into Eq. III.6 results in:

$$\frac{\partial}{\partial x}\left\{C_{55}g(z)\times\frac{\partial w(x,y)}{\partial x}+f'(z)C_{13}\cdot u(x,y)\right\}+\frac{\partial}{\partial y}\left\{C_{44}g(z)\times\frac{\partial w(x,y)}{\partial y}+f'(z)C_{23}\cdot v(x,y)\right\}=0 \qquad \text{III.7}$$

and since $f'(z)\times u(x,y)$ and $f'(z)\times v(x,y)$ can be disregarded if compared to $g(z)\cdot\partial w(x,y)/\partial x$ and $g(z)\cdot\partial w(x,y)/\partial y$, Eq. III.7 further simplifies to give:

$$C_{55}\frac{\partial^2 w(x,y)}{\partial x^2}+C_{44}\frac{\partial^2 w(x,y)}{\partial y^2}=0 \qquad \text{III.8}$$

Concerning the equilibrium equations in the x-direction and in the y-direction, the Airy stress function, ϕ, defined in the x-y plane guarantees that such equilibrium is preserved[19-21]:

$$\tilde{\sigma}_{xx}=\frac{\partial^2\phi}{\partial y^2} \qquad \tilde{\sigma}_{yy}=\frac{\partial^2\phi}{\partial x^2} \qquad \tilde{\sigma}_{xy}=-\frac{\partial^2\phi}{\partial x\partial y} \qquad \text{III.9}$$

Substituting Eq. III.9 into Eq. I.37, further invoking the compatibility equation in the (x,y) plane gives the possibility to formulate the following fourth order differential equation:

$$b_{22}\frac{\partial^4\phi}{\partial x^4}+(2b_{12}+b_{66})\frac{\partial^4\phi}{\partial x^2\partial y^2}+b_{11}\frac{\partial^4\phi}{\partial y^4}=0 \qquad \text{III.10}$$

where:

$$b_{ij}=S_{ij}-\frac{S_{i3}S_{j3}}{S_{33}} \qquad \text{III.11}$$

Equations III.8 and III.10 need to simultaneously hold true. Consequently, solving the subsequent pair of uncoupled differential equations allows for the simplification of the equations governing the three-dimensional elastic fields in a notched plate.

$$\begin{cases} b_{22}\dfrac{\partial^4\phi}{\partial x^4}+(2b_{12}+b_{66})\dfrac{\partial^4\phi}{\partial x^2\partial y^2}+b_{11}\dfrac{\partial^4\phi}{\partial y^4}=0 \\ C_{55}\dfrac{\partial^2 w}{\partial\, x^2}+C_{44}\dfrac{\partial^2 w}{\partial\, y^2}=0 \end{cases} \qquad \text{III.12 a-b}$$

It's important to recognize that Eq. III.12-a pertains to the plane strain problem within the orthotropic theory of elasticity with general solution given by III.104, while Eq. III.12-b defines the solution for the antiplane scenario with general solution given by III.119. The practical implication of Eqs. III.12 is that the imposition of an out-of-plane shear stress, indicated by a non-zero w function, induces a local non-zero Airy φ function due to three-dimensional effects. Simultaneously, any form of in-plane loading, such as bending, tension, or in-plane shear, generates a local non-zero w function. This interdependence is not accommodated by conventional plane strain or plain stress solutions. Specifically, when thick plates undergo loading conditions resulting in a skew-symmetric φ function (mode 2), three-dimensional effects give rise to an antisymmetric w function (mode 3) in the immediate vicinity of the notch tip.

3.3. Elliptical Hole in a Thick Plate Under Shear

Consider a thick plate with an elliptical hole under shear or torsion (see Figure III.1).

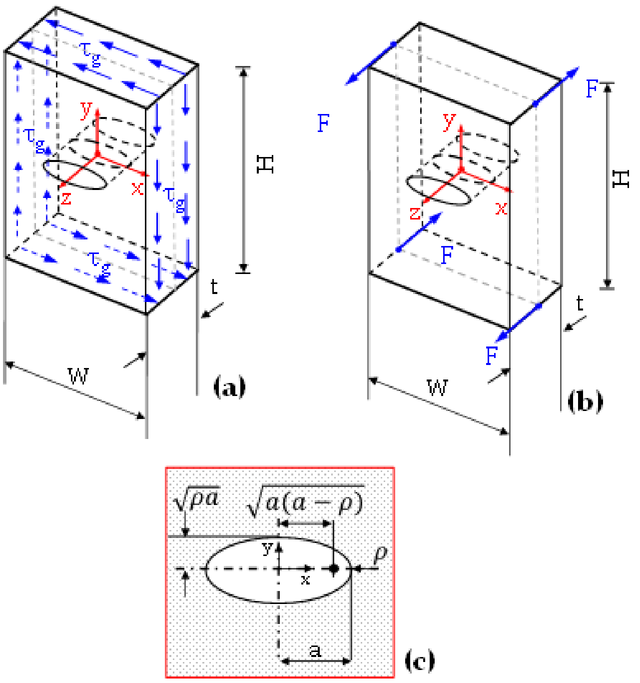

Figure III.1. Elliptic hole in a three-dimensional plate under in-plane shear (a) or twisting (b). In (c) a schematic of elliptic hole is reported together with the dimensions used in the mathematical passages and in the results discussion.

The in-plane stress fields can be determined according to the solution proposed by Savin[33]. Re-arranging Savin equations allows the explicit solution for this problem to be obtained, according to which the stress field is:

$$\begin{aligned}
\sigma_{xx} &= \frac{\tau_{xy}^{Max}(z)}{\omega}\cdot\frac{(a+b\beta_1)(a+b\beta_2)\left(r_1\beta_2{}^2\Lambda_2\Theta_1 - r_2\beta_1{}^2\Lambda_1\Theta_2\right)}{r_1 r_2(\beta_1-\beta_2)\Theta_1\Theta_2}\\
\sigma_{yy} &= \frac{\tau_{xy}^{Max}(z)}{\omega}\cdot\frac{(a+b\beta_1)(a+b\beta_2)\left(r_2\Lambda_1\Theta_2 - r_1\Lambda_2\Theta_1\right)}{r_1 r_2(\beta_1-\beta_2)\Theta_1\Theta_2}\\
\tau_{xy} &= \frac{\tau_{xy}^{Max}(z)}{\omega}\left(1+\frac{(a+b\beta_1)(a+b\beta_2)\left(r_2\beta_1\Theta_1\Omega_2 - r_1\beta_2\Theta_2\Omega_1\right)}{r_1 r_2(\beta_1-\beta_2)\Theta_1\Theta_2}\right)
\end{aligned} \qquad \text{III.13}$$

where $\tau_{xy}^{Max}(z)$ is, for a given z value, the maximum shear stress occurring along the notch bisector line, at a certain distance, x_{Max}, from the notch tip, whereas:

$$\begin{aligned}
r_i &= \sqrt[4]{4x^2y^2\beta_i^2 + \left(a^2 - x^2 + \left(y^2-b^2\right)\beta_i^2\right)^2}\\
\theta_i &= Arg\left\{\left[\left(x^2-a^2\right)-\beta_i^2\left(y^2-b^2\right)\right]+i\left[-2xy\beta_i\ \right]\right\}
\end{aligned} \qquad \text{III.14}$$

$$\begin{aligned}
\Theta_i &= x^2 + r_i{}^2 + y^2\beta_i^2 + 2r_i\left(x\cos\frac{\theta_i}{2} + y\beta_i\sin\frac{\theta_i}{2}\right)\\
\Lambda_i &= x\sin\frac{\theta_i}{2} + r_i\sin\theta_i + y\beta_i\cos\frac{\theta_i}{2}\\
\Omega_i &= x\cos\frac{\theta_i}{2} + r_i\cos\theta_i - y\beta_i\sin\frac{\theta_i}{2}
\end{aligned} \qquad \text{III.15}$$

$$\omega = \frac{\hat{r}_2\beta_1(a+b\beta_1)(a+b\beta_2)\hat{\Omega}_1\hat{\Theta}_2 + \hat{r}_1\hat{\Theta}_1\left(\hat{r}_2(\beta_1-\beta_2)\hat{\Theta}_2 - \left((a+b\beta_1)\beta_2(a+b\beta_2)\hat{\Omega}_2\right)\right)}{\hat{r}_1\hat{r}_2(\beta_1-\beta_2)\hat{\Theta}_1\hat{\Theta}_2} \qquad \text{III.16}$$

$$\hat{r}_i = r_i\left[x_{Max},0\right] \qquad \hat{\Theta}_i = \Theta_i\left[x_{Max},0\right] \qquad \hat{\Omega}_i = \Omega_i\left[x_{Max},0\right] \qquad \text{III.17}$$

Along the notch bisector line, Eq. III.13 simplifies to give:

$$\tau_{xy} = \frac{\tau_{xy}^{Max}(z)}{\omega}\left\{1+\frac{(a+b\beta_1)(a+b\beta_2)\left(\beta_1 r_{2,0}\Theta_{1,0}\Omega_{2,0} - r_{1,0}\beta_{2,0}\Theta_{2,0}\Omega_{1,0}\right)}{r_{1,0}r_{2,0}(\beta_1-\beta_2)\Theta_{1,0}\Theta_{2,0}}\right\} \qquad \text{III.18}$$

where:

$$r_{i,0} = \sqrt[2]{a^2 - x^2 - b^2\beta_i^2} \qquad \Theta_{i,0} = x^2 + {r_{i,0}}^2 + 2r_{i,0}\cdot x \qquad \Omega_{i,0} = x + r_{i,0} \tag{III.19}$$

The out-of-plane stress fields, instead, can be derived starting from the solution obtained by Zappalorto and Salviato[30] for the pure antiplane shear loadings, which can be re-written as:

$$\begin{aligned}
\tau_{zy} &= \tau_{zy}^{Max}(z)\frac{\beta_3\sqrt{\frac{\rho}{a}}}{1-\beta_3^2\frac{\rho}{a}}\left\{\frac{r_3}{\sqrt{r_{31}\cdot r_{32}}}\cos\left(\theta_3 - \frac{\theta_{31}+\theta_{32}}{2}\right) - \beta_3\sqrt{\frac{\rho}{a}}\right\} \\
\tau_{zx} &= \tau_{zy}^{Max}(z)\frac{\beta_3^2\sqrt{\frac{\rho}{a}}}{1-\beta_3^2\frac{\rho}{a}}\left\{\frac{r_3}{\sqrt{r_{31}\cdot r_{32}}}\sin\left(\theta_3 - \frac{\theta_{31}+\theta_{32}}{2}\right)\right\}
\end{aligned} \tag{III.20}$$

where:

$$z_3 = x + i\beta_3 y = r_3 e^{i\theta_3} \qquad z_3^2 - a^2 + \beta_3^2 b^2 = z_3^2 - \hat{c}^2 = \left(z_3 - \hat{c}\right)\left(z_3 + \hat{c}\right) \tag{III.21}$$

$$\left(z_3 - \hat{c}\right) = r_{31}e^{i\theta_{31}} \qquad \left(z_3 + \hat{c}\right) = r_{32}e^{i\theta_{32}} \tag{III.22}$$

and $\tau_{zy}^{Max}(z)$ is, for a given z value, the maximum shear stress occurring at the notch tip.

Along the notch bisector line Eq. III.20 simplifies to give:

$$\tau_{zy} = \tau_{zy}^{Max}(z)\frac{\beta_3\sqrt{\frac{\rho}{a}}}{1-\beta_3^2\frac{\rho}{a}}\left\{\frac{\frac{x}{a}}{\sqrt{\left(\frac{x}{a}\right)^2 - 1 + \beta_3^2\frac{\rho}{a}}} - \beta_3\sqrt{\frac{\rho}{a}}\right\} \tag{III.23}$$

3.4. Lateral Radiused Notch Under Shear

Consider a thick plate with two lateral radiused notches with a generic notch opening angle (2α) and subjected to shear or torsion (see Figure III.2).

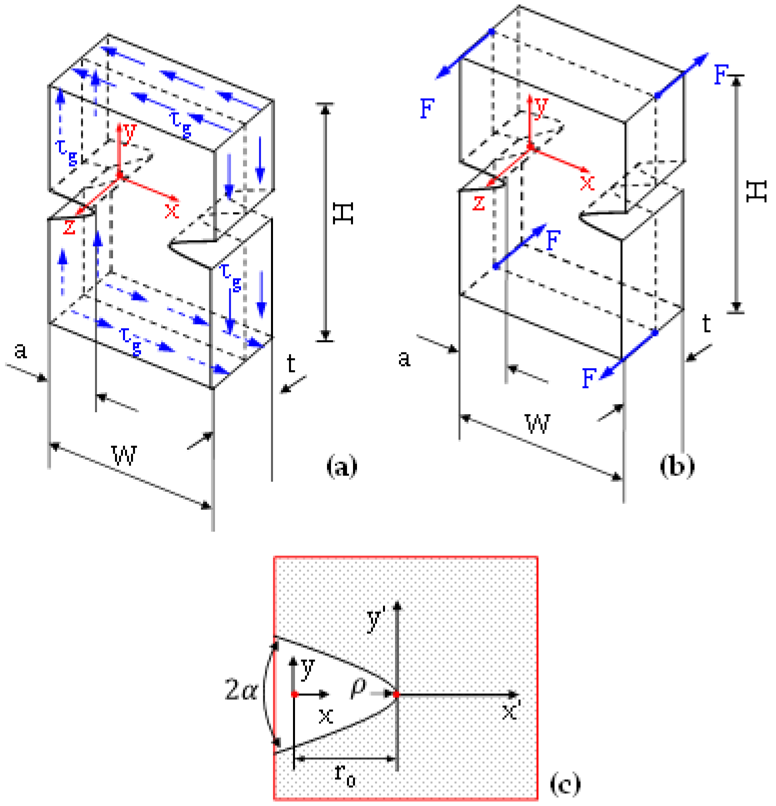

Figure III.2. Rounded V-shaped (hyperbolic) notches in a three-dimensional plate under in-plane shear (a) or twisting (b). In (c) a schematic of elliptic hole is reported together with the dimensions used in the mathematical passages and in the results discussion.

As shown in previous chapters the notch boundary can be described by hyperbola like curves having parametric equations:

$$x = \frac{r_0}{\cos\left(\frac{\theta}{q}\right)^q} \qquad y = \frac{r_0}{\sin\left(\frac{\theta}{q}\right)^q} \qquad \text{III.24}$$

where:

$$r_0 = \frac{q-1}{q}\rho \qquad q = \frac{2\pi - 2\alpha}{\pi} \qquad \text{III.25}$$

and ρ is the notch root radius.

The in-plane stress fields can be determined according to the solution developed in the previous chapter:

$$\sigma_{rr} = A(z)\left\{\left(\frac{r_1}{r_0}\right)^{\lambda_2-1}\left[k_{12}\cos(1-\lambda_2)\theta_1 - k_{11}\sin(1-\lambda_2)\theta_1\right]+\right.$$

$$+\chi_{12}\left(\frac{r_1}{r_0}\right)^{\mu_2-1}\left[k_{12}\cos(1-\mu_2)\theta_1 - k_{11}\sin(1-\mu_2)\theta_1\right]+$$

$$+\chi_{21}\left(\frac{r_2}{r_0}\right)^{\lambda_2-1}\left[k_{22}\cos(1-\lambda_2)\theta_2 - k_{21}\sin(1-\lambda_2)\theta_2\right]+ \qquad \text{III.26}$$

$$+\chi_{22}\left(\frac{r_2}{r_0}\right)^{\mu_2-1}\left[k_{22}\cos(1-\mu_2)\theta_2 - k_{21}\sin(1-\mu_2)\theta_2\right]+$$

$$\left.+\chi_{23}\left(\frac{r_2}{r_0}\right)^{\zeta_2-1}\left[k_{22}\cos(1-\zeta_2)\theta_2 - k_{21}\sin(1-\zeta_2)\theta_2\right]\right\}$$

$$\sigma_{\theta\theta} = A(z)\left\{\left(\frac{r_1}{r_0}\right)^{\lambda_2-1}\left[m_{12}\cos(1-\lambda_2)\theta_1 - m_{11}\sin(1-\lambda_2)\theta_1\right]+\right.$$

$$+\chi_{12}\left(\frac{r_1}{r_0}\right)^{\mu_2-1}\left[m_{12}\cos(1-\mu_2)\theta_1 - m_{11}\sin(1-\mu_2)\theta_1\right]+$$

$$+\chi_{21}\left(\frac{r_2}{r_0}\right)^{\lambda_2-1}\left[m_{22}\cos(1-\lambda_2)\theta_2 - m_{21}\sin(1-\lambda_2)\theta_2\right]+ \qquad \text{III.27}$$

$$+\chi_{22}\left(\frac{r_2}{r_0}\right)^{\mu_2-1}\left[m_{22}\cos(1-\mu_2)\theta_2 - m_{21}\sin(1-\mu_2)\theta_2\right]+$$

$$\left.+\chi_{23}\left(\frac{r_2}{r_0}\right)^{\zeta_2-1}\left[m_{22}\cos(1-\zeta_2)\theta_2 - m_{21}\sin(1-\zeta_2)\theta_2\right]\right\}$$

$$\tau_{r\theta} = A(z)\left\{\left(\frac{r_1}{r_0}\right)^{\lambda_2-1}\left[n_{12}\cos(1-\lambda_2)\theta_1 - n_{11}\sin(1-\lambda_2)\theta_1\right]+\right.$$

$$+\chi_{12}\left(\frac{r_1}{r_0}\right)^{\mu_2-1}\left[n_{12}\cos(1-\mu_2)\theta_1 - n_{11}\sin(1-\mu_2)\theta_1\right]$$

$$+\chi_{21}\left(\frac{r_2}{r_0}\right)^{\lambda_2-1}\left[n_{22}\cos(1-\lambda_2)\theta_2 - n_{21}\sin(1-\lambda_2)\theta_2\right]+ \qquad \text{III.28}$$

$$+\chi_{22}\left(\frac{r_2}{r_0}\right)^{\mu_2-1}\left[n_{22}\cos(1-\mu_2)\theta_2 - n_{21}\sin(1-\mu_2)\theta_2\right]+$$

$$\left.+\chi_{23}\left(\frac{r_2}{r_0}\right)^{\zeta_2-1}\left[n_{22}\cos(1-\zeta_2)\theta_2 - n_{21}\sin(1-\zeta_2)\theta_2\right]\right\}$$

where, denoting with x’ and y’ the distances from the notch tip:

$$x_j = x' + r_0\beta_j^{t_2} \qquad y_j = \beta_j y' \qquad r_j = \sqrt{x_j^2 + y_j^2} \qquad \theta_j = \mathrm{Arg}(x_j + iy_j) \qquad j=1,2 \qquad \text{III.29}$$

Parameters t_2, λ_2, μ_2, ζ_2, χ_{12}, χ_{21}, χ_{22}, χ_{23} depends on the notch geometry and the material properties and can be determined according to the procedure illustrated in the previous chapter.

Furthermore, it is important to observe that parameter A(z) in equations III.26-28 can be represented, for a specific z value, either in terms of the maximum shear stress along the notch bisector, the maximum principal stress along the notch edge, or as a function of a mode 2 Generalised Stress Intensity Factor for the corresponding plane (z value).

The out-of-plane shear stress components can be determined according to:

$$\begin{aligned}
\tau_{z\theta} &= \tau_{z\theta}^{MAX}(z)\left(\frac{r_0\,\beta_3^{t_3}}{r_3}\right)^{1-\lambda_3}\left[\cos(1-\lambda_3)\theta_3\cos\theta + \beta_3\sin(1-\lambda_3)\theta_3\sin\theta\right] \\
\tau_{zr} &= \tau_{z\theta}^{MAX}(z)\left(\frac{r_0\,\beta_3^{t_3}}{r_3}\right)^{1-\lambda_3}\left[\cos(1-\lambda_3)\theta_3\sin\theta - \beta_3\sin(1-\lambda_3)\theta_3\cos\theta\right]
\end{aligned} \qquad \text{III.30}$$

Where $\tau_{z\theta}^{MAX}(z)$ is, for a given z value, the maximum shear stress occurring at the notch tip, whereas:

$$x_3 = x' + r_0\beta_3^{t_3} \qquad y_3 = \beta_3 y' \qquad \text{III.31}$$

$$r_3 = \sqrt{x_3^2 + y_3^2} \qquad \theta_3 = \mathrm{Arg}(x_3 + iy_3) \qquad \text{III.32}$$

3.5. Discussion and Results

To substantiate the aforementioned theoretical findings, a series of numerical simulations were conducted. Specifically, three-dimensional elastic finite element analyses were executed using three distinct material systems, the elastic characteristics of which are outlined in Table III.1. These materials embody typical properties found in certain polymeric composites:

- **Material 1** corresponds to a unidirectional Carbon-Fiber Reinforced Epoxy laminate with fibers aligned in the X-direction.

- **Material 2** mirrors the same composition, but with fibers oriented in the Y-direction.

- **Material 3** represents a quasi-isotropic Carbon-Fiber Reinforced Epoxy laminate, exemplified by the arrangement $[(0/\pm45/90)_n]_S$.

	E_x [GPa]	E_y [GPa]	E_z [GPa]	ν_{xy}	ν_{xz}	ν_{yz}	G_{xy} [GPa]	G_{xz} [GPa]	G_{yz} [GPa]	β_1	β_2	β_3
Material 1	160	10	10	0.3	0.3	0.4	5	5	3.57	0.6614	5.5587	1.1835
Material 2	10	160	10	0.01875	0.4	0.3	5	3.57	5	0.1798	1.5120	0.8450
Material 3	70	70	70	0.3	0.3	0.3	26.9	26.9	26.9	0.9993	1.0006	1.0000

Table III.1. Properties of the materials used in the numerical analyses.

Thick notched discs (refer to Figure III.3) underwent numerical examinations where a pure mode 2 or pure mode 3 displacement field was applied to their external surface (refer to the expressions in Appendix A). The objective was to induce in-plane or out-of-plane stress fields within the notched solids. This modeling approach, employed to facilitate the analysis of the local behavior of a generic 3D solid, was previously utilized by Berto et al.[25].

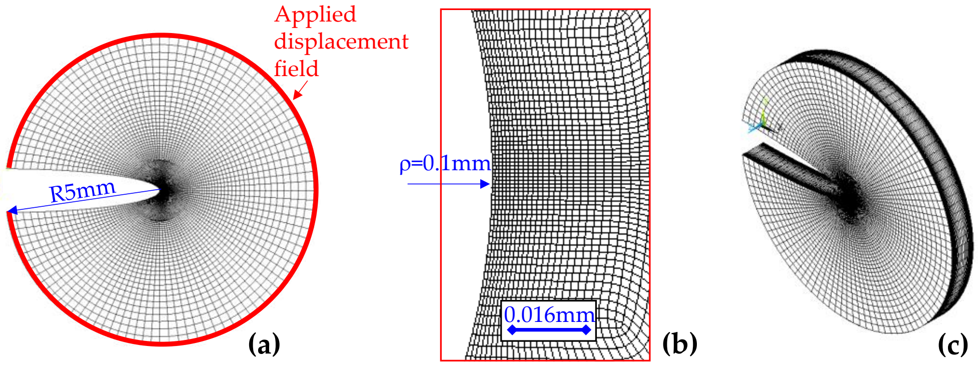

Figure 3. An example of the FE mesh used for an elliptic notch of ρ=0.1 mm, a=5 mm, and t=1 mm. All the discs used for the simulations of elliptic notches have radius 5 mm, while those for hyperbolic notches 10 mm. In (a) a side-view of the notched disk is shown, highlighting in red the border where the displacement field is applied. In (b) a close-up zoom of the mesh at the notch tip is reported. In (c) an isometric view of the meshed geometry is shown.

The following notch geometries were considered:

- semi-elliptical notches with notch depth a=5 mm and different notch root radii (ρ=0.001 mm, 0.01 mm, 0.1 mm, 1 mm); in this case the radius of the disc was 5 mm and various thicknesses were considered (t=1mm, 5 mm and 10 mm);
- hyperbolic notches with a notch depth a=10 mm, a notch root radius ρ=0.01 mm and various notch opening angles (see Tables III.2 and III.3 for the stress field parameters associated to the cases analyzed).

	t_2	λ_2	μ_2	ζ_2	χ_{12}	χ_{21}	χ_{22}	χ_{23}
Material 1, 2α=45°	1.6849	0.8757	0.3533	-0.3806	0.2997	-0.2733	0.0888	-0.4661
Material 2, 2α=90°	1.7319	0.7788	0.2551	-0.8948	0.1629	-0.4744	0.0152	-0.0417
Material 3, 2α=60°	1.5200	0.7309	0.1924	-3.7178	0.0738	-0.9996	-0.0734	$-4.3\cdot10^{-07}$

Table III.2. In plane stress fields parameters for the hyperbolic notches used in the numerical analyses.

	t_3	λ_3	q
Material 1, 2α=45°	1.8111	0.5848	1.7500
Material 2, 2α=90°	1.6055	0.6438	1.5000
Material 3, 2α=60°	1.7519	0.6000	1.6667

Table III.3. Out-of-plane stress fields parameters for the hyperbolic notches used in the numerical analyses.

Finite element analyses were conducted using the ANSYS commercial software, release 19, employing 20-node SOLID186 brick elements with reduced integration and a pure displacement formulation. Nodal displacements were applied along the circular boundary of the disc, as illustrated in Figure III.3-a. Specifically, nodal coordinates of the boundaries were extracted in ANSYS APDL, and an external script was utilized to determine the displacements based on expressions provided in

Appendix A. Subsequently, another APDL script was employed to apply these nodal displacements to the disc boundary.

For mode 2 simulation, the model's symmetry was exploited, utilizing only one-quarter of the disc. Symmetry boundary conditions were applied to the face depicted in Figure III.3-a, at a Z-coordinate equal to half the disc thickness (i.e., the disc midplane), while anti-symmetry conditions were applied to nodes on the other symmetry plane. For mode 3 simulation, only anti-symmetry boundary conditions were used, resulting in a model representing half of a full disc.

An essential consideration in defining the FE model parameters is the elastic property of the plate material. The mesh requirements for convergence vary depending on material orientation, necessitating a multi-variable optimization of the number of elements and spacing ratio in both in-plane and through-the-thickness directions. The parameters for each model were adjusted until the maximum value at the notch tip exhibited a variation of less than 1%. This output variable was chosen for convergence analysis under the rationale that the most critical zone for Mode 2 to Mode 3 coupling is near the notch tip.

The initial focus was on discs with a thickness of t=1 mm subjected to pure mode 2 loading and weakened by elliptical notches with a root radius of ρ=0.001 mm. Results for the plane z/t=0.4 (where z is the distance from the midplane) are presented in Figures III.4-8. Figure III.4 shows the normal in-plane stress component tangent to the notch edge, σ_{vv}, plotted against the polar angle θ, measured with respect to the ellipse foci. In Figure III.5, the shear stress τ_{xy}, evaluated along the notch bisector line, is presented as a function of the distance from the notch tip. In both cases, the results from three-dimensional numerical analyses align perfectly with the two-dimensional solution provided by Eq. III.13 and Eq. III.18.

Figures III.6 and III.7 shift attention to out-of-plane shear stresses induced by three-dimensional effects. These stress components can be accurately predicted using the solutions derived for antiplane deformation, as expressed in Eq. III.26-28 and Eq. III.30. Figure III.8 demonstrates that, for various z/t values, induced out-of-plane shear stresses remain self-similar, except when very close to the free surface of the disc. The choice of z/t=0.4 was made to ensure comparable magnitudes between the induced stresses and the main stresses generated by the imposed loading conditions in the numerical simulations, making it representative for any z value at a sufficient distance from the free edge of the disc.

Subsequently, exploring various thickness values for the disc (t=1 mm, 5 mm, and 10 mm), the patterns of the maximum in-plane shear stress $\tau_{xy}^{Max}(z)$, and the maximum out-of-plane shear stress $\tau_{zy}^{Max}(z)$, are depicted in Figures III.9-a and III.9-b, respectively. In these figures, it is evident that:

- The maximum in plane shear stress $\tau_{xy}^{Max}(z)$ remains constant for most of the plane thickness, and significantly increases as approaching the free surface of the plate (Figure III.9-a);
- The maximum out-of-plane shear stress $\tau_{zy}^{Max}(z)$ has almost a linear trend up to z/t around 0.3. Approaching the free surface of the disc the trend becomes strongly nonlinear;
- Increasing the disc thickness, the intensity of induced out-of-plane shear stresses significantly increases (Figure III.9-b), whereas the influence of the thickness on $\tau_{xy}^{Max}(z)$ is limited (Figure III.9-a).

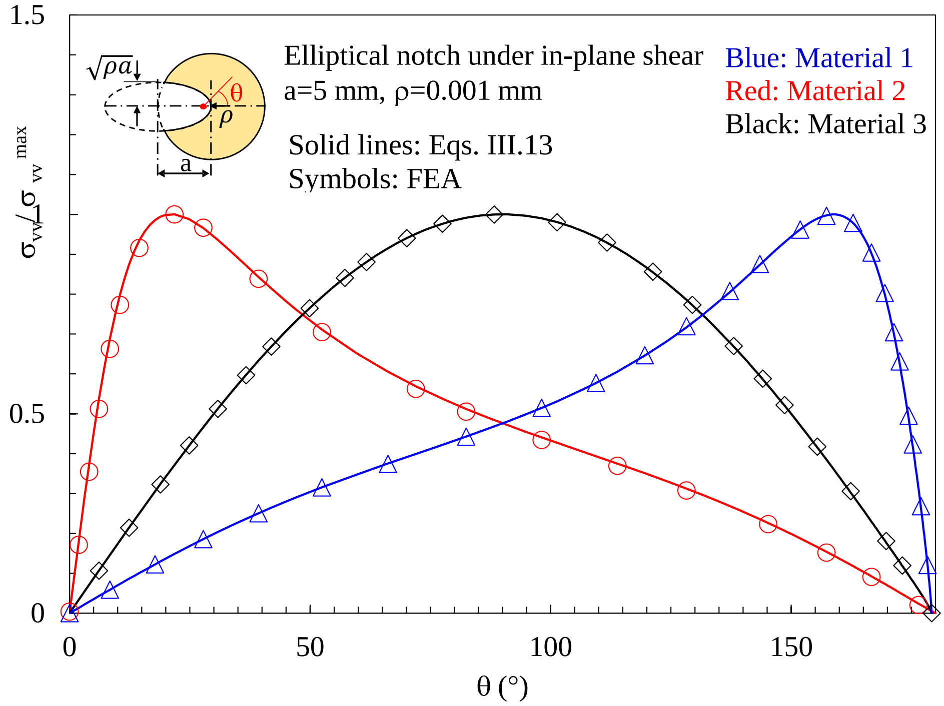

Figure III.4. Disc with t=1 mm and weakened by an elliptical notch with ρ=0.001 mm. Mode 2 loadings, different materials. Representation of the in-plane stress component σ_{vv} along the notch edge together with a comparison with Eqs. III.13. Distance from the midplane z/t=0.4.

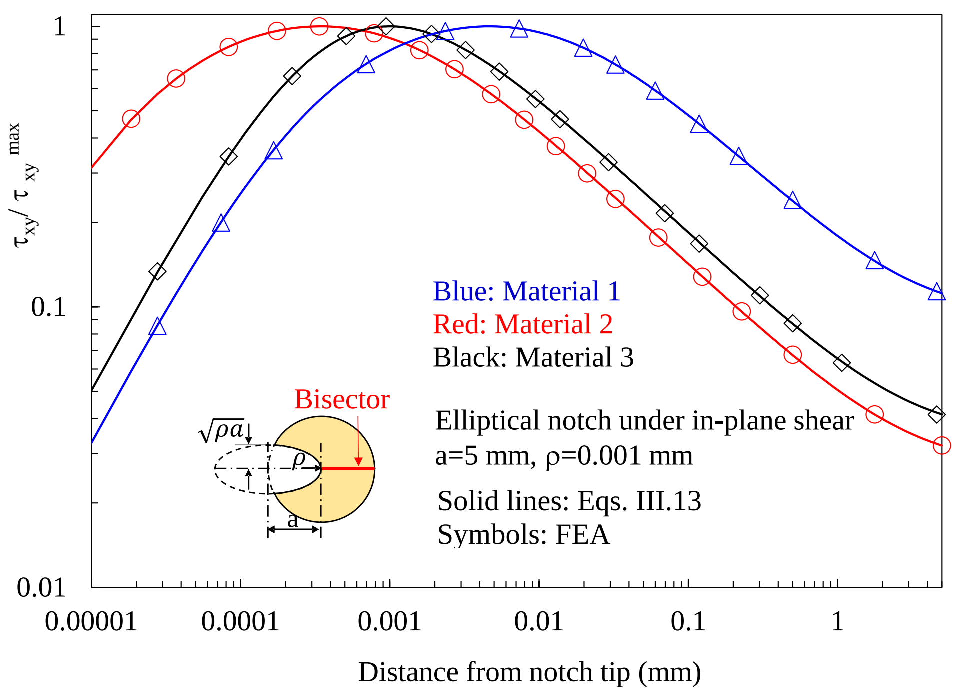

Figure III.5. Disc with t=1 mm and weakened by an elliptical notch with ρ=0.001 mm. Mode 2 loadings, different materials. Representation of the in-plane stress component τ_{xy} along the notch bisector together with a comparison with Eq. III.13. Distance from the midplane z/t=0.4.

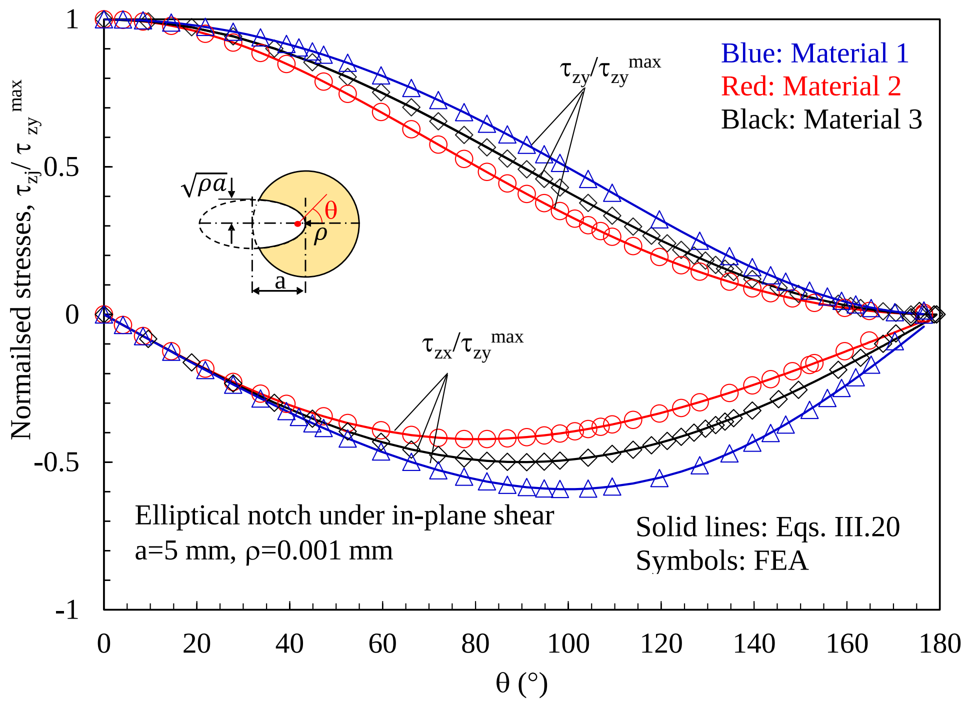

Figure III.6. Disc with t=1 mm and weakened by an elliptical notch with ρ=0.001 mm. Mode 2 loadings, different materials. Representation of the induced out-of-plane stress components τ_{xz} and τ_{yz} along the notch edge together with a comparison with Eq. III.20. Distance from the midplane z/t=0.4.

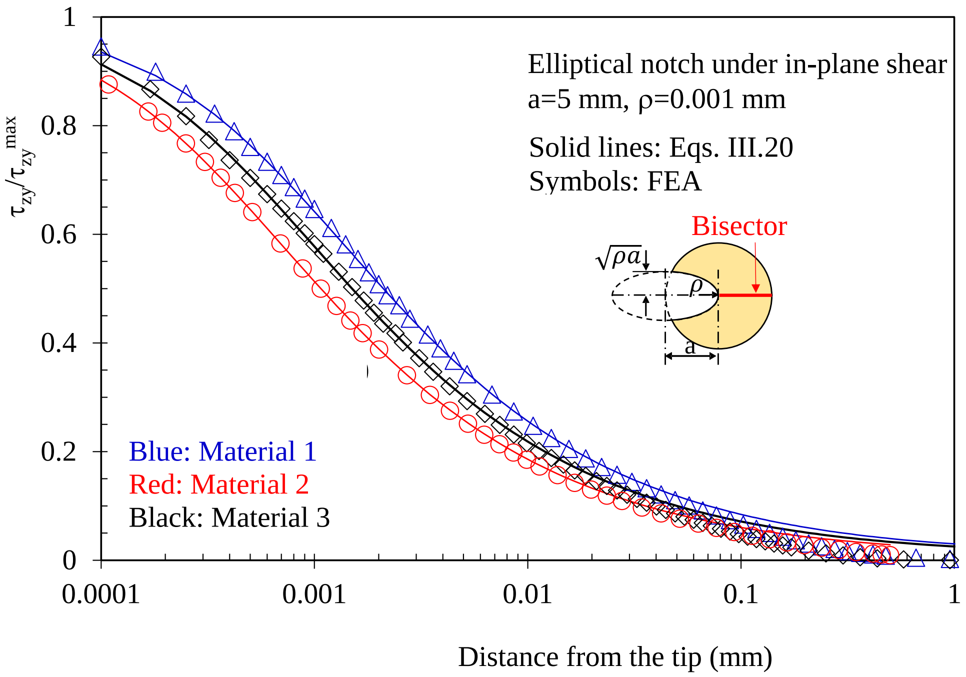

Figure III.7. Disc with t=1 mm and weakened by an elliptical notch with ρ=0.001 mm. Mode 2 loadings, different materials. Representation of the induced out-of-plane stress component τ_{zy} along the notch bisector together with a comparison with Eq. III.20. Distance from the midplane z/t=0.4.

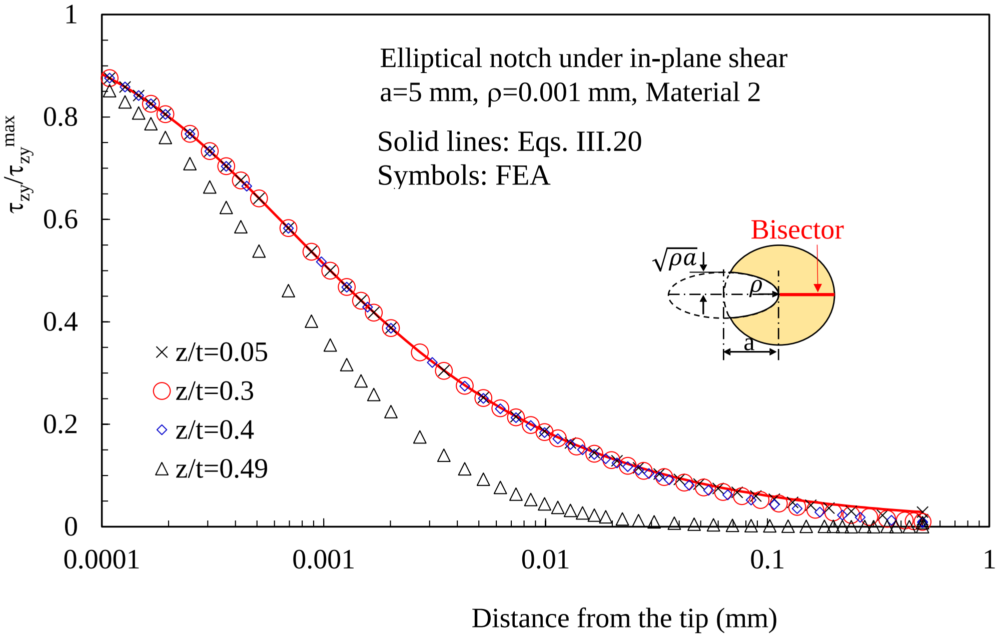

Figure III.8. Disc with t=1 mm and weakened by an elliptical notch with ρ=0.001 mm. Mode 2 loadings, material 2. Representation of the induced out-of-plane stress component τ_{zy} along the notch bisector together with a comparison with Eq. III.20. Different distances from the midplane (z/t).

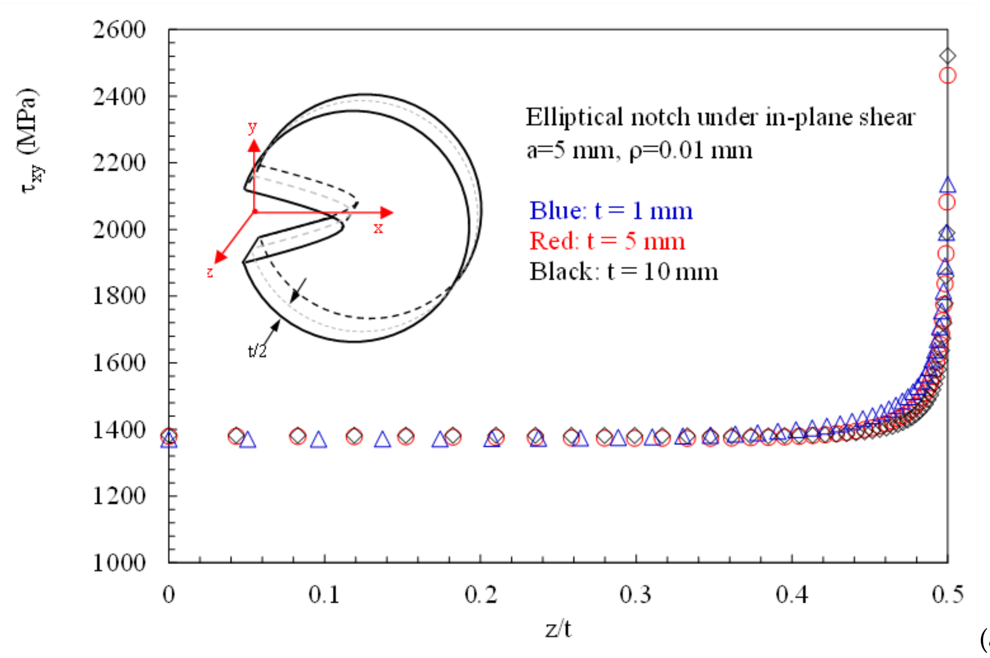

(a)

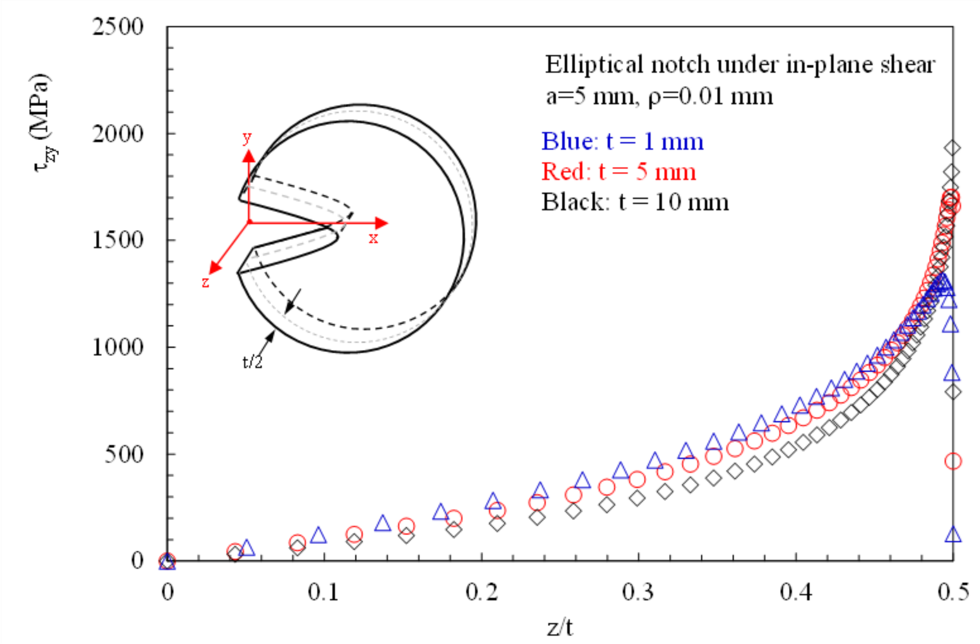

(b)

Figure III.9. Disc weakened by an elliptical notch with ρ=0.01 mm. Mode 2 loadings, material 2. Representation of the $\tau_{xy}^{Max}(z)$ (a) and $\tau_{zy}^{Max}(z)$ (b) as a function of the distance from the mid plane (z/t). Different thicknesses (t=1 mm, 5 mm, 10 mm).

Figures III.10 and III.11 illustrate the impact of varying notch root radii on out-of-plane shear stresses. Specifically, observations from Figure 10 reveal that increasing the notch radius leads to the following effects:

- The accuracy of Eq. III.20 diminishes. As per the analytical discussion in section 2, this decline is attributed to the increasing significance of terms $f'(z)\times u(x,y)$ and $f'(z)\times v(x,y)$ when reducing the notch root radius, in comparison to $g(z)\cdot\partial w(x,y)/\partial x$ and $g(z)\cdot\partial w(x,y)/\partial y$

- The area ahead of the notch tip, where out-of-plane shear stresses are noteworthy, progressively contracts.

Furthermore, Figure III.11 highlights that with an increase in the notch radius, the intensity of $\tau_{zy}^{Max}(z)$ experiences a significant reduction. Subsequent to this analysis, focus shifted to discs with a thickness of t=1 mm subjected to pure mode 2 loading and weakened by hyperbolic notches with a root radius ρ=0.01 mm and varying notch opening angles. Results for the plane z/t=0.4 (where z is the distance from the midplane) are presented in Figures III.12-14. Particularly, in Figure III.12, the normal stress component tangent to the notch edge, σ_{vv}, is plotted against the polar angle θ. Once again, the results from three-dimensional numerical analyses perfectly align with the two-dimensional solution, as expressed in Eqs. III.26-28.

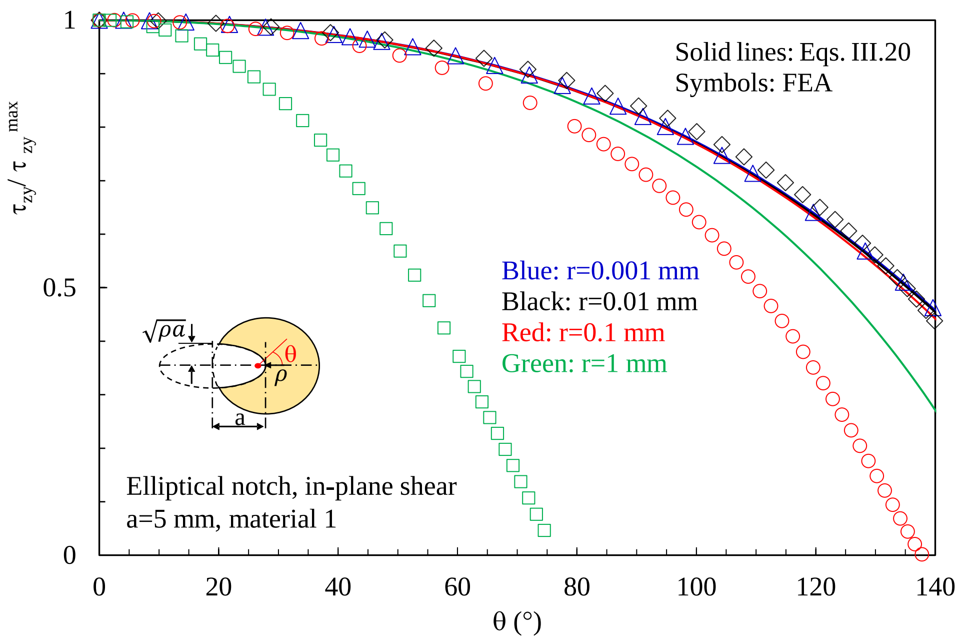

Figure III.10. Discs with t=1 mm and weakened by elliptical notches. Mode 2 loadings, material 2. Representation of the induced out-of-plane stress component τ_{zy} along the notch bisector together with a comparison with Eq. III.20. Different values for the notch root radius.

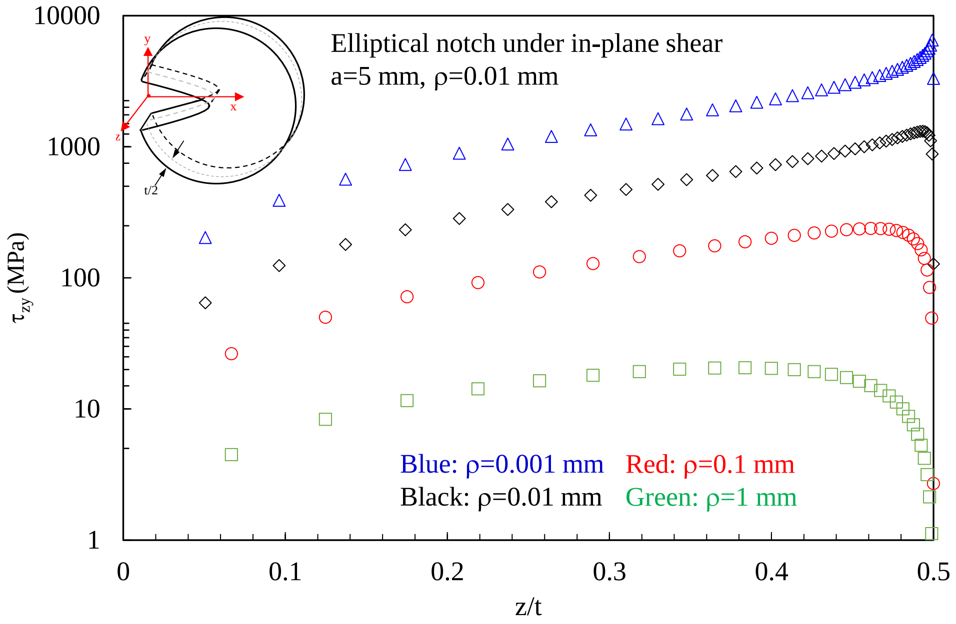

Figure III.11. Discs with t=1 mm and weakened by elliptical notches. Mode 2 loadings, material 1. Representation of the $\tau_{zy}^{Max}(z)$ as a function of the distance from the mid plane (z/t). Different values for the notch root radius.

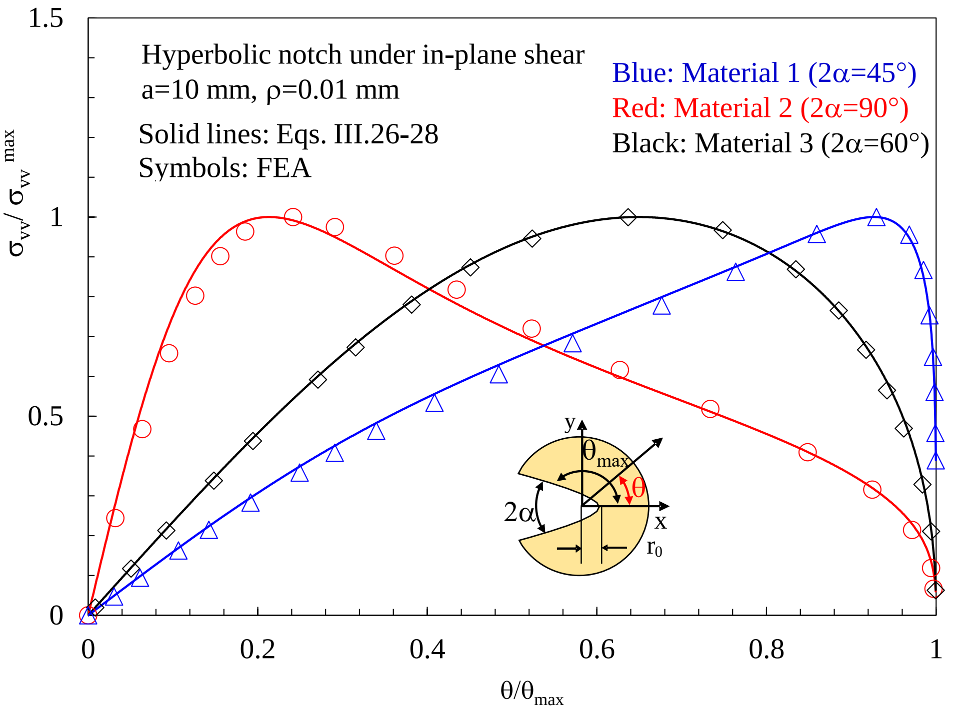

Figure III.12. Discs with t=1 mm and weakened by hyperbolic notches with ρ=0.01 mm. Mode 2 loadings, different materials. Representation of the in-plane stress component σ_{vv} along the notch edge together with a comparison with Eqs. III.26-28. Distance from the midplane z/t=0.4.

Figures III.13 and III.14 reaffirm that three-dimensional effects result in out-of-plane shear stresses that can be precisely anticipated using the solutions derived for the antiplane deformation problem, as indicated by Eq. III.30, regardless of the specific material system under consideration.

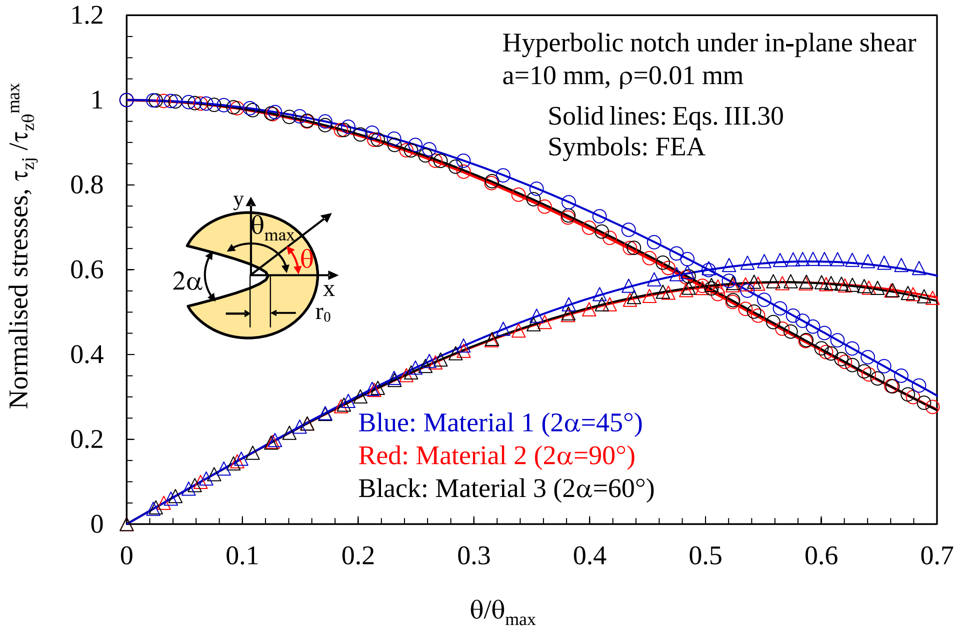

Figure III.13. Discs with t=1 mm and weakened by hyperbolic notches with ρ=0.01 mm. Mode 2 loadings, different materials. Representation of the induced out-of-plane stress components τ_{xz} and τ_{yz} along the notch edge together with a comparison with Eq. III.30. Distance from the midplane z/t=0.4.

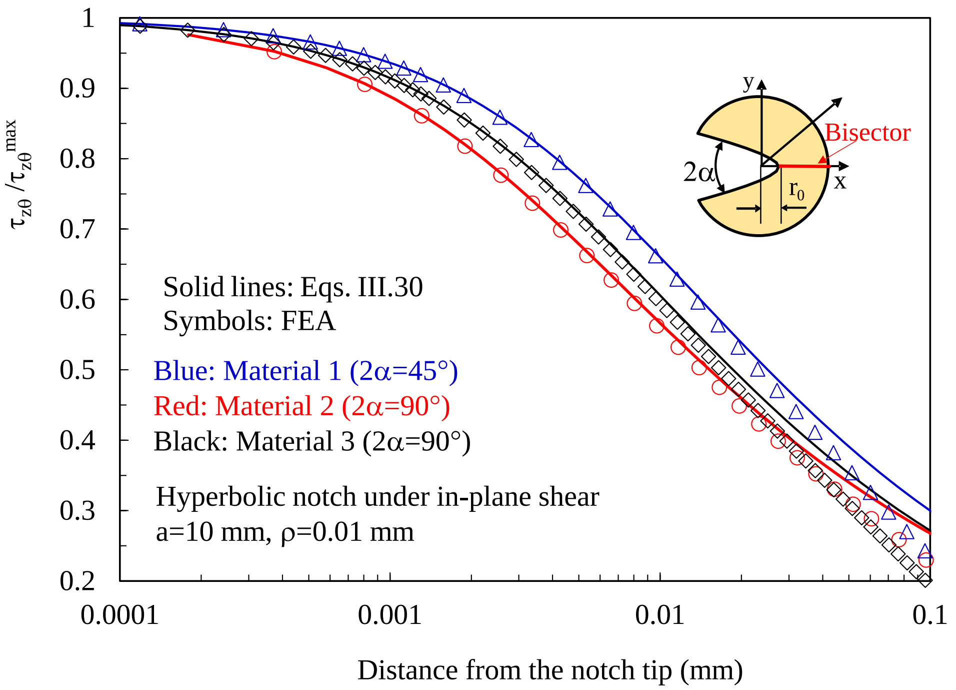

Figure III.14. Discs with t=1 mm and weakened by hyperbolic notches with ρ=0.01 mm. Mode 2 loadings, different materials. Representation of the induced out-of-plane stress component τ_{zy} along the notch bisector together with a comparison with Eq. III.30. Distance from the midplane z/t=0.4.

Ultimately, the disc composed of Material 2 and featuring a hyperbolic notch with ρ=0.01 mm and 2α=90° underwent loading under pure mode III, applying the displacement fields outlined in Appendix A. In this instance, Figure III.15 illustrates the presence of induced in-plane shear stresses (induced mode 2), accurately predictable using Eqs. III.26-28.

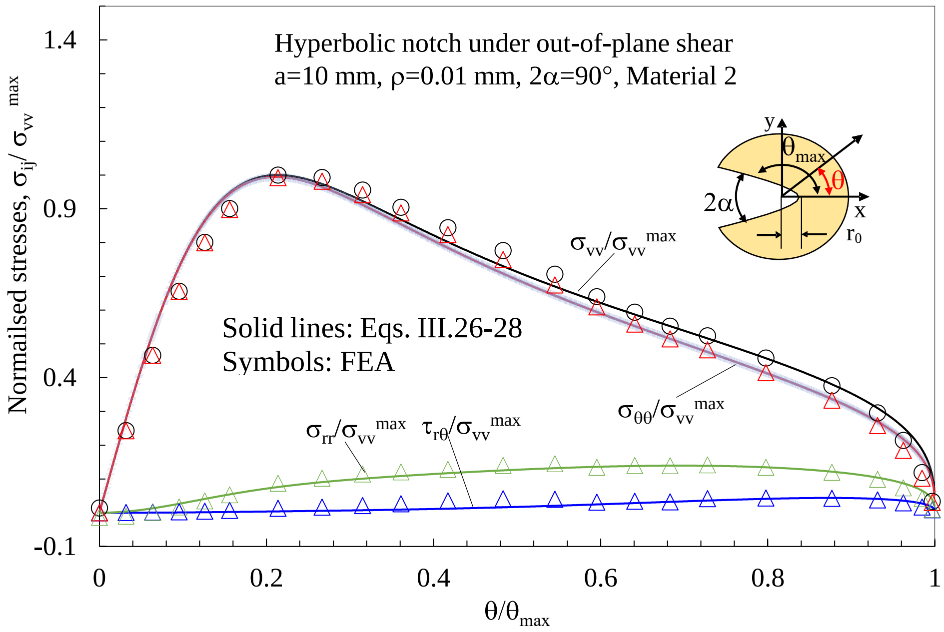

Figure III.15. Discs with t=1 mm and weakened by hyperbolic notches with ρ=0.01 mm and 2α=90°. Mode 3 loadings, materials 2. Representation of the induced in-plane stress components along the notch edge together with a comparison with Eqs. III.26-28. Distance from the midplane z/t=0.4.

3.6. Conclusions

This chapter presents an analytical solution for stress fields in the immediate vicinity of radiused notches in thick orthotropic plates subjected to shear loading and twisting. Initially, the three-dimensional theory of elasticity equations are successfully transformed into two uncoupled equations in the two-dimensional space. Subsequently, the paper provides a 3D stress field solution for orthotropic plates with radiused notches, and the accuracy of this solution is discussed by comparing theoretical results with numerical data obtained from 3D finite element analyses.

Based on the presented and discussed results, the following key conclusions can be drawn:

- Three-dimensional effects in thick plates or discs lead to coupling phenomena between loading modes. Specifically, out-of-plane shear stresses (mode 3) are induced on in-plane shear-loaded (mode 2) solids, and their accurate prediction can be achieved using solutions derived for the antiplane deformation problem. The reverse holds true as well, irrespective of the orthotropic material system considered.

- The increase in disc or plate thickness correlates with a rise in the intensity of stresses induced by 3D effects.
- The intensity of induced stresses is significantly influenced by the notch root radius, and this phenomenon tends to diminish in the presence of large notch root radii.

3.7. References

1. Neuber, H. "Theory of notch stresses." Springer-Verlag, Berlin, Germany. 1958.

2. Creager M, Paris, P.C.; "Elastic field equations for blunt cracks with reference to stress corrosion cracking." Int. J. Fract. Mech. 1967, 3, 247-252; DOI: 10.1007/BF00182890

3. Lazzarin P., Tovo R. "A unified approach to the evaluation of linear elastic stress fields in the neighborhood of cracks and notches." Int. J. Fract. 1996, 78, 3-19; DOI: 10.1007/BF00018497

4. Zappalorto M., Lazzarin P., Filippi S. "Stress field equations for U and blunt V-shaped notches in axisymmetric shafts under torsion." Int. J. Fract. 2010, 164, 253-269; DOI: 10.1007/s10704-010-9493-6

5. Zappalorto M., Lazzarin P. "Stress fields due to inclined notches and shoulder fillets in shafts under torsion." J. Strain Anal. Eng. 2011, 46, 187-199 DOI: 10.1177/0309324710396019

6. Zappalorto M., Lazzarin P. "In-plane and out-of-plane stress field solutions for V-notches with end holes." Int. J. Fract. 2011, 168, 167-180. DOI: 10.1007/s10704-010-9567-5

7. Lekhnitskii S.G. "Theory of Elasticity of an Anisotropic Body." Mir Publishers, Moscow. 1984.

8. Bonora N., Costanzi M., Marchetti M. "On closed form solution for the elastic stress field around holes in orthotropic composite plates under in-plane stress conditions." Compos. Struct. 1993, 25, 139-156. DOI: 10.1016/0263-8223(93)90160-R

9. Bonora N., Costanzi M., Marchetti M. "A computational procedure to calculate stress-strain field around simple shape holes in composite laminates." Compos. Struct. 1994, 53, 1167–1179. DOI: 10.1016/0045-7949(94)90164-3

10. Zappalorto M., Carraro P.A. "Stress distributions for blunt cracks and radiused slits in anisotropic plates under in-plane loadings." Int. J. Solids Struct. 2015, 56–57, 136-141. DOI: 10.1016/j.ijsolstr.2014.11.024

11. Sih G.C., Paris P.C., Irwin G.R. "On cracks in rectilinearly anisotropic bodies." Int. J. Fract. Mech. 1965, 1, 189-203. DOI: 10.1007/BF00186854

12. Kazberuk A., Savruk M.P., Chornenkyi A.B. "Stress distribution at sharp and rounded V-notches in quasi-orthotropic plane." Int. J. Solids Struct. 2016, 85-86, 134-143. DOI:10.1016/j.ijsolstr.2016.02.012

13. Prabhu S., Lambros J. "A Numerical Investigation of Three Dimensional Effects in Cracked Orthotropic Plates." J. Compos. Mater. 2000, 34, 116-134. DOI: 10.1177/002199830003400203

14. Cheng C.Z., Zhou W., Niu Z.R., Recho N. "Stress singularity analysis for orthotropic V-notches in the generalised plane strain state." Fatigue Fract. Eng. M. 2015, 38, 881–896. DOI: 10.1111/ffe.12282

15. Pageau S.S., Biggers S.B.J. "A finite element approach to three-dimensional singular stress states in anisotropic multi-material wedges and junctions." Int. J. Solids Struct. 1996, 33, 33–47.

16. Choi Y.K., Folias E.S. "The 3D stress field in a laminated composite plate with a hole based on an h-r finite element method." In Failure Mechanics in Advanced Polymeric Composites ASME AMD. 1994, 196, 31-42.

17. Kotousov A., Wang C.H. "Three-dimensional solutions for transversally isotropic composite plates." Compos. Struct. 2002, 57, 445–452. DOI: 10.1016/S0263-8223(02)00112-5

18. Kotousov A., Wang C.H. "A generalized plane-strain theory for transversally isotropic plates." Acta Mech. 2003, 161, 53–64. DOI: 10.1007/s00707-002-0988-8

19. Zappalorto M., Carraro P.A. "Stress fields at sharp angular corners in thick anisotropic composite plates." Compos. Struct. 2014, 117, 346–353. DOI: 10.1016/j.compstruct.2014.06.036

20. Zappalorto M., Carraro P.A., Quaresimin M. "Analytical solution for the three-dimensional stress fields in anisotropic composite bimaterial corners." Comp. Struct. 2015, 122, 127-138. DOI: 10.1016/j.compstruct.2014.11.045

21. Zappalorto M. "On the stress state in rectilinear anisotropic thick plates with blunt cracks." Fatigue Fract. Eng. Mater. Struct. 2017, 40, 103-119. DOI: 10.1111/ffe.12479

22. Shi Y., Wang B., Wu H., Wang B., Liu C., Li R. "A Theoretical and Experimental Study on Extreme Stress Concentration-Free Designs of Circumferentially Notched Thin Cylindrical Shells." J. Appl. Mech. 2020, 87, 021004. DOI: 10.1115/1.4045281

23. Wang B., Shi Y., Li R., Wang B. "A Simplified Indirect Measuring Method for the Notch Stress in a Thin Cylindrical Shell." J. Appl. Mech. 2018, 85, 071009. DOI: 10.1115/1.4039950

24. Kotousov A., Lew Y.T. "Stress singularities resulting from various boundary conditions in angular corners of plates of arbitrary thickness in extension." Int. J. Solids Struct. 2006, 43, 5100–5109. DOI: 10.1016/j.ijsolstr.2005.06.037

25. Berto F., Lazzarin P., Kotousov A., Pook L P. "Induced out-of-plane mode at the tip of blunt lateral notches and holes under in-plane shear loading." Fatigue Fract. Eng. M. 2012, 35, 538–555. DOI: 10.1111/j.1460-2695.2011.01647.x

26. Berto F., Marangon C. "Three-dimensional effects in finite thickness plates weakened by rounded notches and holes under in-plane shear." Fatigue Fract. Eng. M. 2013 36, 1139–1152. DOI: 10.1111/ffe.12098

27. Lazzarin P., Zappalorto M. "A three-dimensional stress field solution for pointed and sharply radiused V-notches in plates of finite thickness." Fatigue Fract. Eng. M. 2012 35, 1105–1119. DOI: 10.1111/j.1460-2695.2012.01698.x

28. Zappalorto M., Lazzarin P. "Three-dimensional elastic stress fields ahead of notches in thick plates under various loading conditions." Eng. Fract. Mech. 2013, 108, 75–88. DOI: 10.1016/j.engfracmech.2013.02.031

29. Lazzarin P., Zappalorto M., Berto F. "Three-dimensional stress fields due to notches in plates under linear elastic and elastic–plastic conditions." Fatigue Fract. Eng. M. 2015, 38, 140–153. DOI: 10.1111/ffe.12138

30. Zappalorto M., Carraro P.A. "Stress distributions for blunt cracks and radiused slits in anisotropic plates under in-plane loadings." Int. J. Solids Struct. 2015, 56-57, 136-141. DOI: 10.1016/j.ijsolstr.2014.11.024

31. Zappalorto M., Carraro P.A. "An engineering formula for the stress concentration factor of orthotropic composite plates." Composites Part B, 2015, 68, 51-58. DOI: 10.1016/j.compositesb.2014.08.020

32. Zappalorto M., Salviato M. "Antiplane shear stresses in orthotropic plates with lateral blunt notches." Eur. J. Mech. A-Solids, 2019, 77, 103815 DOI: 10.1016/j.euromechsol.2019.103815

33. Savin G. N. "Stress Concentration Around Holes." Pergamon, London. 1961.

34. Zappalorto M., Carraro P.A. "Two-dimensional stress distributions in tensioned orthotropic plates weakened by blunt V-shaped notches." Fatigue Fract. Eng. Mater. Struct. 2017, 40, 804-819. DOI: 10.1111/ffe.12554

35. Pastrello, M; Salviato, M and Zappalorto, M. "Analytical study on the mode III stress fields due to blunt notches with cracks." Fatigue Fract. Eng. M. 42, 612-626. https://doi.org/10.1111/ffe.12936

4. A semi-analytical approach to calculate Generalized Stress Intensity Factors and Stress concentration factors

4.1. Introduction

The detailed characterization of stress states in notched or bonded components requires knowledge of stress singularity orders, characteristic angular functions, and generalized stress intensity factors (GSIF). In the literature, detailed analytical formulations for singularity orders and characteristic angular functions can be found; for example, Williams ML 1952[1], Neuber 1958[2], Barroso A. et al. 2003[3]. However, for the calculation of GSIF, it is still common practice to rely on numerical modelling such as FEM and BEM. These methods can be precise and reliable but present various challenges. One of the classic techniques utilizing finite element modelling is the method by Gross and Mendelson 1972[4] and Dunn et al. 1997[5].

However, this method has the disadvantage of requiring an extremely fine mesh in the vicinity of the notch apex, where the singularity influences stress fields.

Over the years, many researchers have focused on developing methods for calculating GSIF that can avoid this drawback. An example of such a method is the Peak Stress Method (PSM) developed by Meneghetti G. and Lazzarin P. 2007[6]. Through a sparse but regular mesh in a finite element model, PSM correlates GSIF with the stress calculated near the singularity in the numerical model through a proportionality factor. Another strategy to avoid very fine meshes is to exploit the mesh insensitivity property of deformation energy. This method, developed by Lazzarin P. et al. 2010[7], requires calculating the average elastic energy density in a control volume that encompasses the singularity. The calculated value can then be correlated with GSIF through a simple analytical equation, at the cost of defining the control volume within the FEM model. Other methods, on the other hand, use

BEM analysis. Barroso A. et al. 2012[8] demonstrate how it is possible to use a least squares optimization procedure to obtain GSIF from nodal displacements near the singularity.

This chapter presents a new method that completely departs from FEM or BEM modelling to overcome all the associated challenges. The proposed method relies on a careful analytical description of the shape of stress fields around a singularity, coupled with a procedure for minimizing the square of stress residuals along the boundary of the analysed domain. This method seeks to establish itself as an alternative to the above-mentioned methods while maintaining accuracy. For this reason, the results obtained with the new methodology will be compared with accurate FEM analyses.

4.2. Stress fields in the vicinity of a multi-material singularity

A multimaterial singularity in the tensional fields of a component occurs when different materials meet at a point in the component. Referring to Figure IV.1, in a singularity generated by N materials, each material is identified with an integer n ranging from 1 to N, with the domains of each material delimited by radial boundaries located at angles θ_{n-1} and θ_n, where θ_0 and θ_N are the free boundaries of the component. The multimaterial cut can be viewed as the general case of a V-cut when only one material is present and if $\theta_N - \theta_0 > \pi$.

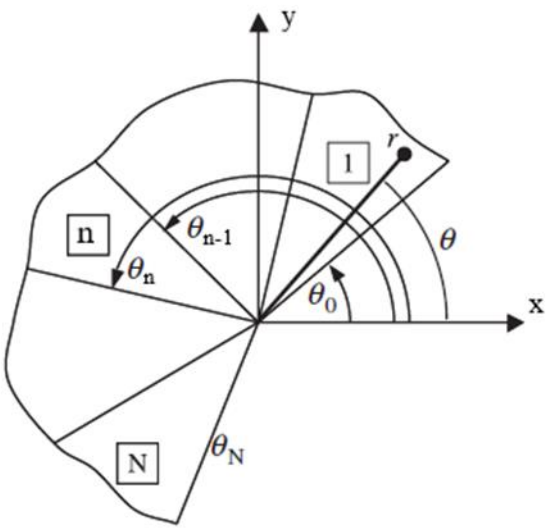

Figure IV.1. Diagram illustrating the geometry and parameters used to describe a multimaterial singularity.

For each domain n of the multimaterial corner, the tensional and displacement fields can be expressed using two complex potential functions as follows:

$$\begin{aligned}
\sigma_{rr}^{(n)}(r,\theta) &= 2\,\mathrm{Re}\left[\frac{d\Phi_1^{(n)}(z)}{dz}\right] - \mathrm{Re}\left[e^{2i\theta}\left(\bar{z}\frac{d^2\Phi_1^{(n)}(z)}{dz^2} + \frac{d\Phi_2^{(n)}(z)}{dz}\right)\right] \\
\sigma_{\theta\theta}^{(n)}(r,\theta) &= 2\,\mathrm{Re}\left[\frac{d\Phi_1^{(n)}(z)}{dz}\right] + \mathrm{Re}\left[e^{2i\theta}\left(\bar{z}\frac{d^2\Phi_1^{(n)}(z)}{dz^2} + \frac{d\Phi_2^{(n)}(z)}{dz}\right)\right] \\
\sigma_{r\theta}^{(n)}(r,\theta) &= \mathrm{Im}\left[e^{2i\theta}\left(\bar{z}\frac{d^2\Phi_1^{(n)}(z)}{dz^2} + \frac{d\Phi_2^{(n)}(z)}{dz}\right)\right]
\end{aligned} \qquad \text{IV.1}$$

$$\begin{aligned}
2\mu^{(n)}\left(u_x^{(n)}(r,\theta) + \mathbf{i}u_y^{(n)}(r,\theta)\right) &= \kappa^{(n)}\Phi_1^{(n)}(z) - z\overline{\frac{d\Phi_1^{(n)}(z)}{dz}} - \overline{\Phi_2^{(n)}(z)} \\
u_r^{(n)}(r,\theta) + \mathbf{i}u_\theta^{(n)}(r,\theta) &= e^{-i\theta}\left(u_x^{(n)}(r,\theta) + \mathbf{i}u_y^{(n)}(r,\theta)\right)
\end{aligned} \qquad \text{IV.2}$$

With:

$$\kappa^{(n)} = \begin{cases} 3 - 4\nu^{(n)} & \text{Plain Strain} \\ \dfrac{3-\nu^{(n)}}{1+\nu^{(n)}} & \text{Plane Stress} \end{cases} \qquad \text{IV.3}$$

The chosen potential functions are:

$$\begin{aligned}
\Phi_1^{(n)}(z) &= \sum_{m=1}^{M}\left(A_{1,1}^{(n,m)}z^{\lambda_m} + A_{1,2}^{(n,m)}z^{\bar{\lambda}_m}\right) \\
\Phi_2^{(n)}(z) &= \sum_{m=1}^{M}\left(A_{2,1}^{(n,m)}z^{\lambda_m} + A_{2,2}^{(n,m)}z^{\bar{\lambda}_m}\right)
\end{aligned} \qquad \text{IV.4}$$

Where λ_m is the complex eigenvalue associated with the m-th term of the potentials, and $A_{i,j}^{(n,m)}$ are complex constants. To determine the eigenvalues and constants $A_{i,j}^{(n,m)}$, it is necessary to apply boundary conditions along all radial boundaries between different materials:

$$\begin{cases}
\sigma_{\theta\theta}^{(n)}(r,\theta_{n-1}) = \sigma_{\theta\theta}^{(n-1)}(r,\theta_{n-1}) \\
\sigma_{r\theta}^{(n)}(r,\theta_{n-1}) = \sigma_{r\theta}^{(n-1)}(r,\theta_{n-1}) \\
u_r^{(n)}(r,\theta_{n-1}) = u_r^{(n-1)}(r,\theta_{n-1}) \\
u_\theta^{(n)}(r,\theta_{n-1}) = u_\theta^{(n-1)}(r,\theta_{n-1})
\end{cases} \qquad \forall n \in [2,\dots,N] \qquad \text{IV.5}$$

And along the notch boundaries:

$$
\begin{aligned}
&\sigma_{\theta\theta}^{(1)}(r,\theta_0)=0\\
&\sigma_{r\theta}^{(1)}(r,\theta_0)=0\\
&\sigma_{\theta\theta}^{(N)}(r,\theta_N)=0\\
&\sigma_{r\theta}^{(N)}(r,\theta_N)=0
\end{aligned}
\qquad \text{IV.6}
$$

These conditions can be expressed in matrix form:

$$\mathbf{L}^{(m)}\cdot\tilde{A}^{(m)}=\mathbf{0} \qquad \text{IV.7}$$

With:

$$\mathbf{L}^{(m)}=\begin{bmatrix} l_{1,1}^{(m)} & \cdots & l_{1,4N}^{(m)} \\ \vdots & \ddots & \vdots \\ l_{4N,1}^{(m)} & \cdots & l_{4N,4N}^{(m)} \end{bmatrix} \quad \tilde{A}^{(m)}=\begin{bmatrix} A_{1,1}^{(1,m)} \\ A_{1,2}^{(1,m)} \\ A_{2,1}^{(1,m)} \\ A_{2,2}^{(1,m)} \\ \vdots \\ A_{1,1}^{(N,m)} \\ A_{1,2}^{(N,m)} \\ A_{2,1}^{(N,m)} \\ A_{2,2}^{(N,m)} \end{bmatrix} \qquad \text{IV.8}$$

The M eigenvalues can be determined by imposing:

$$\mathrm{Det}\left[\mathbf{L}^{(m)}\right]=0 \qquad \text{IV.9}$$

While the constants $A_{i,j}^{(n,m)}$ are found by solving the system IV.7 minus M constants $A_{1,1}^{(1,m)}$, and it is possible to redefine them as follows

$$
\begin{aligned}
&A_{s,t}^{(n,m)}=\chi_{s,t}^{(n,m)}K_m\\
&A_{1,1}^{(1,m)}=K_m
\end{aligned}
\qquad \text{IV.10}
$$

Reducing the number of constants to be determined in IV.4 to M values K_m

4.3. Determination of the Generalized Stress Intensity Factors

To determine the constants K_m, it is necessary to impose boundary conditions only on the remaining boundaries of the domain. This is made possible by the choice of potentials made in the previous chapter, which exactly satisfy the boundary conditions along the edges of the cut and between the various materials. Considering Figure IV.2, the external boundaries where it is necessary to apply boundary conditions are highlighted in red, and for each domain, it is possible to define the parametric equation describing the boundary, $B_n(s)$. The u and v directions are then defined, which are respectively the normal and tangential directions to the boundaries, and the relevant external loads for the application of boundary conditions: $\sigma_{uu}^{(n),ext}(s)$ the external normal stress applied to the boundary $B_n(s)$, $\sigma_{uv}^{(n),ext}(s)$ the shear stress, $u_u^{(n),ext}(s)$ and $u_v^{(n),ext}(s)$ the normal and tangential displacements.

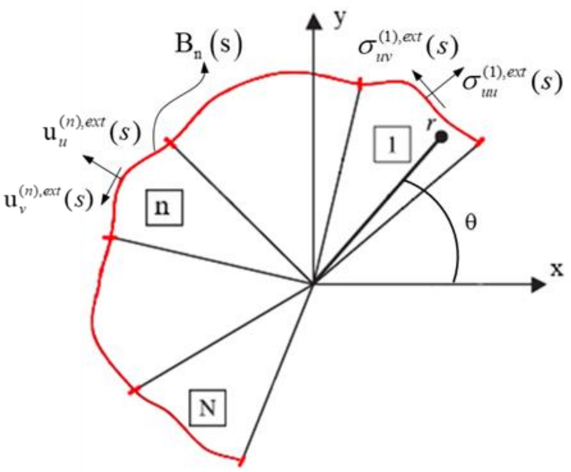

Figure IV.2. Diagram for defining external boundaries and applied external loads for the minimization of residues in a multimaterial singularity.

It is possible to define the average distance from the external boundary to the frame of reference's origin:

$$r_{avg} = \frac{\sum_{n=1}^{N} \int_{B_n} \|B_n(s)\| ds}{\sum_{n=1}^{N} \int_{B_n} ds} \qquad \text{IV.11}$$

While substituting IV.10 into IV.4 one can redefine the potential functions as follows:

$$
\begin{aligned}
\Phi_1^{(n)}(z) &= \sum_{m=1}^{M} \frac{K_m}{r_{avg}^{\mathrm{Re}[\lambda_m]}} \left(z^{\lambda_m} + \chi_{1,2}^{(n,m)} z^{\overline{\lambda}_m} \right) \\
\Phi_2^{(n)}(z) &= \sum_{m=1}^{M} \frac{K_m}{r_{avg}^{\mathrm{Re}[\lambda_m]}} \left(\chi_{2,1}^{(n,m)} z^{\lambda_m} + \chi_{2,2}^{(n,m)} z^{\overline{\lambda}_m} \right)
\end{aligned}
\qquad \text{IV.12}
$$

And substituting IV.12 into IV.1-2 one obtains:

$$
\begin{aligned}
\sigma_{st}^{(n)}(r,\theta) &= \sum_{m=1}^{M} \frac{K_m}{r^{1-\lambda_m}} f_{st}^{(n,m)}(\theta) \\
u_s^{(n)}(r,\theta) &= \sum_{m=1}^{M} K_m r^{\lambda_m} g_s^{(n,m)}(\theta)
\end{aligned}
\qquad \mathrm{con\,s,t} \in \{r,\theta\} \qquad \text{IV.13}
$$

The external boundary conditions are:

$$
\begin{cases}
\sigma_{uu}^{(n)}(r,\theta) - \sigma_{uu}^{(n),ext}(s)\Big|_{\{r,\theta\}\in B_n(s)} = 0 \\
\sigma_{uv}^{(n)}(r,\theta) - \sigma_{uv}^{(n),ext}(s)\Big|_{\{r,\theta\}\in B_n(s)} = 0 \\
\dfrac{E^{(n)}}{2r_{avg}\left(1+\nu^{(n)}\right)}\left(\mathrm{u}_u^{(n)}(r,\theta) - \mathrm{u}_u^{(n),ext}(s)\Big|_{\{r,\theta\}\in B_n(s)} \right) = 0 \\
\dfrac{E^{(n)}}{2r_{avg}\left(1+\nu^{(n)}\right)}\left(\mathrm{u}_v^{(n)}(r,\theta) - \mathrm{u}_v^{(n),ext}(s)\Big|_{\{r,\theta\}\in B_n(s)} \right) = 0
\end{cases}
\quad \forall n : 1 < n < N \qquad \text{IV.14}
$$

Which can be rewritten in matrix form:

$$
\widehat{\mathbf{P}}_n \cdot \widetilde{K} = \widehat{d}_n \qquad \forall n : 1 < n < N \qquad \text{IV.15}
$$

With:

$$
\widehat{\mathbf{P}}_n = \begin{bmatrix} \widehat{p}_{1,1}^{(n)} & \cdots & \widehat{p}_{1,M}^{(n)} \\ \vdots & \ddots & \vdots \\ \widehat{p}_{P,1}^{(n)} & \cdots & \widehat{p}_{P,M}^{(n)} \end{bmatrix}; \ \widetilde{K} = \begin{bmatrix} K_1 \\ \vdots \\ K_M \end{bmatrix}; \ \widehat{d}_n = \begin{bmatrix} \widehat{d}_1^{(n)} \\ \vdots \\ \widehat{d}_P^{(n)} \end{bmatrix} \qquad \text{IV.16}
$$

And P is the number of conditions to be satisfied for each boundary section. In most cases, these boundary conditions cannot be solved exactly, and therefore, a procedure of minimizing residual stresses at the boundary is employed. The objective is to minimize the square of residues at the boundary, along all sections of the external boundary:

$$
\mathrm{Min}\left[\sum_{n=1}^{N} \int_{B_n} \left\| \left(\widehat{\mathbf{P}}_n \cdot \widetilde{K} - \widehat{d}_n \right) \right\|^2 ds \right] = \mathrm{Min}\left[\left\| \mathbf{P} \cdot \widetilde{K} - \tilde{d} \right\|^2 \right] \qquad \text{IV.17}
$$

With:

$$\mathbf{P} = \begin{bmatrix} p_{1,1} & \cdots & p_{1,M} \\ \vdots & \ddots & \vdots \\ p_{N\cdot P,1} & \cdots & p_{N\cdot P,M} \end{bmatrix}; \ \tilde{d} = \begin{bmatrix} d_1 \\ \vdots \\ d_{N\cdot P} \end{bmatrix} \qquad \text{IV.18}$$

By minimizing equation IV.17, it is possible to obtain a solution for the constants K_m, and this solution will provide an increasingly better approximation for stresses in the component's domain as M increases. However, for some boundary conditions, this may result in a considerable number of terms in IV.12, leading to an increase in the computational power required to solve the numerical procedure. To mitigate this issue, it is possible to minimize IV.17 under certain auxiliary boundary conditions that allow for a faster convergence of the procedure. Referring to Figure IV.3, the external boundary, highlighted in blue, can be divided into $J = \frac{M}{4}$ sections $b_j(s)$ with $j \in \{1, \cdots, J\}$, all of the same angular length θ_{div}.

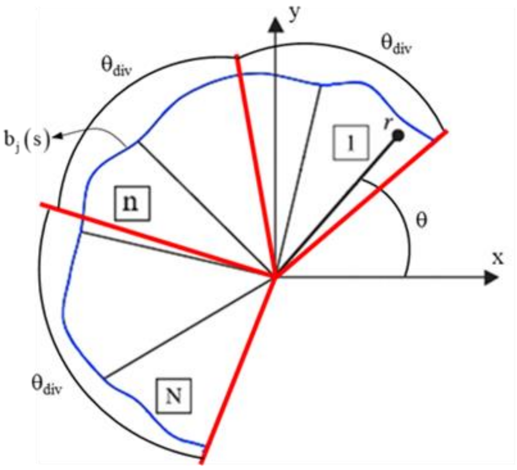

Figure IV.3. Diagram for the definition of auxiliary boundary conditions for a multimaterial singularity

For every section the following boundary conditions can be imposed:

$$\begin{cases} \int_{b_j(s)} \left(\sigma_{uu}^{(n)}\left(r,\theta\right) - \sigma_{uu}^{(n),ext}(s)\right) ds = 0 \\ \int_{b_j(s)} \left(\sigma_{uv}^{(n)}\left(r,\theta\right) - \sigma_{uv}^{(n),ext}(s)\right) ds = 0 \\ \int_{b_j(s)} \left(\mathrm{u}_{u}^{(n)}\left(r,\theta\right) - \mathrm{u}_{u}^{(n),ext}(s)\right) ds = 0 \\ \int_{b_j(s)} \left(\mathrm{u}_{v}^{(n)}\left(r,\theta\right) - \mathrm{u}_{v}^{(n),ext}(s)\right) ds = 0 \end{cases} \forall j : 1 < j < J \qquad \text{IV.19}$$

Or in matrix form:

$$\mathbf{C} \cdot \tilde{\mathrm{K}} = \tilde{\mathrm{h}} \qquad \text{IV.20}$$

With:

$$\mathbf{C} = \begin{bmatrix} \mathrm{c}_{1,1} & \cdots & \mathrm{c}_{1,\mathrm{M}} \\ \vdots & \ddots & \vdots \\ \mathrm{c}_{\hat{\mathrm{J}},1} & \cdots & \mathrm{c}_{\hat{\mathrm{J}},\mathrm{M}} \end{bmatrix}; \; \tilde{\mathrm{h}} = \begin{bmatrix} \mathrm{h}_1 \\ \vdots \\ \mathrm{d}_{\hat{\mathrm{J}}} \end{bmatrix} \qquad \text{IV.21}$$

It is therefore possible to solve the minimization problem under the constraints expressed by IV.19 using the method of Lagrange multipliers. Defining the Lagrangian:

$$Fo = \left(\left\| \mathbf{P} \cdot K - \tilde{d} \right\|^2 + 2\tilde{\eta}^{\mathrm{T}} \cdot \left(\mathbf{C} \cdot K - \tilde{h} \right) \right) \qquad \text{IV.22}$$

With Lagrangian multiplier vector:

$$\tilde{\eta} = \begin{bmatrix} \eta_1 \\ \vdots \\ \eta_{\hat{J}} \end{bmatrix} \qquad \text{IV.23}$$

And solving the linear system:

$$\begin{gathered} \nabla Fo = 0 \\ \begin{bmatrix} \mathbf{P}^{\mathrm{T}} \cdot \mathbf{P} & \mathbf{C}^{\mathrm{T}} \\ \mathbf{C} & \mathbf{0} \end{bmatrix} \begin{bmatrix} K \\ \tilde{\eta} \end{bmatrix} = \begin{bmatrix} \mathbf{P}^{\mathrm{T}} \tilde{d} \\ \tilde{h} \end{bmatrix} \end{gathered} \qquad \text{IV.24}$$

By substituting the solution of IV.24 into IV.13, it is possible to obtain the entire stress field in the domain and consequently the Generalized Stress Intensity Factors.

4.4. Comparison with finite element method

In order to verify the accuracy of the proposed method, the stress fields and the estimation of the Generalized Stress Intensity Factors (GSIF) obtained were compared with finite element analyses. Four benchmark cases were analysed, including a plate with a V-notch subjected to tension and pure planar shear, and two bi-material junctions. Finite element analyses were performed using the Ansys® software package version 21, employing isoparametric parabolic elements (PLANE183 in ANSYS) and a particularly fine mesh near the singularity. Figures IV.4-7 show the comparison between the stress fields along the $\theta=0°$ direction calculated with the proposed method (solid lines) and the results of finite element analyses (symbols). It can be observed that in all analysed cases, the stress fields and GSIF calculated are in excellent agreement with finite element analyses. Particularly, the stress fields are very accurate not only in the vicinity of the singularity but throughout the entire component domain.

In Figure IV.7, it is shown how the developed procedure can be used for components with multiple different singularities, and the obtained results are excellent for the analysis of all singularities. The elastic properties used for the analysis in Figure IV.4-7 are E=20600 MPa and ν=0.3, while for Figure IV.6-7, the elastic properties of Mat1 are E=2000 MPa and ν=0.4, and those of Mat2 are E=200 MPa and ν=0.4.

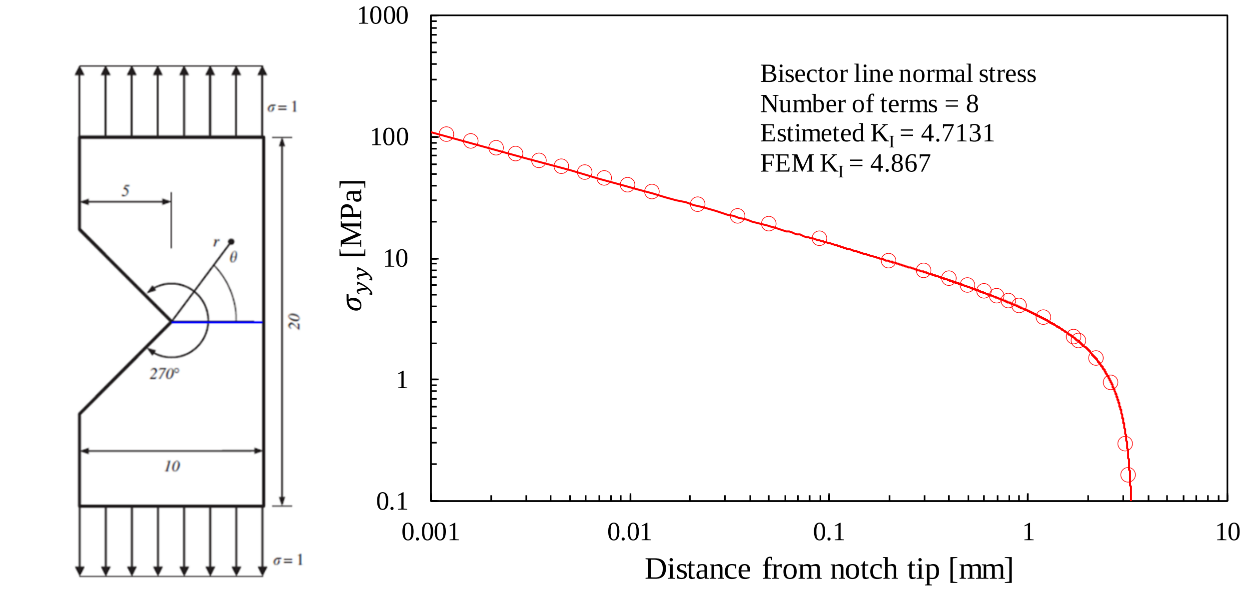

(a) (b)

Figure IV.4. (a) Diagram of the analysed plate with V-notch subjected to tension. Analysed direction for stress field comparison highlighted in blue. (b) Stress component $\sigma_{\theta\theta}$ along the bisector of the notch. Number of terms used M = 8, comparison between equations IV.13 and finite element analysis. Plate elastic properties: E = 20600 MPa, ν=0.3.

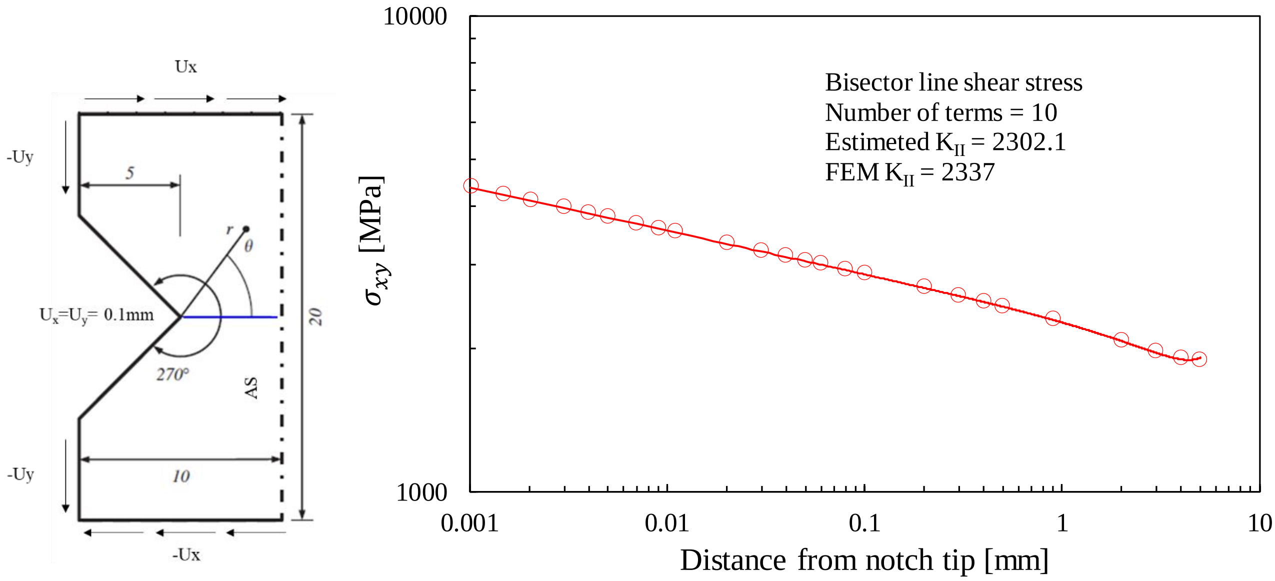

(a) (b)

Figure IV.5. (a) Diagram of the analysed plate with V-notch subjected to pure planar shear. Analysed direction for stress field comparison highlighted in blue. (b) Stress component $\sigma_{r\theta}$ along the bisector of the notch. Number of terms used M = 10, comparison between equations IV.13 and finite element analysis. Plate elastic properties: E = 20600 MPa, ν=0.3.

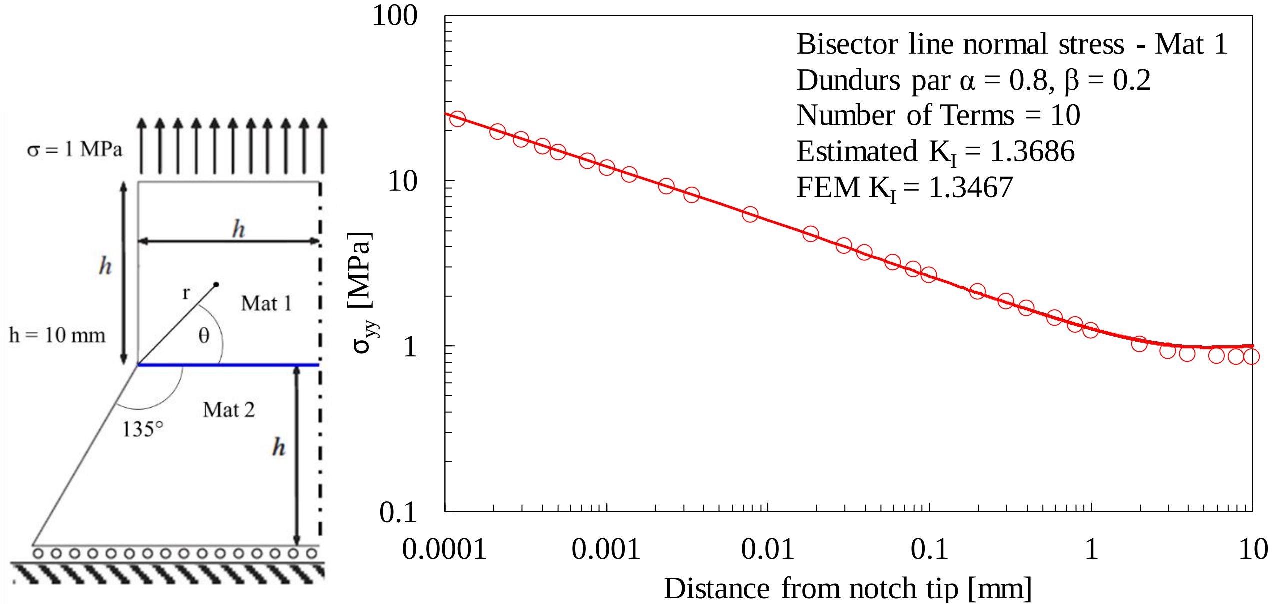

(a) (b)

Figure IV.6. (a) Diagram of the analysed bi-material junction. Analysed direction for stress field comparison highlighted in blue. (b) Stress component $\sigma_{\theta\theta}$ along the junction direction. Number of terms used M = 10, comparison between equations IV.13 and finite element analysis. Elastic properties Mat 1: E = 2000 MPa, ν=0.4; Mat 2: E = 200 MPa, ν=0.4.

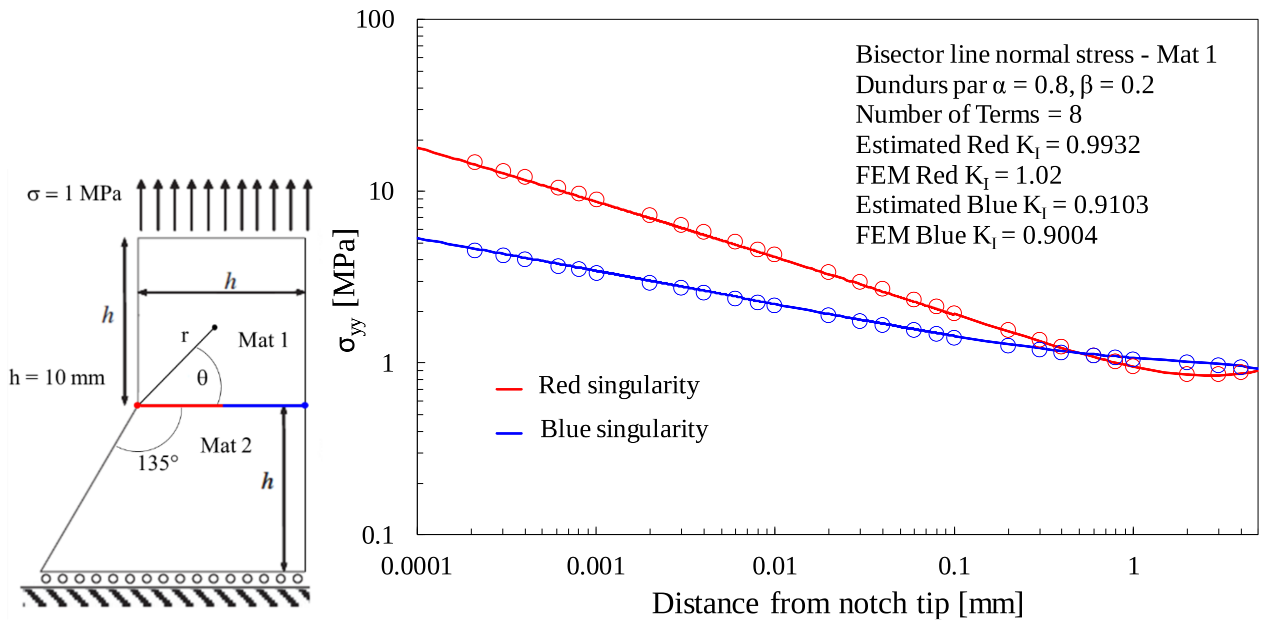

(a) (b)

Figure IV.7. (a) Diagram of the analyzed bi-material junction. Analyzed direction for stress field comparison highlighted in red for the first singularity, in blue for the second. (b) Stress component $\sigma_{\theta\theta}$ along the junction direction, in red for stresses near the first singularity, in blue for stresses near the second singularity. Number of terms used M = 10, comparison between equations IV.13 and finite element analysis. Elastic properties Mat 1: E = 2000 MPa, ν=0.4; Mat 2: E = 200 MPa, ν=0.4.

4.5. Conclusions

In this chapter, a new method for calculating Generalized Stress Intensity Factors (GSIF) and stress fields in components with multi-material singularities is presented. The developed algorithm utilizes a minimization procedure of the square of stress residuals on the component boundary, combined with auxiliary boundary conditions specifically designed to enhance convergence. The algorithm can be applied to analyze both multi-material junctions and sharp corner notches in components with multiple singularities of this kind. Examples include welded or bonded joints. The solutions obtained with the proposed method were compared with finite element analyses in four benchmark cases, and the results demonstrate excellent agreement.

The developed method can serve as an effective alternative to finite element simulations for GSIF calculation and stress distributions in components with multi-material singularities. Additionally, it can be a valuable tool for sub-modeling specific welded or bonded joints in large structures. In fact, it is possible to numerically obtain nominal stress fields through finite element analyses with coarse meshes, which can then be applied as boundary conditions using the proposed semi-analytical model.

4.6. References

1. Williams M.L. "Stress singularities resulting from various boundary conditions in angular corners of plates in tension." J Appl Mech, 1952, 19, 526–528.
2. Neuber, H. "Theory of notch stresses: principles for exact calculation of strength with reference to structural form and material." Splinger-Verlag, Berlin. 1958.
3. Barroso A, Manticˇ V, Parı´s F. "Singularity analysis of anisotropic multimaterial corners." Int. J. Fract, 2003, 119, 1–23.
4. Gross B., Mendelson A. "Plane elastostatic analysis of V-notched plates." Int J Fract 8, 1972, 267–276.
5. Dunn L., Suwito W., Cunningham S. "Stress intensities at notch singularities." Eng Fract Mech, 1997, 57, 4, 417–430.
6. Meneghetti G, Lazzarin P. "Significance of the elastic peak stress evaluated by FE analyses at the point of singularity of sharp V-notched components." Fatigue Fract. Eng. Mater. Struct., 2007, 30, 95–106.
7. Lazzarin, P., Berto, F., Zappalorto, M. "Rapid calculations of notch stress intensity factors based on averaged strain energy density from coarse meshes: Theoretical bases and applications." Int J Fract, 2010, 32(10), 1559–1567.
8. Barroso A., Graciani E., Manticˇ V., Parı´s F. "A least squares procedure for the evaluation of multiple generalized stress intensity factors at 2D multimaterial corners by BEM." Eng. An. Bound. Ele., 2012, 36(3), 458–470.

5. Stress fields around reinforced holes

5.1. Introduction

Panels, plates, and shells, as ubiquitous elements in engineering structures, exhibit diverse shapes, with one geometric dimension significantly greater or smaller than the other two. Despite their prevalence, the need to create holes and notches in these elements to meet service requirements compromises their structural strength. The prediction of effective stress distributions in weakened plates due to geometrical variations has been a subject of extensive research, dating back to Kirsch in 1898[1]. Muskhelishvili's complex potential approach for isotropic plates in 1953[2] facilitated the study of complex geometries, while Lekhnitskii[3] and Savin[4] extended similar approaches to anisotropic materials, using conformal mapping for various hole shapes.

Efforts to verify and improve these solutions continued with Batista's efficient algorithms for stress fields around complex non-convex hole shapes[5], Sharma's analysis of polygonal holes[13], and Rezaeepazhand and Jafari's study of metallic panels with special-shaped cut-outs[14]. Recent endeavours have aimed at characterizing stress distributions associated with different notch geometries and loading conditions[8-12].

To enhance the strength of components with holes, strategies like reinforcing them with stiff rings or inserts have been explored. Noteworthy works include Savin's analytical solution for an elliptic hole reinforced by rigid arc-shaped plates[5] and Chao et al.'s investigation into stress fields around an elliptic hole with an elliptic isotropic annulus[26]. Lekhnitskii extended the study to orthotropic solids, validated experimentally by Toubal et al.[34]. Belfield et al.[35] provided an analytical solution for concentrically anisotropic reinforcements around holes in isotropic plates, laying the foundation for subsequent research[30-33].

Simultaneously, modern additive manufacturing technologies for long fibre composites have revolutionized geometric possibilities and reinforcement placement, unconstrained by traditional limitations. Efforts have been directed towards optimizing fused deposition modelling technologies for long fibre composites[14], as well as understanding fracture behaviour around geometrical discontinuities in 3D printed specimens[15].

In a parallel avenue, the study of stress distribution around geometrical variations in composite components has investigated the possibility of strengthening and stress relieving regions close to such variations. Dave and Sharma[32] explored the effect of functionally graded laminas around holes, while Yang et al.[33] derived stress fields in an isotropic plate with an elliptic hole reinforced with a functionally graded annulus. To mitigate damage from stress concentrations, reinforcement with stronger and stiffer materials has been explored, initially using stiff rings, inserts, and patches. In composite laminates, stacking laminae with graded stiffness achieved a strengthening effect[33]. With additive manufacturing technologies, functionally graded materials have opened new design possibilities, demanding novel theoretical and numerical tools for design.

In this chapter two new models are presented that describe the elastic behaviour of reinforcement around holes. The first is the elastic problem of an isotropic infinite plate with a circular hole reinforced with a polarly orthotropic material subject to generic loadings. The analytical formulation combines the Muskhelishvili complex potential approach for isotropic plates[2] and Spencer's solution[36] for a polarly orthotropic annulus. The resulting explicit expressions for displacement and stress fields account for the plate's geometry and the reinforcing region's elastic properties. The analytical solution is validated through comparisons with finite element analyses on finite geometries under various loading conditions.

The second discussed solution is the elastic problem of a finite convex plates of arbitrary geometry weakened by a concentrically reinforced hole subject to diverse loads.

Despite extensive scrutiny, the analysis of notch stress and strength remains a focal point for researchers[15-21]. Few have successfully determined analytical solutions for finite bodies weakened by holes or notches comparable in size to the plate. Pioneering works by Howland[22] and Ling[23] in the early 20th century focused on notched strips, while recent studies addressed finite plates weakened by various hole shapes[24-27].

This second model builds upon the first discussed solution for an infinite plate. It proposes a method for deriving stress fields in finite convex plates of arbitrary geometry weakened by a concentrically reinforced hole, subject to diverse loads. Various boundary conditions, especially those for hole edges, are precisely described and applied. External boundary conditions are approximated to obtain accurate stress fields for the entire plate region.

The model is then validated against a variety of finite element analyses, considering all relevant geometrical parameters. This expanded solution contributes to understanding stress distributions in plates with locally reinforced geometrical variations, a valuable resource for designing additively manufactured mechanical components.

5.2. Exact in-plane stress field solution for isotropic plates with circular holes reinforced with cylindrically orthotropic rings

5.2.1. Analytical solution

5.2.1.1. Statement of the problem

Consider an infinite isotropic plate with a circular hole of radius r_0, reinforced with a concentric polarly orthotropic annulus of thickness s and outer radius r_1, giving $s = r_1 - r_0$. The plate is subjected to radial and shear stresses in the hole boundary, generally given in the following Fourier series form:

$$\begin{aligned} \bar{\sigma}_{rr}(\theta) &= S_0 + \sum_{n=1}^{N}\left(S_{n,1}\cos(n\theta) + S_{n,2}\sin(n\theta)\right) \\ \bar{\sigma}_{r\theta}(\theta) &= T_0 + \sum_{n=1}^{N}\left(T_{n,1}\cos(n\theta) + T_{n,2}\sin(n\theta)\right) \end{aligned} \qquad \text{V.1}$$

where $S_0, T_0, S_{ij}, T_{ij} \in \mathbb{R}\ \forall\, i : 1 \le i \le N \in \mathbb{N};\ j \in \{1, 2\}$.

Moreover, external far-field constant stresses $\sigma_{xx}^{\infty}, \sigma_{yy}^{\infty}, \sigma_{xy}^{\infty}$ are applied to the plate (see Figure V.1).

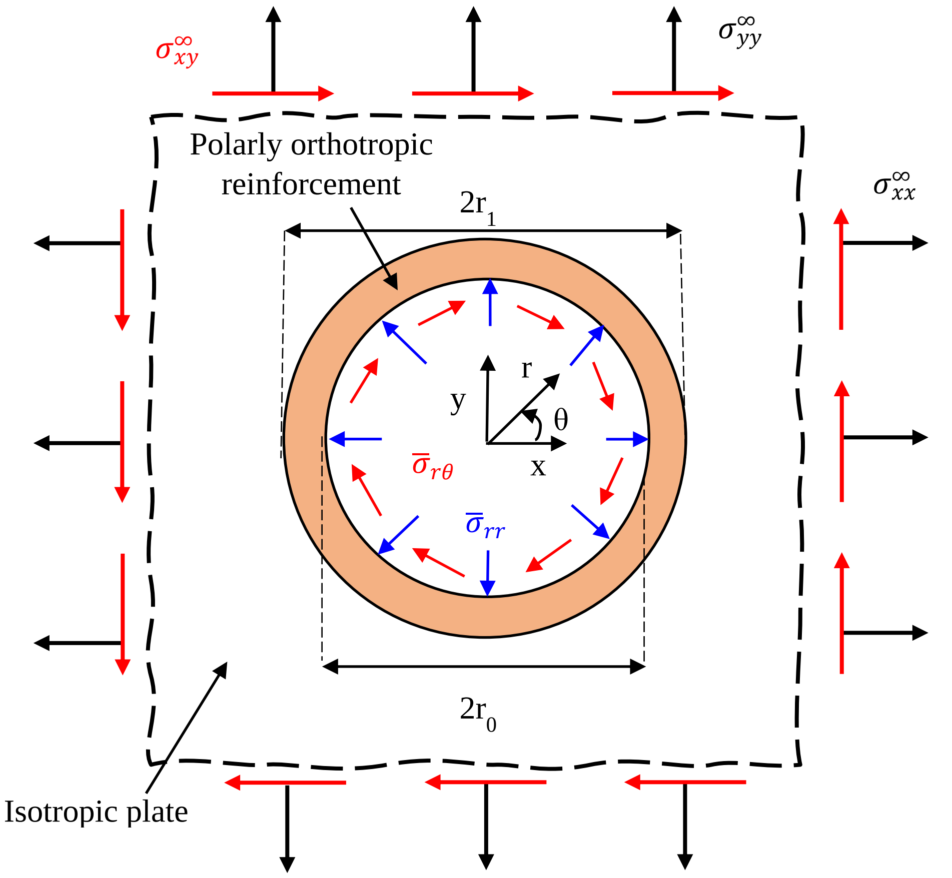

Figure V.1. Infinite plate with a reinforced circular hole under generic loading conditions.

5.2.1.2. General form for the displacement and stress fields in the reinforcing region

In the (x, y) plane, depict the reinforcing area as a polarly orthotropic ring where the radial and circumferential directions serve as principal elasticity directions. Consequently, the stress and displacement fields within the reinforcing region can be investigated using the same format outlined in chapter 1.6.2.3 for the concentric annulus problem. Hence, the subsequent formulations for displacements and stresses can be applied (refer to the coordinate system depicted in Figure V.1).

$$\begin{aligned} u_r^{(1)} = {} & A_0\left(\frac{r_0}{r}\right)^{\alpha_0} + a_0\left(\frac{r}{r_1}\right)^{\alpha_0} - E_1\left(\frac{1+d^{-2}}{1+\epsilon^{-2}}\right)\cos\theta + \left(E_1\cos\theta + F_1\sin\theta\right)\log\left(\frac{r}{r_0}\right) + \\ & + \sum_{n=1}^{N}\left(\left(A_n\cos n\theta + B_n\sin n\theta\right)\left(\frac{r_0}{r}\right)^{\alpha_n} + \left(a_n\cos n\theta + b_n\sin n\theta\right)\left(\frac{r}{r_1}\right)^{\alpha_n}\right) + \\ & + \sum_{n=2}^{N}\left(\left(E_n\cos n\theta + F_n\sin n\theta\right)\left(\frac{r_0}{r}\right)^{\beta_n} + \left(e_n\cos n\theta + f_n\sin n\theta\right)\left(\frac{r}{r_1}\right)^{\beta_n}\right) \end{aligned} \tag{V.2}$$

$$
\begin{aligned}
u_\theta^{(1)} = {} & F_1\left(\frac{1+d^{-2}}{1+\epsilon^{-2}}\right)\cos\theta - H_0\left(\frac{r_0}{r}\right) + \left(F_1\cos\theta - E_1\sin\theta\right)\log\left(\frac{r}{r_0}\right) + \\
& + \sum_{n=1}^{N}\left(\left(C_n\sin n\theta - D_n\cos n\theta\right)\left(\frac{r_0}{r}\right)^{\alpha_n} + \left(c_n\sin n\theta - d_n\cos n\theta\right)\left(\frac{r}{r_1}\right)^{\alpha_n}\right) + \\
& + \sum_{n=2}^{N}\left(\left(G_n\sin n\theta - H_n\cos n\theta\right)\left(\frac{r_0}{r}\right)^{\beta_n} + \left(g_n\sin n\theta - h_n\cos n\theta\right)\left(\frac{r}{r_1}\right)^{\beta_n}\right)
\end{aligned}
\tag{V.3}
$$

$$
\begin{aligned}
\sigma_{rr}^{(1)} = {} & \frac{G_{\theta r}^{(1)}}{rc^2d_1^2}\Bigg\{\left(\frac{r_0}{r}\right)^{\alpha_0} A_0\left(c^2 - d^2\alpha_0\right) + \left(\frac{r}{r_1}\right)^{\alpha_0} a_0\left(c^2 + d^2\alpha_0\right) + \\
& + E_1\frac{d^4 - \left(c^2\left(1+d^2\right) - d^4\right)\epsilon^2}{d^2\left(1+\epsilon^2\right)}\cos\theta + F_1\frac{d^4 - \left(c^2\left(1+d^2\right) - d^4\right)\epsilon^2}{d^2\left(1+\epsilon^2\right)}\sin\theta + \\
& + \sum_{n=1}^{N}\Bigg[\left(\frac{r_0}{r}\right)^{\alpha_n}\left[\left(A_n\cos(n\theta) + B_n\sin(n\theta)\right)\left(c^2 - d^2\alpha_n\right) + \left(C_n\cos(n\theta) + D_n\sin(n\theta)\right)nc^2\right] + \\
& + \left(\frac{r}{r_1}\right)^{\alpha_n}\left[\left(a_n\cos(n\theta) + b_n\sin(n\theta)\right)\left(c^2 + d^2\alpha_n\right) + \left(c_n\cos(n\theta) + d_n\sin(n\theta)\right)nc^2\right]\Bigg] + \\
& + \sum_{n=2}^{N}\Bigg[\left(\frac{r_0}{r}\right)^{\beta_n}\left[\left(E_n\cos(n\theta) + F_n\sin(n\theta)\right)\left(c^2 - d^2\beta_n\right) + \left(G_n\cos(n\theta) + H_n\sin(n\theta)\right)nc^2\right] + \\
& + \left(\frac{r}{r_1}\right)^{\beta_n}\left[\left(e_n\cos(n\theta) + f_n\sin(n\theta)\right)\left(c^2 + d^2\beta_n\right) + \left(g_n\cos(n\theta) + h_n\sin(n\theta)\right)nc^2\right]\Bigg]\Bigg\}
\end{aligned}
\tag{V.4}
$$

$$
\begin{aligned}
\sigma_{\theta\theta}^{(1)} = {} & \frac{G_{\theta r}^{(1)}}{rd^2\epsilon_1^2}\Bigg\{\left(\frac{r_0}{r}\right)^{\alpha_0} A_0\left(d^2 - \epsilon^2\alpha_0\right) + \left(\frac{r}{r_1}\right)^{\alpha_0} a_0\left(d^2 + \epsilon^2\alpha_0\right) + \\
& + E_1\frac{\epsilon^2\left(\epsilon^2 - d^2\right)}{1+\epsilon^2}\cos\theta + F_1\frac{\epsilon^2\left(\epsilon^2 - d^2\right)}{1+\epsilon^2}\sin\theta + \\
& + \sum_{n=1}^{N}\Bigg[\left(\frac{r_0}{r}\right)^{\alpha_n}\left[\left(A_n\cos(n\theta) + B_n\sin(n\theta)\right)\left(d^2 - \epsilon^2\alpha_n\right) + \left(C_n\cos(n\theta) + D_n\sin(n\theta)\right)nd^2\right] + \\
& + \left(\frac{r}{r_1}\right)^{\alpha_n}\left[\left(a_n\cos(n\theta) + b_n\sin(n\theta)\right)\left(d^2 + \epsilon^2\alpha_n\right) + \left(c_n\cos(n\theta) + d_n\sin(n\theta)\right)nd^2\right]\Bigg] + \\
& + \sum_{n=2}^{N}\Bigg[\left(\frac{r_0}{r}\right)^{\beta_n}\left[\left(E_n\cos(n\theta) + F_n\sin(n\theta)\right)\left(d^2 - \epsilon^2\beta_n\right) + \left(G_n\cos(n\theta) + H_n\sin(n\theta)\right)nd^2\right] + \\
& + \left(\frac{r}{r_1}\right)^{\beta_n}\left[\left(e_n\cos(n\theta) + f_n\sin(n\theta)\right)\left(d^2 + \epsilon^2\beta_n\right) + \left(g_n\cos(n\theta) + h_n\sin(n\theta)\right)nd^2\right]\Bigg]\Bigg\}
\end{aligned}
\tag{V.5}
$$

$$\sigma_{r\theta}^{(1)} = \frac{G_{\theta r}^{(1)}}{r}\left\{\frac{2r_0H_0}{r} + F_1\frac{d^2-\epsilon^2}{d^2\left(1+\epsilon^2\right)}\cos\theta + E_1\frac{d^2-\epsilon^2}{d^2\left(1+\epsilon^2\right)}\sin\theta + \right.$$
$$+\sum_{n=1}^{N}\left[\left(\frac{r_0}{r}\right)^{\alpha_n}\left[n\left(B_n\cos(n\theta)-A_n\sin(n\theta)\right)+\left(D_n\cos(n\theta)-C_n\sin(n\theta)\right)(\alpha_n+1)\right]+\right.$$
$$\left.+\left(\frac{r}{r_1}\right)^{\alpha_n}\left[n\left(b_n\cos(n\theta)-a_n\sin(n\theta)\right)+\left(c_n\sin(n\theta)-d_n\cos(n\theta)\right)(\alpha_n-1)\right]\right]+ \qquad \text{V.6}$$
$$+\sum_{n=2}^{N}\left[\left(\frac{r_0}{r}\right)^{\beta_n}\left[n\left(F_n\cos(n\theta)-E_n\sin(n\theta)\right)+\left(H_n\cos(n\theta)-G_n\sin(n\theta)\right)(\beta_n+1)\right]+\right.$$
$$\left.\left.+\left(\frac{r}{r_1}\right)^{\beta_n}\left[n\left(f_n\cos(n\theta)-e_n\sin(n\theta)\right)+\left(g_n\sin(n\theta)-h_n\cos(n\theta)\right)(\beta_n-1)\right]\right]\right\}$$

In Eqs. V.2-3 and V.4-6, the superscript (1) refers to the elastic constants, stresses and displacements of the reinforcing region.

Unknowns $A_n, a_n, B_n, b_n, C_n, c_n, D_n, d_n, E_n, e_n, F_n, f_n, G_n, g_n, H_n, h_n$ $\forall n \le N \in \mathbb{N}$ are linearly dependent constants to determine by applying proper boundary conditions and linked through the following relations:

$$\begin{array}{lll} A_n = C_n\phi_{\alpha,n} & a_n = c_n\phi_{-\alpha,n} & n \ge 1 \\ B_n = D_n\phi_{\alpha,n} & b_n = d_n\phi_{-\alpha,n} & n \ge 1 \\ E_n = G_n\phi_{\beta,n} & e_n = g_n\phi_{-\beta,n} & n \ge 2 \\ F_n = H_n\phi_{\beta,n} & f_n = h_n\phi_{-\beta,n} & n \ge 2 \end{array} \qquad \text{V.7}$$

In Eq. V.7:

$$\phi_{\gamma,n} = \frac{\gamma_n^{\ 2} - \epsilon^{-2}n^2 - 1}{n\left(\left(1+\epsilon^{-2}\right)-\gamma_n\left(1+d^{-2}\right)\right)} \qquad \text{V.8}$$

whilst $\pm\alpha_n$ and $\pm\beta_n$ $\forall n \in \mathbb{N}$ are the roots of the following characteristic equations:

$$f(\gamma_n) = \gamma_n^{\ 4} - \gamma_n^{\ 2}\left(\epsilon^{-2}\left(n^2+c^2\right)-n^2c^2d^{-2}\left(2+d^{-2}\right)+1\right)+c^2\epsilon^{-2}\left(n^2-1\right)^2 = 0 \qquad \text{V.9}$$

where:

$$\epsilon^2 = \frac{G_{\theta r}^{(1)}}{L} \qquad d^2 = \frac{G_{\theta r}^{(1)}}{M} \qquad c^2 = \frac{G_{\theta r}^{(1)}}{N} \qquad \text{V.10}$$

and:

$$L = \frac{\frac{E_\theta^{(1)}}{\nu_{r\theta}^{(1)}}}{\frac{1}{\nu_{r\theta}^{(1)}} - \frac{E_r^{(1)}}{E_\theta^{(1)}}\nu_{r\theta}^{(1)}} \qquad M = \frac{E_\theta^{(1)}}{\frac{1}{\nu_{r\theta}^{(1)}}\frac{E_\theta^{(1)}}{E_r^{(1)}} - \nu_{r\theta}^{(1)}} \qquad N = \frac{\frac{E_\theta^{(1)}}{\nu_{r\theta}^{(1)}}}{\frac{1}{\nu_{r\theta}^{(1)}}\frac{E_\theta^{(1)}}{E_r^{(1)}} - \nu_{r\theta}^{(1)}} \qquad \text{V.11}$$

for plane stress.

Alternatively, the situation of plain strain can be addressed by assuming a transversely isotropic behavior in the through-thickness direction, a common practice for Fiber Reinforced Polymers. In this scenario, $E_z^{(1)} = E_r^{(1)}$ and $G_{rz}^{(1)} = \frac{E_r^{(1)}}{2\left(1+\nu_{rz}^{(1)}\right)}$. Consequently, in this particular instance, the constants L, M, and N are governed by the following expressions:

$$L = \frac{E_\theta^{(1)}\frac{1-\nu_{rz}^{(1)}}{\nu_{r\theta}^{(1)}}}{\frac{1-\nu_{rz}^{(1)}}{\nu_{r\theta}^{(1)}} - 2\frac{E_r^{(1)}}{E_\theta^{(1)}}\nu_{r\theta}^{(1)}} \qquad M = \frac{E_\theta^{(1)}}{\frac{1-\nu_{rz}^{(1)}}{\nu_{r\theta}^{(1)}}\frac{E_\theta^{(1)}}{E_r^{(1)}} - 2\nu_{r\theta}^{(1)}}$$

$$N = \frac{E_\theta^{(1)}}{\nu_{rz}^{(1)}+1}\frac{\frac{1}{\nu_{r\theta}^{(1)}} - \nu_{r\theta}^{(1)}\frac{E_r^{(1)}}{E_\theta^{(1)}}}{\frac{E_\theta^{(1)}}{E_r^{(1)}}\frac{1-\nu_{rz}^{(1)}}{\nu_{r\theta}^{(1)}} - 2\nu_{r\theta}^{(1)}} \qquad \text{V.12}$$

where $E_\theta^{(1)}, E_r^{(1)}, E_z^{(1)}$ are the Young's moduli, $\nu_{r\theta}^{(1)}, \nu_{rz}^{(1)}$ the Poisson ratios and $G_{\theta r}^{(1)}, G_{rz}^{(1)}$ the shear moduli

5.2.1.3. General form for the displacement and stress fields in the reinforced plate (outside the reinforcing region)

The Muskhelishvili complex function[2] can be employed to establish the overall expressions for the displacement and stress fields in the plate beyond the reinforcing region:

$$
\begin{aligned}
&\sigma_{rr}^{(2)}+\sigma_{\theta\theta}^{(2)}=4\,\mathrm{Re}\left[\frac{d\Phi(z)}{dz}\right]\\
&\sigma_{\theta\theta}^{(2)}-\sigma_{rr}^{(2)}+2i\sigma_{r\theta}^{(2)}=2e^{2i\theta}\left(\bar{z}\,\frac{d^2\Phi(z)}{dz^2}+\frac{d\mathrm{X}(z)}{dz}\right)\\
&u_r^{(2)}+iu_\theta^{(2)}=\frac{1+\nu^{(2)}}{E^{(2)}}\left(\kappa\,\Phi(z)-z\,\overline{\frac{d\Phi(z)}{dz}}-\overline{\mathrm{X}(z)}\right)e^{-i\theta}
\end{aligned}
\qquad \text{V.13}
$$

where superscript (2) identifies the elastic constants, stresses and displacements in the isotropic plate and $E^{(2)},\nu^{(2)}$ are the Young's modulus and Poisson ratio respectively

The following two potential functions are used:

$$
\begin{aligned}
&\Phi(z)=\left(\bar{A}_0+i\bar{B}_0\right)log\left(z\right)+\left(\bar{A}_1+i\bar{B}_1\right)z+\left(\bar{A}_c+i\bar{B}_c\right)+\sum_{n=1}^{N-1}\left(\bar{A}_{-n}+i\bar{B}_{-n}\right)z^{-n}\\
&\mathrm{X}(z)=-\kappa\left(\bar{A}_0-i\bar{B}_0\right)log\left(z\right)+\left(\bar{C}_1+i\bar{D}_1\right)z+\sum_{n=1}^{N+1}\left(\bar{C}_{-n}+i\bar{D}_{-n}\right)z^{-n}
\end{aligned}
\qquad \text{V.14}
$$

Substituting Eq. V.14 into Eq. V.13 results in the following displacement and stress fields (according to the reference system shown in Figure V.1):

$$
\begin{aligned}
u_r^{(2)}=\frac{\left(\nu^{(2)}+1\right)}{E^{(2)}}\Bigg\{&\frac{\left(r^2\left(\kappa-1\right)\bar{A}_1-\bar{C}_{-1}\right)}{r}+\\
&+\frac{\left(r^2\left(\left(\kappa\log\left(r^2\right)-1\right)\bar{A}_0+\kappa\bar{A}_c\right)-\bar{C}_{-2}\right)}{r^2}\cos\left(\theta\right)+\frac{\left(r^2\left(\left(\kappa\log\left(r^2\right)-1\right)\bar{B}_0+\kappa\bar{B}_c\right)-\bar{D}_{-2}\right)}{r^2}\sin\left(\theta\right)+\\
&+\frac{\left(r^2\left(1+\kappa\right)\bar{A}_{-1}-\bar{C}_{-3}-r^4\bar{C}_1\right)}{r^3}\cos\left(2\theta\right)+\frac{\left(r^2\left(1+\kappa\right)\bar{B}_{-1}-\bar{D}_{-3}+r^4\bar{D}_1\right)}{E^{(2)}r^3}\sin\left(2\theta\right)+\\
&+\sum_{n=3}^{N}\left[\frac{\left(r^2\left(\left(n-1\right)+\kappa\right)\bar{A}_{-(n-1)}-\bar{C}_{-(n+1)}\right)}{r^{n+1}}\cos\left(n\theta\right)+\frac{\left(r^2\left(\left(n-1\right)+\kappa\right)\bar{B}_{-(n-1)}-\bar{D}_{-(n+1)}\right)}{r^{n+1}}\sin\left(n\theta\right)\right]\Bigg\}
\end{aligned}
\qquad \text{V.15}
$$

$$
\begin{aligned}
u_\theta^{(2)}=\frac{\left(\nu^{(2)}+1\right)}{E^{(2)}}\Bigg\{&\frac{\left(r^2\left(1+\kappa\right)\bar{B}_1+\bar{D}_{-1}\right)}{r}+\\
&+\frac{\left(r^2\left(\left(1+\kappa\log\left(r^2\right)\right)\bar{B}_0+\kappa\bar{B}_c\right)+\bar{D}_{-2}\right)}{r^2}\cos\left(\theta\right)-\frac{\left(r^2\left(\left(1+\kappa\log\left(r^2\right)\right)\bar{A}_0+\kappa\bar{A}_c\right)+\bar{C}_{-2}\right)}{r^2}\sin\left(\theta\right)+\\
&+\frac{\left(r^2\left(\kappa-1\right)\bar{B}_{-1}+\bar{D}_{-3}+r^4\bar{D}_1\right)}{r^3}\cos\left(2\theta\right)+\frac{\left(r^2\left(1-\kappa\right)\bar{A}_{-1}-\bar{C}_{-3}+r^4\bar{C}_1\right)}{E^{(2)}r^3}\sin\left(2\theta\right)+\\
&+\sum_{n=3}^{N}\left[\frac{\left(r^2\left(\kappa-\left(n-1\right)\right)\bar{B}_{-(n-1)}+\bar{D}_{-(n+1)}\right)}{r^{n+1}}\cos\left(n\theta\right)+\frac{\left(r^2\left(\left(n-1\right)-\kappa\right)\bar{A}_{-(n-1)}-\bar{C}_{-(n+1)}\right)}{r^{n+1}}\sin\left(n\theta\right)\right]\Bigg\}
\end{aligned}
\qquad \text{V.16}
$$

$$\sigma_{rr}^{(2)} = \frac{1}{(\tilde{\nu}-1)}\left\{\frac{\left(\bar{C}_{-1}(\tilde{\nu}-1)-r^2(\kappa-1)(\tilde{\nu}+1)\bar{A}_1\right)}{r^2}+(\tilde{\nu}-1)\left(D_1\sin(2\theta)-C_1\cos(2\theta)\right)+\right.$$
$$+\frac{2\left(r^2(\tilde{\nu}-\kappa)\bar{A}_0+(\tilde{\nu}-1)\bar{C}_{-2}\right)}{r^3}\cos(\theta)+\frac{2\left(r^2(\tilde{\nu}-\kappa)\bar{B}_0+(\tilde{\nu}-1)\bar{D}_{-2}\right)}{r^3}\sin(\theta)+$$
$$+\sum_{n=2}^{N}\left[\frac{\left((n-1)r^2\left((n-1)-(n+1)\tilde{\nu}+\kappa(\tilde{\nu}+1)\right)\bar{A}_{-(n-1)}+(n+1)(\tilde{\nu}-1)\bar{C}_{-(n+1)}\right)}{r^{n+1}}\cos(n\theta)+\right. \tag{V.17}$$
$$\left.\left.\frac{\left((n-1)r^2\left((n-1)-(n+1)\tilde{\nu}+\kappa(\tilde{\nu}+1)\right)\bar{B}_{-(n-1)}+(n+1)(\tilde{\nu}-1)\bar{D}_{-(n+1)}\right)}{r^{n+1}}\sin(n\theta)\right]\right\}$$

$$\sigma_{\theta\theta}^{(2)} = \frac{1}{(\tilde{\nu}-1)}\left\{\frac{\left(\bar{C}_{-1}(1-\tilde{\nu})-r^2(\kappa-1)(\tilde{\nu}+1)\bar{A}_1\right)}{r^2}+(\tilde{\nu}-1)\left(C_1\cos(2\theta)-D_1\sin(2\theta)\right)+\right.$$
$$+\frac{2\left(r^2(1-\tilde{\nu}\kappa)\bar{A}_0-(\tilde{\nu}-1)\bar{C}_{-2}\right)}{r^3}\cos(\theta)+\frac{2\left(r^2(1-\tilde{\nu}\kappa)\bar{B}_0-(\tilde{\nu}-1)\bar{D}_{-2}\right)}{r^3}\sin(\theta)+$$
$$+\sum_{n=2}^{N}\left[\frac{\left((n-1)r^2\left((n-1)\tilde{\nu}-(n+1)+\kappa(\tilde{\nu}+1)\right)\bar{A}_{-(n-1)}-(n+1)(\tilde{\nu}-1)\bar{C}_{-(n+1)}\right)}{r^{n+1}}\cos(n\theta)+\right. \tag{V.18}$$
$$\left.\left.+\frac{\left((n-1)r^2\left((n-1)\tilde{\nu}-(n+1)+\kappa(\tilde{\nu}+1)\right)\bar{B}_{-(n-1)}-(n+1)(\tilde{\nu}-1)\bar{D}_{-(n+1)}\right)}{r^{n+1}}\sin(n\theta)\right]\right\}$$

$$\sigma_{r\theta}^{(2)} = -\frac{\bar{D}_{-1}}{r^2}+D_1\cos(2\theta)+C_1\sin(2\theta)+$$
$$+\frac{\left(r^2(\kappa-1)\bar{B}_0-2\bar{D}_{-2}\right)}{r^3}\cos(\theta)+\frac{\left(r^2(1-\kappa)\bar{A}_0+2\bar{C}_{-2}\right)}{r^3}\sin(\theta)+$$
$$+\sum_{n=2}^{N}\left[\frac{\left((n+1)(n-1)\bar{B}_{-(n-1)}-(n+1)\bar{D}_{-(n+1)}\right)}{r^{n+1}}\cos(n\theta)+\right. \tag{V.19}$$
$$\left.+\frac{\left((n+1)\bar{C}_{-(n+1)}-(n+1)(n-1)\bar{A}_{-(n-1)}\right)}{r^{n+1}}\sin(n\theta)\right]$$

$\bar{A}_c, \bar{B}_c, \bar{A}_n, \bar{B}_n, \bar{C}_n, \bar{D}_n \;\; \forall n \le N \in \mathbb{N}$ are integration constants to determine by applying proper boundary conditions, and $\kappa = \frac{3-\nu^{(2)}}{1+\nu^{(2)}}$, $\tilde{\nu} = \frac{\nu^{(2)}}{1-\nu^{(2)}}$ for plane stress conditions, whilst for plane strain $\kappa = 3-4\nu^{(2)}$, $\tilde{\nu} = \nu^{(2)}$.

5.2.1.4. Boundary conditions and explicit solution for unknown coefficients

The unknowns in the expressions derived in the previous sections can be determined by applying the following boundary conditions:

i. Far away from the hole ($r \to \infty$) the following conditions must be verified:

$$\lim_{r\to\infty}\sigma_{xx}^{(2)}(r,\theta)=\lim_{r\to\infty}\left(\frac{\sigma_{rr}^{(2)}+\sigma_{\theta\theta}^{(2)}}{2}+\frac{\sigma_{rr}^{(2)}-\sigma_{\theta\theta}^{(2)}}{2}\cos 2\theta-\sigma_{r\theta}^{(2)}\sin 2\theta\right)=\sigma_{xx}^{\infty}$$
$$\lim_{r\to\infty}\sigma_{yy}^{(2)}(r,\theta)=\lim_{r\to\infty}\left(\frac{\sigma_{rr}^{(2)}+\sigma_{\theta\theta}^{(2)}}{2}-\frac{\sigma_{rr}^{(2)}-\sigma_{\theta\theta}^{(2)}}{2}\cos 2\theta-\sigma_{r\theta}^{(2)}\sin 2\theta\right)=\sigma_{yy}^{\infty} \qquad \text{V.20}$$
$$\lim_{r\to\infty}\sigma_{xy}^{(2)}(r,\theta)=\lim_{r\to\infty}\left(-\frac{\sigma_{rr}^{(2)}-\sigma_{\theta\theta}^{(2)}}{2}\cos 2\theta-\sigma_{r\theta}^{(2)}\sin 2\theta\right)=\sigma_{xy}^{\infty}$$

Explicitly substituting Eq. V.17-19 into Eqs. V.20 results in:

$$\bar{A}_1=\frac{\sigma_{xx}^{\infty}+\sigma_{yy}^{\infty}}{4} \qquad \bar{C}_1=\frac{\sigma_{yy}^{\infty}-\sigma_{xx}^{\infty}}{2} \qquad \bar{D}_1=\sigma_{xy}^{\infty} \qquad \text{V.21}$$

ii. Along the boundary of the reinforcing annulus, equilibrium and compatibility conditions should be guaranteed, namely:

$$\sigma_{rr}^{(1)}(r=r_0,\theta)=\bar{\sigma}_{rr}(\theta) \qquad \sigma_{r\theta}^{(1)}(r=r_1,\theta)=\sigma_{r\theta}^{(2)}(r=r_1,\theta)$$
$$\sigma_{r\theta}^{(1)}(r=r_0,\theta)=\bar{\sigma}_{r\theta}(\theta) \qquad u_{r}^{(1)}(r=r_1,\theta)=u_{r}^{(2)}(r=r_1,\theta) \qquad \text{V.22}$$
$$\sigma_{rr}^{(1)}(r=r_1,\theta)=\sigma_{rr}^{(2)}(r=r_1,\theta) \qquad u_{\theta}^{(1)}(r=r_1,\theta)=u_{\theta}^{(2)}(r=r_1,\theta)$$

With, $r_1=r_0+s$.

Eqs. V.22 gives a total of $12N+6$ linearly independent equations, enough to determine all the remaining unknowns, where N is the number of terms used to express internal loads, according to Eqs. V.1.

To simplify the expressions for the determined constants, the following auxiliary parameters are introduced:

$$\xi = \frac{d^2 - \epsilon^2}{d^2\left(1+\epsilon^2\right)} \qquad \zeta = \frac{\left(1+d^2\right)\epsilon^2}{d^2\left(1+\epsilon^2\right)} \qquad \delta = \frac{1}{c^2} - \frac{\left(1+d^2\right)\epsilon^2}{d^4\left(1+\epsilon^2\right)}$$

$$\eta = \frac{1}{d^2} - \frac{\alpha_0}{c^2} \qquad \varrho = \frac{1}{d^2} + \frac{\alpha_0}{c^2} \qquad \text{V.23}$$

Under the condition of plane stress, the following close form expressions for the unknowns can be determined, for the reinforcing annulus:

$$E_1 = \frac{\Xi_{E_1} * S_{1,1} + \Upsilon_{E_1} * T_{1,2}}{\Omega_{E_1}} \qquad F_1 = \frac{\Xi_{F_1} * S_{1,2} + \Upsilon_{F_1} * T_{1,1}}{\Omega_{F_1}} \qquad H_0 = \frac{r_0 T_0}{2G_{\theta r}^{(2)}}$$

$$A_0 = \frac{r_1^{\alpha_0}\left(-r_0^{\alpha_0} r_1 G_{\theta r}^{(1)} \varrho\left(\sigma_{xx}^{\infty} + \sigma_{yy}^{\infty}\right) + r_0 r_1^{\alpha_0}\left(E^{(2)} + G_{\theta r}^{(1)}\left(1+\nu^{(2)}\right)\varrho\right) S_0\right)}{G_{\theta r}^{(1)}\left(-r_0^{2\alpha_0}\left(E^{(2)} + G_{\theta r}^{(1)}\left(1+\nu^{(2)}\right)\eta\right)\varrho + r_1^{2\alpha_0}\eta\left(E^{(2)} + G_{\theta r}^{(1)}\left(1+\nu^{(2)}\right)\varrho\right)\right)} \qquad \text{V.24}$$

$$a_0 = \frac{r_1^{\alpha_0}\left(r_1^{1+\alpha_0} G_{\theta r}^{(1)} \eta\left(\sigma_{xx}^{\infty} + \sigma_{yy}^{\infty}\right) - r_0^{1+\alpha_0}\left(E^{(2)} + G_{\theta r}^{(1)}\left(1+\nu^{(2)}\right)\eta\right) S_0\right)}{G_{\theta r}^{(1)}\left(-r_0^{2\alpha_0}\left(E^{(2)} + G_{\theta r}^{(1)}\left(1+\nu^{(2)}\right)\eta\right)\varrho + r_1^{2\alpha_0}\eta\left(E^{(2)} + G_{\theta r}^{(1)}\left(1+\nu^{(2)}\right)\varrho\right)\right)}$$

$$C_n = \frac{\Xi_{C_n} * S_{n,1} + \Upsilon_{C_n} * T_{n,2} + \Theta_{C_n} * \left(\sigma_{xx}^{\infty} - \sigma_{yy}^{\infty}\right)}{\Omega_{C_n}}$$

$$D_n = \frac{\Xi_{D_n} * S_{n,2} + \Upsilon_{D_n} * T_{n,1} + \Theta_{D_n} * \sigma_{xy}^{\infty}}{\Omega_{D_n}}$$

$$G_n = \frac{\Xi_{G_n} * S_{n,1} + \Upsilon_{G_n} * T_{n,2} + \Theta_{G_n} * \left(\sigma_{xx}^{\infty} - \sigma_{yy}^{\infty}\right)}{\Omega_{G_n}} \qquad \text{V.25}$$

$$H_n = \frac{\Xi_{H_n} * S_{n,2} + \Upsilon_{H_n} * T_{n,1} + \Theta_{H_n} * \sigma_{xy}^{\infty}}{\Omega_{H_n}}$$

$$c_n = \frac{\Xi_{c_n} * S_{n,1} + \Upsilon_{c_n} * T_{n,2} + \Theta_{c_n} * \left(\sigma_{xx}^{\infty} - \sigma_{yy}^{\infty}\right)}{\Omega_{c_n}}$$

$$d_n = \frac{\Xi_{d_n} * S_{n,2} + \Upsilon_{d_n} * T_{n,1} + \Theta_{d_n} * \sigma_{xy}^{\infty}}{\Omega_{d_n}}$$

$$g_n = \frac{\Xi_{g_n} * S_{n,1} + \Upsilon_{g_n} * T_{n,2} + \Theta_{g_n} * \left(\sigma_{xx}^{\infty} - \sigma_{yy}^{\infty}\right)}{\Omega_{g_n}} \qquad \text{V.26}$$

$$h_n = \frac{\Xi_{h_n} * S_{n,2} + \Upsilon_{h_n} * T_{n,1} + \Theta_{h_n} * \sigma_{xy}^{\infty}}{\Omega_{h_n}}$$

whereas for the isotropic reinforced plate the constants are:

$$\bar{C}_{-1}=\frac{r_1^{\,2}\left(-r_0^{\,2\alpha_0}\left(E^{(2)}+G_{\theta r}^{(1)}\left(\nu^{(2)}-1\right)\eta\right)\varrho+r_1^{\,2\alpha_0}\eta\left(E^{(2)}+G_{\theta r}^{(1)}\left(\nu^{(2)}-1\right)\varrho\right)\right)\left(\sigma_{xx}^{\infty}+\sigma_{yy}^{\infty}\right)}{2\left(r_0^{\,2\alpha_0}\left(E^{(2)}+G_{\theta r}^{(1)}\left(1+\nu^{(2)}\right)\eta\right)\varrho-r_1^{\,2\alpha_0}\eta\left(E^{(2)}+G_{\theta r}^{(1)}\left(1+\nu^{(2)}\right)\varrho\right)\right)}+$$

$$+\frac{r_1\left(-2r_0^{1+\alpha_0}r_1^{\alpha_0}E^{(2)}\left(\eta-\varrho\right)S_0\right)}{2\left(r_0^{\,2\alpha_0}\left(E^{(2)}+G_{\theta r}^{(1)}\left(1+\nu^{(2)}\right)\eta\right)\varrho-r_1^{\,2\alpha_0}\eta\left(E^{(2)}+G_{\theta r}^{(1)}\left(1+\nu^{(2)}\right)\varrho\right)\right)} \qquad \text{V.27}$$

$$\bar{D}_{-1}=-r_0^{\,2}T_0 \qquad \bar{B}_1=\frac{r_0^{\,2}\left(-E^{(2)}+2G_{\theta r}^{(1)}\left(1+\nu^{(2)}\right)\right)T_0}{8r_1^{\,2}G_{\theta r}^{(1)}}$$

$$\bar{A}_n=\frac{\Xi_{\bar{A}_n}*S_{n,1}+\Upsilon_{\bar{A}_n}*T_{n,2}+\Theta_{C_n}*\left(\sigma_{xx}^{\infty}-\sigma_{yy}^{\infty}\right)}{\Omega_{\bar{A}_n}}$$

$$\bar{B}_n=\frac{\Xi_{\bar{B}_n}*S_{n,2}+\Upsilon_{\bar{B}_n}*T_{n,1}+\Theta_{D_n}*\sigma_{xy}^{\infty}}{\Omega_{\bar{B}_n}}$$

$$\bar{C}_n=\frac{\Xi_{\bar{C}_n}*S_{n,1}+\Upsilon_{\bar{C}_n}*T_{n,2}+\Theta_{C_n}*\left(\sigma_{xx}^{\infty}-\sigma_{yy}^{\infty}\right)}{\Omega_{\bar{C}_n}}$$

$$\bar{D}_n=\frac{\Xi_{\bar{D}_n}*S_{n,2}+\Upsilon_{\bar{D}_n}*T_{n,1}+\Theta_{D_n}*\sigma_{xy}^{\infty}}{\Omega_{\bar{D}_n}} \qquad \text{V.28}$$

$$\bar{A}_c=\frac{\Xi_{\bar{A}_c}*S_{n,1}+\Upsilon_{\bar{A}_c}*T_{n,2}}{\Omega_{\bar{A}_c}}$$

$$\bar{B}_c=\frac{\Xi_{\bar{B}_c}*S_{n,2}+\Upsilon_{\bar{B}_c}*T_{n,1}}{\Omega_{\bar{B}_c}}$$

where $\Xi_i,\Upsilon_i,\Theta_i,\Omega_i$ are real terms explicitly reported in [30] and satisfying the following equalities:

$$\begin{array}{llll}
\Xi_{E_1}=\Xi_{F_1} & \Upsilon_{E_1}=-\Upsilon_{F_1} & \Omega_{E_1}=\Omega_{F_1} & \\
\Xi_{C_n}=\Xi_{D_n} & \Xi_{c_n}=\Xi_{d_n} & \Xi_{G_n}=\Xi_{H_n} & \Xi_{g_n}=\Xi_{h_n} \\
\Upsilon_{C_n}=-\Upsilon_{D_n} & \Upsilon_{c_n}=-\Upsilon_{d_n} & \Upsilon_{G_n}=-\Upsilon_{H_n} & \Upsilon_{g_n}=-\Upsilon_{h_n}
\end{array}$$

$$\Omega_{C_n}=\Omega_{c_n}=\Omega_{D_n}=\Omega_{d_n}=\Omega_{G_n}=\Omega_{g_n}=\Omega_{H_n}=\Omega_{h_n} \qquad \text{V.29}$$

$$\Theta_{C_n}=\Theta_{c_n}=\Theta_{D_n}=\Theta_{d_n}=\Theta_{G_n}=\Theta_{g_n}=\Theta_{H_n}=\Theta_{h_n}=0 \qquad \forall n\neq 2$$

$$2\Theta_{D_2}=\Theta_{C_n} \qquad 2\Theta_{d_2}=\Theta_{c_n} \qquad 2\Theta_{G_2}=\Theta_{H_n} \qquad 2\Theta_{g_2}=\Theta_{h_n}$$

$$\begin{aligned}
&\Xi_{\bar{A}_n} = \Xi_{\bar{B}_n} \qquad \Xi_{\bar{C}_n} = \Xi_{\bar{D}_n} \qquad \Xi_{\bar{A}_c} = \Xi_{\bar{B}_c} \\
&\Upsilon_{\bar{A}_n} = -\Upsilon_{\bar{B}_n} \qquad \Upsilon_{\bar{C}_n} = -\Upsilon_{\bar{D}_n} \qquad \Upsilon_{\bar{A}_c} = -\Upsilon_{\bar{B}_c} \\
&\Omega_{\bar{A}_n} = \Omega_{\bar{B}_n} = \Omega_{\bar{C}_{n+2}} = \Omega_{\bar{D}_{n+2}} \qquad \Omega_{\bar{A}_c} = \Omega_{\bar{B}_c} \\
&\Theta_{\bar{A}_n} = \Theta_{\bar{B}_n} = 0 \quad \forall n \neq -1 \qquad \Theta_{\bar{C}_n} = \Theta_{\bar{D}_n} = 0 \qquad \forall n \neq -3 \\
&2\Theta_{\bar{A}_{-1}} = \Theta_{\bar{B}_{-1}} \qquad 2\Theta_{\bar{C}_{-3}} = \Theta_{\bar{D}_{-3}}
\end{aligned} \tag{V.30}$$

The constants under plane strain conditions have similar expressions, and can be easily obtained:

i. changing $E^{(2)}$ for $\dfrac{E^{(2)}}{1-\left[\nu^{(2)}\right]^2}$;

ii. changing $\nu^{(2)}$ for $\dfrac{\nu^{(2)}}{1-\nu^{(2)}}$;

iii. Using Eqs. V.12 instead of Eq. V.11 for parameters L, M and N.

5.2.2. Discussion and comparison with numerical results

Although the solution derived in this chapter is mathematically exact for infinite plates, the stress fields generated from the developed framework were cross-validated against various numerical analyses performed on finite plates with reinforced holes. This comparison aimed to assess the accuracy of the solution, particularly when applied to finite bodies.

For the numerical investigations, finite plates measuring 250 mm in height and width were considered. These plates featured a central hole with a radius (r_0) of 10 mm, reinforced with annuli of thickness (s) equal to 2, 5, and 10 mm. The numerical analyses were conducted using Ansys® version 21 software with Ansys PLANE183 quadrilateral plane elements under plane stress conditions and a pure displacement formulation.

The mesh generation process involved dividing the perimeter of the plate hole into elements with a specified edge length (e_0). Subsequently, a mapped mesh was created up to a radius of 40 mm from the hole center, with the length of quadrilateral elements in the radial direction set equal to e_0. For the remaining plate region, the mesh remained mapped, imposing 100 elements in the radial direction with a spacing ratio of 100.

A convergence analysis was conducted by progressively reducing e_0 for a 250x250 mm plate made of quasi-isotropic GFRP. This plate had a hole with a radius (r_0) of 10 mm, reinforced with a ring of width (s) equal to 2 mm (s/r_0 = 0.2) and was subjected to uniaxial tension. The chosen value for e_0 was 0.05 mm for all subsequent analyses, resulting in meshes of approximately 620k nodes and 220k elements for each plate quadrant.

e_0 [mm]	FE Nodes	$\sigma_{\theta\theta}\Big\vert_{\substack{\theta=0 \\ r=r_0}} / \sigma_{yy}^{g}$
1	$4{,}348 \cdot 10^3$	4.11
0.5	$11.176 \cdot 10^3$	4.23
0.1	$167.374 \cdot 10^3$	4.24
0.05	$618.748 \cdot 10^3$	4.24

Table V.1. Results of the mesh convergence analysis. FE nodes are those of one-quarter of plate.

This approach yielded finely detailed and regular mesh patterns, especially in the region near the reinforced hole, ensuring a high level of accuracy in all cases. Symmetry or skew-symmetry boundary conditions were employed whenever possible, modeling one quarter of the plate. In instances where this was not feasible due to loading conditions, the entire plate was modeled. As an illustrative example, Figures V.2a-d present contours for $\sigma_{\theta\theta}$, σ_{rr}, u_θ, and u_r in the case of biaxial tension and internal pressure.

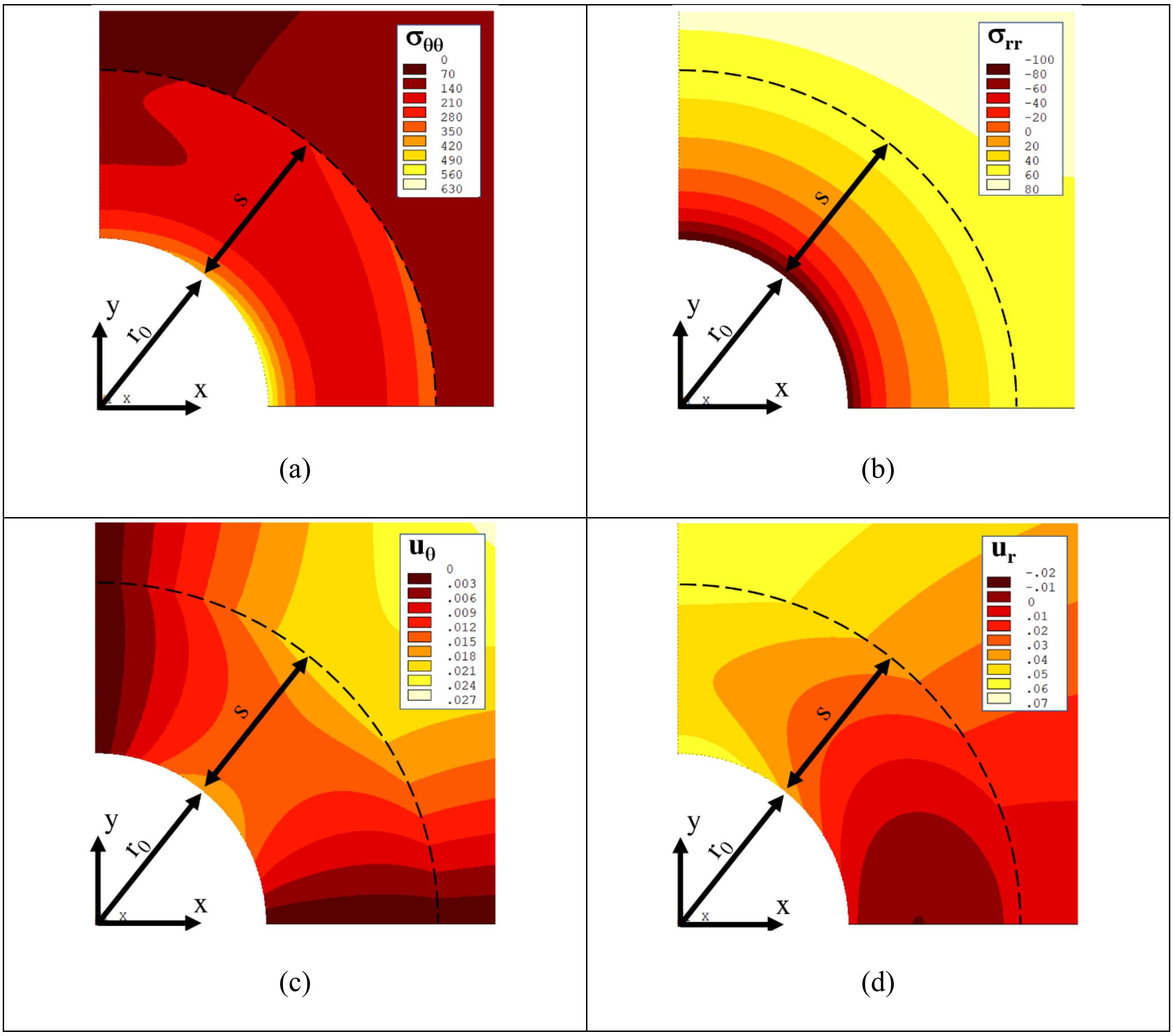

Figure V.2. Example of contour plots in 250x250 mm plates made of quasi-isotropic GFRP; hole radius r_0=10 mm reinforced with a ring of width s =10 mm. Applied loads: biaxial tension ($\sigma_{yy}^{g} = 100\,MPa$, $\sigma_{xx}^{g} = 50\,MPa$) and internal pressure ($\bar{\sigma}_{rr} = 100\,MPa$). Stresses in MPa; displacements in mm.

According to the diagram presented in Figure V.3, stress assessments for each analysed scenario involved three primary linear paths originating from the hole's centre and inclined along the θ=0°, 45°, and 90° directions (designated as paths 1, 2, and 3 in Figure V.3). Additionally, stresses were appraised along the hole boundary (path 4) and the reinforcing region's boundary (path 5). Various loading conditions were examined, including uniaxial tension, biaxial tension, pure shear, and both uniform and non-uniform internal pressure.

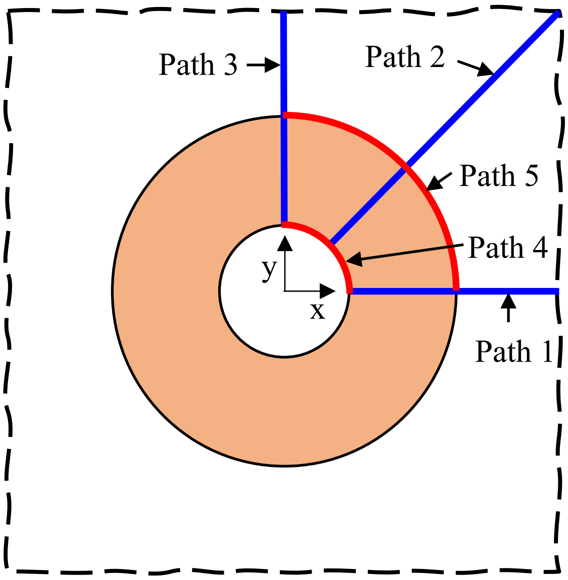

Figure 3. Schematics of the paths used for comparing the analytical solution with numerical (FE) results.

All analyses considered an annular Carbon Fibre Reinforced Polymer (CFRP) reinforcement with the following properties: E_θ=147 GPa, E_r=10.3 GPa, $G_{\theta r}$=7 GPa, $\nu_{r\theta}$=0.02. In contrast, reinforced plates utilized two different isotropic materials:

- Polyamide (PA) with E=3 GPa and ν=0.35;
- Quasi-isotropic laminate made of Glass Fiber Reinforced Polymer (GFRP) with E_x=E_y=54 GPa, and ν_{12}=ν_{21}=0.31.

Comparisons between the analytical solution and numerical analysis results are depicted in Figures V.4-12 for various material combinations, geometries, and loading conditions. The agreement is consistently satisfactory, affirming the suitability of the proposed solution, originally exact for infinite plates, for characterizing stress and displacement fields in finite plates.

Specifically, Figure 4 illustrates the hoop stress component along the hole boundary for plates under uniaxial tension, revealing an increase in stress magnitude with a decreasing ratio. Figure V.5 showcases stress components along the boundary of the reinforcing annulus for a PA plate, emphasizing the precision of the proposed framework.

The accuracy of the analytical solution under different loading conditions is demonstrated in Figures V.6-11 for various materials and reinforcing ring sizes. Disparate loading conditions, such as biaxial tension with constant internal radial pressure (Figure V.6), pure in-plane shear (Figure V.7), and in-plane shear combined with internal radial pressure (Figure V.8), are considered. Additionally, in-plane shear combined with non-uniform internal pressure, simulating pressure exerted by a pin, is explored with results presented in Figure V.9b:

i. biaxial tension combined with a constant internal radial pressure (Figure V.6);
ii. pure in-plane shear (Figure V.7);
iii. in-plane shear combined with a constant internal radial pressure (Figure V.8);
iv. in-plane shear combined with a non-uniform internal pressure, simulating the pressure exerted by a pin. In this case, the internal pressure was described taking advantage of the following equation (see also Figure V.9a):

$$\bar{\sigma}_{rr}(\theta) = \Phi(\theta) = \frac{100}{\pi} + 50\sin\left[\theta\right] - \frac{200\cos\left[2\theta\right]}{3\pi} - \frac{40\cos\left[4\theta\right]}{3\pi} - \frac{40\cos\left[6\theta\right]}{7\pi} - \frac{200\cos\left[8\theta\right]}{63\pi} - \frac{200\cos\left[10\theta\right]}{99\pi} \qquad \text{V.31}$$

Displacement distributions are illustrated in Figures V.10 and V.11, showcasing continuous fields despite the discontinuity observed in the hoop stress component (Figures V.6, V.8, and V.9) due to elastic material mismatch.

Finally, Figure V.12 focuses on a 100x100 mm plate with a 10 mm radius hole and a 5 mm thick reinforcement under complex loading conditions. Despite the plate size approaching the hole radius, the proposed solution's accuracy remains acceptable, with a maximum difference between numerical and theoretical results within 10%.

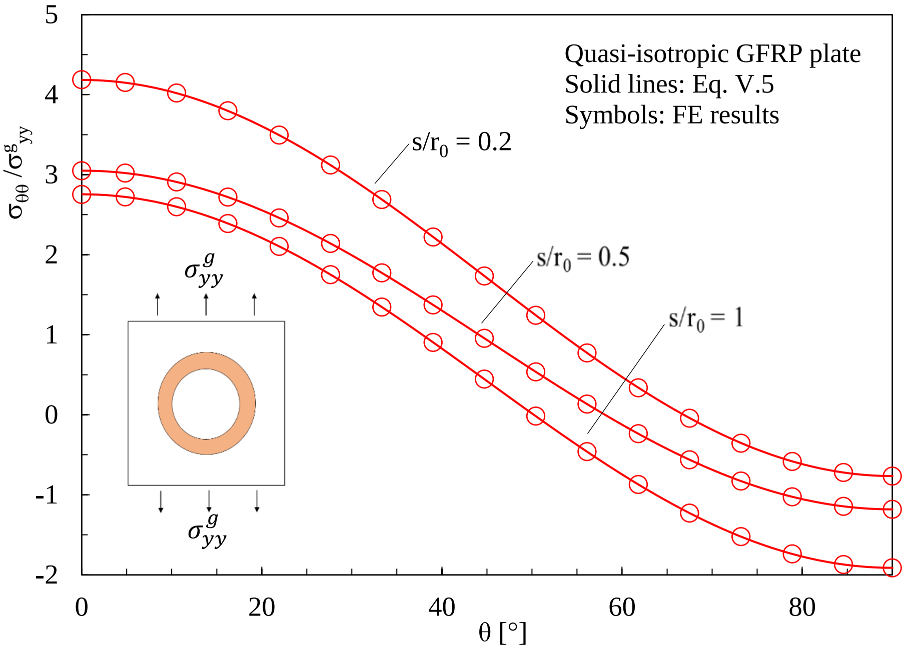

Figure V.4. Stress component $\sigma_{\theta\theta}$ evaluated along the boundary of the hole (path 4 in Figure V.3). 250x250 mm isotropic plates made of quasi-isotropic GFRP; hole radius r_0=10 mm reinforced with rings of width s = 2, 5 and 10 mm. Uniaxial tension $\sigma_{yy}^{g}=100\,MPa$. Analytical solution compared with the results from FE analyses.

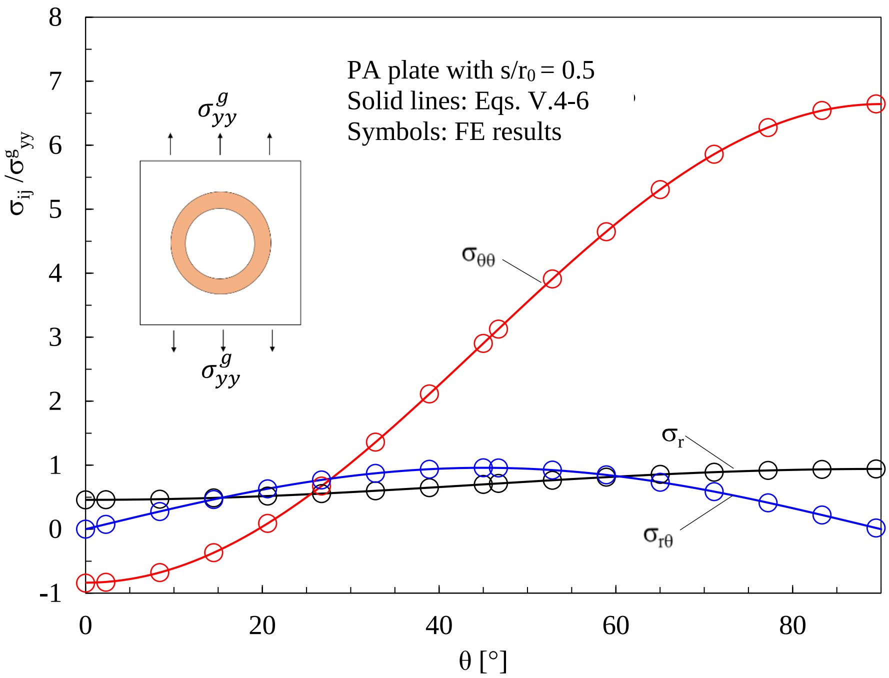

Figure V.5. Stress components $\sigma_{rr}, \sigma_{\theta\theta}, \sigma_{r\theta}$ evaluated along the edge of the reinforcing ring (path 5 in Figure V.3). 250x250 mm plates made of PA; hole radius r_0=10 mm reinforced with a ring of width s =5 mm. Uniaxial tension, $\sigma_{yy}^{g}=100\,MPa$. Analytical solution compared with the results from FE analyses.

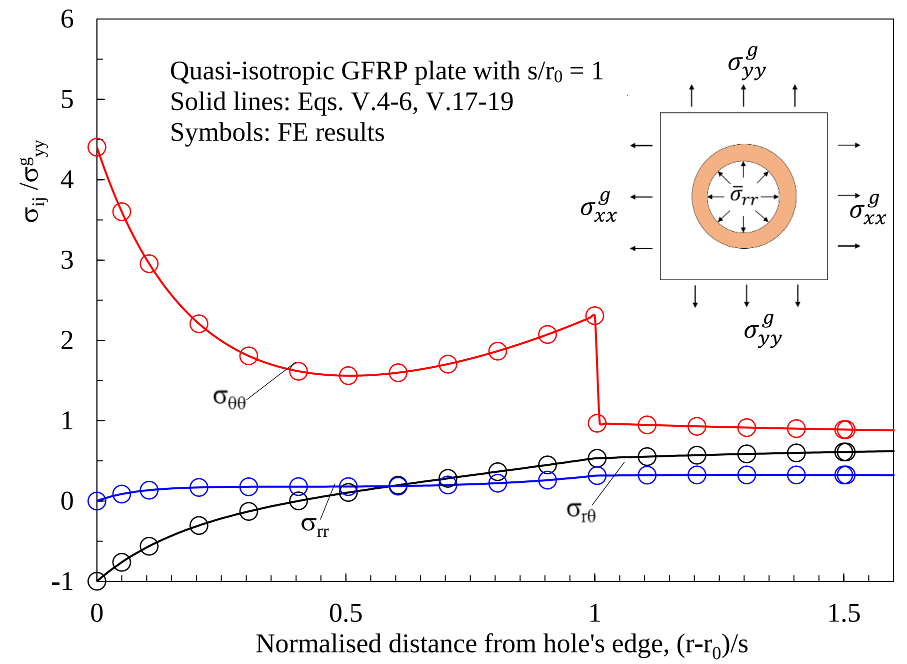

Figure V.6. Stress components $\sigma_{rr}, \sigma_{\theta\theta}, \sigma_{r\theta}$ evaluated along a straight path with θ=45° (path 2 in Figure V.3). 250x250 mm plates made of quasi-isotropic GFRP; hole radius r_0=10 mm reinforced with a ring of width s =10 mm. Applied loads: biaxial tension ($\sigma^{g}_{yy} = 100\,MPa$, $\sigma^{g}_{xx} = 50\,MPa$) and internal pressure ($\bar{\sigma}_{rr} = 100\,MPa$). Analytical solution compared with the results from FE analyses.

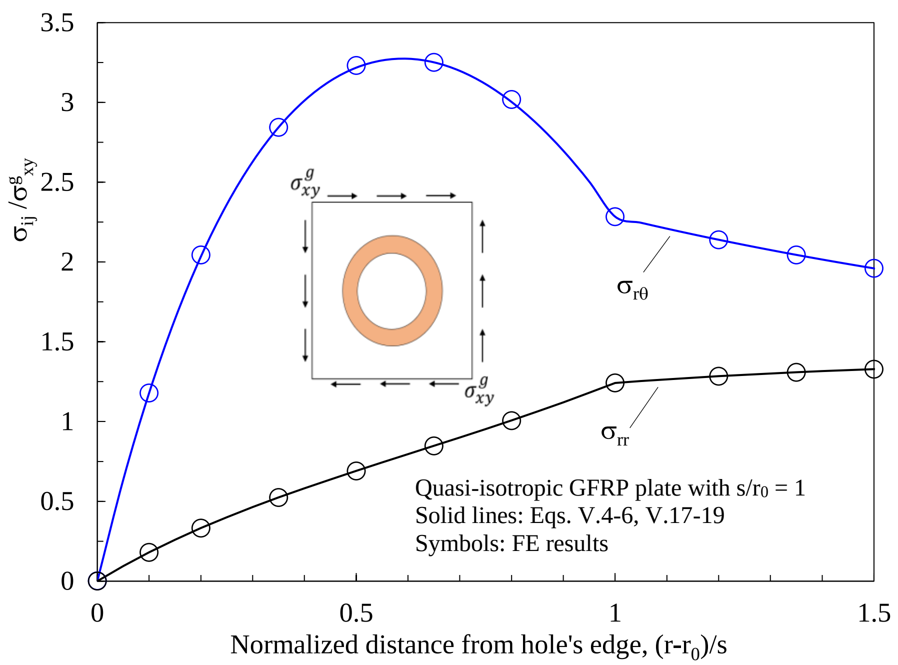

Figure V.7. Stress components σ_{rr}, $\sigma_{r\theta}$ evaluated along a straight path with θ=90° (path 3 in Figure V.3). 250x250 mm plates made of quasi-isotropic GFRP; hole radius r_0=10 mm reinforced with a ring of width s = 10 mm. Pure shear loadings, $\sigma^{g}_{xy} = 100\,MPa$. Analytical solution compared with the results from FE analyses.

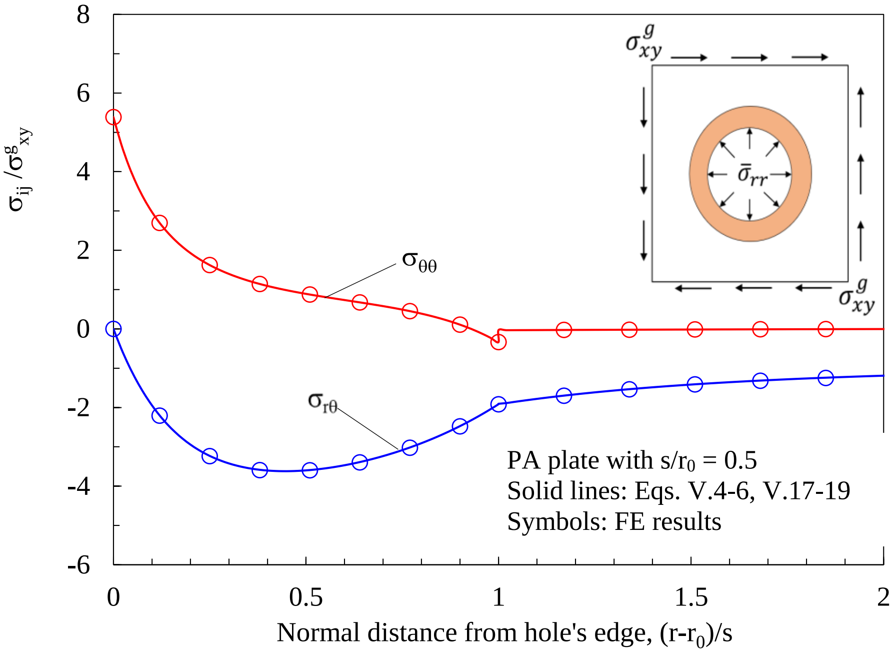

Figure V.8. Stress components $\sigma_{\theta\theta}$ and $\sigma_{r\theta}$ evaluated along a straight path with θ=0° (path 1 in Figure V.3). 250x250 mm plates made of PA; hole radius r_0=10 mm reinforced with a ring of width s = 5 mm. Applied loads: pure shear loadings $\sigma_{xy}^{g} = 100\,MPa$ and internal pressure ($\bar{\sigma}_{rr} = 100\,MPa$). Analytical solution compared with the results from FE analyses.

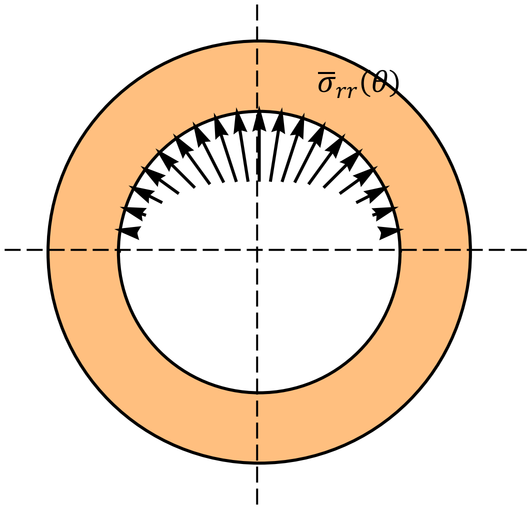

(a)

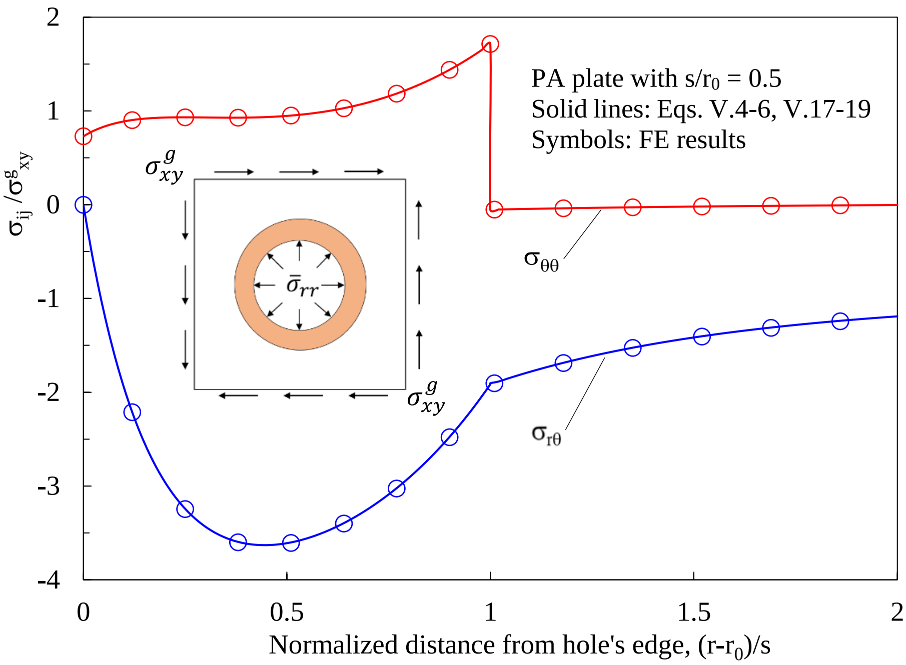

(b)

Figure V.9. (a) Schematic of the internal pressure exerted by a pin, according to the Eq. V.31.
(b) Stress components $\sigma_{\theta\theta}$ and $\sigma_{r\theta}$ evaluated along a straight path with θ=90° (path 3 in Figure V.3). 250x250 mm plates made of PA; hole radius r_0=10 mm reinforced with a ring of width s = 5 mm. Applied loads: pure shear loadings $\sigma_{xy}^{g} = 100\,MPa$ and non-uniform internal pressure according to Eq. V.31 (see also Figure V.9a). Analytical solution compared with the results from FE analyses

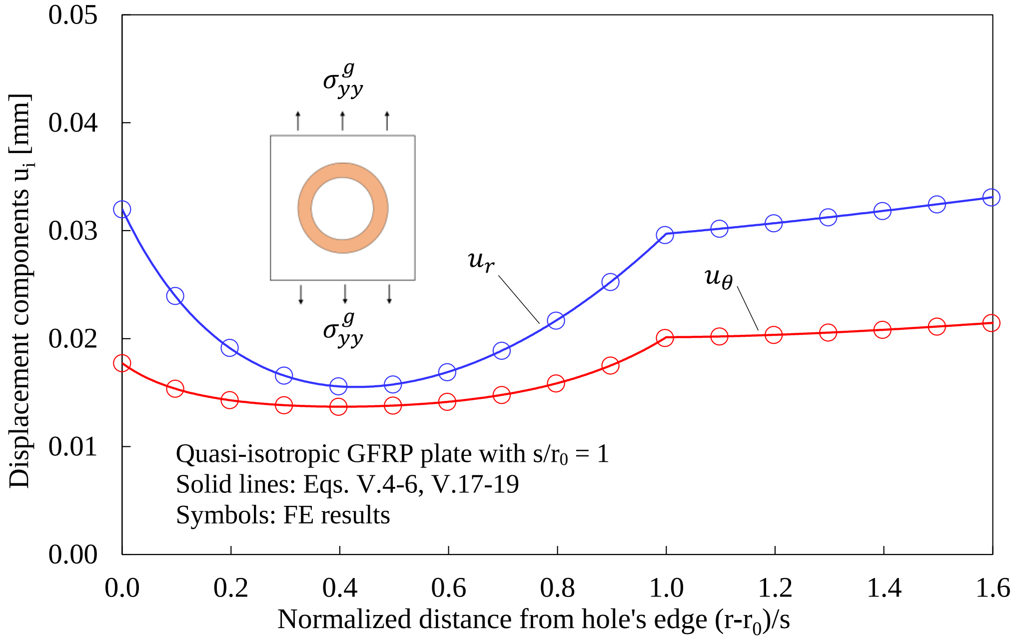

Figure V.10. Displacement components u_r and u_θ evaluated along a straight path with θ=0° (path 3 in Figure V.3). 250x250 mm plates made of quasi-isotropic GFRP; hole radius r_0=10 mm reinforced with a ring of width s = 10 mm. Applied loads: biaxial tension ($\sigma_{yy}^{g} = 100\,MPa$, $\sigma_{xx}^{g} = 50\,MPa$) and internal pressure ($\bar{\sigma}_{rr} = 100\,MPa$). Analytical solution compared with the results from FE analyses.

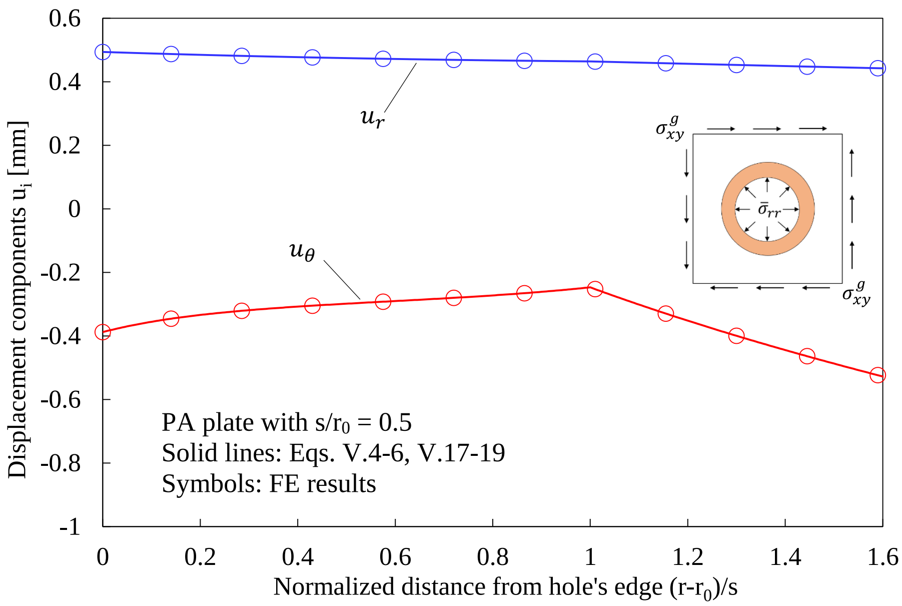

Figure 11. Displacement components u_r and u_θ evaluated along a straight path with θ=90° (path 3 in Figure V.3). 250x250 mm plates made of PA; hole radius r0=10 mm reinforced with a ring of width s = 5 mm. Applied loads: pure shear loadings $\sigma^g_{xy} = 100\,MPa$ and non-uniform internal pressure according to Eq. V.31 (see also Figure V.8a). Analytical solution compared with the results from FE analyses.

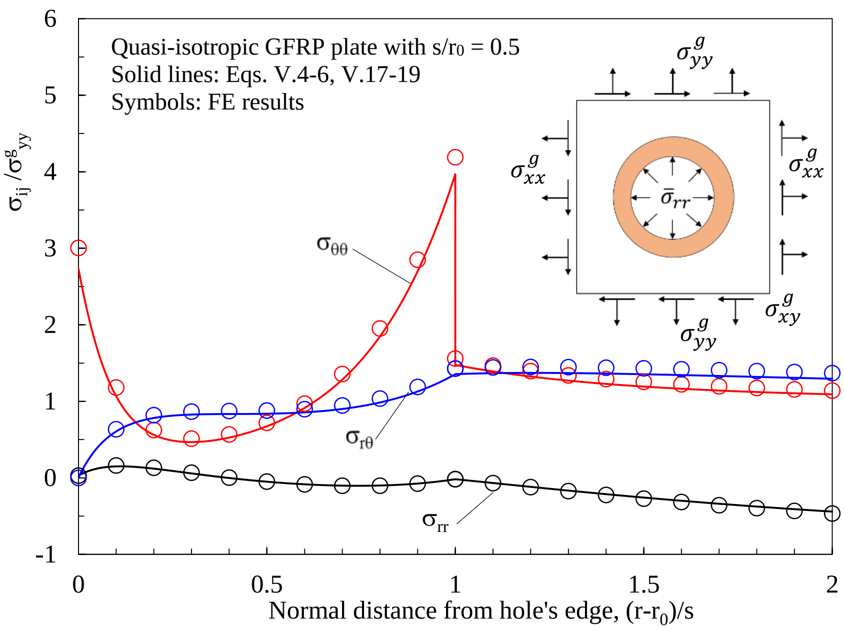

Figure V.12. Stress components $\sigma_{rr}, \sigma_{\theta\theta}, \sigma_{r\theta}$ evaluated along a straight path with θ=0° (path 1 in Figure V.3). 100x100 mm plates made of quasi-isotropic GFRP; hole radius r_0=10 mm reinforced with a ring of width s =5 mm. Applied loads: biaxial tension-compression ($\sigma^g_{yy} = 100\,MPa$ $\sigma^g_{xx} = -50MPa$) shear stress ($\sigma^g_{xy} = 100\,MPa$) and non-uniform internal pressure according to Eq. V.31 (see also figure V.8a). Analytical solution compared with the results from FE analyses.

5.3. A Semi-Analytical Solution for the in-plane Stress Fields in Isotropic Convex Finite Solids with Circular Holes Reinforced with Cylindrically Orthotropic Rings

5.3.1. Analytical solution

5.3.1.1. Statement of the problem

Consider a generic convex isotropic plate with a circular hole of radius r_0, surrounded by a concentric polarly orthotropic annulus of thickness s (reinforced region) and outer radius r_1, $\left(s = r_1 - r_0\right)$ as shown in Figure V.13. Suppose that the solid is subjected to shear and radial stresses along the hole boundary, that can be expressed in the following Fourier series form:

$$\begin{aligned} \bar{\sigma}_{rr}(\theta) &= S_0 + \sum_{n=1}^{N}\left(S_{n,1}\cos(n\theta) + S_{n,2}\sin(n\theta)\right) \\ \bar{\sigma}_{r\theta}(\theta) &= T_0 + \sum_{n=1}^{N}\left(T_{n,1}\cos(n\theta) + T_{n,2}\sin(n\theta)\right) \end{aligned} \qquad \text{V.32}$$

where $S_0, T_0, S_{ij}, T_{ij} \in \mathbb{R}\ \forall i : 1 \le i \le N \in \mathbb{N}; j \in \{1,2\}$. Suppose also that external stresses are applied to the solid's external boundaries, described according to the following Fourier series (see Figure V.13):

$$\sigma_{ij}^{g}(\theta) = \Omega_0^{ij} + \sum_{n=1}^{M}\left(\Omega_{n,1}^{ij}\cos(n\theta) + \Omega_{n,1}^{ij}\sin(n\theta)\right) \qquad \text{V.33}$$

where $\Omega_0^{ij}, \Omega_{n,p}^{ij} \in \mathbb{R}\ \forall n : 1 \le n \le M \in \mathbb{N}; p \in \{1,2\}$, i and j are the direction perpendicular or tangent to the external surface of the solid in every point.

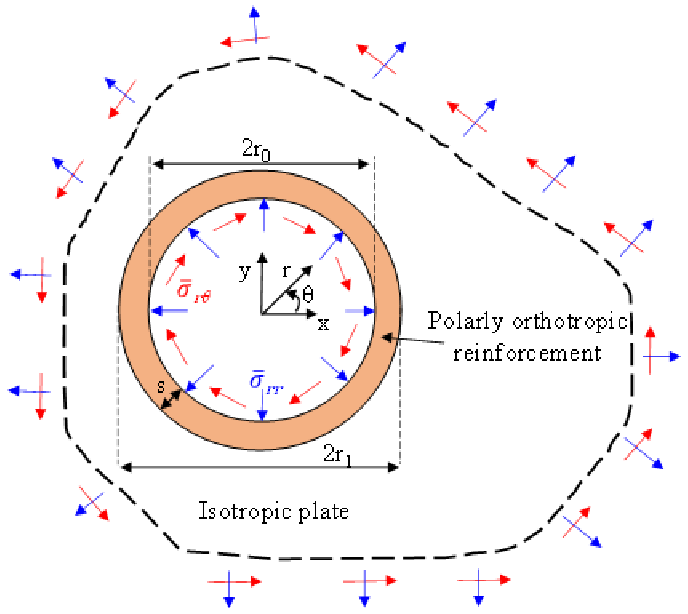

Figure V.13. Finite plate with a reinforced circular hole under generic loading conditions.

5.3.1.2. Universal form for the stress and displacement fields in the reinforced region (reinforcing annulus)

The reinforced region is an annulus concentric with the hole, made of polarly orthotropic material having principal directions of elasticity in the radial and circumferential directions (Figure V.13). Stress and displacements fields in this region can be sought in the same form used by Pastrello et al.[30]:

$$\begin{aligned} u_r^{(1)} = {} & A_0\left(\frac{r_0}{r}\right)^{\alpha_0} + a_0\left(\frac{r}{r_1}\right)^{\alpha_0} - E_1\left(\frac{1+d^{-2}}{1+\epsilon^{-2}}\right)\cos\theta + \left(E_1\cos\theta + F_1\sin\theta\right)\log\left(\frac{r}{r_0}\right) + \\ & + \sum_{n=1}^{P}\left(\left(A_n\cos n\theta + B_n\sin n\theta\right)\left(\frac{r_0}{r}\right)^{\alpha_n} + \left(a_n\cos n\theta + b_n\sin n\theta\right)\left(\frac{r}{r_1}\right)^{\alpha_n}\right) + \\ & + \sum_{n=2}^{P}\left(\left(E_n\cos n\theta + F_n\sin n\theta\right)\left(\frac{r_0}{r}\right)^{\beta_n} + \left(e_n\cos n\theta + f_n\sin n\theta\right)\left(\frac{r}{r_1}\right)^{\beta_n}\right) \end{aligned} \qquad \text{V.34}$$

$$u_\theta^{(1)} = F_1\left(\frac{1+d^{-2}}{1+\epsilon^{-2}}\right)\cos\theta - H_0\left(\frac{r_0}{r}\right) + \left(F_1\cos\theta - E_1\sin\theta\right)\log\left(\frac{r}{r_0}\right) +$$
$$+\sum_{n=1}^{P}\left(\left(C_n \sin n\theta - D_n \cos n\theta\right)\left(\frac{r_0}{r}\right)^{\alpha_n} + \left(c_n \sin n\theta - d_n \cos n\theta\right)\left(\frac{r}{r_1}\right)^{\alpha_n}\right) +$$
$$+\sum_{n=2}^{P}\left(\left(G_n \sin n\theta - H_n \cos n\theta\right)\left(\frac{r_0}{r}\right)^{\beta_n} + \left(g_n \sin n\theta - h_n \cos n\theta\right)\left(\frac{r}{r_1}\right)^{\beta_n}\right) \qquad \text{V.35}$$

$$\sigma_{rr}^{(1)} = \frac{G_{\theta r}^{(1)}}{rc^2 d_1^2}\Bigg\{\left(\frac{r_0}{r}\right)^{\alpha_0} A_0\left(c^2 - d^2\alpha_0\right) + \left(\frac{r}{r_1}\right)^{\alpha_0} a_0\left(c^2 + d^2\alpha_0\right) +$$
$$+E_1 \frac{d^4 - \left(c^2\left(1+d^2\right) - d^4\right)\epsilon^2}{d^2\left(1+\epsilon^2\right)}\cos\theta + F_1 \frac{d^4 - \left(c^2\left(1+d^2\right) - d^4\right)\epsilon^2}{d^2\left(1+\epsilon^2\right)}\sin\theta +$$
$$+\sum_{n=1}^{P}\Bigg[\left(\frac{r_0}{r}\right)^{\alpha_n}\left[\left(A_n\cos(n\theta) + B_n\sin(n\theta)\right)\left(c^2 - d^2\alpha_n\right) + \left(C_n\cos(n\theta) + D_n\sin(n\theta)\right)nc^2\right] +$$
$$+\left(\frac{r}{r_1}\right)^{\alpha_n}\left[\left(a_n\cos(n\theta) + b_n\sin(n\theta)\right)\left(c^2 + d^2\alpha_n\right) + \left(c_n\cos(n\theta) + d_n\sin(n\theta)\right)nc^2\right]\Bigg] + \qquad \text{V.36}$$
$$+\sum_{n=2}^{P}\Bigg[\left(\frac{r_0}{r}\right)^{\beta_n}\left[\left(E_n\cos(n\theta) + F_n\sin(n\theta)\right)\left(c^2 - d^2\beta_n\right) + \left(G_n\cos(n\theta) + H_n\sin(n\theta)\right)nc^2\right] +$$
$$+\left(\frac{r}{r_1}\right)^{\beta_n}\left[\left(e_n\cos(n\theta) + f_n\sin(n\theta)\right)\left(c^2 + d^2\beta_n\right) + \left(g_n\cos(n\theta) + h_n\sin(n\theta)\right)nc^2\right]\Bigg]\Bigg\}$$

$$\sigma_{\theta\theta}^{(1)} = \frac{G_{\theta r}^{(1)}}{rd^2 \epsilon_1^2}\Bigg\{\left(\frac{r_0}{r}\right)^{\alpha_0} A_0\left(d^2 - \epsilon^2\alpha_0\right) + \left(\frac{r}{r_1}\right)^{\alpha_0} a_0\left(d^2 + \epsilon^2\alpha_0\right) +$$
$$+E_1 \frac{\epsilon^2\left(\epsilon^2 - d^2\right)}{1+\epsilon^2}\cos\theta + F_1 \frac{\epsilon^2\left(\epsilon^2 - d^2\right)}{1+\epsilon^2}\sin\theta +$$
$$+\sum_{n=1}^{P}\Bigg[\left(\frac{r_0}{r}\right)^{\alpha_n}\left[\left(A_n\cos(n\theta) + B_n\sin(n\theta)\right)\left(d^2 - \epsilon^2\alpha_n\right) + \left(C_n\cos(n\theta) + D_n\sin(n\theta)\right)nd^2\right] +$$
$$+\left(\frac{r}{r_1}\right)^{\alpha_n}\left[\left(a_n\cos(n\theta) + b_n\sin(n\theta)\right)\left(d^2 + \epsilon^2\alpha_n\right) + \left(c_n\cos(n\theta) + d_n\sin(n\theta)\right)nd^2\right]\Bigg] + \qquad \text{V.37}$$
$$+\sum_{n=2}^{P}\Bigg[\left(\frac{r_0}{r}\right)^{\beta_n}\left[\left(E_n\cos(n\theta) + F_n\sin(n\theta)\right)\left(d^2 - \epsilon^2\beta_n\right) + \left(G_n\cos(n\theta) + H_n\sin(n\theta)\right)nd^2\right] +$$
$$+\left(\frac{r}{r_1}\right)^{\beta_n}\left[\left(e_n\cos(n\theta) + f_n\sin(n\theta)\right)\left(d^2 + \epsilon^2\beta_n\right) + \left(g_n\cos(n\theta) + h_n\sin(n\theta)\right)nd^2\right]\Bigg]\Bigg\}$$

$$
\begin{aligned}
\sigma_{r\theta}^{(1)} = \frac{G_{\theta r}^{(1)}}{r} \Bigg\{ & \frac{2r_0 H_0}{r} + F_1 \frac{d^2-\epsilon^2}{d^2\left(1+\epsilon^2\right)}\cos\theta + E_1 \frac{d^2-\epsilon^2}{d^2\left(1+\epsilon^2\right)}\sin\theta + \\
& +\sum_{n=1}^{P}\Bigg[\left(\frac{r_0}{r}\right)^{\alpha_n}\Big[n\big(B_n\cos(n\theta)-A_n\sin(n\theta)\big)+\big(D_n\cos(n\theta)-C_n\sin(n\theta)\big)(\alpha_n+1)\Big]+ \\
& +\left(\frac{r}{r_1}\right)^{\alpha_n}\Big[n\big(b_n\cos(n\theta)-a_n\sin(n\theta)\big)+\big(c_n\sin(n\theta)-d_n\cos(n\theta)\big)(\alpha_n-1)\Big]\Bigg]+ \\
& +\sum_{n=2}^{P}\Bigg[\left(\frac{r_0}{r}\right)^{\beta_n}\Big[n\big(F_n\cos(n\theta)-E_n\sin(n\theta)\big)+\big(H_n\cos(n\theta)-G_n\sin(n\theta)\big)(\beta_n+1)\Big]+ \\
& +\left(\frac{r}{r_1}\right)^{\beta_n}\Big[n\big(f_n\cos(n\theta)-e_n\sin(n\theta)\big)+\big(g_n\sin(n\theta)-h_n\cos(n\theta)\big)(\beta_n-1)\Big]\Bigg]\Bigg\}
\end{aligned}
\qquad \text{V.38}
$$

In Eqs. V.34 to V.38, the superscript (1) refers to the elastic constants, stresses and displacements of the material the reinforcing region is made of.

Unknowns A_n, a_n, B_n, b_n, C_n, c_n, D_n, d_n, E_n, e_n, F_n, f_n, G_n, g_n, H_n, h_n, $\forall n \le P \in \mathbb{N} \,\big|\, N, M \le P$ as well as all the other constants in Eqs. V.34 to V.38 have the same expressions given in the previous chapter.

5.3.1.3. Universal form for the stress and displacement fields outside the reinforced region (plate)

The universal form for the stress and displacement fields in the isotropic solid outside the reinforced region can be determined by means of Muskhelishvili formulation[2]:

$$
\begin{aligned}
&\sigma_{rr}^{(2)} + \sigma_{\theta\theta}^{(2)} = 4\,\mathrm{Re}\left[\frac{d\Phi(z)}{dz}\right] \\
&\sigma_{\theta\theta}^{(2)} - \sigma_{rr}^{(2)} + 2i\sigma_{r\theta}^{(2)} = 2e^{2i\theta}\left(\bar{z}\,\frac{d^2\Phi(z)}{dz^2} + \frac{d\mathrm{X}(z)}{dz}\right) \\
&u_r^{(2)} + iu_\theta^{(2)} = \frac{1+\nu^{(2)}}{E^{(2)}}\left(\kappa\,\Phi(z) - z\,\overline{\frac{d\Phi(z)}{dz}} - \overline{\mathrm{X}(z)}\right)e^{-i\theta}
\end{aligned}
\qquad \text{V.39}
$$

where E and ν represent the elastic modulus and the Poisson ratio, and superscript (2) identifies the properties of the isotropic unreinforced region.

The following two potential functions are used for the problem under investigation, being them suitable forms to apply proper boundary conditions:

$$\begin{aligned}
\Phi(z) &= \left(\bar{A}_0 + i\bar{B}_0\right) log\left(z\right) + \left(\bar{A}_c + i\bar{B}_c\right) + \sum_{n=1}^{P-1}\left(\bar{A}_{-n} + i\bar{B}_{-n}\right)z^{-n} + \sum_{n=1}^{P+1}\left(\bar{A}_n + i\bar{B}_n\right)z^n \\
\mathrm{X}(z) &= -\kappa\left(\bar{A}_0 - i\bar{B}_0\right) log\left(z\right) + \sum_{n=1}^{P+1}\left(\bar{C}_{-n} + i\bar{D}_{-n}\right)z^{-n} + \sum_{n=1}^{P-1}\left(\bar{C}_n + i\bar{D}_n\right)z^n
\end{aligned} \qquad \text{V.40}$$

Substituting Eq. V.40 into Eq. V.39 it results in the following stress and displacement fields:

$$\begin{aligned}
u_r^{(2)} = \frac{\left(\nu^{(2)}+1\right)}{E^{(2)}}\Bigg\{ & \frac{\left(r^2\left(\kappa-1\right)\bar{A}_1 - \bar{C}_{-1}\right)}{r} + \\
& + \frac{\left(r^2\left(\left(\kappa\log\left(r^2\right)-1\right)\bar{A}_0 + r^2\left(\kappa-2\right)\bar{A}_2 + \kappa\bar{A}_c\right) - \bar{C}_{-2}\right)}{r^2}\cos\left(\theta\right) + \\
& + \frac{\left(r^2\left(\left(\kappa\log\left(r^2\right)-1\right)\bar{B}_0 - r^2\left(\kappa-2\right)\bar{B}_2 + \kappa\bar{B}_c\right) - \bar{D}_{-2}\right)}{r^2}\sin\left(\theta\right) + \\
& + \sum_{n=3}^{P}\Bigg[\frac{\left(r^2\left(\left(n-1\right)+\kappa\right)\bar{A}_{-(n-1)} + r^{2(n+1)}\left(\kappa-\left(n+1\right)\right)\bar{A}_{(n+1)} - \bar{C}_{-(n+1)} - r^{2(n-1)}\bar{C}_{(n-1)}\right)}{r^{n+1}}\cos\left(n\theta\right) + \\
& + \frac{\left(r^2\left(\left(n-1\right)+\kappa\right)\bar{B}_{-(n-1)} - r^{2(n+1)}\left(\kappa-\left(n+1\right)\right)\bar{B}_{(n+1)} - \bar{D}_{-(n+1)} + r^{2(n-1)}\bar{D}_{(n-1)}\right)}{r^{n+1}}\sin\left(n\theta\right)\Bigg]\Bigg\}
\end{aligned} \qquad \text{V.41}$$

$$\begin{aligned}
u_\theta^{(2)} = \frac{\left(\nu^{(2)}+1\right)}{E^{(2)}}\Bigg\{ & \frac{\left(r^2\left(1+\kappa\right)\bar{B}_1 + \bar{D}_{-1}\right)}{r} + \\
& + \frac{\left(r^2\left(\left(1+\kappa\log\left(r^2\right)\right)\bar{B}_0 + r^2\left(2+\kappa\right)\bar{B}_2 + \kappa\bar{B}_c\right) + \bar{D}_{-2}\right)}{r^2}\cos\left(\theta\right) - \\
& - \frac{\left(r^2\left(\left(1+\kappa\log\left(r^2\right)\right)\bar{A}_0 - r^2\left(2+\kappa\right)\bar{A}_2 + \kappa\bar{A}_c\right) + \bar{C}_{-2}\right)}{r^2}\sin\left(\theta\right) + \\
& + \sum_{n=2}^{P}\Bigg[\frac{\left(r^2\left(\kappa-\left(n-1\right)\right)\bar{B}_{-(n-1)} + r^{2(n+1)}\left(\kappa+\left(n+1\right)\right)\bar{B}_{(n+1)} + \bar{D}_{-(n+1)} + r^{2n}\bar{D}_{(n-1)}\right)}{r^{n+1}}\cos\left(n\theta\right) - \\
& + \frac{\left(r^2\left(\left(n-1\right)-\kappa\right)\bar{A}_{-(n-1)} + r^{2(n+1)}\left(\kappa+\left(n+1\right)\right)\bar{A}_{(n+1)} - \bar{C}_{-(n+1)} + r^{2n}\bar{C}_{(n-1)}\right)}{r^{n+1}}\sin\left(n\theta\right)\Bigg]\Bigg\}
\end{aligned} \qquad \text{V.42}$$

$$\sigma_{rr}^{(2)}=\frac{1}{(\tilde{\nu}-1)}\left\{\frac{\left(\bar{C}_{-1}(\tilde{\nu}-1)-r^{2}(\kappa-1)(\tilde{\nu}+1)\bar{A}_{1}\right)}{r^{2}}+\right.$$

$$+\frac{2\left(r^{2}(\tilde{\nu}-\kappa)\bar{A}_{0}-r^{4}(\kappa+\kappa\tilde{\nu}-2)\bar{A}_{2}+(\tilde{\nu}-1)\bar{C}_{-2}\right)}{r^{3}}\cos(\theta)+$$

$$+\frac{2\left(r^{2}(\tilde{\nu}-\kappa)\bar{B}_{0}+r^{4}(\kappa+\kappa\tilde{\nu}-2)\bar{B}_{2}+(\tilde{\nu}-1)\bar{D}_{-2}\right)}{r^{3}}\sin(\theta)+$$

$$+\sum_{n=2}^{P}\left[\frac{\left((n-1)r^{2}\left((n-1)-(n+1)\tilde{\nu}+\kappa(\tilde{\nu}+1)\right)\bar{A}_{-(n-1)}+(n+1)(\tilde{\nu}-1)\bar{C}_{-(n+1)}\right)}{r^{n+1}}\cos(n\theta)-\right.$$

$$-\frac{(n+1)r^{2(n+1)}\left(\kappa-(n+1)+\left((n-1)+\kappa\right)\tilde{\nu}\right)\bar{A}_{(n+1)}+(n-1)(\tilde{\nu}-1)r^{2n}\bar{C}_{(n-1)}}{r^{n+1}}\cos(n\theta)+$$

$$+\frac{\left((n-1)r^{2}\left((n-1)-(n+1)\tilde{\nu}+\kappa(\tilde{\nu}+1)\right)\bar{B}_{-(n-1)}+(n+1)(\tilde{\nu}-1)\bar{D}_{-(n+1)}\right)}{r^{n+1}}\sin(n\theta)+$$

$$\left.\left.+\frac{(n+1)r^{2(n+1)}\left(\kappa-(n+1)+\left((n-1)+\kappa\right)\tilde{\nu}\right)\bar{B}_{(n+1)}+(n-1)(\tilde{\nu}-1)r^{2n}\bar{D}_{(n-1)}}{r^{n+1}}\sin(n\theta)\right]\right\} \qquad \text{V.43}$$

$$\sigma_{\theta\theta}^{(2)}=\frac{1}{(\tilde{\nu}-1)}\left\{\frac{\left(\bar{C}_{-1}(\tilde{\nu}-1)+r^{2}(\kappa-1)(\tilde{\nu}+1)\bar{A}_{1}\right)}{r^{2}}+\right.$$

$$+\frac{2\left(r^{2}(1-\tilde{\nu}\kappa)\bar{A}_{0}+r^{4}\left(\kappa+(\kappa-2)\tilde{\nu}\right)\bar{A}_{2}-(\tilde{\nu}-1)\bar{C}_{-2}\right)}{r^{3}}\cos(\theta)$$

$$+\frac{2\left(r^{2}(1-\tilde{\nu}\kappa)\bar{B}_{0}+r^{4}\left(\kappa+(\kappa-2)\tilde{\nu}\right)\bar{B}_{2}-(\tilde{\nu}-1)\bar{D}_{-2}\right)}{r^{3}}\sin(\theta)+$$

$$+\sum_{n=2}^{P}\left[\frac{\left((n-1)r^{2}\left((n-1)\tilde{\nu}-(n+1)+\kappa(\tilde{\nu}+1)\right)\bar{A}_{-(n-1)}-(n+1)(\tilde{\nu}-1)\bar{C}_{-(n+1)}\right)}{r^{n+1}}\cos(n\theta)-\right.$$

$$-\frac{(n+1)r^{2(n+1)}\left((n-1)+\kappa+\left(\kappa-(n+1)\right)\tilde{\nu}\right)\bar{A}_{(n+1)}+(n-1)(\tilde{\nu}-1)r^{2n}\bar{C}_{(n-1)}}{r^{n+1}}\cos(n\theta)+$$

$$+\frac{\left((n-1)r^{2}\left((n-1)\tilde{\nu}-(n+1)+\kappa(\tilde{\nu}+1)\right)\bar{B}_{-(n-1)}-(n+1)(\tilde{\nu}-1)\bar{D}_{-(n+1)}\right)}{r^{n+1}}\sin(n\theta)+$$

$$\left.\left.+\frac{(n+1)r^{2(n+1)}\left((n-1)+\kappa+\left(\kappa-(n+1)\right)\tilde{\nu}\right)\bar{B}_{(n+1)}+(n-1)(\tilde{\nu}-1)r^{2n}\bar{D}_{(n-1)}}{r^{n+1}}\sin(n\theta)\right]\right\} \qquad \text{V.44}$$

$$\sigma_{r\theta}^{(2)} = -\frac{\bar{D}_{-1}}{r^2} + \frac{\left(r^2(1-\kappa)\bar{B}_0 + 2\left(r^4\bar{B}_2 + \bar{D}_{-2}\right)\right)}{r^3}\cos(\theta) + $$
$$+\frac{\left(r^2(1-\kappa)\bar{A}_0 + 2\left(r^4\bar{A}_2 + \bar{C}_{-2}\right)\right)}{r^3}\sin(\theta) +$$
$$+\sum_{n=2}^{P}\left[\frac{\left(\left(n^2-n\right)\bar{B}_{-(n-1)} + (n-1)r^{2n}\bar{D}_{(n-1)} - (n+1)\bar{D}_{-(n+1)} + \left(n^2+n\right)r^n\bar{B}_{(n+1)}\right)}{r^{n+2}}\cos(n\theta) + \right. \qquad \text{V.45}$$
$$\left.+\frac{\left((n+1)\bar{C}_{-(n+1)} + (n-1)r^{2n}\bar{C}_{(n-1)} - \left(n^2-n\right)\bar{A}_{-(n-1)} + \left(n^2+n\right)r^n\bar{A}_{(n+1)}\right)}{r^{n+2}}\sin(n\theta)\right]\Bigg\}$$

$\bar{A}_c, \bar{B}_c, \bar{A}_n, \bar{B}_n, \bar{C}_n, \bar{D}_n \ \forall n \le P \in \mathbb{N}$ are integration constants to determine applying proper boundary conditions, remembering that $\kappa = 3 - 4\nu^{(2)}$ for plane strain conditions, whilst for plane stress $\kappa = \frac{3-\nu^{(2)}}{1+\nu^{(2)}}$, and $\tilde{\nu} = \nu^{(2)}$ for plane stress while $\tilde{\nu} = \frac{\nu^{(2)}}{1-\nu^{(2)}}$ for plain strain.

5.3.1.4. Boundary conditions and explicit solution for unknown coefficients

Since compatibility and equilibrium conditions should be guaranteed along the boundary of the reinforcing annulus, it is possible to write the following system of equations:

$$\begin{array}{ll} \sigma_{rr}^{(1)}(r=r_0,\theta) = \bar{\sigma}_{rr}(\theta) & \sigma_{r\theta}^{(1)}(r=r_1,\theta) = \sigma_{r\theta}^{(2)}(r=r_1,\theta) \\ \sigma_{r\theta}^{(1)}(r=r_0,\theta) = \bar{\sigma}_{r\theta}(\theta) & u_r^{(1)}(r=r_1,\theta) = u_r^{(2)}(r=r_1,\theta) \\ \sigma_{rr}^{(1)}(r=r_1,\theta) = \sigma_{rr}^{(2)}(r=r_1,\theta) & u_\theta^{(1)}(r=r_1,\theta) = u_\theta^{(2)}(r=r_1,\theta) \end{array} \qquad \text{V.46}$$

where, $r_1 = r_0 + s$.

Eqs. V.45 can be rewritten in matrix form as it follows:

$$\hat{\mathbf{H}} \cdot \bar{\mathrm{v}} = \bar{\mathrm{k}} \qquad \text{V.47}$$

Where $\hat{\mathbf{H}}$ is a diagonal block matrix defined as:

$$\hat{\mathbf{H}} = \mathrm{Diag}\left[\hat{\mathbf{H}}_0, \hat{\mathbf{H}}_1, \cdots, \hat{\mathbf{H}}_{\mathrm{N}}\right] \qquad \text{V.48}$$

And $\hat{\mathbf{H}}_i$ are defined in M. Pastrello et al.[31]. $\bar{\mathbf{v}}$ is the coefficient vector:

$$\bar{\mathrm{v}} = \left\{\bar{\mathrm{v}}_0, \bar{\mathrm{v}}_1, \cdots, \bar{\mathrm{v}}_N\right\} \qquad \text{V.49}$$

Where:

$$\bar{\mathrm{v}}_0 = \left\{A_0, a_0, \bar{C}_{-1}, \bar{D}_{-1}, H_0, \bar{B}_1\right\}; \qquad \text{V.50}$$

$$\bar{\mathrm{v}}_1 = \left\{C_1, c_1, E_1, \bar{A}_0, \bar{C}_{-2}, \bar{A}_c, D_1, d_1, F_1, \bar{B}_0, \bar{D}_{-2}, \bar{B}_c\right\} \qquad \text{V.51}$$

$$\bar{\mathrm{v}}_n = \left\{C_n, G_n, c_n, g_n, \bar{A}_{1-n}, \bar{C}_{-n-1}, D_n, H_n, d_n, h_n, \bar{B}_{1-n}, \bar{D}_{-n-1}\right\} \qquad \forall\, 2 \le n \le P \qquad \text{V.52}$$

and $\bar{\mathrm{k}}$ is a vector defined in M. Pastrello et al.[31].

By solving the system defined in Equation V.47, one can derive expressions for coefficients as functions of the remaining coefficients, where n varies from 2 to P. To determine these coefficients, it is necessary to impose boundary conditions on the external boundaries. However, conventional equilibrium equations cannot be precisely solved for a finite value of P. Hence, this solution employs a numerical approximation technique based on minimizing residual stresses.

The external boundary can be divided into $\mathrm{N}_{\mathrm{div}}$ number of divisions, each described with parametric equations $\mathrm{l}_{\mathrm{n}}(\mathrm{s})$, $\mathrm{n} \in \{1, \cdots, \mathrm{N}_{\mathrm{div}}\}$ (for $\mathrm{N}_{\mathrm{div}} = 1$, $l_1(s)$ is the parametric description of the whole external boundary).

The residual stresses calculated along these curves are:

$$\Delta_{ij}^{n} = \left\{\sigma_{ij}^{(2)}(r,\theta) - \sigma_{ij}^{g}(\theta)\right\}\Big|_{\{r,\theta\}\in l_n(s)} \qquad \text{V.53}$$

where $\sigma_{\mathrm{ij}}^{\mathrm{g}}(\mathrm{r})$ are the stresses applied to the external boundary with i, j being the directions perpendicular or tangent to the boundary.

Taking into account the maximum distance, denoted as r_{max}, of the external boundaries from the centre of the hole, the goal is to standardize the minimization procedure based on the solid's maximum size. To achieve this, the following substitutions can be applied in equation V.53:

$$\bar{A}_n = \frac{\hat{A}_n}{r_{max}^{n}}; \qquad \bar{B}_n = \frac{\hat{B}_n}{r_{\max}^{n}}; \qquad \bar{C}_n = \frac{\hat{C}_n}{r_{\max}^{n}}; \qquad \bar{D}_n = \frac{\hat{D}_n}{r_{\max}^{n}} \qquad \text{V.54}$$

with n ranging from 2 to P. From V.53 and V.54 the following function describing the total residual stresses can be defined:

$$FO = \sum_{n=1}^{N_{div}} \left\{ \int_{l_n} \left[\sum_{i,j} \left(\Delta_{ij}^{n} \right)^2 \right] ds \right\} \qquad \text{V.55}$$

Function FO is a convex function in the variables $\hat{A}_1, \hat{A}_2, \hat{B}_2, \hat{A}_{n+1}, \hat{B}_{n+1}, \hat{C}_{n-1}, \hat{D}_{n-1}$ with n ranging from 2 to P, and has only one minimum to be found by solving the linear system:

$$\nabla FO = \underline{0} \qquad \text{V.56}$$

Eventually, solving V.56 and substituting the results into the solutions of system V.47 yields an expression for all the coefficients of equations V.34 to V.38, and V.41 to V.45.

5.3.1.5. Particular case: the isotropic reinforced annulus

Let us consider the case of an isotropic annulus of internal radius r_0, external radius r_2 and reinforced by a polarly orthotropic material of width $s = r_1 - r_0$. The following internal pressures are applied:

$$\begin{aligned} \bar{\sigma}_{rr}(\theta) &= S_0 + \sum_{n=2}^{N} \left(S_{n,1} \cos(n\theta) + S_{n,2} \sin(n\theta) \right) \\ \bar{\sigma}_{r\theta}(\theta) &= T_0 + \sum_{n=2}^{N} \left(T_{n,1} \cos(n\theta) + T_{n,2} \sin(n\theta) \right) \end{aligned} \qquad \text{V.57}$$

where $S_0, S_{ij}, T_{ij} \in \mathbb{R}\ \forall i : 2 \le i \le N \in \mathbb{N}; j \in \{1,2\}$. Moreover, the following stresses are applied at the outer boundary of the annulus:

$$\begin{aligned} \sigma_{rr}^{g}(\theta) &= \Omega_0 + \sum_{n=2}^{M} \left(\Omega_{n,1} \cos(n\theta) + \Omega_{n,2} \sin(n\theta) \right) \\ \sigma_{r\theta}^{g}(\theta) &= \left(\frac{r_0}{r_2} \right)^2 T_0 + \sum_{n=2}^{M} \left(\Psi_{n,1} \cos(n\theta) + \Psi_{n,2} \sin(n\theta) \right) \end{aligned} \qquad \text{V.58}$$

where $\Omega_0, \Omega_{ij}, \Psi_{ij} \in \mathbb{R}\ \forall i : 2 \le i \le M \in \mathbb{N}; j \in \{1,2\}$.

This particular problem can be solved exactly imposing the boundary conditions:

$$
\begin{array}{ll}
\sigma_{rr}^{(1)}\left(r=r_0,\theta\right)=\bar{\sigma}_{rr}(\theta) & \sigma_{rr}^{(2)}\left(r=r_2,\theta\right)=\sigma_{rr}^{g}\left(\theta\right) \\
\sigma_{r\theta}^{(1)}\left(r=r_0,\theta\right)=\bar{\sigma}_{r\theta}(\theta) & \sigma_{r\theta}^{(2)}\left(r=r_2,\theta\right)=\sigma_{r\theta}^{g}\left(\theta\right) \\
\sigma_{rr}^{(1)}\left(r=r_1,\theta\right)=\sigma_{rr}^{(2)}\left(r=r_1,\theta\right) & u_{\theta}^{(1)}\left(r=r_1,\theta\right)=u_{\theta}^{(2)}\left(r=r_1,\theta\right) \\
\sigma_{r\theta}^{(1)}\left(r=r_1,\theta\right)=\sigma_{r\theta}^{(2)}\left(r=r_1,\theta\right) & u_{r}^{(1)}\left(r=r_1,\theta\right)=u_{r}^{(2)}\left(r=r_1,\theta\right)
\end{array}
\tag{V.59}
$$

Eqs. V.45 can be rewritten in matrix form as follows:

$$\hat{\mathbf{H}}^* \cdot \overline{\mathrm{v}}^* = \overline{\mathrm{k}}^* \tag{V.60}$$

Where $\hat{\mathbf{H}}^*$ is a diagonal block matrix defined as:

$$\hat{\mathbf{H}}^* = \mathrm{Diag}\left[\hat{\mathbf{H}}_0^*, \hat{\mathbf{H}}_1^*, \cdots, \hat{\mathbf{H}}_N^*\right] \tag{V.61}$$

And $\hat{\mathbf{H}}_i^*$ are defined in M. Pastrello et al.[31]. $\overline{\mathrm{v}}^*$ is the coefficient vector:

$$\overline{\mathrm{v}}^* = \left\{\overline{\mathrm{v}}_0^*, \overline{\mathrm{v}}_1^*, \cdots, \overline{\mathrm{v}}_N^*\right\} \tag{V.62}$$

where:

$$\overline{\mathrm{v}}_0^* = \left\{A_0, a_0, \bar{C}_{-1}, \bar{A}_1, \bar{D}_{-1}, H_0, \bar{B}_1\right\}; \tag{V.63}$$

$$\overline{\mathrm{v}}_1^* = \left\{C_1, c_1, E_1, \bar{A}_0, \bar{C}_{-2}, \bar{A}_c, \bar{A}_2, D_1, d_1, F_1, \bar{B}_0, \bar{D}_{-2}, \bar{B}_c, \bar{B}_2\right\}; \tag{V.64}$$

and

$$\overline{\mathrm{v}}_n^* = \left\{C_n, G_n, c_n, g_n, \bar{A}_{1-n}, \bar{C}_{-n-1}, \bar{A}_{n+1}, \bar{C}_{n-1}, D_n, H_n, d_n, h_n, \bar{B}_{1-n}, \bar{D}_{-n-1}, \bar{B}_{n+1}, \bar{D}_{n-1}\right\} \forall\, 2 \le n \le P \tag{V.65}$$

and $\overline{\mathrm{k}}^*$ is a vector defined in M. Pastrello et al.[31].

5.3.2. Discussion and comparison with numerical results

5.3.2.1. Convergence analysis

Since the proposed solution relies on a numerical approximation, a convergence analysis is due. For this purpose, various boundary conditions have been imposed on a series of rectangular plates with varying dimensions, including width (W), height (H), internal radius (r_0), and interface radius (r_1), all the while incrementing the number of Fourier terms (P) employed to approximate the loads. The ensuing load cases have been taken into account:

1. **L1**: uniaxial tension, with $\sigma_{yy}^{g}=100\,\mathrm{MPa}$.
2. **L2**: biaxial tension, with $\sigma_{yy}^{g}=100\,\mathrm{MPa}$ and $\sigma_{xx}^{g}=50\mathrm{MPa}$, and internal pressure $\bar{\sigma}_{rr}=100\,\mathrm{MPa}$.
3. **L3**: biaxial tension, with $\sigma_{yy}^{g}=100\,\mathrm{MPa}$ and $\sigma_{xx}^{g}=50\mathrm{MPa}$, and non-uniform internal pressure. In this case, the internal pressure, approximating a stress distribution enacted by a pin, was described taking advantage of the following equation:

$$\bar{\sigma}_{rr}(\theta)=\Phi(\theta)=\frac{100}{\pi}+50\sin[\theta]-\frac{200\cos[2\theta]}{3\pi}-\frac{40\cos[4\theta]}{3\pi}-\frac{40\cos[6\theta]}{7\pi}-\frac{200\cos[8\theta]}{63\pi}-\frac{200\cos[10\theta]}{99\pi} \qquad \text{V.66}$$

4. **L4**: biaxial tension-compression, with $\sigma_{yy}^{g}=100\,\mathrm{MPa}$ and $\sigma_{xx}^{g}=-50\mathrm{MPa}$.
5. **L5**: biaxial tension-compression, with $\sigma_{yy}^{g}=100\,\mathrm{MPa}$ and $\sigma_{xx}^{g}=-50\mathrm{MPa}$, and non-uniform internal pressure as per Equation V.65.
6. **L6**: harmonic load. With the following expressions:
    a. Pressure applied on the hole boundary as per Equation V.66.
    b. Tension applied on the lateral left and right edges as: $100\sin(4\theta)$.
    c. Tension applied to the upper and lower edges as: $100\sin[2(\theta-\pi/4)]$.
7. **L7**: harmonic load. With the following expressions:
    a. Pressure applied on the hole boundary as per Equation V.66.
    b. Tension applied on the lateral edges as: $100[\sin(4\theta)+\sin(8\theta)]$.
    c. Tension applied to the upper and lower edges as:

$$100\{\sin[2(\theta-\pi/4)]+\sin[4(\theta-\pi/4)]\}.$$

In all examined plates, the annular reinforcement was selected to be made of Carbon Fibre Reinforced Polymer (CFRP) with the following elastic properties: E_{θ}=147 GPa, E_r=10.3 GPa, $G_{\theta r}$=7 GPa,

$\nu_{r\theta}$=0.02. Conversely, the plates were made of epoxy resin, possessing the subsequent elastic properties: E_x=E_y=54 GPa, and ν_{12}=ν_{21}=0.31. In all the considered scenarios, the hole diameter was maintained at 10 mm.

Model results are assessed in terms of $\sigma_{\theta\theta}$ and compared with the outcomes of Finite Element (FE) analyses conducted using Ansys® version 21 software. Ansys PLANE183 quadrilateral plane elements were utilized under plane stress conditions with a pure displacement formulation. Mesh patterns were created following the methodology outlined in the previous chapter, ensuring dependable FE results. The accuracy of the analytical model was evaluated using the following parameter:

$$\Delta = \left\| \frac{\sigma_{\theta\theta} - \sigma_{\theta\theta,FE}}{\sigma_{\theta\theta,FE}} \right\| = \left\| \mathrm{var}(\sigma_{\theta\theta}) \right\| \qquad \text{V.67}$$

where $\sigma_{\theta\theta}$ represents the stress value predicted by the semi-analytical solution, and $\sigma_{\theta\theta,FE}$ is the stress value obtained from the numerical analysis. The stresses from numerical analyses were assessed at Points P1, P2, and P3, considered representative for studying solution convergence (refer to Table V.2 and Figure V.13), and compared with theoretical predictions (see Figures V.14 to V.16).

Examining Point P1 in Figure V.14 reveals fast convergence, with deviations below 5% at 10 Fourier terms across all considered scenarios. In contrast, Point P2 in Figure V.15 exhibits slower convergence, especially for r_1 of 20mm, and load case L4 appears most affected by this behaviour. Similarly, considering Point P3 in Figure V.16 shows a convergence trend resembling that of Point P2.

Irrespective of the load case, plate and annulus size, increasing terms in the Fourier series results in stress values converging to asymptotic values. However, the convergence speed is influenced by the annulus size, plate aspect ratio, and the specific point under investigation. While the load case does impact convergence, it does so marginally compared to the aforementioned parameters.

The convergence analysis yields reasonable outcomes. Similar to methodologies employing numerical approximations over a geometric domain, accuracy diminishes when the domain exhibits significant dimensional variations. The load case's influence is less pronounced than that of geometric dimensions due to the model's use of Fourier approximations. In the case of a squared plate, acceptable precision can be achieved by employing terms in the Fourier expansions corresponding to the highest degree used to describe applied loads in V.32 and V.33, with a minimum of 5. However, for rectangular plates, the accuracy of results is less predictable, and a universal rule covering all aspect ratios and load cases cannot be provided a priori; hence, a convergence analysis is recommended for such cases.

Point	r coordinate	θ coordinate	Material phase
P1	r_0	0	CFRP
P2	r_1	0	CFRP
P3	r_1	0	Epoxy

Table V.2. Coordinate list of the points used in the convergence analysis.

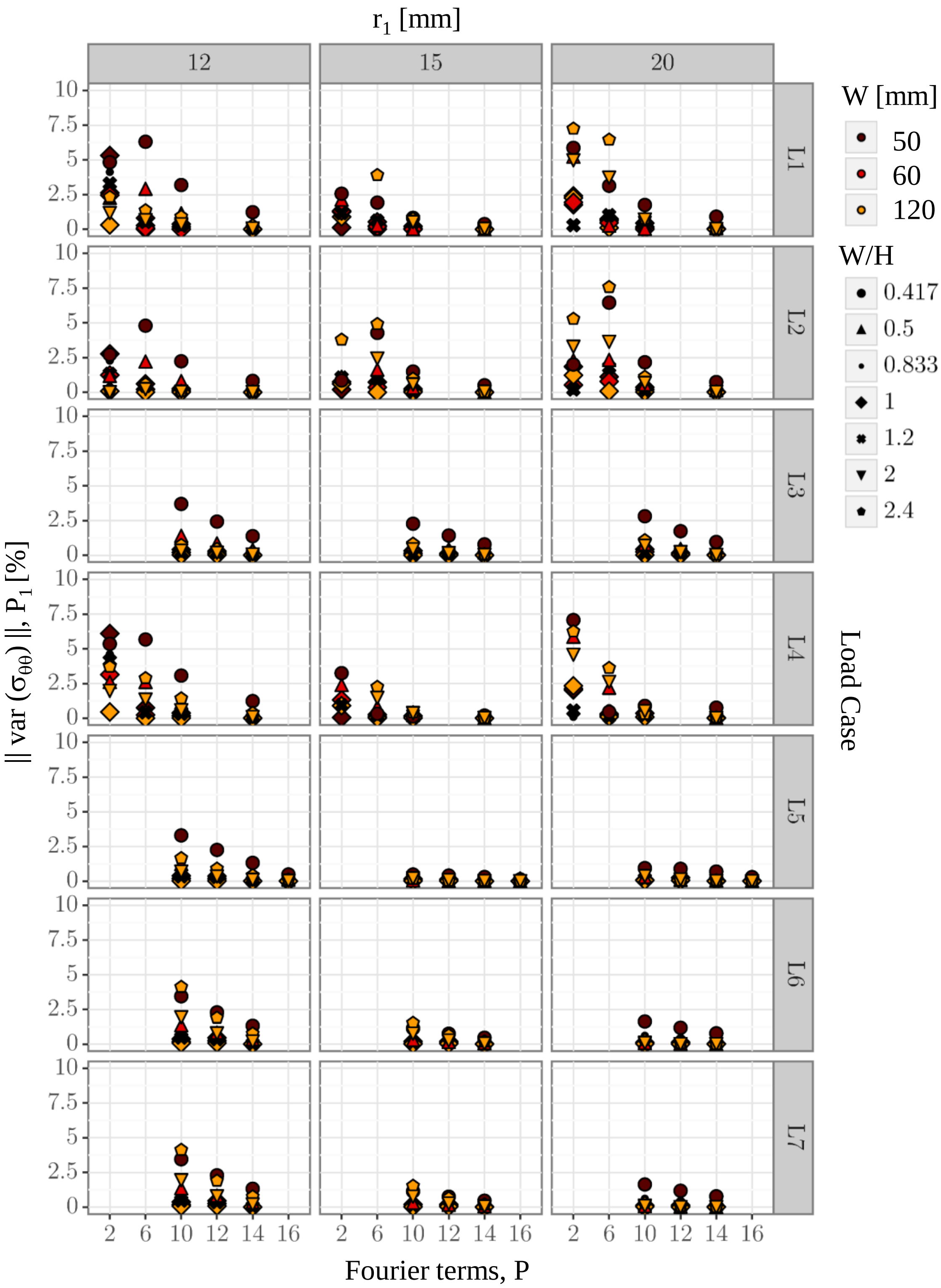

Figure V.14. Convergence analysis for $\sigma_{\theta\theta}$ at point P1 for rectangular plates of width W and height H, under different load cases and r_1 values.

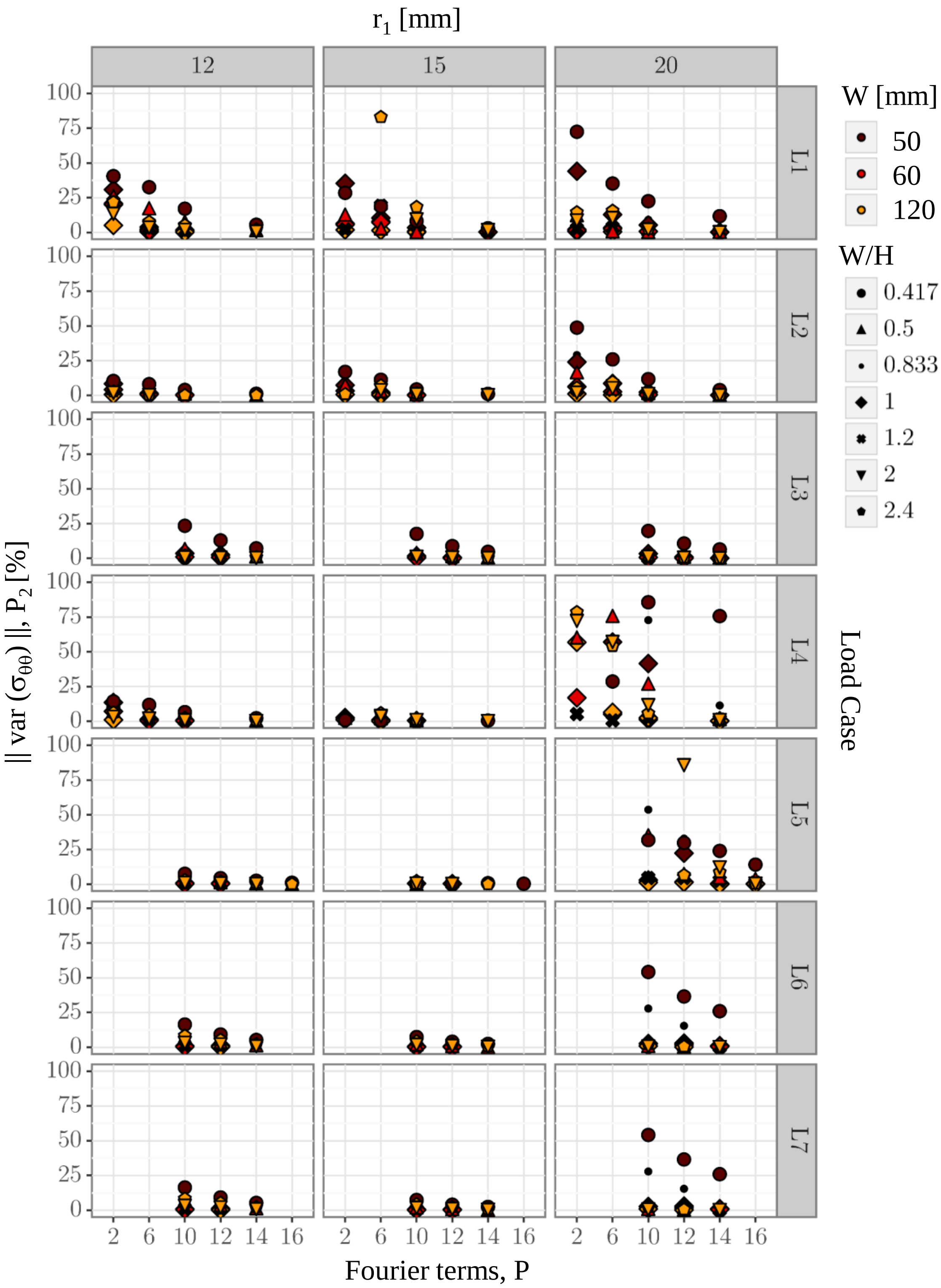

Figure V.15. Convergence analysis for $\sigma_{\theta\theta}$ at point P2 for rectangular plates of width W and height H, under different load cases and r_1 values.

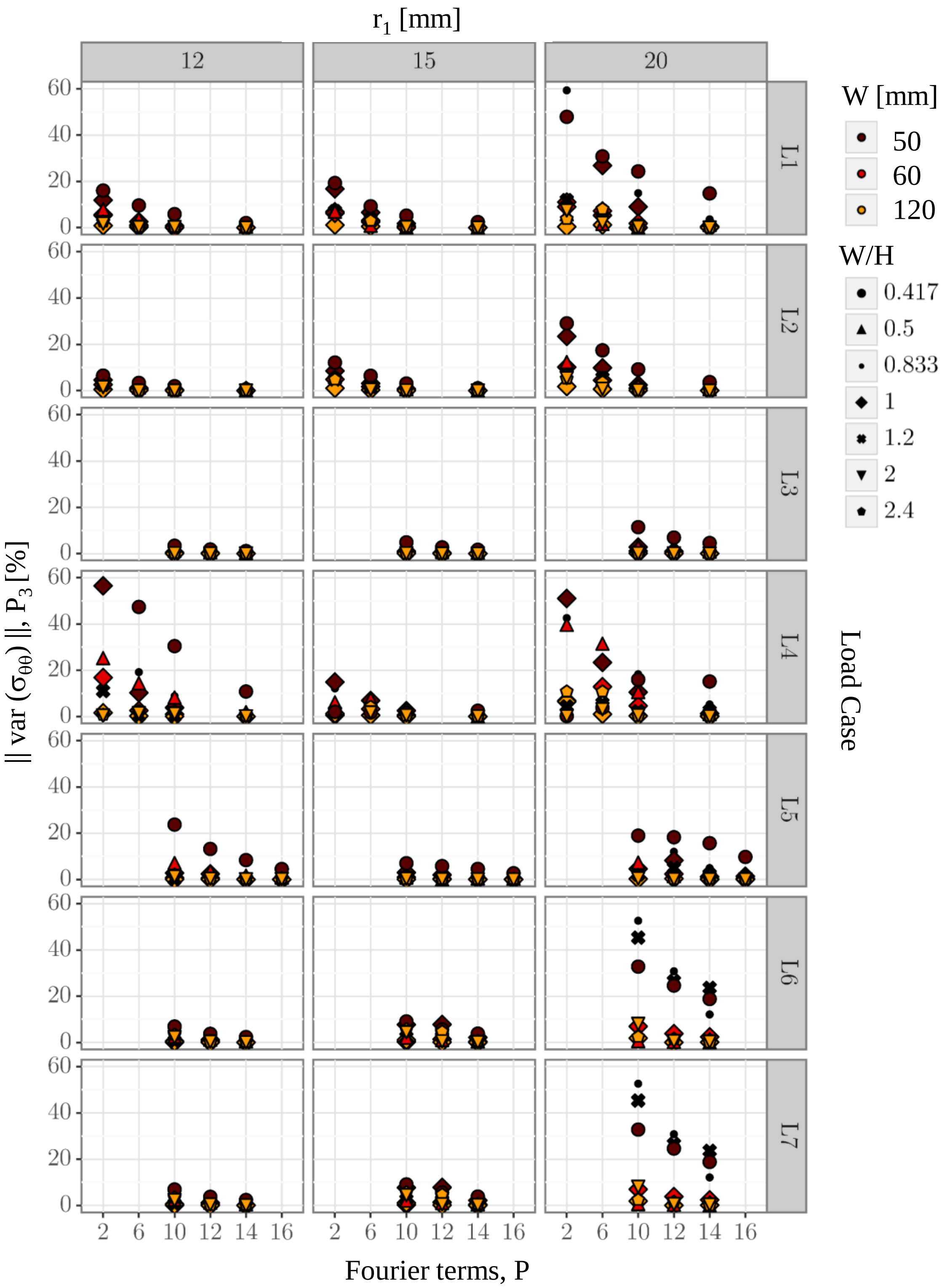

Figure V.16. Convergence analysis for $\sigma_{\theta\theta}$ at point P3 for rectangular plates of width W and height H, under different load cases and r_1 values.

5.3.2.2. Stress fields comparisons

The preceding section delved into the deviations in convergence without establishing a reference to the absolute values of the stresses at the investigated points. High errors in a region with low stresses might still be acceptable, underscoring the importance of evaluating the actual stress values rather than just their errors. To address this aspect, this section directly reports the comparison between model predictions and Finite Element (FE) results in terms of stresses along various paths in selected cases. Additionally, the results are compared with predictions from the previous model for infinite plates to explicitly highlight the improved accuracy of the new solution.

The examined plates featured a central hole with a radius r_0 = 10 mm, varying width between 50 and 60 mm, height ranging from 50 to 250 mm, and reinforcement annuli of thickness s = 2, 5, and 10 mm. Stresses were assessed along five paths according to Figure V.17, comprising three straight paths starting from the hole center inclined along θ = 0°, 45°, and 90° directions (paths 1, 2, and 3, respectively), one along the hole boundary (path 4), and the last along the boundary of the reinforcing region (path 5). Analyzed loading conditions included uniaxial tension, biaxial tension, and uniform/non-uniform internal pressure. The materials used in the FE analyses matched those in the convergence analyses, and the number of terms for Fourier expansions for analytical evaluations was consistently 10, aligning with the convergence analysis target of an overall error of less than 5%.

Across all discussed cases, the agreement between the proposed model and numerical analyses is excellent. Notably, the model for infinite plates tends to either underestimate or overestimate stress concentrations depending on the configuration, while the proposed model adeptly approximates stress fields along the hole boundary.

Figures V.18 and V.19 highlight stresses along the boundary of the reinforced region (path 5) and along path 3 for a reference 60x60 mm² plate with $s/r_0 = 1$ under the same loading conditions. The proposed model consistently outperforms the infinite plate theory, especially evident in the overestimation of stress concentration by almost 30% in the radial stress of Figure V.18 and hoop stress of Figure V.19.

Figures V.20 and V.21 present stress components for a 60x250 mm^2 rectangular plate under biaxial tension and internal constant pressure along paths 2 and 1, respectively. The proposed solution demonstrates remarkable accuracy in these cases.

Figure V.22 focuses on a circular plate with a central hole under external tension and internal pressure, showing that the proposed formulation provides an exact solution in this particular case, aligning perfectly with numerical analyses.

Figures V.23-25 explore cases of non-constant loadings, particularly considering internal pressure exerted by a pin, as per Equation V.66.

Figure V.26 emphasizes that the convergence analysis, while showing high errors at one point, can still be an excellent approximation of overall stress fields. Despite a relative error of up to 75% in the case of load case L4 and angular stresses at P2, the predicted stresses along path 1 align excellently with Finite Element analysis, with the higher error at the normalized distance $(r-r_0)/s = 1$ attributed to the normalized stresses in that point being close to null.

In summary, the model consistently exhibits excellent agreement with numerical analyses in all discussed cases, showcasing significant improvements over the infinite plate theory. Particularly, the latter solution's hoop stress is severely affected by the finiteness of the plate. Thus, for practical engineering applications involving finite-sized bodies, the solution presented in this manuscript offers superior modeling of plate stress and displacement fields compared to the closed-form solution presented in the previous chapter, justifying the additional efforts invested in addressing this problem.

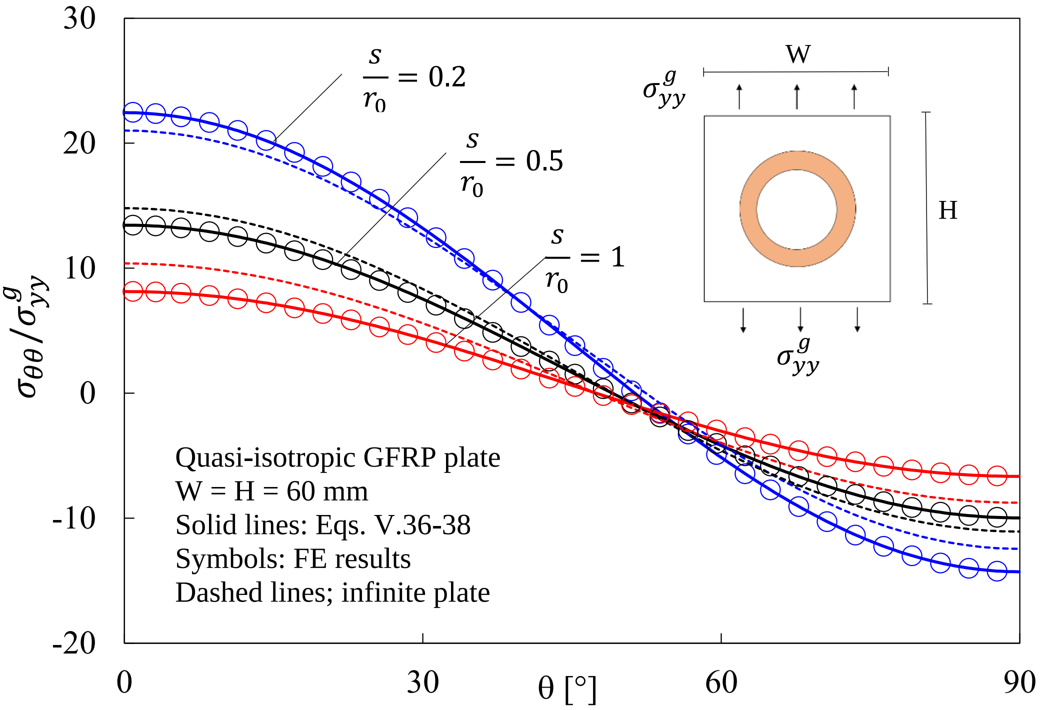

Figure V.17. Stress component $\sigma_{\theta\theta}$ evaluated along the boundary of the hole (path 4 in Figure V.13). 60x60 mm isotropic plates made of quasi-isotropic GFRP; hole radius r_0=10 mm reinforced with rings of width s = 2, 5 and 10 mm. Applied load according to load case L1. Analytical solution compared with the results from FE analyses and infinite plate theory.

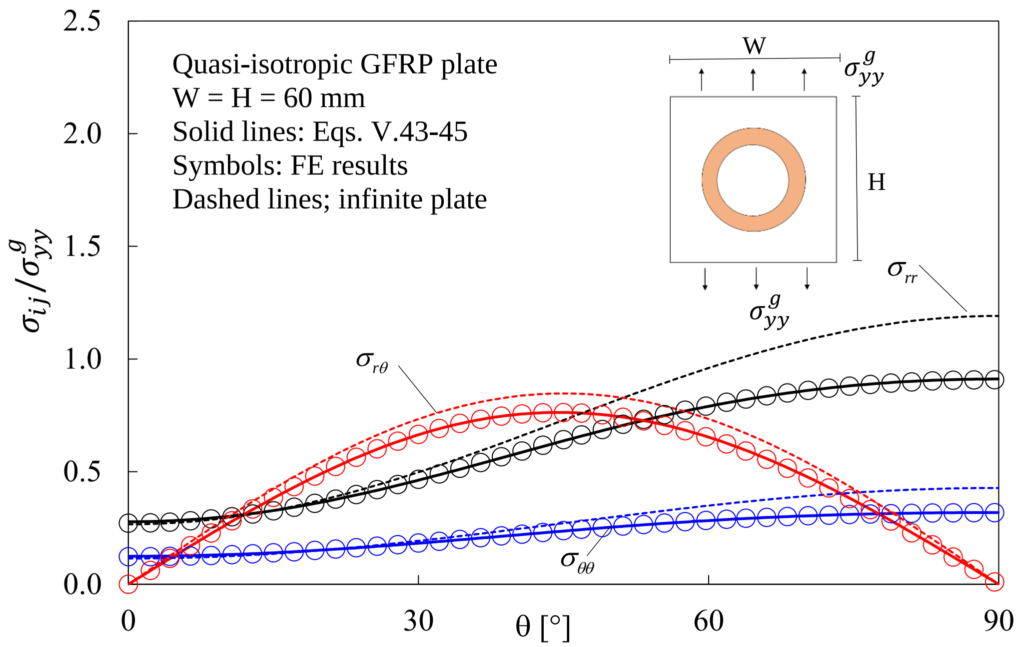

Figure V.18. Stress components $\sigma_{rr}, \sigma_{\theta\theta}, \sigma_{r\theta}$ evaluated along the edge of the reinforcing ring (path 5 in Figure V.13) in the plate material. P = 10; 60x60 mm plates made of quasi-isotropic GFRP; hole radius r_0 = 10 mm reinforced with a ring of width s =10 mm. Applied load according to load case L1. Analytical solution compared with the results from FE analyses and infinite plate theory.

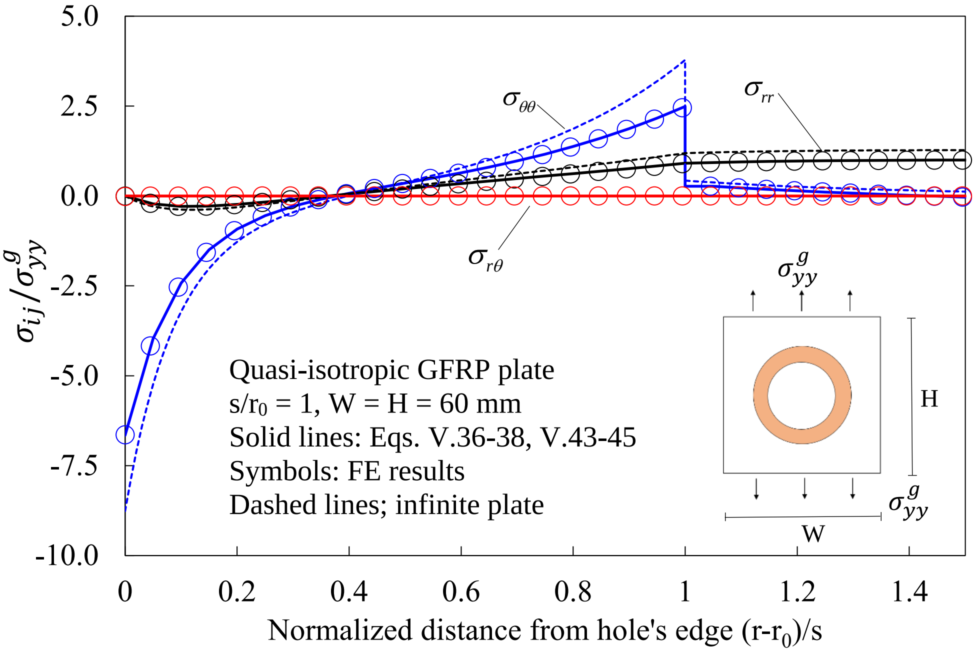

Figure V.19. Stress components $\sigma_{rr}, \sigma_{\theta\theta}, \sigma_{r\theta}$ evaluated along a straight path with θ = 90° (path 3 in Figure V.13). P = 10; 60x60 mm plates made of quasi-isotropic GFRP; hole radius r_0 = 10 mm reinforced with a ring of width s = 10 mm. Applied load according to load case L1. Analytical solution compared with the results from FE analyses and infinite plate theory.

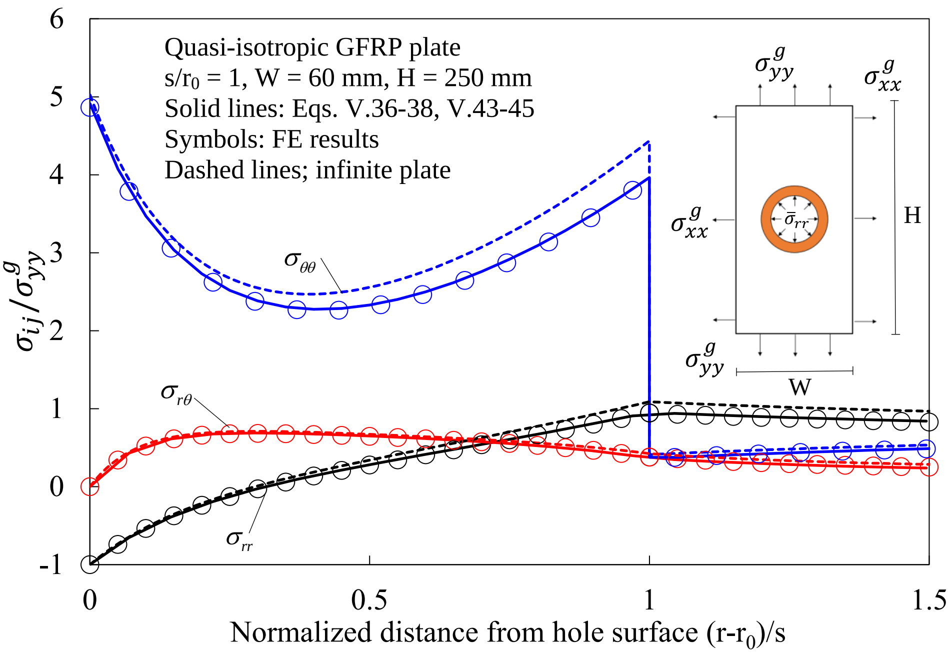

Figure V.20. Stress components $\sigma_{rr}, \sigma_{\theta\theta}, \sigma_{r\theta}$ evaluated along a straight path with θ = 45° (path 2 in Figure V.13). P = 10; 60x250 mm plates made of quasi-isotropic GFRP; hole radius r_0 = 10 mm reinforced with a ring of width s = 10 mm. Applied load according to load case L2. Analytical solution compared with the results from FE analyses and infinite plate theory.

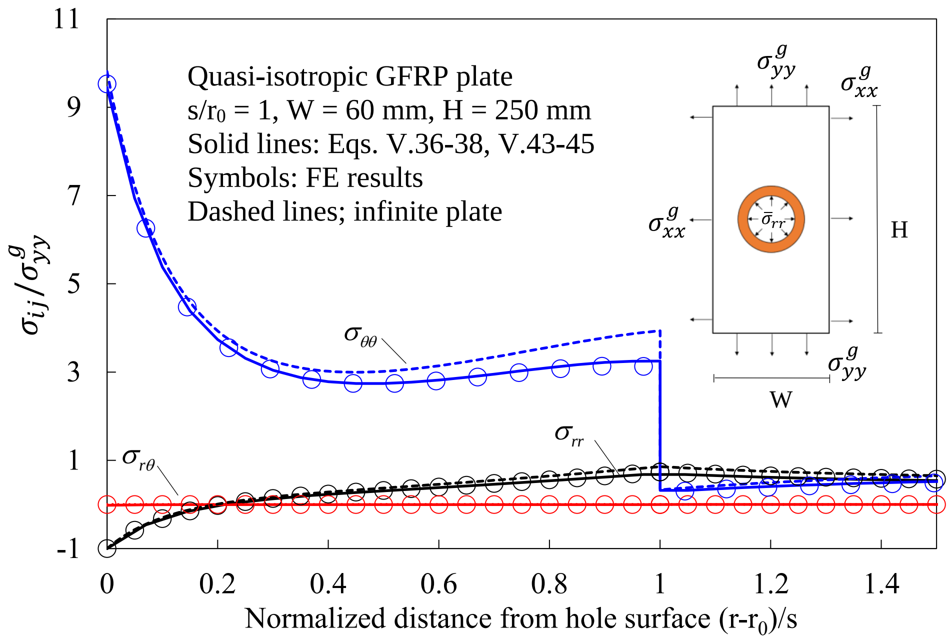

Figure V.21. Stress components $\sigma_{rr}, \sigma_{\theta\theta}, \sigma_{r\theta}$ evaluated along a straight path with θ = 0° (path 1 in Figure V.13). P = 10; 60x250 mm plates made of quasi-isotropic GFRP; hole radius r_0 = 10 mm reinforced with a ring of width s = 10 mm. Applied load according to load case L2. Analytical solution compared with the results from FE analyses and infinite plate theory.

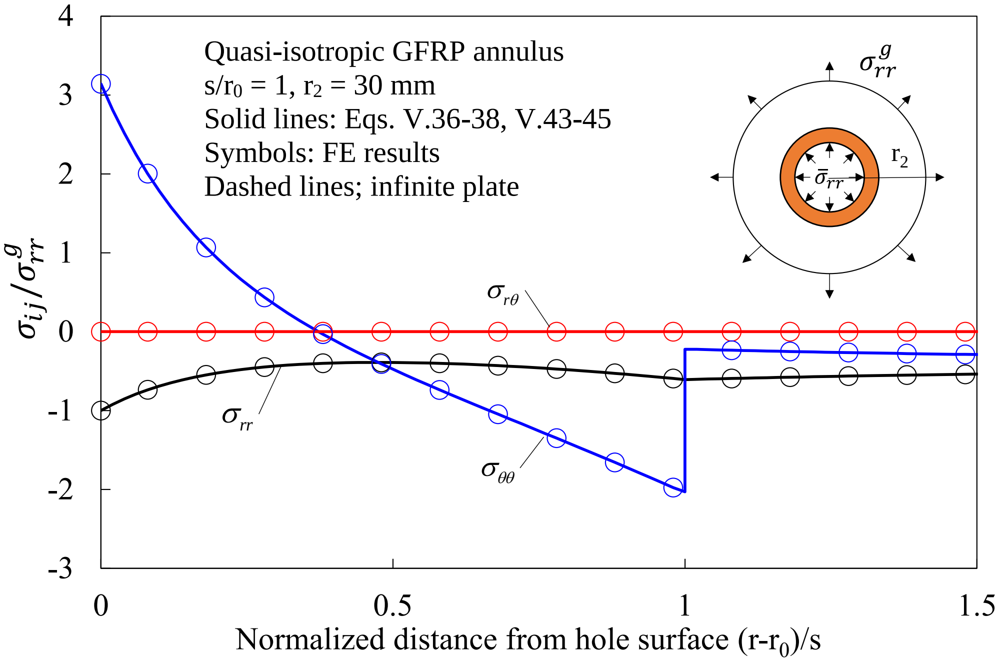

Figure V.22. Stress components $\sigma_{rr}, \sigma_{\theta\theta}, \sigma_{r\theta}$ evaluated along a straight path with θ = 45° (path 2 in Figure V.13). Quasi-isotropic GFRP annulus of external radius r_2 = 30 mm internal radius r_0 = 10 mm reinforced with a ring of width s = 10 mm. Applied loads: external radial tension ($\sigma_{rr}^{g} = 100\,\text{MPa}$) and internal pressure ($\bar{\sigma}_{rr} = -100\,\text{MPa}$). Analytical solution compared with the results from FE analyses.

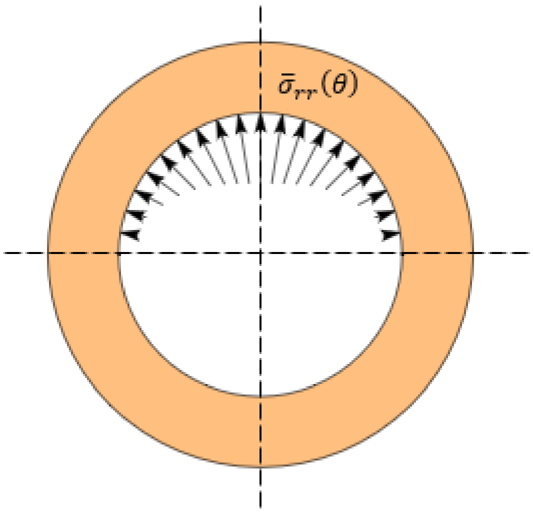

(a)

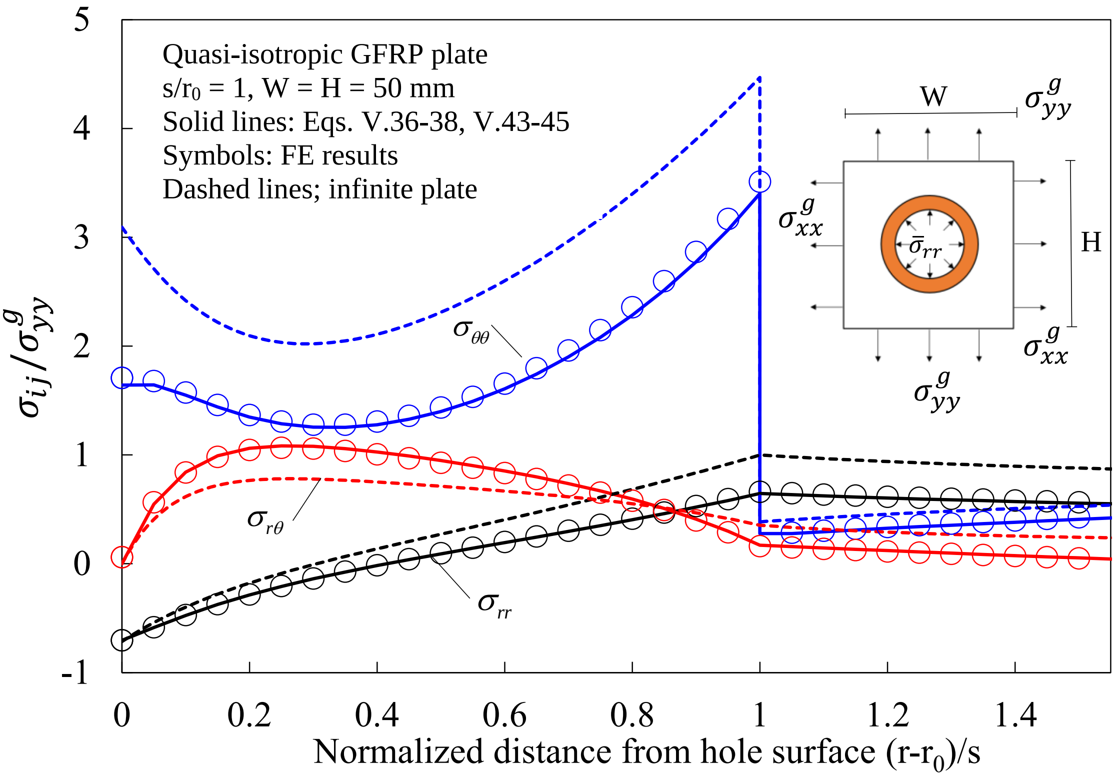

(b)

Figure V.23. (a) Schematic of the internal pressure exerted by a pin, according to the Eq. V.66. (b) Stress components $\sigma_{rr}, \sigma_{\theta\theta}, \sigma_{r\theta}$ evaluated along a straight path with θ = 45° (path 2 in Figure V.13). P = 10; 50x50 mm plates made of quasi-isotropic GFRP; hole radius r_0 = 10 mm reinforced with a ring of width s = 10 mm. Applied load according to load case L3, non-uniform internal pressure according to Eq. V.66 (see also Figure V.23a). Analytical solution compared with the results from FE analyses and infinite plate theory.

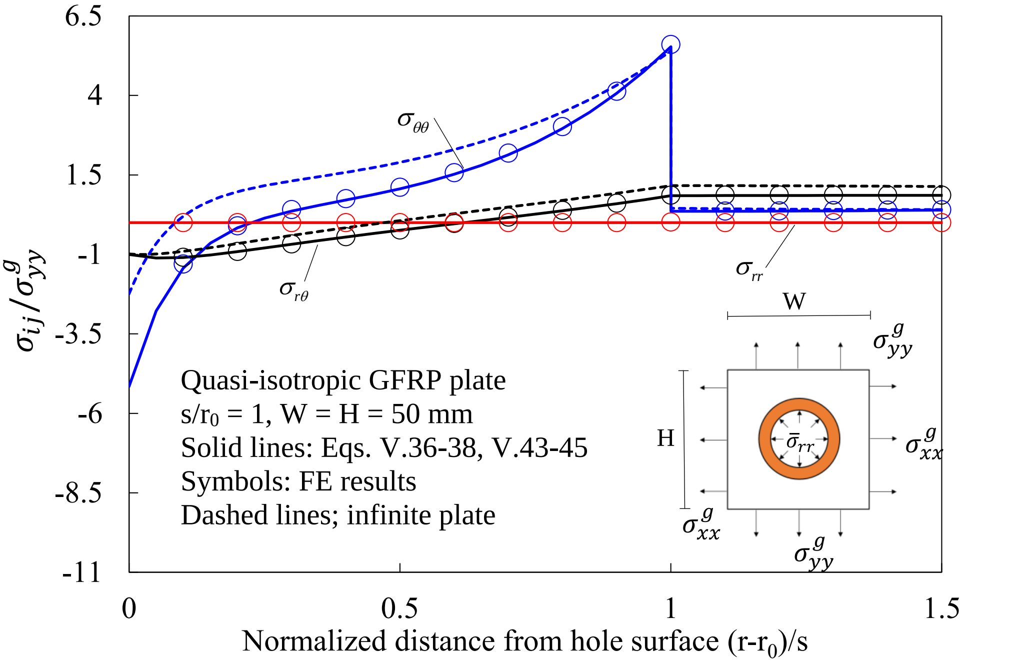

Figure V.24. Stress components $\sigma_{rr}, \sigma_{\theta\theta}, \sigma_{r\theta}$ evaluated along a straight path with θ = 90° (path 3 in Figure V.13). P = 10; 50x50 mm plates made of quasi-isotropic GFRP; hole radius r_0 = 10 mm reinforced with a ring of width s = 10 mm. Applied load according to load case L3. Analytical solution compared with the results from FE analyses and infinite plate theory.

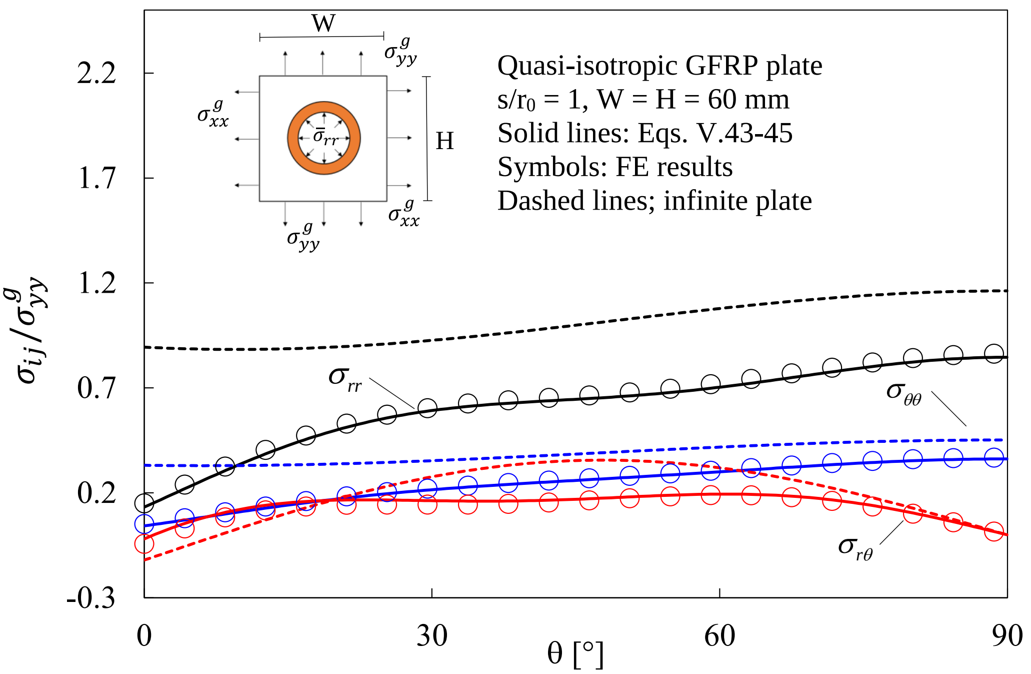

Figure V.25. Stress components $\sigma_{rr}, \sigma_{\theta\theta}, \sigma_{r\theta}$ evaluated along the edge of the reinforcing ring (path 5 in Figure V.13) in the matrix. 60x60 mm plates made of quasi-isotropic GFRP; hole radius r_0 = 10 mm reinforced with a ring of width s = 10 mm. Applied load according to load case L5. Analytical solution compared with the results from FE analyses and infinite plate theory.

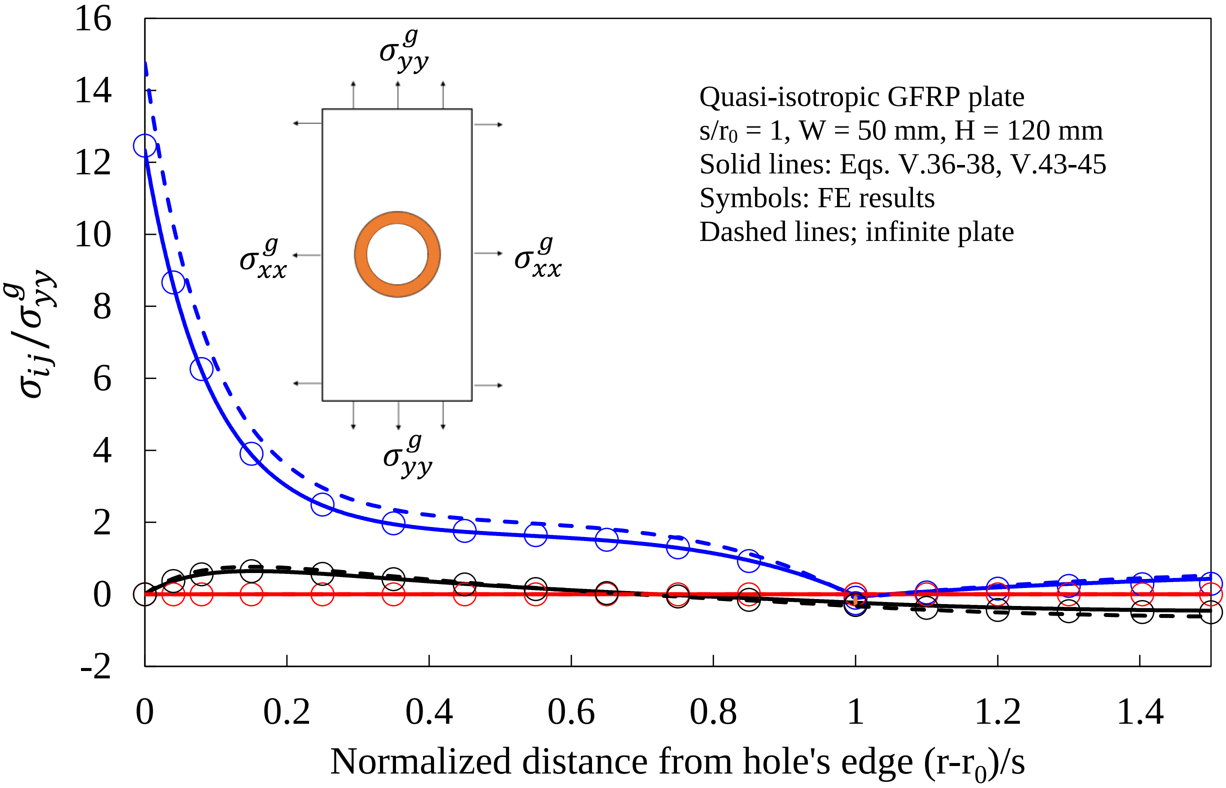

Figure V.26. Stress components $\sigma_{rr}, \sigma_{\theta\theta}, \sigma_{r\theta}$ evaluated along a straight path with θ = 0° (path 1 in Figure V.13). P = 14; 50x120 mm plates made of quasi-isotropic GFRP; hole radius r_0 = 10 mm reinforced with a ring of width s = 10 mm. Applied load according to load case L4. Analytical solution compared with the results from FE analyses and infinite plate theory.

5.3.3. Discussion and comparison with experimental results

To increase the validity of the proposed model, an experimental campaign was carried out comparing the analytical strain fields obtain through the proposed analytical model with the strain fields of 3D printed plates measured via DIC technology.

5.3.3.1. Specimen description

Three rectangular plates with a central hole were manufactured using 9T Labs Red Series Build Module, using a 3D-printing system named Additive Fusion Technology (AFT).

The plates were made of PA12 thermoplastic material, with a polarly reinforced annulus around the hole, made with PA12 and continuous carbon fibre reinforcement with volume fraction $V_f \approx 45\%$, CF/PA12. The characterization of the material was previously done resulting in the elastic properties expressed in Table V.3, these are the properties that were used in the analytical model.

	E_1 [MPa]	E_2 [MPa]	G_{21} [MPa]	ν_{21}
CF/PA12	12700	5300	2000	0.014
	E [MPa]	ν		
PA12	1800	0.4		

Table V.3. Material properties used in the analytical model measured from 3D printed specimens with quasi-static mechanical testing.

The dimensions of the tested plates are shown in figure V.27, with a thickness of 3.3 mm. The rectangular plate has a height of 250mm and width of 43.3mm, there is a central circular hole of 20mm in diameter, the reinforcement annulus embracing the hole ha a thickness of 4.8mm and it is made of 6 layers of width 0.8mm arranged in a spiral around the hole. The thickness of the plate is composed of 16 layers of 0.2mm height, stacked on top of one another, the first layer attached to the printing plate is made of pure PA12 for manufacturing reasons, the other 14 layers are printed with the reinforced annulus. The reinforced layers are divided into two sections, a 0.18mm of actual reinforced layer and a 0.02mm interlayer of pure PA12 needed to guaranteeing the bonding of different layers. The starting point of the spiral configuration to create the reinforced section is then incrementally rotated by 24° from the horizontal axis for every layer according to Table V.4 to guarantee overall homogeneity in the whole plate.

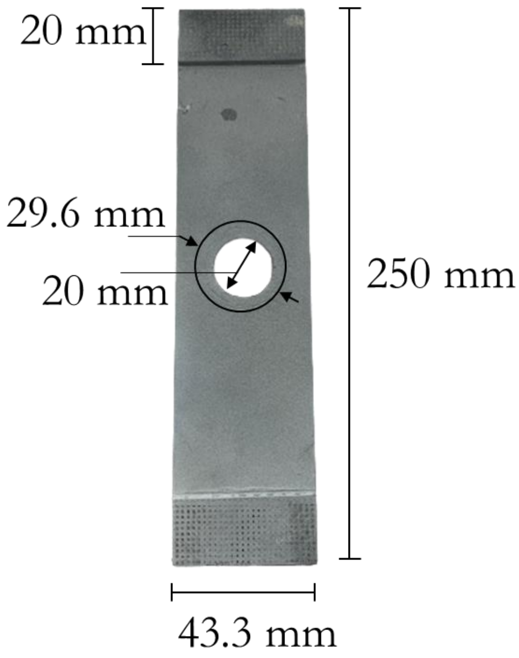

Figure V.27. Dimensions of the tested plates.

layer #	rotation angle [°]
1	0
2	192
3	24
4	216
5	48
6	240
7	72
8	264
9	96
10	288
11	120
12	312
13	144
14	336
15	168

Table V.4. Starting point rotation of the reinforcing spiral for every layer measured from the x axis.

The printing parameters used for the manufacturing process were:

Printing bed temperature: 100°C

Building chamber temperature: Off

Fibre nozzle temperature: 220°C

Plastic nozzle temperature: 230°C

Printing speed: 500 mm/min

Infill: rectilinear ±45°

The specimens were postprocessed in an oven at 185°C in a vacuum for 1.5h.

After the manufacturing procedure the specimens were subjected to tensile testing with a load of 2 kN with an MTS 809 axial/torsional servo-hydraulic machine equipped with a 100 kN load cell and displacement rate of 1 mm/min. The displacement fields were then recorded using a Gom Aramis DIC as shown in figure V.28, in a measuring area of 38 mm by 30 mm embracing the hole with a camera resolution of 4096 x 3000 pixels and 5 Hz of acquisition rate.

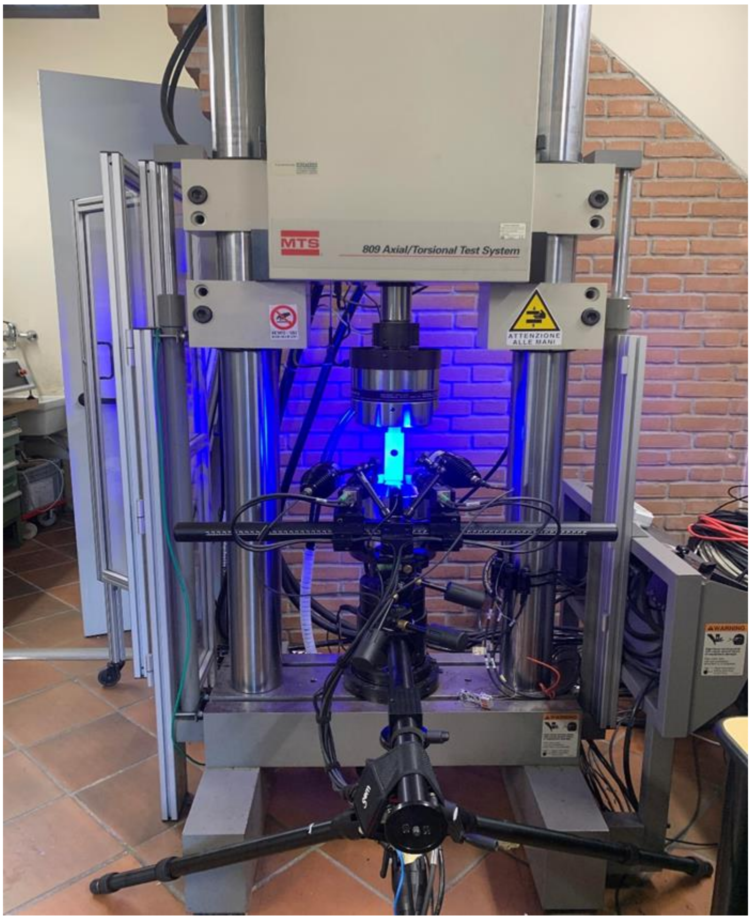

Figure V.28. Testing set-up for tensile testing and DIC measurement.

5.3.3.2. Results comparisons

The results of the measurements are summarized in figures V.29 and V.30, were contour plots of the ε_{yy} and ε_{xx} strain fields calculated with the analytical model are compared with the DIC measurements with a 0.5mm moving average. From these comparisons one can see that the overall agreement between the model and experimental results is very good.

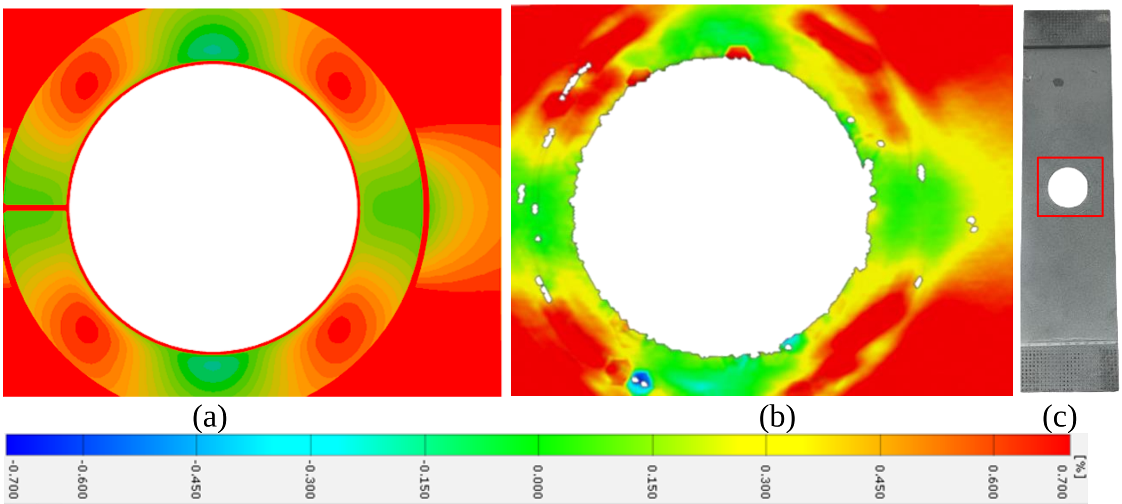

Figure V.29. Comparison of contour plot for ε_{yy} strain field in the observed region of the plate, (a) analytical model, (b) DIC measurement, (c) observed region of the plate.

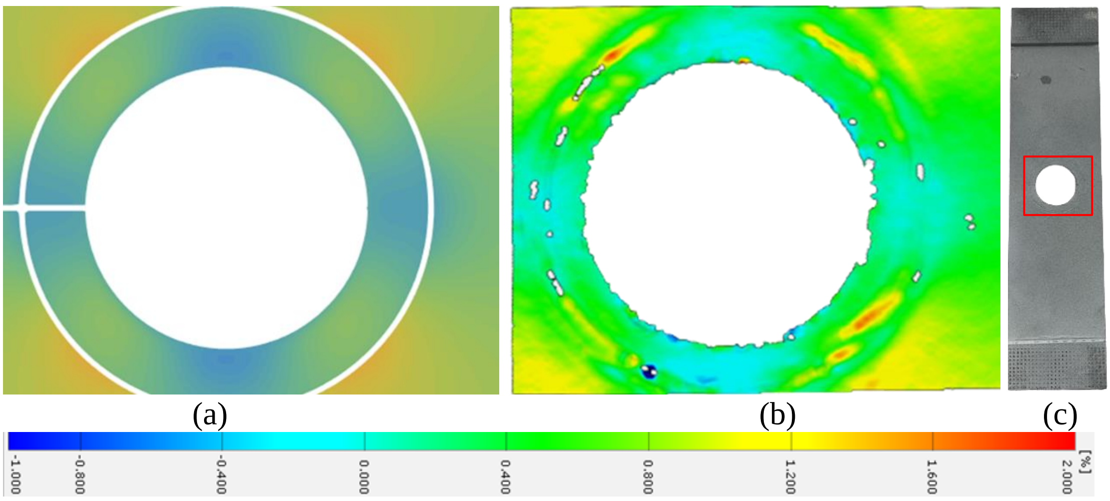

Figure V.30. Comparison of contour plot for ε_{xx} strain field in the observed region of the plate, (a) analytical model, (b) DIC measurement, (c) observed region of the plate.

In figures V.32 and V.33 a more precise comparison is made between the measured strain fields and the model results. The plots show the strain fields measured and calculated along the horizontal bisector line, shown in blue on the loading diagram in figure V.31. The DIC measurements were taken for every plate and the moving average value of all the data was calculated in a 0.05 mm domain and then plotted in the graphs with the standard deviations. These values are compared with the analytical model showing an overall good agreement between the two. Interesting to note how in the reinforced region, the DIC measurements reflect the spiral composition of the reinforcement in the specimens, while the analytical model shows the average level of strain as a result of the modelling choice of treating the reinforcement as a homogeneous material.

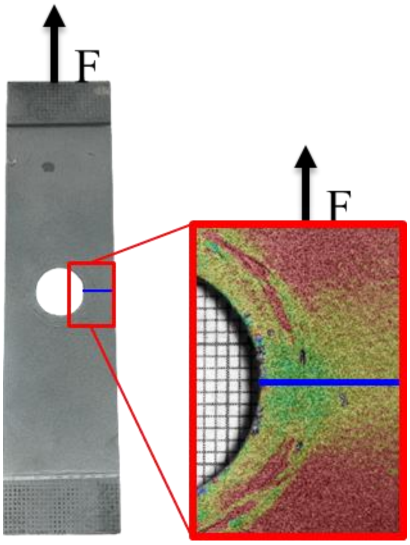

Figure V.31. Schematics of the path used for comparing the analytical solution with DIC experimental results

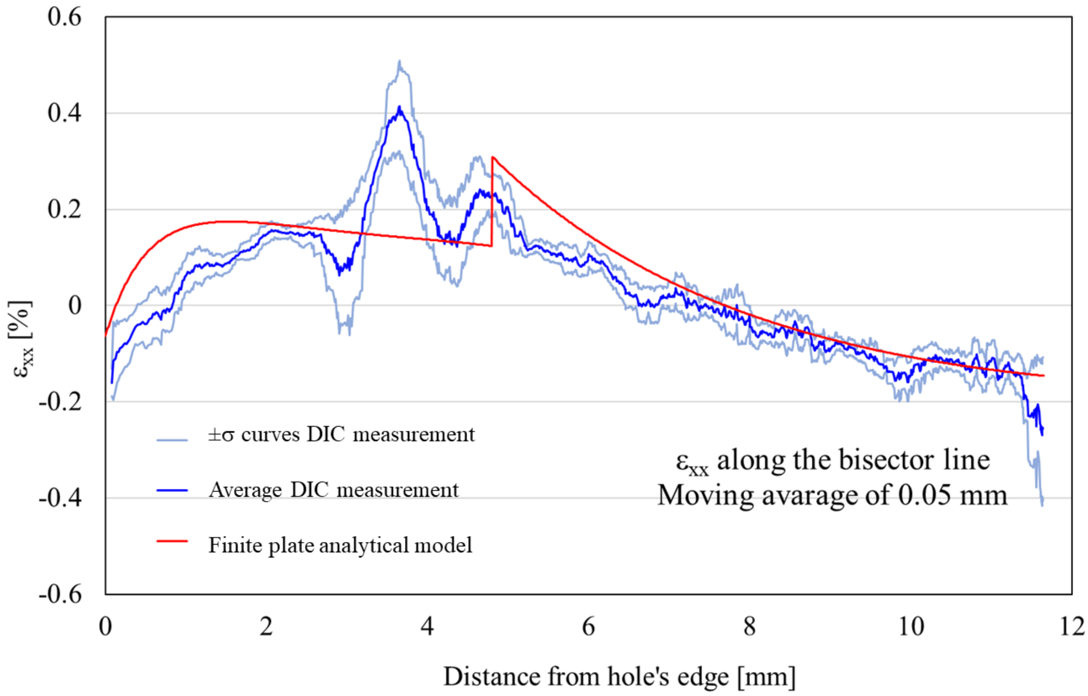

Figure V.32. Strain component ε_{xx} evaluated along the straight path with θ = 0° (Figure V.31) according to finite plate theory, comparison with DIC measurements of three 3D printed plates under 2000 kN tension force and a moving average of 0.05 mm.

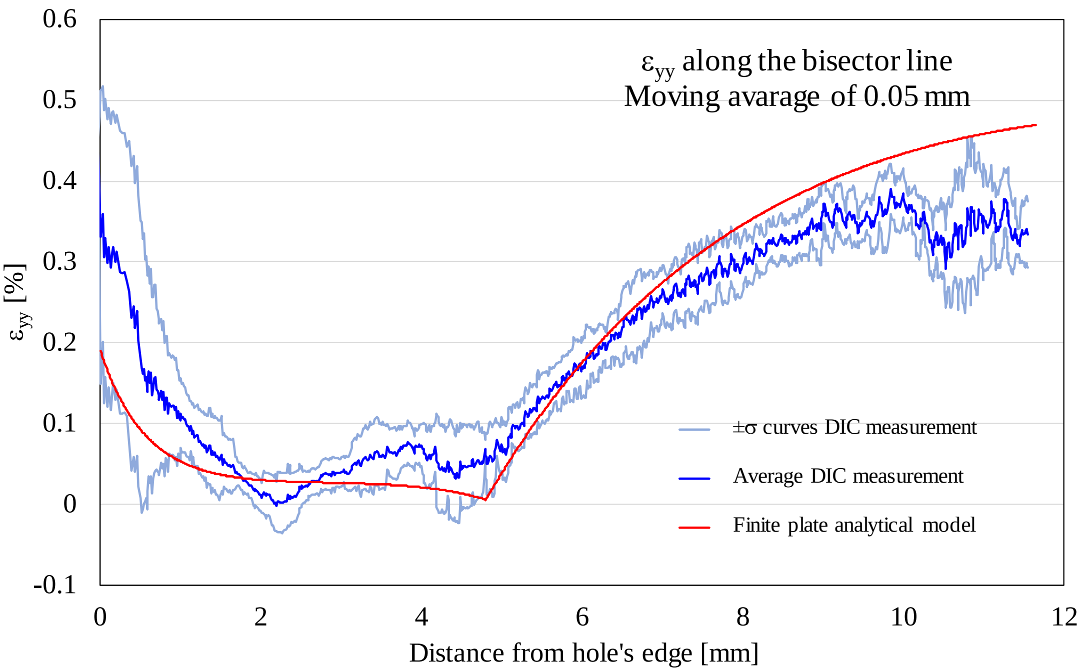

Figure V.33. Strain component ε_{yy} evaluated along the straight path with θ = 0° (Figure V.31) according to finite plate theory, comparison with DIC measurements of three 3D printed plates under 2000 kN tension force and a moving average of 0.05 mm.

5.4. Conclusions

This chapter introduces both an exact analytical solution for an isotropic infinite plate and an approximate solution for a finite plate, both featuring a circular hole reinforced with a polarly orthotropic material and subject to generic loading conditions. The proposed closed-form solution, exact for infinite bodies, adeptly captures the geometric features and elastic properties of the plate and reinforcing region. Its accuracy was extensively validated through comparisons with finite element analyses on diverse cases of plates with finite sizes, demonstrating highly satisfactory agreement. This analytical framework serves as a valuable tool for comprehending stress fields in polymeric components with reinforced holes, particularly those produced through fused deposition modeling technologies. Additionally, the approximate solution for finite plates, though not exact, exhibits remarkable accuracy across various plane loadings and geometric parameters. The solution's effectiveness was verified through comprehensive finite element analyses involving different combinations of geometrical and loading parameters, showcasing exceptional performance. Notably, the solution accommodates complex loading conditions with arbitrary precision, relying on a stable convergence of the proposed numerical method. The discussed solution was also tested against experimental results by measuring displacements and strains in three additive manufactured plates with a concentrically reinforced hole. The comparisons revealed a good precision of the model with the experimental tests, confirming its efficacy as a tool to predict stress fields in additive manufactured components.

5.5. References

1. E.G. Kirsch, "Die Theorie der Elastizität und die Bedürfnisse der Festigkeitslehre," Zeitschrift Des Vereines Deutscher Ingenieure, 42, 1898.
2. N.I. Muskhelishvili, "Some Basic Problems of the Mathematical Theory of Elasticity," Noordhoff International Publishing, Leyden, 1977.
3. S.G. Lekhnitskii, "Theory of Elasticity of an Anisotropic Elastic Body," AIP Publishing, 1964.
4. G. Savin, "Stress Concentration Around Holes," Pergamon Press, 1961.
5. M. Batista, "On the stress concentration around a hole in an infinite plate subject to a uniform load at infinity," Int J Mech Sci, 53, 2011, 254–261. DOI.
6. Y. Huang, R.K.N.D. Rajapakse, "Practical stress solutions for single-edge V-notched tension specimen," Theoretical and Applied Fracture Mechanics, 102, 2019, 193–209. DOI.
7. M. Zappalorto, M. Ricotta, "Understanding the effect of notches in orthotropic solids subjected to static loads," Theoretical and Applied Fracture Mechanics, 116, 2021, 103110. DOI.
8. M. Zappalorto, P. Lazzarin, "Stress fields due to inclined notches and shoulder fillets in shafts under torsion," J Strain Anal Eng Des, 46, 2011, 187–199. DOI.
9. M. Zappalorto, P.A. Carraro, "Stress distributions for blunt cracks and radiused slits in anisotropic plates under in-plane loadings," Int J Solids Struct, 56–57, 2015, 136–141. DOI.
10. M. Pastrello, A. Pontefisso, M. Zappalorto, "A new explicit solution for the mode I stress fields in notched orthotropic solids," European Journal of Mechanics - A/Solids, 97, 2023, 104819. DOI.
11. M. Pastrello, M. Salviato, M. Zappalorto, "Stress distributions in orthotropic solids with blunt notches under in-plane shear loadings," European Journal of Mechanics - A/Solids, 92, 2022, 104436. DOI.
12. M. Zappalorto, P.A. Carraro, "Two-dimensional stress distributions in tensioned orthotropic plates weakened by blunt V-shaped notches," Fatigue Fract Eng Mater Struct, 40, 2017, 804–819. DOI.

13. D.S. Sharma, "Stress distribution around polygonal holes," Int J Mech Sci, 65, 2012, 115–124. DOI.
14. J. Rezaeepazhand, M. Jafari, "Stress Analysis of Composite Plates with a Quasi-Square Cutout Subjected to Uniaxial Tension," Journal of Reinforced Plastics and Composites, 29, 2010, 2015–2026. DOI.
15. L. Quagliato, M. Ricotta, M. Zappalorto, S.C. Ryu, N. Kim, "Notch effect in 20% short carbon fibre-PA reinforced composites under quasi-static tensile loads," Theoretical and Applied Fracture Mechanics, 122, 2022, 103649. DOI.
16. M. Kazeruni, A. Ince, "Data-driven artificial neural network for elastic plastic stress and strain computation for notched bodies," Theoretical and Applied Fracture Mechanics, 125, 2023, 103917. DOI.
17. S. Karen Alavi, M.R. Ayatollahi, J. Jamali, M. Petru, "On the applicability of digital image correlation method in extracting the higher order terms in stress field around blunt notches," Theoretical and Applied Fracture Mechanics, 121, 2022, 103436. DOI.
18. A.A. Alshaya, "A developed hybrid experimental–analytical method for thermal stress analysis of a deep U-notched plate," Theoretical and Applied Fracture Mechanics, 124, 2023, 103753. DOI.
19. S. Cicero, S. Arrieta, M. Sánchez, L. Castanon-Jano, "Analysis of additively manufactured notched PLA plates using failure assessment diagrams," Theoretical and Applied Fracture Mechanics, 125, 2023, 103926. DOI.
20. A.R. Torabi, H. Talebi, M.R. Ayatollahi, M. Petru, "Mixed mode I-III fracture resistance of stainless steel 316L weakened by V-notches with end holes," Theoretical and Applied Fracture Mechanics, 122, 2022, 103574. DOI.
21. A.R. Torabi, B. Bahrami, M.A. Motamedi, H. Hasanvand, "On the use of Brazilian disk specimen for measuring mixed-mode I/II translaminar fracture toughness of notched glass/epoxy composite

laminates: A comprehensive study," Theoretical and Applied Fracture Mechanics, 121, 2022, 103541. DOI.

22. R.C.J. Howland, "On the stresses in the neighbourhood of a circular hole in a strip under tension," Philosophical Transactions of the Royal Society of London. Series A, Containing Papers of a Mathematical or Physical Character, 229, 1930, 49–86. DOI.
23. C.-B. Ling, "Stresses in a Notched Strip Under Tension," J Appl Mech, 14, 1947, A275–A280. DOI.
24. T. Wah, "Stresses in polygonal plates with circular holes," Eng Fract Mech, 23, 1986, 489–493. DOI.
25. Z. Pan, Y. Cheng, J. Liu, "Stress analysis of a finite plate with a rectangular hole subjected to uniaxial tension using modified stress functions," Int J Mech Sci, 75, 2013, 265–277. DOI.
26. C.-C. Lin, C.-C. Ko, "Stress and Strength Analysis of Finite Composite Laminates with Elliptical Holes," J Compos Mater, 22, 1988, 373–385. DOI.
27. X. Xu, L. Sun, X. Fan, "Stress concentration of finite composite laminates with elliptical hole," Comput Struct, 57, 1995, 29–34. DOI.
28. M. Salviato, M. Zappalorto, "A unified solution approach for a large variety of antiplane shear and torsion notch problems: Theory and examples," Int J Solids Struct, 102–103, 2016, 10–20. DOI.
29. M. Salviato, M. Zappalorto, L. Maragoni, "Exact solution for the mode III stress fields ahead of cracks initiated at sharp notch tips," European Journal of Mechanics - A/Solids, 72, 2018, 88–96. DOI.
30. M. Pastrello, A. Pontefisso, M. Zappalorto, "Exact in-plane stress field solution for isotropic plates with circular holes reinforced with cylindrically orthotropic rings," Theoretical and Applied Fracture Mechanics, 125, 2023, 103821. DOI.

31. M. Pastrello, A. Pontefisso, M. Zappalorto. (2023). "A semi-analytical solution for the in-plane stress fields in isotropic convex finite solids with circular holes reinforced with cylindrically orthotropic rings," Theoretical and Applied Fracture Mechanics, 128, 104146. DOI.
32. J.M. Dave, D.S. Sharma, "Stress field around rectangular hole in functionally graded plate," Int J Mech Sci, 136, 2018, 360–370. DOI.
33. Q. Yang, C. Gao, W. Chen, "Stress concentration in a finite functionally graded material plate," Sci China Phys Mech Astron, 55, 2012, 1263–1271. DOI.
34. L. Toubal, M. Karama, B. Lorrain, “Stress concentration in a circular hole in composite plate”, Composite Structures, 68-1, 2005, 31-36. https://doi.org/10.1016/j.compstruct.2004.02.016.
35. A.J. Belfield, T.G. Rogers, A.J.M. Spencer, “Stress in elastic plates reinforced by fibres lying in concentric circles”, J. of the Mechanics and Physics of Solids, 31-1, 1983, 5-54. https://doi.org/10.1016/0022-5096(83)90018-2.
36. A.J.M. Spencer, “Boundary layers in highly anisotropic plane elasticity”, Int. J. of Solids and Structures 10-10, 1974, 1103-1123. https://doi.org/10.1016/0020-7683(74)90061-4.

6. Conclusions

This thesis analyzes two of the main features that distinguish additive manufactured continuous fibre composite components from more traditional manufacturing processes: porosity defects and localized reinforcements.

An analytical framework and two different solutions have been developed that use a localize approach to obtain an accurate description of the stress fields in the vicinity of a porosity.

These solutions examine stress distributions in orthotropic solids with blunted notches under in-plane shear loading and under tensions. These models incorporate geometric and material parameters and involves a numerical optimization procedure. They offer general insights into the effects of key parameters, making it advantageous compared to fully numerical approaches. The role of stress field solutions in developing fracture criteria for notched bodies is highlighted, and the solution's applicability to orthotropic materials meeting specific conditions is emphasized.

These solutions are then incorporated into a 3D analytical framework developed to fully describe the three-dimensional stress fields in the proximity of a porosity in bodies subjected to shear loading and twisting. Three-dimensional theory of elasticity equations are transformed into two uncoupled equations, and the accuracy of the 3D stress field solution is discussed through comparisons with numerical data from 3D finite element analyses.

Key conclusions from the presented results include the coupling phenomena between loading modes in thick bodies, the correlation between the body thickness and the intensity of stresses induced by 3D effects, and the influence of the porosity root radius on induced stresses.

The attention is then shifted to the calculation of the magnitude of the stress fields near porosities and geometrical feature. A novel method is proposed for computing the intensity of the stress fields that do not rely on the use of Finite Element methodologies. The proposed algorithm involves minimizing the square of stress residuals on the component boundary, complemented by auxiliary boundary conditions for enhanced convergence. This method is applicable to a variety of contexts and problems like multi-material junctions, sharp or blunt corner notches and porosities, offering an effective alternative to finite element simulations. The proposed method is tested in simple cases like sharp V notches and bi-material joints and validated through comparisons with finite element analyses and demonstrated to be a valuable alternative to traditional methods and for sub-modeling large structures. Lastly an analytical model is developed that takes into account the effects of localized polar reinforcements around holes in plates.

Two models are presented:

- An exact analytical solution for isotropic infinite plates with circular holes reinforced by polarly orthotropic material
- An approximate solution for finite plates with circular holes reinforced by polarly orthotropic material.

The models show remarkable accuracy across various plane loadings and geometric parameters, validated through extensive finite element analyses and experimental tests on additive manufactured plates. This analytical framework is useful for understanding stress fields in polymeric components with reinforced holes and will serve as a solid base for future developments in more generalized cases.